DUALITY DERIVED TOPOLOGICAL MODEL OF SINGLE PHASE FOUR LIMB TRANSFORMERS FOR GIC AND DC BIAS STUDIES

THESIS BY:

LESLIE DAVID BORRILL
DEPARTMENT OF ELECTRICAL ENGINEERING
UNIVERSITY OF CAPE TOWN

SUPERVISOR:
PROF. C T GAUNT

A Thesis submitted to the University of Cape Town in fulfilment of the academic requirements for the Doctor of Philosophy degree in Electrical Engineering

Declaration

I declare that this thesis is my own original work. The knowledge generated by other researchers is acknowledged and referenced as appropriate.

The work contained herein has not been submitted to any other university or institution for any other degree or examination.

Leslie David Borrill

April 2017
Date

Dedicated in loving memory of my Dad

Richard Steven Borrill

Thank you for your exceptional work ethic that has left a lasting impression on me

An Abstract of

Duality derived topological model of single phase four limb transformers for GIC and dc bias studies

Thesis by
Leslie David Borrill

March 2017

Geomagnetic disturbances brought about by solar activity cause geo-electric fields in the Earth that drive geomagnetically induced currents through the earthed neutrals of transformers and through power transmission networks. The flow of these currents causes the magnetic cores of transformers to half-wave saturate. Saturated transformers pose problems for power system operators since they can cause harmonics, transformer heating, mal-operation of protection relays, generator heating and vibration, and consume a large reactive power that can cause voltage collapse.

Network studies of slow transient phenomena such as transformer half-wave saturation require appropriate models with parameters that represent the transformer transient state aptly. In this thesis a novel duality derived reversible model is developed of a single phase four limb transformer. The test transformers' non-step lap butt type core joints are shown to be problematic and the model is developed further to include the core joints. Due to the irregular core stacking method joint parameter determination is at best an approximation and the model is reduced to a duality compliant equivalent pi model for accuracy reasons. The pi model parameters and saturation characteristics are determined through laboratory testing and a complete pi model is presented.

An understanding of a single phase transformer's physical behavior to slow transients is undertaken through the use of appropriately developed test circuits. Search coils are used extensively to understand the transformer core's behaviour through flux mapping of the core and stray flux in the surrounding air space when the transformer saturates. Three phase testing is included using a three phase bank of test transformers. The electrical measurements of waveforms are analysed and fast Fourier transforms carried out to obtain the harmonic components. The effect on a motor load of the distortion caused by transformer half-wave saturation is determined.

A novel method of determining the effective core joint area of the problematic non-step lap butt type core joints is developed and a joint utilization factor is proposed that can be used in the absence of transformer manufacturer design information about this joint type in other transformer models.

Table of Contents

Chapter 9

Chapter 10

Acknowledgements

I would like to thank my research supervisor Prof. C T Gaunt for his patience and belief that kept me motivated and determined to succeed. You have an amazing ability to turn what at first appears to be a hopeless situation into a research opportunity.

To my wife, thank you for your love and support on this journey.

To my Father in heaven who answers my prayers through the knowledge of his son Jesus Christ, all praise be to your name.

In addition, I would like to thank:

the Eskom Power Plant Engineering Institute for the opportunity to conduct the research on a full time basis with financial support;

Hilary Chisepo my fellow PhD student for his friendship and the long days we spent in the laboratory debating theories and conducting tests;

Jan Scholtz - Eskom Distribution, Western Cape, for his support that made it possible to obtain test facilities and test equipment at the Eskom - Brackenfell complex;

Jos Doumen, Kees Spoorenberg and Coen de Beer - Royal Smit Transformatoren, for the donation of three test transformers and the technical discussions; and

Chris Wozniak – UCT electrical machines laboratory for providing the test equipment.

List of abbreviations

A_{rms}	Root mean square amperes
ac winding	Transformer winding with ac applied to it
AT	Ampere turns
cct	Circuit
csa	Cross-sectional area
dc winding	Transformer winding with dc applied to it
EMF	Electromotive force
EMTP	Electromagnetic transient program
FEM	Finite element method
FFT	Fast Fourier Transform
GIC	Geomagnetically induced current
GMD	Geomagnetic disturbances
GOES	Grain orientated electrical steel
GSU	Generator step-up
I_{ave}	The average current
IEC	International Electrotechnical Commission
IEEE	Institute of Electrical and Electronic Engineers
I_{oc}	Current flowing into the energized winding during a no load or open-circuit transformer test
I_{peak}	The peak current
I_{sc}	Current flowing into the energized winding during an impedance voltage or no short-circuit transformer test
IY	Interconnecting yoke
I_{nom}	Rated rms current of the transformer.
MMF	magnetomotive force
MSL	Multi-step lap
NSL	Non-step lap

PSCAD	Commercially available software simulation tool for analysing power systems transients. It is also known as PSCAD/EMTDC.
p.u.	per unit
RL	Return limb path
SC	Search coil.
SP-4L	Single phase four limb transformer
$T_{ambient}$	Ambient temperature at the time of taking a measurement
T1	Test transformer 1
T2	Test transformer 2
T3	Test transformer 3
t	Turns
THD	Total harmonic distortion. $\mathrm{THD} = \sqrt{\sum_{h=2}^{N} \left[\frac{I(h)}{I(1)}\right]^2}$
TDD	Total demand distortion. $\mathrm{TTD} = \sqrt{\sum_{h=2}^{N} \left[\frac{I(h)}{I_{rated}}\right]^2}$
V_{oc}	Voltage across the energised winding during a no load or open-circuit transformer test
V_{sc}	Voltage across the energised winding during impedance voltage or short-circuit transformer test
V_p	Voltage of the primary winding
V_s	Voltage of the secondary winding
V_{rms}	Root mean square volts
V_{knee}	The rms value of applied voltage at which the transformer core is at its maximum permeability. Beyond the knee point voltage the core's permeability drops off sharply.
WL	Wound limb

Chapter 1

Introduction

Geomagnetic disturbances brought about by solar activity cause geo-electric fields in the Earth that drive geomagnetically induced currents (GICs) through the earthed neutrals of transformers and through power transmission networks. The flow of these currents causes the magnetic cores of transformers to half-wave saturate. This produces distortion of the electrical current that can be detrimental to the power system operation.

Single phase power transformers are becoming more popular than very large three phase transformers as they are easier to transport because of their smaller physical dimensions. Single phase transformers are mainly of the two, three and four limb construction types. The four limb core form single phase transformer has not been extensively studied especially when subjected to both ac and dc (GICs included) components of current simultaneously.

1.1 Geomagnetically induced currents (GICs)

A GMD is a natural occurring phenomenon initiated by eruptions on the sun, also called solar activity. These eruptions can take the form of solar flares and coronal mass ejections (CMEs). Solar activity is caused by sun spots on the surface of the Sun. The occurrence of these sun spots follows an 11 year cycle where the peak or solar maximum of a cycle is defined by intensity and frequency of occurrence [Molinski 1996]. The frequency of geomagnetic storms therefore increases and decreases with the sunspot cycle.

In addition to eruptions there is also the solar wind which is rarefied plasma of protons and electrons emitted from the sun. Coronal holes are a prime source of high speed streams in the solar wind. They are long-lived, much longer than the roughly 27 day rotation period of the Sun and can exist for eight or nine rotations. If a coronal hole causes geomagnetic activity on one rotation, there is a potential for a repeat performance on later rotations [IEEE 1993; Boteler 2003].

Marti *et al.* [2013] explain that solar wind that is Earth directed interacts with the Earth's magnetic field producing geomagnetic disturbances (GMDs). Geomagnetic disturbances increase the electrojet in boreal and austral auroral zones. Charged particle movement in the conductive ionosphere increases the current flows in these electrojets, which are currents in the order of millions of amperes located more than 100 km above the Earth's surface. These electrojet currents induce quasi-dc voltages (0.1 mHz – 0.1 Hz) in transmission lines and the Earth that can drive the flow of GICs wherever there is a path for them to flow.

A GMD event can last for days and continually generates relatively low to moderate levels of GICs with several intermittent periods of high GICs. GICs of high magnitude exist for only a few minutes with each such maximum separated by relatively long times [IEEE 2013] .

1.2 Flow of GICs in Power Transformers

GICs flowing through the high voltage (HV) winding of transformers as illustrated in Figure 1.1 are the root cause of nearly all GMD-related issues in power systems. If a GIC is of sufficient magnitude it can cause half-wave saturation of the core of a power transformer.

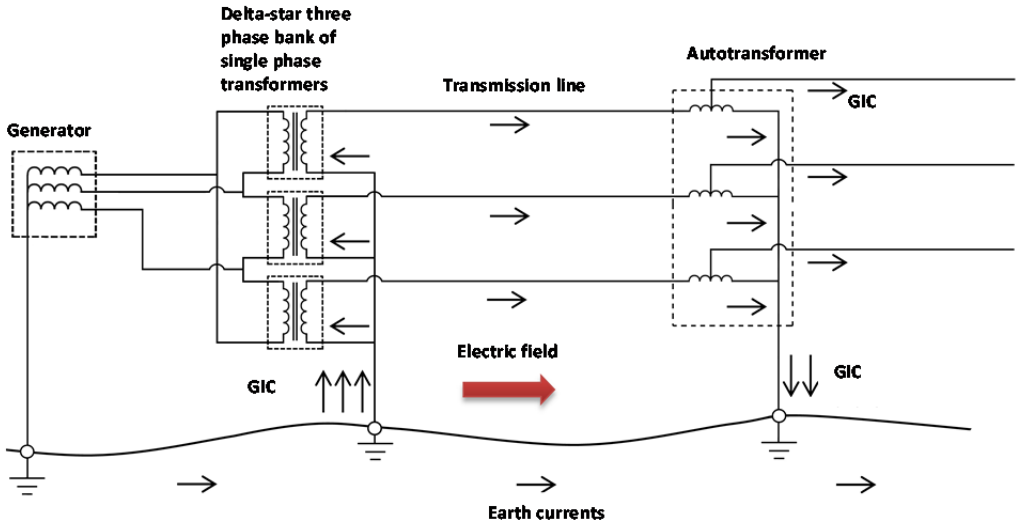

Figure 1.1. Geomagnetically induced current flow in a generator step-up transformer

The phenomenon is best described using the simplified example of a dc bias added to an isolated single-phase ac energised transformer. When a power transformer is subjected to dc it experiences a unidirectional dc flux in its core dependent on the dc polarity. The magnitude of this flux depends on the dc ampere-turns and reluctance of the magnetic circuit path followed by the dc flux. The dc flux adds to the ac flux in one half–cycle and when large enough, this leads to core peak flux densities in the range of core pre–saturation. At higher magnitudes of dc, the core provides a much higher reluctance to the dc ampere–turns. This results in a smaller further increase in the dc flux density shift. Correspondingly, the magnetizing current becomes a high peak short duration pulse as illustrated in Figure 1.2. The duration of this pulse is in the range of only 1/6th to 1/10th of the cycle. The exciting current in the other half-cycle is almost negligible. This highly non-linear current wave form is rich in odd and even harmonics [Price 2002; Girgis & Vedante 2012; EPRI 2012].

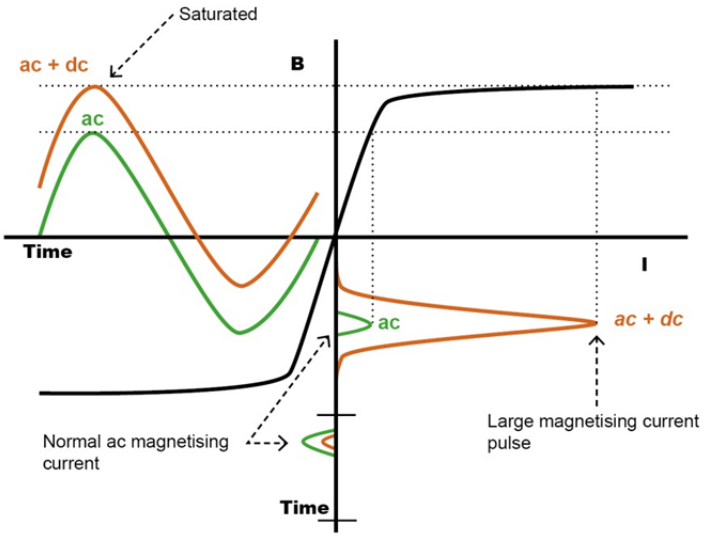

Figure 1.2 B-H curve showing part-cycle, semi-saturation in the core caused by dc flux shift [Dommel *et al.* 1986; Bolduc *et al.* 2000; Girgis & Vedante 2012].

Table 1.1 lists the power system symptoms that can occur with one or more transformers half-wave saturating.

Table 1.1 Power system symptoms associated with GIC saturation of transformers

Symptom	References
Even and odd current harmonics are generated	[Albertson *et al.* 1972; Molinski 2002; Boteler 2003; Berge 2011; Girgis & Vedante 2012]
Transformer heating	[Albertson *et al.* 1972; Molinski 2002; Boteler 2003; Berge 2011; Rezaei-Zare & Marti 2013; Girgis & Vedante 2012]
Mal-operation of protection relays	[Albertson *et al.* 1972; Boteler 2003; Molinski 2002; Berge 2011]
Abnormal transformer reactive power absorption and system voltage instability	[Albertson *et al.* 1972; Boteler 2003; Molinski 2002; Berge 2011; Girgis & Vedante 2012]
Generator rotor heating and vibration in the turbo-generator	[Gish *et al.* 1994; Molinski 2002; Berge 2011; Rezaei-Zare & Marti 2013]
Overloading capacitor banks	[Berge 2011; Rezaei-Zare & Marti 2013]

The core saturation phenomenon is more pronounced in single phase transformers since the flux return limbs seen in Figure 1.3 (b) provides a low reluctance path to the flow of zero sequence flux (dc bias flux). The three limb three phase transformer in Figure 1.3(a) with equal dc ampere–turns in each phase does not provide a zero sequence flux return path through its core and the flux will then follow the high reluctance path posed by the core top yoke-air-tank-air-core bottom yoke and this type of transformer will therefore be less affected by GICs [Girgis & Vedante 2012].

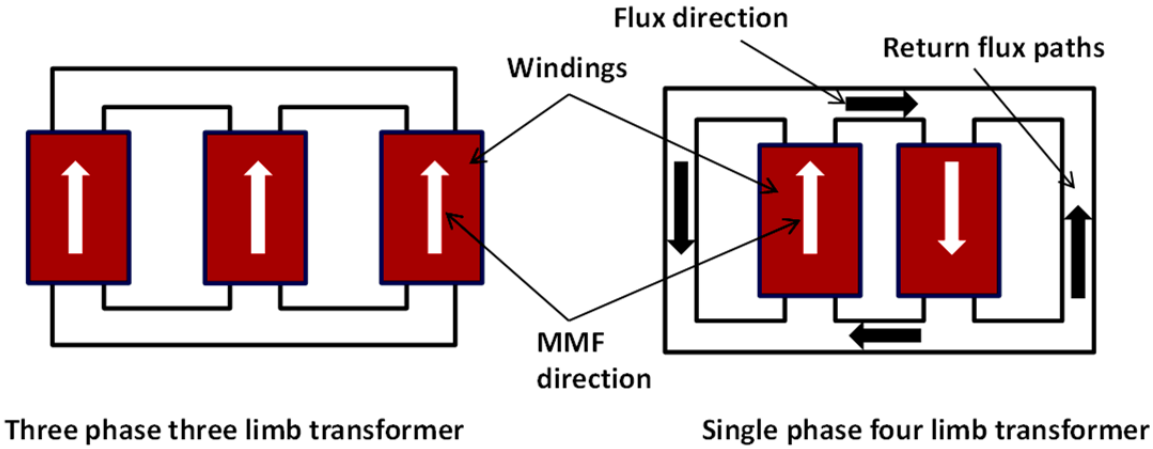

Figure 1.3 Core DC flux path in (a) three phase three limb core type transformer and (b) single phase four limb core form transformer (return path provided).

In order to understand the effect of GICs on a generator step-up (GSU) transformer (consisting of a bank of single phase transformers) and since ac and dc flux paths in transformers may vary with core designs as shown in figure 1.3, accurate transformer models are necessary to evaluate the impact of very low frequency transients flowing in the windings of a transformer.

1.3 Harmonic components in a GIC affected single phase transformer

Walling and Khan [1991] carried out electromagnetic transient program (EMTP) simulations on the effect of dc on a three limb single phase transformer bank, a three phase shell form transformer and a three phase five limb core form transformer. They report that the exciting current of the single phase transformer saturated by GIC has both even and odd-order harmonic components, with the overall trend for magnitude to decrease with increasing order at a given GIC magnitude [Walling & Khan 1991].

Furthermore, they mention that since harmonic current component phase angles are directly related to the fundamental voltage phase, the harmonics injected by transformers will tend to constructively and destructively interfere at various system locations [Walling & Khan 1991] .

Should these harmonics be of large enough magnitude and repetition, and be able to penetrate the delta winding of the GSU transformer, damage to the power station generators could occur [Gish *et al.* 1994; Rezaei-Zare & Marti 2013].

1.4 Large power plants

Large electrical power plants powered by a thermal cycle make use of either fossil or nuclear fuel for steam production. Should the GSU transformers at these plants part-cycle, semi-saturate under the influence of dc or quasi-dc, distortion is generated. The degree to which this distortion can penetrate the delta winding of a power transformer should be quantified to

determine of it could be a potential concern for the health of the generators at a power station. The electrical grid requirements at nuclear thermal plants differ from those of the fossil fuel plants and it should be determined if these requirements are compromised when dc or quasi-dc flow through their GSU transformers.

1.4.1 GSU transformers comprised of single phase transformer banks

Three phase transformers with very large power (1000 MVA and above) and voltage (400 kV and above) ratings have a physical size and weight that make them very difficult to transport. It is for this reason that GSU transformers at thermal power stations with large turbo-generators typically require a bank of single phase transformers connected in a three phase configuration instead of one single three phase GSU transformer. This statement is supported by 'The Infrastructure Security and Energy Restoration Office of Electricity Delivery and Energy Reliability U.S. Department of Energy'. In their report, 'Large Power Transformers and the U.S. Electric Grid', they assess the procurement and supply environment of large power transformers. The concluding remarks in the report notes the difficulty of transformer transportation and also mentions an EHV recovery transformer (RecX) that cuts down on transport and installation time. Utilising this 200 MVA single phase transformer entails constructing a 600 MVA three phase interconnected transformer bank [U.S. DEPT ENERGY 2012] .

Kappenman [EPRI 2006] reports that, 'grids are becoming increasingly vulnerable to GICs because: (a) 97% of transformers are single phase at 500 kV and 765 kV, b) megavolt amperes reactive (MVAR) consumption is larger on a per-ampere GIC basis for these larger transformers; c) winding resistance is lower in the larger transformers; and d) transmission line resistance per unit length decreases with increasing line voltage'.

Single phase transformer cores can be built with two, three and four limbs. The design considerations for single phase transformer core configuration are [EPRI 2009]:

- Steel utilisation – two limb single phase design is most efficient since all limbs are active.
- Shipping height limits – three and four limb single phase designs are such that they require yokes having only half of the active limb area.
- Window space - three and four limb single phase designs have reduced yoke height that allows more vertical space in the window within the core frame for windings and insulation, which has a beneficial effect on design economics for large transformers.
- Flux return limbs - three and four limb single phase designs have increased core weight and loss.

Electrical utilities with single phase GSU transformer banks installed have further advantages:

- The strategic spare transformer at the facility is a single phase transformer that is much cheaper than a three phase transformer spare meaning that less capital is tied up in the investment over the transformer life.

- Storage costs are cheaper for the single phase transformer as the storage facility, maintenance and long term storage routines are cheaper.

- Only the faulted transformer phase is replaced in the event of an internal transformer fault making recovery time for the effected generating unit much quicker.

There are however, disadvantages associated with the manufacturing duplication associated with single phase transformers but these are far outweighed by the advantages if measured over the transformer life cycle.

As transformer ratings continue to increase, the popularity of the four limb core form single phase transformers is also likely to increase, since it is physically and financially cheaper to transport and store for long periods until required in service. The core configuration of a four limb single phase transformer is illustrated in figure 1.4.

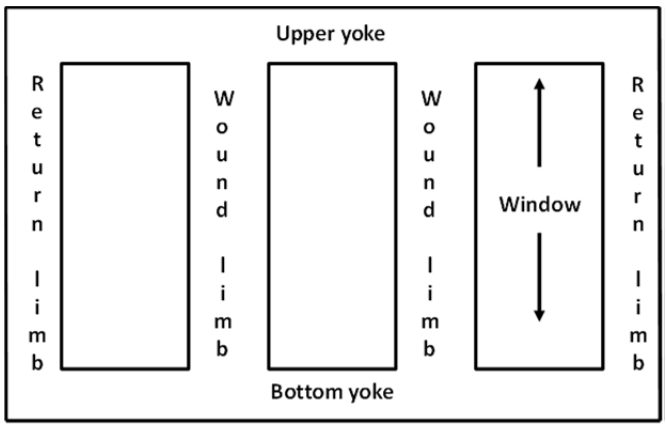

Figure 1.4 Core configuration of a four limb core type single phase transformer where the cross-sectional area (csa) of the yoke = csa of the return limb = 50% of csa of the wound limb.

As mentioned in section 1.2, single phase transformers are more prone to saturation by dc and GICs than three phase three limb transformers since they provide a path for zero sequence dc flux to flow in their magnetic circuits. In order to understand the core response of a single phase four limb transformer (SP-4L) or a three phase bank of SP-4L transformers requires research.

No evidence is found in the literature of a slow transient model of single phase four limb transformers either as a standalone transformer and/or in a three phase bank of transformers. Furthermore, all models in the literature ignore the core joints without mention of the reason for this exclusion. However, three references to four limb single phase transformers are found of which two consider flux distribution in the core at low to nominal induction levels and a further reference considers flux distribution in the core due to a GIC current with a value around the maximum magnetization current without GIC:

- Nakata & Takahashi [1985] carried out finite element method (FEM) studies of magnetic fields in transformer cores at 1.7 T. With respect to the SP-4L transformer they found that since the inner limbs are excited, with the outer limbs free, this created a phase difference and distortion of the flux waveforms that is greater than that of a two limb single phase transformer they studied.

- TeNyenhuis *et al.* [2000] perform accurate flux distribution and loss calculations on two, three and four limb single phase transformers at induction levels up 1.8 T and find that with respect to the four limb core it has a highly non-uniform flux distribution and high level of harmonics in the flux wave shapes.

- Mousavi *et al.* [2013] use FEM to model the magnetic flux density distribution in various core types due to a GIC current with a value around the maximum magnetization current without GIC. Among the core types is a four limb single phase transformer. The flux distributions show that the various single phase core types, comprising two limb, three limb and four limb, show similar behaviour. The reason is that the dc current can easily saturate the core in single phase transformers.

These findings may be of significance when testing for the effect of saturation due to dc bias current in this type of transformer since it may further increase the distortion caused by the large magnetising current pulses in half-wave saturation.

1.4.2 Nuclear power stations

Globally there is great sensitivity and opposition from lobby groups and the public at large to the use of nuclear energy in the electricity generation cycle.

Major incidents have occurred at the Three Mile Island, Chernobyl and Fukushima power stations in the USA, Russia and Japan respectively. This has resulted in a strong anti-nuclear sentiment internationally.

The U.S. Nuclear Regulatory Commission's regulation 10 CFR 50 Appendix A - General Design Criteria for Nuclear Power Plants [NRC 2014], has identified electric power as important to permit the functioning of structures, systems and components important to safety. Both the World Association of Nuclear Operators (WANO) and the Institute of Nuclear Power Operations (INPO) support these design criteria.

Undesirable phenomena such as the distortion caused when a transformer is driven into part-cycle, semi-saturation due to dc or GICs (quasi-dc) could be potentially damaging to the continuous operation of these power stations. The responsible attitude of utilities making use of nuclear power should be to determine the potential impact this distortion has on its plant.

The CP1, French pressurised water reactor design with a 900 MW_e output is of a vintage that requires the replacement of their GSU transformers shown in Figure 1.5. Life of plant requirements such as insulation paper degradation, dissolved gas analysis outside of the acceptable limits or in the extreme transformer failure have already occurred. These transformers are typically 3 limb single phase transformers. The replacement transformers in are likely to be SP-4L for reasons as already mentioned.

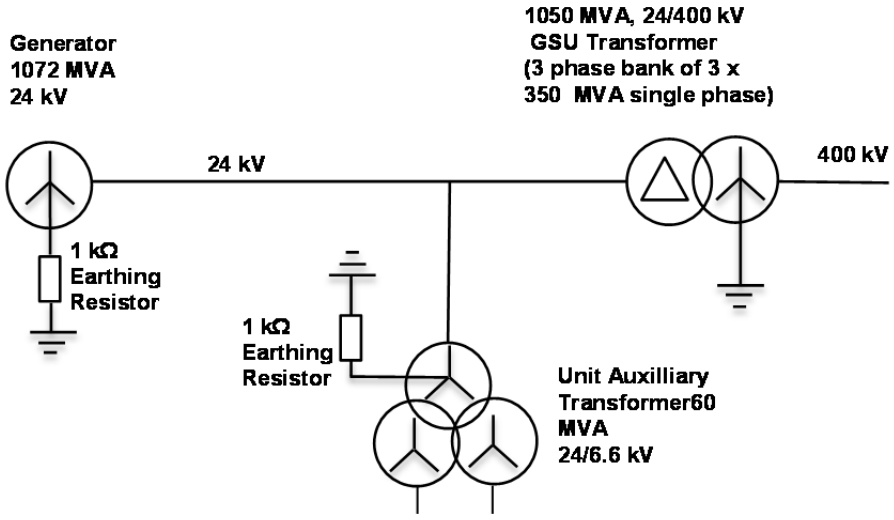

Figure 1.5 Generator power evacuation path of a typical French CP1 PWR nuclear power station.

1.5 Hypothesis

Martinez & Mork [2005] make the statement that the transformer is one of the weakest components of modern transient simulation software. Furthermore, Cigré [2000] explain that the exact representation of transformers in simulation software is complex. Opportunities therefore exist to develop more accurate EMTP transformer models. In order to study the effect on a nuclear power station when dc or GICs half-cycle saturate a bank of SP-4L transformers an appropriate transformer model is required.

Work by TeNyenhuis *et al.* [2000] and Nakata & Takahashi [1985] both indicate that there is distortion of the flux wave shapes in the core for the single phase four limb transformer at induction levels of up 1.8 T and 1.7 T for their respective studies. Furthermore, TeNyenhuis *et al.* [2000] state that a high level of harmonics in the flux can be expected. Mousavi *et al.* [2013] show a FEM model of a core flux distribution image of a four limb single phase transformer due to a GIC current. Their FEM image shows a similar core flux distribution to that of two and three limb single phase transformers and this demonstrates that dc can easily saturate the cores of single phase transformers.

Walling and Khan [1991] show through their EMTP simulations that dc biased single phase transformers of the two and three limb type produce odd and even harmonics. It is therefore conceivable that a SP-4L transformer will also produce both odd and even harmonics of higher magnitudes than those of the two and three limb types. It is speculated that laboratory testing will show that appreciable distortion occurs when a SP-4L transformer half-cycle saturates.

The preceding discussion demonstrates support for the need for a slow transient transformer model. An initial literature review shows that a transformer model for studying the effect of slow transients such as GICs and dc has not been developed for a four limb core form single phase transformer.

Duality derived topological model of single phase four limb transformers for GIC and dc bias studies

This thesis tests the following hypothesis:

A slow transient equivalent model of a single phase four limb transformer can be derived using the principle of duality that can be used to study its response to slow transient phenomena such as geomagnetically induced currents and dc.

1.6 Research Questions

In order to model a transformer its response to the phenomena specific to the model needs to be understood. Laboratory measurements conducted under the appropriate slow transient conditions are required to validate the derived model. This requires laboratory testing of the transformer both as a standalone single phase transformer and as a three phase bank of single phase transformers using a slow transient such as dc bias. The effect of an external load on the transformers response is also important for validating the derived model models performance as all transformers service a load in a real life scenario.

The following research questions are formulated to guide the research:

- Can flux search coils be used to map the flux response of a transformer?
- What distortion is created when a four limb core type single phase transformer saturates?
- How to derive an electrical equivalent circuit for a four limb core type single phase transformer that can be used to simulate the transformer's response under low frequency transient conditions, namely dc and GIC?
- Do the core joints constitute an important core component or can they be ignored in an equivalent circuit?
- Does the dc bias applied to a three phase bank of single phase transformers split equally between the phases?
- Is the distortion different when the three phase bank of single phase transformers saturates in a YNyn or YNd configuration?
- Does the addition of a load to the secondary of a dc biased three phase bank of single phase four limb transformers reduce the distortion caused by half-wave saturation?

A further research question relates not to the testing of the hypothesis as to the effects on other equipment, specifically motors, supplied from the transformer:

- Does the distortion contain signals that are harmful to motors?

1.7 Research methodology

A thorough literature review will be undertaken to gain knowledge and confirm the proposed research is a novel contribution. The literature review will look at:

- The types of models available for modelling transformers and the appropriate parameters to be included in a slow transient model,
- Distortion reported when transformers saturate,

- Industry standards for transformer testing useful for determining transformer equivalent circuit parameters,
- Published research methods for transformer testing for equivalent circuit parameter determination, and
- Electrical equivalent circuits, modelling parameters necessary and techniques available for creating an accurate model of a single phase transformer under slow transient conditions.

Laboratory work will entail the:

- Design of a test protocol and test circuits, and
- Extensive testing to answer the research questions and determine model parameters.

Desktop work will entail:

- Analysis of data and determining the relevance of the results,
- Determining how saturation evolves in the core as it responds to the ac and dc components of current,
- Application of the modelling principles to a single phase four limb transformer to derive a topologically correct equivalent circuit for modelling its behaviour to slow transients,
- Calculating the equivalent electrical circuit parameters for correct core and coil structures of the transformer from measurement data, and
- Populating the reversible electrical equivalent circuit.

1.8 Structure of the thesis

This section provides a brief outline of the chapters.

Chapter 2 reviews the literature to determine appropriate models for modelling transformer slow transient response, model parameters that are needed for such models, the need to include core joint details in the models, distortion that arises from transformer half-cycle saturation and the effect of the distortion on a rotating load such as a motor.

Chapter 3 develops a duality derived topologically correct model for assessing the slow transient response of the SP-4L transformer but excludes the parameter determination.

Chapter 4 describes the SP-4L test transformer design and identifies problematic areas for concern. Flux search coils are introduced as a tool for determining core flux distribution in the core and sources of stray flux leaving the core.

Chapter 5 provides a theoretical analysis of the core and its joints. The effect of inaccuracies and uneven core stacking are discussed and a method for assessing core joint quality is introduced that uses a joint utilization factor. The benefits of using multi-step lap mitred joints is demonstrated.

Chapter 6 provides a testing protocol required to answer the research questions and determine parameters of a reversible equivalent circuit model.

Chapter 7 presents and analyses the results of the testing relating to flux mapping the response of the SP-4L transformer core using search coils and distortion created when the transformer saturates when both ac and dc components are present in the transformer windings.

Chapter 8 calculates the pi equivalent circuit parameter values for the SP-4L test transformers and the duality derived reversible pi equivalent circuit is presented for EMTP GIC simulations.

Chapter 9 presents and analyses the results of the testing relating to the division of the dc bias current between the phases of a three transformer bank of single phase transformers, the distortion in the three phase bank and the effect of a motor load on the distortion. The effect of the distortion on the motor's performance is also analysed.

Chapter 10 assesses the hypothesis and answers the research questions.

1.9 Onward

Sufficient evidence is in the literature to make a prediction that four limb core form single phase transformers will produce distortion when biased by dc or GICs. A slow transient model for this transformer does not appear to have been developed. There is therefore a concern in that a potential problem cannot be examined meaningfully without proper investigation that requires better transformer models.

The next chapter explores to what extent the research questions have already been answered by others and finds relevant data and techniques that can be used to explore the validity of the hypothesis.

Chapter 2

Literature review

This chapter explores to what extent the research questions have already been answered by others and finds relevant data and techniques that can be used to explore the validity of the hypothesis.

2.1 Transformer modelling

Martinez & Mork [2005] make the statement that the transformer is one of the weakest components of modern transient simulation software. Furthermore, 'Guidelines for Representation of Network Elements when Calculating Transients' [Cigré 2000] states that the exact representation of transformers in simulation software is complex. Opportunities therefore exist to improve the simulation of the complicated behaviours of transformers, which include magnetic saturation of the core, frequency-dependency, capacitive coupling, and topological correctness of core and coil structure. Representation of some of the transformer parameters can be very complicated due to them being non-linear and frequency dependent. These non-linear and/or frequency dependent parameters are due to three major effects: saturation, hysteresis, and eddy currents [Martinez & Mork 2005].

2.1.1 White-box and grey-box transformer models

Gustavsen & Portillo [2014] explain that transformer white-box models can be categorized as lumped circuit models based on a spatial discretization of the windings. The model's parameters are based on a detailed description of the transformer's geometry and material properties and the model's parameters are extracted using formulae and/or finite-element method computations.

This view is shared by Jazebi *et al*. [2016b] who add that white-box models are built from basic electrical components such as inductors, resistor, capacitors. The components correspond to physical parts of the transformer structure and carry a physical meaning.

Both strongly agree that the main drawback of the white-box models is the need to gain access to the actual transformer dimensions and design details that normally are known only by the transformer manufacturer.

Jazebi *et al*. [2016b] describe grey-box modelling as using techniques that help overcome the limitations associated with access to the transformer's construction and material information. Grey box models are a compromise between black-box models (see below) and white-box models; they can be fairly accurate and retain some physicality. The topology and the structure components are derived physically as for white-box models but the model parameters are estimated from terminal measurement data, such as transformer open- and short-circuit tests and saturation inductance measurements. The open-circuit and short-circuit tests are also known as the no-load losses and excitation current, and load losses and impedance voltage tests respectively [IEEE Std C57.12.91-2011].

Black-box models on the other hand, take advantage of mathematical identification methods to fit the terminal behaviour of transformers with respect to field measurements (either time domain and/or frequency-domain data).

2.1.2 Low frequency transformer modelling based on measurements

Any model obtained from test measurements has the drawback that its performance can only be guaranteed for the tested transformer. Some general trends can be inferred from the tests, according to design, size and manufacturer, but accurate predictions for non-tested transformers cannot be assured [de León & Semlyen 1994*a*].

IEC (International Electrotechnical Commission) Standard 60076 and IEEE (Institute of Electrical and Electronics Engineers) Standard C57 both establish tests that are useful for determining parameters of some low-frequency transformer models [Martinez 2010].

The two main components to be considered when creating a low-frequency transformer model are the windings and the iron core. The windings' representation determines the transfer characteristic of the transformer (short-circuit response), while the iron core representation controls the flux balance (no-load response) and the phase-to-phase coupling [Chiesa 2010].

Transformer parameters required when modelling for low frequency transients are provided in Table 5 of Cigré guideline [2000]. These parameters can be determined from name plate ratings, excitation and short-circuit test data and the saturation curve. According to Table 5, short circuit impedance, saturation and eddy currents are very important when modelling low frequency transients (<3 kHz), iron losses are important and capacitive coupling has negligible effect.

2.1.3 Laboratory testing

Laboratory testing is used to determine parameters necessary for modelling and for developing a benchmark to validate the results obtained from transformer models [Martinez 2010].

Laboratory testing can be done using full scale power transformers where these and appropriate testing facilities are readily available [*Girgis & Nevins 1992; Gaudreau et al.* 2002; Chiesa 2010; Bachinger *et al.* 2013; Rezaei-Zare 2013] . Alternatively, small scale tests are acceptable for developing models where full scale testing is not available [Takasu *et al.* 1994; Berge, Varma & Marti 2011; Ngnegueu *et al.* 2012; Jazebi *et al.* 2013].

2.1.4 Transformer Models

In their review of transformer modelling for low- and mid-frequency transients, Martinez & Mork [2005] revealed that there are three distinct groups of transformer models. The first two groups are:

- The branch impedance or an admittance matrix (BCTRAN Model).

- The saturable transformer component model (STC model).

Both of these models have been implemented in the Electromagnetic Transient Program (EMTP) and both have important limitations but the main criticism is that they are not topologically correct. The STC model suffers from numerical instability and is limited to 3 windings. The BCTRAN Model permits only linear models and the non-linear excitation elements must be added externally at the model terminals.

The third group are topology-based models and form a larger group for which many approaches have been proposed. Their derivation is performed from the core topology and can represent very accurately any type of core design in low-frequency transients if parameters are properly determined.

Topology-based models are split into two subgroups:

- Duality models: models constructed with a circuit-based approach without any previous mathematical description, and
- Geometric models (Matrix Representation): core topology is considered, but their solution passes through a mathematical description.

Most low frequency transients are dominated by the behaviour of the transformer's magnetic core. Topology-based transformer models are used more extensively for low frequency electromagnetic transients modelling based on reports by Dick & Watson [1981]; Arturi [1991]; Narang & Brierley [1994]; Picher *et al.* [1997]; Chen & Venkata [1997]; Wang *et al.* [1999]; Iravani *et al.* [2000]; Cho [2002]; Li *et al.* [2010]; Chiesa [2010]; Høidalen *et al.* [2011]; Zirka *et al.* [2012]; de León *et al.* [2012]; Alvarez-Marino *et al.* [2012]; Jazebi *et al.* [2013]; Jazebi & de León [2015a] and Rezaei-Zare 2015].

2.1.5 Topological duality based model

Duality based models make use of the duality principle which enables derivation of an equivalent electrical circuit from magnetic equations in such a way that the effects of magnetic non-linearity are preserved [Cherry 1949; Slemon 1953]. They derive topologically correct electrical equivalent circuit models from a magnetic circuit model. This results in models that include the effects of saturation in each individual leg of the core, interphase magnetic coupling, and leakage effects. In the equivalent magnetic circuit, windings appear as magnetomotive force (MMF) sources, leakage paths appear as reluctances, and magnetic cores appear as saturable reluctances, [Martinez & Mork 2005].

To make models practically useful, the current sources resulting from the transformation are replaced with ideal transformers to provide primary to secondary isolation and coupling to the core, while preserving the overall primary to secondary turns ratios. Turns ratios are chosen so that core parameters are referenced to the low-voltage winding. The portion of a model inside the coupling transformers represents the core and leakages. Winding resistances and interconnection of the windings appear external to the coupling

transformers, so that the derived core equivalent functions are independent of the winding configuration.

Winding resistance, core losses, and capacitive coupling effects are not obtained directly from the transformation, but can be added to this equivalent electrical circuit. The negligible capacitive coupling effects in low frequency models can be excluded.

The literature shows that white- and grey box models exist for the single phase two and three limb transformers [Walling & Khan 1991; Arrillaga *et al.* 1997; Wang *et al.* 1999; Martinez *et al.* 2005; EPRI 2006; EPRI 2013; Jazebi *et al*. 2013; Rezaei-Zare 2015b; Jazebi *et al.* 2016a; Jazebi *et al.* 2016b]. Other than Mousavi [2012] where the single phase four limb transformer is modelled in FEM there appears to be no slow transient model for simulating this type of transformer in EMTP software programs.

De León et al. 2012 proved experimentally that the traditional T-model (also known as the Steinmetz equivalent circuit) for transformers is accurate for steady state studies. When dealing with low frequency transient phenomenon such as inrush currents the model yields large errors in simulations. De León explains that unlike the T-model there is one leakage inductance, L_S, since the leakage inductance cannot be divided into two inductances while still keeping a physical meaning. Figure 2.1 shows the equivalent circuit of a single-phase transformer, with concentric windings derived using the duality theorem [Slemon 1992; Wang et al. 1999; de León et al. 2012; Jazebi et al. 2013]. This equivalent circuit is termed the pi-model for a single-phase transformer. Elements internal to the ideal transformers physically represent the magnetic circuit. The two magnetising branches shown can have different values but typically $L_X = L_Y = 2L_m$ and $R_X = R_Y = 2R_C$ and L_m and R_C are the parameters determined from the transformer open-circuit test [Blume et al. 1967; Martinez-Velasco 2010].

Grey-box modelling makes use of the reduction of a duality derived model to an equivalent pi circuit and then specifying the parameter values including saturation characteristic for energisation from the different voltage windings [Jazebi *et al.* 2013]. Using the method of Jazebi *et al.* [2013] the final equivalent pi circuit is similar to that of Figure 2.1 but contains additional detail relating to the deep saturation of the transformer core.

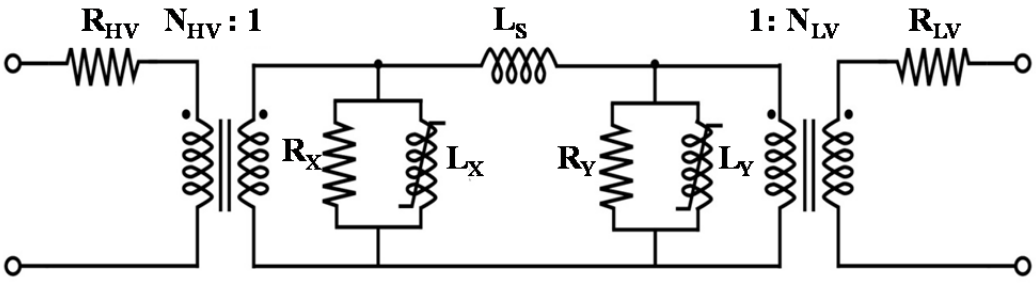

Figure 2.1 Pi-shaped model for a single phase transformer where:
R_{HV} and R_{LV} are the series resistances which include the Joule losses and eddy current losses in the HV and LV windings,
L_S represents the leakage inductance,
R_X, L_X, R_Y and L_Y represent the two magnetising branches and include non-linearities (saturation and hysteresis) and eddy current phenomena.

2.2 Non-linear magnetic core losses and saturation

Martinez-Velasco [2010] explains that low frequency transients saturate transformer cores. Saturation dominates the behaviour of the core and this parameter needs to be modelled correctly

2.2.1 Hysteresis loss

De León & Semlyen [1995] and Berge [2011] both agree that modern transformer iron cores have narrow hysteresis loops and that the hysteresis losses are much smaller than eddy current losses. The hysteresis loops of modern transformers have a negligible influence on the magnitude of the magnetizing current and the GIC phenomenon is a quasi-steady-state one. This allows the hysteresis to be ignored and all core losses can be lumped into the shunt resistance of Figure 2.2.

2.2.2 Eddy current loss in the core laminations

If the electrical resistance of the core is high, the eddy current will be low; therefore, a feature of low-loss material such as grain oriented electrical steel is high electrical resistance. Silicon is added to the steel used to manufacture the core laminations to increase its electrical resistivity and this reduces the eddy current losses [McLyman 2004].

The EMTP simulation conducted by Walling & Khan [1991] on a saturated three limb single phase transformer show all the consecutive harmonic orders present up to the fourteenth harmonic. This is due to the large asymmetrical exciting current once per cycle. These harmonics will contribute to some additional eddy current losses in the core but as stated below by Tarasiewicz et al. 1993 these will only slightly effect the model accuracy.

In figure 2.2 the iron path magnetization and eddy current losses are represented by L_m and R_c respectively. Tarasiewicz *et al.* [1993] demonstrated through extensive modelling of core losses that the core magnetising branch of figure 2.2 represents the core losses up to frequencies of 3 kHz with an accuracy of 5%.

Iravani *et al.* [2000] and Martinez-Velasco & Mork [2003] both agree that using the value of R_c closest to the transformer rated voltage provides a good estimate of core loss. Mork [1992] has shown low sensitivities to fairly large changes in $\boldsymbol{R_c}$ for single phase transformers. However, the same is not true for three phase transformers.

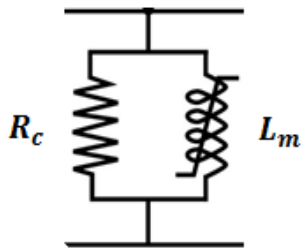

Figure 2.2 Transformer iron core model showing the core loss and magnetisation parameters.

The core loss parameter $\boldsymbol{R_c}$ is determined by the standard open-circuit test or no-load test as described in IEEE Std C57.12.91™ [2011]. The determination of the values of R_C and L_m parameters are dealt with in chapter 6.

2.3 Eddy current loss parameter of the windings

Winding resistances are frequency dependent and must incorporate eddy current and stray loss effects [Martinez-Velasco & Mork 2003]. The two physical phenomena, skin effect and proximity effect, occur simultaneously in the windings of a transformer and are the eddy current phenomenon of the windings.

Blume *et al.* [1967], provide useful insight into the effect that a properly constructed stranded conductor has on the stray losses of the winding. If the individual strands are insulated from each other and transposed in such a way that the leakage flux linkages of each strand is the same, the eddy current loss may then be calculated using the width of one strand.

Holmberg *et al*. [2003] and Krah [2005] use Cauer equivalent circuits to model skin effects in transformer windings. The windings of a coil that is wound with a stranded cable with a coaxial insulation system is modelled. They find that for frequencies up to 1000Hz the conductor resistance remained constant for the 1m sample conductor and the insulation between the strands does not affect the skin effect losses. In contrast to the skin effect the proximity losses are strongly dependant on the contact resistance between the strands. The simulations of the complete eddy current model show that the skin effect dominates the proximity losses below 1kHz in the coil, mainly because of the dc losses. Above 10kHz, the contribution from the proximity loss is larger, but for the coil studied, the skin effect still makes a substantial contribution to the losses at higher frequencies.

Jazebi *et al. [*2013] in their paper propose the use of a Physical Cauer circuit that fulfils the principle of duality in every aspect and precisely represents frequency dependency. They report that for low frequency transients (f_{max} = 3 kHz) the penetration depth is maximum (100%) for conductor diameters less than 4mm and that frequency dependent modelling is unnecessary.

2.4 Equivalent circuit parameters

Three phase transformer banks of single phase transformers have natural phase segregation and therefore do not suffer from magnetic interphase coupling. In single phase transformers that are phase segregated there are therefore three groups of parameters needed when deriving the equivalent circuit and model for a single phase transformer:

- The electrical windings parameters,
- The magnetic core parameters, and
- The core magnetic saturation representation in the model.

The winding and core parameter values are added to the pi equivalent circuit of the model and the non-linearity of the core (saturation curve) is entered directly into the model as a piecewise linear inductance with two slopes [Martinez-Velasco & Mork 2003; Manitoba HVDC Research Centre 2010].

2.4.1 Core material saturation

A typical B-H curve of a soft magnetic material is shown in Figure 2.3 with the changing relative permeability as the flux density varies. When a high magnetizing force is encountered, a point is reached where further increase in, H, does not cause useful increase in, B. This point is known as the saturation point of that material and is illustrated by the red line in figure 2.4 [McLyman 2004].

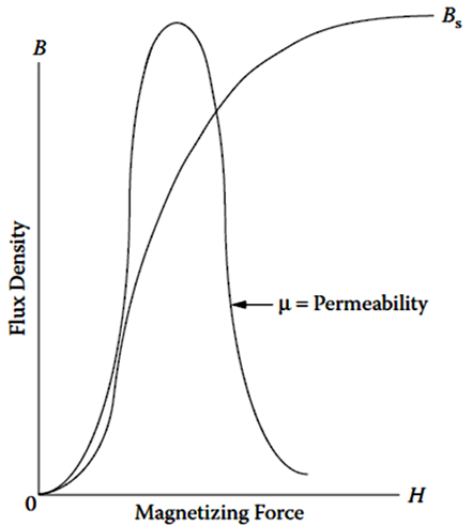

Figure 2.3. Graphical illustration of both the B-H curve and the changing relative permeability of a soft magnetic material [McLyman 2004].

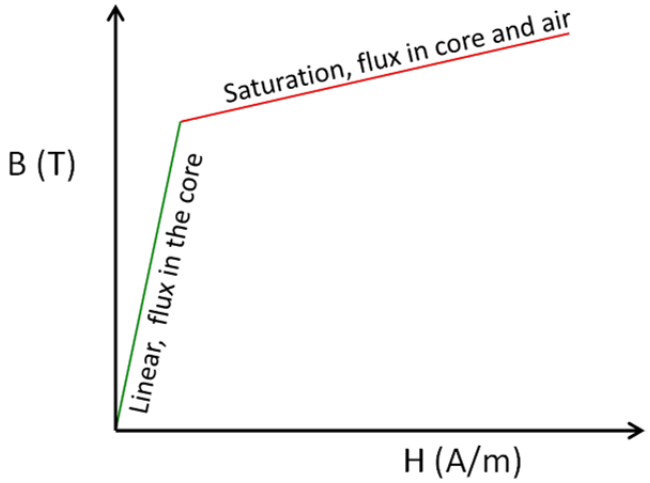

Figure 2.4. A more simplistic illustration of the B-H graph indicating linear and saturated operation of a transformer core [McLyman 2004].

The permeability, μ, of this magnetic material is a measure of the ease in magnetizing the material and is defined by Equation (2.1).

$$\mu = \frac{B}{H} \qquad (2.1)$$

where:
B is the flux density in Tesla and
H is the magnetizing force in A/m.

This relationship is not linear, as shown in Figure 2.3, and μ rises to a maximum and thereafter declines to minimum value of 1. The maximum μ coincides with the knee point of the B-H curve since it represents the slope of a line drawn between the origin and the knee point. This is significant since beyond this point as μ declines the reluctance of core components will change in such a way as to affect the distribution of the flux in in the available core flux paths.

McLyman [2004] explains that saturation begins when the peak exciting current is twice the average exciting current, so when $I_{pk} \geq I_{ave}$ the core is in saturation. This is illustrated in Figure 2.5 and is a useful measure for determining consistently the point of saturation of a transformer core during testing.

As the excitation is increased the laminations adjoining a core air gap will start to saturate. As the excitation is increased further and the adjacent lamination bridging the air gap approaches saturation its permeability drops and the flux goes in a straight line and crosses the small air gap.

Another phenomenon that occurs with the core response prior to saturation is fringing. As the reluctance seen by the flux increases, the flux seeks alternative paths and at the sharp lamination edges the flux exits the core producing the phenomenon called fringing. Fringing decreases the total reluctance of the magnetic path and therefore, increases the inductance as is evident when examining Equation (2.2).

$$L = \frac{N^2}{\Re} \qquad (2.2)$$

where:
L is the inductance,
N is the number of turns of the energizing coil, and
$\Re$ is the reluctance.

Fringing occurs at air gaps and also along the core length as μ approaches unity. If the fringing flux is not handled correctly, there will be premature core saturation.

Del Vecchio *et al.* [2010], state that, "*As saturation is approached, the flux will no longer remain confined to the core, but will spill into the air or oil space inside the coil that supplies the exciting current. Thus, beyond saturation, the entire area inside the exciting coil, including the core, must be considered the flux-carrying area with an incremental relative permeability of 1*". This is also significant since stray flux can be expected in the transformer airspace prior to complete saturation.

These references point to saturation as being achieved when the permeability beyond the knee of the B-H curve drops off dramatically and the core material is no longer the preferred path for the flux.

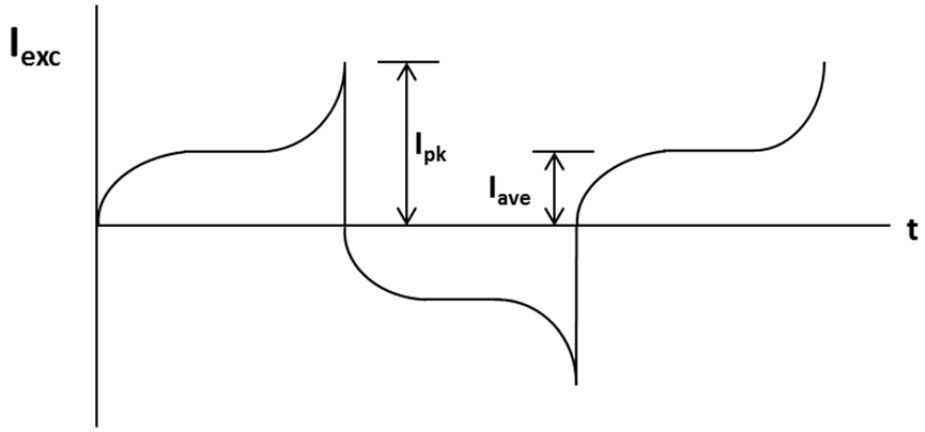

Figure 2.5. Definition of saturation (McLyman 2004).

2.4.2 Saturation Curve

In Brandwajn *et al.* [1982], it is said that grain oriented steel cores saturate with a sharply defined knee on the B-H curve and a two- slope piecewise linear inductance is sufficient to model such curves. Dommel *et al.* [1986], Martinez & Mork [2005] and Rezaei-zare [2014] agree that the saturation characteristic can be modelled by a piecewise linear inductance with two slopes as shown in Figure 2.8, since increasing the number of slopes does not significantly improve the accuracy. Unlike ferroresonance, that requires a more detailed representation of the saturation characteristic, a very accurate hysteresis model is not required for GICs.

Transformer saturation is a very important component when modelling low frequency electromagnetic transient phenomena. For most phenomena, the critical transformer saturation parameters are the slope (air-core inductance) and the zero-current intercept of the saturation curve. The location of the saturation representation in the transformer model topology is also important (Martinez, Walling, Mork, et al. 2005).

Saturation can be incorporated into a power transformer model using test data and/or manufacturer's curves or estimating the key parameters from transformer geometry, e.g. UMEC model found in PSCAD.

Martinez [2010] explains that compiling the piecewise linear inductance saturation characteristic of Figure 2.6 requires the following transformer parameters:

- The saturation slope (air-core inductance)
- The zero-current intercept of the saturation curve
- The nominal flux and the corresponding excitation current
- The location of the saturation representation in the transformer model topology

Jazebi *et al*. [2016b] propose that in the case of single phase transformers when the core components in the transformer have reached their saturation inductance, the slope of the terminal saturation inductance is equal to the air-core inductance. They explain that for a specific transformer winding, the air core inductance is always constant and in the absence of a tank, shunts, shields and metallic clamps the representation in Figure 2.6 is acceptable

as the saturation characteristic in deep saturation. They are then in agreement with Martinez [2010] in this instance.

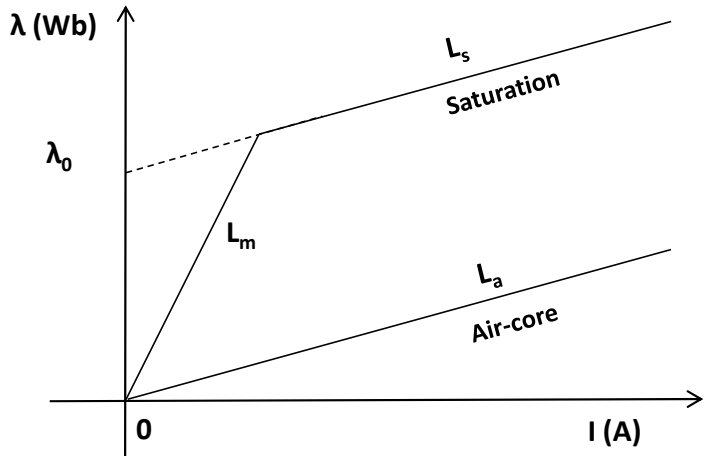

Figure 2.6 Transformer saturation curve showing critical points for curve determination [Jazebi *et al.* 2016b].

2.5 Parameters for transformer modelling

This section explains the methods proposed in the literature for determining the equivalent circuit parameters used in transformer modelling.

2.5.1 Winding Resistances

The individual winding resistance parameters are considered part of the external electric circuits and are placed outside the ideal transformers of the equivalent circuit of Figure 2.1 [Slemon 1953].

The impedance voltage test [IEEE Std C57.12.91 2011] can be used to determine the combined series resistance value, R_s of a single phase transformer. MIT [1965], Mork *et al.* [2004], Martinez *et al.* [2005], Chiesa [2010] and Jazebi *et al.* [2013] all suggest that this resistance value can then be divided between the two windings in proportion to the dc resistance values for each winding.

Wilson 2001, recommends that a measurement bridge or an impedance analyser at very low frequency be used to determine, R_{dc} for each winding.

Snelling [1969], suggests a theoretical method for estimating the dc resistance or the low frequency resistance of a conductor. He modifies the well know Equation (2.3) by substituting the conductor length with the product of the winding turns, N, and a mean turn length, l_w. The area is substituted with the area of a circle to take the circular conductor cross section into account. It is important to note that the resistivity, ρ_c, in equation (2.4) is temperature dependent.

$$R = \frac{\rho l}{A} \qquad (2.3)$$

$$R_{dc} = \frac{4\rho_c N l_w}{\pi d^2} = N l_w R_{cond} \quad \Omega \qquad (2.4)$$

where: R_{cond} is the resistance per unit length of the conductor.

2.5.1.1 Winding resistance determined by measurement

The load losses and impedance voltage (short-circuit) test [IEEE Std C57.12.91 2011] describes this test that is used to determine the series winding resistance of the transformer under test. Typically, the low winding is short-circuited and the high voltage winding is energised via an adjustable autotransformer. The source voltage is adjusted upwards from zero using the adjustable autotransformer until rated current flows through the transformer short circuited winding.

The impedance voltage of the transformer is the voltage required to circulate rated current through the transformer. The reactive component of this impedance voltage, called the reactance drop, is in quadrature with the current and corresponds to the leakage-flux linkages of the windings.

The total of winding resistance is related to the active power measurement by the square if the rms current measurement.

The series winding resistance (R_s) are then computed as follows:

$$R_s = \frac{P_{sc}}{I_{sc}^2} \qquad (2.5)$$

where P_{SC} is the active power measurement and I_{SC} is the rms current measurement.

2.5.2 Leakage Inductance

The terms short circuit impedance and impedance voltage value are used interchangeably in the literature to describe the vector sum of the leakage inductive reactance and resistance measured during a short circuit test, since it is not practical to measure the effective resistance drop and the reactance drop separately [Blume *et al*. 1967].

Unless the transformer design specifically requires a large leakage inductance, e.g. fault limiting impedance requirement, it is normally desirable to limit the leakage inductance to as low a value as possible since it negatively impacts on the voltage regulation of the transformer. Blume *et al*. [1967] state that the impedance voltage of the transformer generally falls within the range 2.4% to 16% at the rated voltage of the excited winding, unless designed otherwise for a particular reason.

Considering a set of concentric windings, ideally all the flux produced by the primary winding should link with the secondary winding. In practical transformers this is not true, since a part of the flux produced by the primary winding ampere-turns passes down the air path between the windings, thus avoiding the opposing ampere-turns of the secondary winding. Its distribution depends on the geometric configuration of the coils [MIT 1965; Say 1978;

Slemon 1992]. Leakage flux typically passes through the air, the space occupied by the windings or other non-magnetic materials and low reluctance paths through the transformer tank and other metallic fittings.

Short circuit impedance is therefore a parameter assigned to a transformer model to account for the imperfect magnetic flux coupling between a set of mutually coupled windings, e.g. the primary and secondary windings of a two winding transformers, and the load losses in the windings

The leakage inductance of a transformer can be determined either from an impedance voltage test as described in [IEEE Std C57.12.91 2001] or using the physical dimensions of transformer windings and substituted them into an approximate formula.

2.5.2.1 Leakage inductance by calculation – approximation by formula

The approximate calculation of leakage inductance is a useful method of determining the leakage inductance but is idealised since certain assumptions are made for simplicity. The MMF required to establish the field in the core section of the path taken by the leakage flux is considered to be negligible. The windings are considered to be infinitely long solenoids insofar as the magnetic field is concerned and the ampere-turns are considered to be uniformly distributed along the windings.

Numerous authors have documented Equation (2.6) which is commonly used for the approximate calculation of the leakage inductance of a concentric winding pair of equal winding height as illustrated in Figure 2.9, [MIT 1965; Say 1978; Slemon 1992; Bharat Heavy Electricals Limited 2003; Martinez-Velasco 2010].

$$L_{l12} = \mu_0 \frac{N^2 2\pi R_{mg}}{h}\left(\frac{b_1}{3} + g + \frac{b_2}{3}\right) \qquad (2.6)$$

where:
L_{l12} is the leakage inductance (H),
h is the winding height (m),
N is the number of winding turns,
μ_0 is the permeability of free space (H/m),
R_{mg} is the mean radius of the duct between the windings (m),
b_1 and b_2 are the winding thicknesses (m), and
g is the gap between the windings (m).

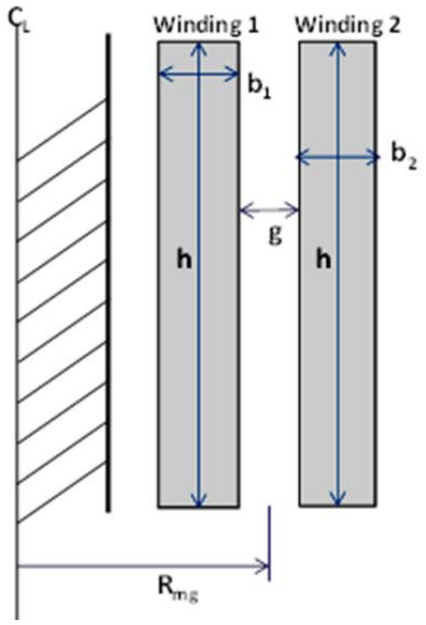

Figure 2.7 Geometric parameters used in two winding leakage reactance calculation - both windings of equal height.

When the windings of the concentric pair have different heights there is an appreciable increase in the radial flux present and this cannot be ignored. Del Vecchio *et al.* [2010] derived the two winding leakage reactance Equation (2.7) for this core–winding configuration. This equation caters for the difference in winding heights and also considers flux fringing at the winding ends.

The two winding leakage inductance of winding 1 with respect to winding 2 is given by:

$$L_{l12} = \frac{2\pi\mu_0 N_1^2}{h+s}\left[\frac{R_{m1}b_1}{3} + \frac{R_{m2}b_2}{3} + R_{mg}g + \frac{b_1^2}{12} - \frac{b_2^2}{12}\right] \qquad (2.7)$$

where:
L_{l12} is the leakage inductance (H),
$\mathrm{h} = \frac{(\mathrm{h}_1+\mathrm{h}_2)}{2}$ is an approximation (m),
h_1 and h_2 are the heights of windings 1 and 2 respectively (m),
R_{m1} and R_{m2} are the mean radii of windings 1 and 2 respectively (m),
R_{mg} is the mean radius (m) as indicated in Figure 2.9,
b_1 and b_2 are the winding thicknesses (m), and
g is the gap between the windings (m).

To correct for flux fringing at the winding ends, a good approximation is to increase h by the amount $\mathrm{s} = 0.32(\mathrm{R_o} - \mathrm{R_c})$
where R_o is the outer radius of winding 2 and R_c is the core radius.

2.5.2.2 Leakage inductance by measurement

The load losses and impedance voltage (short-circuit) test is also used to determine the leakage inductance, L_s , and is computed as follows [IEEE Std C57.12.91 - 2011; Jazebi *et al.* 2013]:

$$\boldsymbol{L_s = \frac{1}{\omega_s}\sqrt{\left(\frac{V_{sc}}{I_{sc}}\right)^2 - \left(\frac{P_{sc}}{I_{sc}{}^2}\right)^2}} \qquad (2.8)$$

where:
P_{sc} is the active power measurement,
I_{sc} is the rms current measurement, and
V_{sc} is the rms terminal voltage measurement.

2.5.3 Transformer no load losses and magnetizing inductance

The main no load loss component is the core loss in the transformer core, which is a function of the magnitude, frequency, and waveform of the test voltage.

No-load losses change with:

- the excitation voltage,
- vary with temperature, and
- are particularly sensitive to waveform distortion.

Factors that cause differences in the no-load losses of transformers of the same design include variability in characteristics of the core steel, mechanical stresses induced in manufacturing, and variation in the joint gaps [Martinez-Velasco 2010].

In according to IEEE Std C57.12.91 of 2011the transformer no-load loss test is used to determine the parameters of the transformer equivalent circuit magnetising branch.

The loss resistor and magnetising inductance values of the magnetising branches of the pi equivalent circuit are determined using Equations (2.9) and (2.10) respectively [Martinez-Velasco 2010; Jazebi *et al.* 2013].

$$R_X = R_Y = 2\frac{\left(V_{oc} - R_{S_{LV}} I_{oc}\right)^2}{P_{oc}} \qquad (2.9)$$

$$L_X = L_Y = 2L_m = 2\frac{(V_{oc})^2}{\omega Q_{oc}} \qquad (2.10)$$

where:
V_{oc} is the open circuit voltage measured on the LV winding side,
I_{oc} is the open circuit current,
P_{oc} is the power,
Q_{oc} is the reactive power, and

R_{sLV} is the resistance of the LV winding.

2.5.4 Terminal saturation inductance

Girgis & Nevins [1992] explain that the superposition of AC load current and quasi-DC current causes transformer core to saturate for portion of each half-cycle. The transition from unsaturated to saturated core represents a change in inductance of many orders of magnitude. Typical values of magnetizing inductances are in the order of 10 000 p.u. at a given MVA base whereas air core inductances fall within the range of 0.25 to 0.40 p.u.

The effective core inductance variations reflect in the magnitudes of exciting current which accounts for the large reactive power absorbed by the transformer in saturation.

The transformer core and winding geometries influence the sensitivity of the transformer to saturation. One transformer parameter variation having impact on GIC effects is the per-unit saturation reactance, which is the slope of the saturation curve in the fully-saturated region [Walling & Khan 1991; Molinski 2002; Zirka et al. 2012].

The saturation inductance and the winding resistance increase for windings with larger radii. In concentric windings the saturation inductance of the internal winding can be as low as half that of the outer winding. The energisation of the transformer from its internal winding will therefore produce much higher currents than the values obtained when it is energised from its outer winding [Abu-Nasser 1981; Martinez-Velasco & Mork 2003; Jazebi, de León, Farazmand, et al. 2013].

Abdulsalam et al. [2006] propose a method to estimate transformer saturation characteristics that extend into the deep saturation region. The basic idea of the method is to use recorded inrush voltage and current waveforms to estimate the saturation characteristics. Accurate representation of a transformer's deep saturation region is important for studying the impact of transformer energisation and its inrush currents.

Jazebi *et al.* [2013] and de León *et al.* [2014] propose a method of determining the saturation inductance of a transformer for use in a reversible duality based model. This method builds on the work of Stumberger *et al*. [2005] and proposes a new method of determining the saturation inductance by using a low power static uncontrolled rectifier with ripple. What makes this method different is the fact that it does not need demagnetization, zero crossing switching, or synchronization between measuring and switching devices; the experiment runs in steady state and is free from the uncertainties imposed by transients.

The low power static uncontrolled rectifier with ripple is connected to the primary winding, with the secondary winding open-circuited. The primary ac current and the secondary ac voltage are measured. To extract the amplitude of the fundamental voltage and current, Fourier transform is applied. As an alternative, they also recommend using the dominant harmonic quantities to determine the saturation inductance since this should give the same result.

The saturation curves of the two magnetising branches of the pi model determined in the open circuit test are extended using these two parameters from the last measured point to infinity.

2.6 Application of duality theorem to derive a pi model

Cherry [1949], describes the theory for deriving a dual equivalent electrical circuit of a transformer from its magnetic circuit. Each reluctance in a magnetic circuit causes a loss of MMF proportional to the flux passing through it. In the electrical equivalent circuit all MMFs must be replaced by their representative current that must flow through an admittance that gives a drop in voltage dual to its $\frac{d\Phi}{dt}$. These admittances are then the dual of their respective reluctances and must be inductive. The inductance is determined using Equation (2.11).

$$\boldsymbol{L} = \frac{(N)^2}{\mathfrak{R}} \qquad (2.11)$$

where N is the number of turns of the energising winding and $\mathfrak{R}$ is the reluctance of the core component.

The final electrical model is then derived directly from the actual magnetic structure of the transformer, and all the parameters in the model have a one to one relationship with the corresponding physical quantities of the original magnetic structure. The final electrical equivalent circuit is then a topological dual representation of the actual transformer.

Cherry [1949]; Slemon [1953]; Slemon [1992] and Wang et al. [1999], describe how to apply the duality theorem to obtain a topologically correct transformer electrical equivalent circuit.

A ferroresonance study to compare the equivalent T and Pi models is made by Jazebi *et al.* [2013], and the pi model is recommended as the preferred model for low frequency transient studies.

Obtaining a pi equivalent circuit from the duality derived circuit requires further processing and this is demonstrated by Wang *et al.* [1999]; Jazebi *et al.* [2013]; Jazebi *et al.* [2016a]; Jazebi *et al.* [2016b]. Their work is based mainly on three limb single phase transformers that have a geometric axis of symmetry allowing only half of the transformer to be studied.

Jazebi *et al.* [2013], describe the calculation of the parameters of the pi model for a dual reversible model for low frequency transient study. Based on FEM study that assumes perfect core stacking and geometric symmetry they demonstrate the need to consider using inductors to represent the leakage field in the air that is affected by the magnetic behaviour of the transformer core. A method of determining the parameters for a reversible model where the magnetising branches are estimated from the terminal saturation inductance is described in detail by using an uncontrolled rectifier with ripple. A more detailed description is given in de León *et al.* [2014] where the term air core inductance is used to describe the terminal measurement of the saturation inductance of the transformer. A measurement is made from both the inner and outer windings for a two winding transformer. This method

treats the transformer as a grey-box and the saturation of the transformer parameters are estimated from the terminal measurements for utilisation in the equivalent Pi model.

In a most recent publication, Jazebi *et al.* [2016b] clarify the difference between the terms saturation and air-core inductance. For low frequency transformer models saturation inductance is applicable since the value of the saturation inductance depends on the topology of the transformer and its accessories such as tank and shunts that are involved in the saturation. Air-core inductance on the other hand refers to the inductance of the winding in air as if the ferromagnetic core does not exist.

In the grey-box model the behaviour of an individual core component such as the core joints are not known and a true understanding of the core response is neglected with this approach. It is however, recommended by Jazebi *et al.* [2016b], where there are limitations associated with access to the transformer's construction and material information.

2.7 Transformer core joints

There are two main types of joints used in transformers and these are non-mitred and mitred joints.
The major regions where the flux deviates from the rolling direction are the corners where the flux passes from the yoke to the limbs. Here several harmful effects can occur because of the flux flowing out of the rolling direction. The power loss will naturally increase, as will the magnetostriction and hence the noise output of the core. The associated drop in permeability also means that an increased magnetizing current is necessary to produce the same core flux density.

The non-mitered joint is illustrated in Figure 2.8(a) and (c) are simple butt type joints with a 90^0 overlap angle that requires the flux to move across the grain of the core material when crossing from the limb to the yoke at the corner joints and vice versa. Because of this cross grain flux flow the energy loss of this type of joint is more than with miter type joints [Kulkarni & Khaparde 2004].

Mitered joints are illustrated in Figure 2.8(b) and (d) and typically have angles in the range of 30^0 to 60^0. As the flux crosses from limb to yoke along the grain orientation of the core material less losses are experienced than with the non-mitered type of joint. Kulkarni & Khaparde [2004] explain that for air gaps of equal length, the excitation requirement of cores with mitered joints is sin $\boldsymbol{\alpha}$ times that with non-mitred joints, where α is the angle of overlap of the mitred joint.

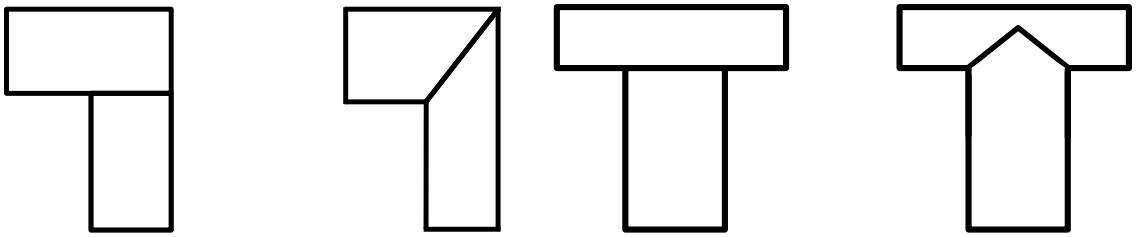

Figure 2.8. Core joints where (a) is a non-mitred or butt type corner joint, (b) is a 45^0 mitred corner joint, (c) is a non-mitred or butt type T-joint and (d) is a 30^0 mitred T-joint.

2.7.1 Effect of core joints on transformer saturation

Transformers are designed to operate at a flux density based on the core material chosen by the designer and the requirements of the customer's system [Heathcote 1998]. Ilo *et al.* [2000] states "*the performance of a transformer's core is directly related to its joints*". Joints are interleaved laminations that allow the flux to negotiate the joint air gap by traversing to a neighbouring lamination that bridges the joint gap. Core joints reduce the effective core cross-sectional area of a core section but counter measures such as the number of steps per joint, the number of laminations per step, the air gap length, and overlap length play a significant role in dealing with joint saturation during normal operation [Jones *et al.* 1973; Nakata *et al.* 1982; Nakata & Kawase 1986; Loffler *et al.* 1995; Mechler & Girgis 2000]

Steps are groups of laminations, N, and form a repetitive pattern throughout the whole steel package. To avoid the high reluctance path of the core joint gap, the flux escapes to the neighboring laminations which act as bridges over the air gap and can become "overloaded" if the transformer is operating above B_c, the critical flux density of the core joints. B_c is the induction level at which the laminations adjacent to the joint air gaps saturate and the flux enters the air gap. It is therefore a requirement when designing transformers to ensure that the peak design flux density, B_{design}, is less than B_c. When the induction level of the transformer, B, increases above B_c the same transformer can be driven into saturation at its joints.

McLyman [2004] supports this theory describing the phenomenon of "overloading" the gap bridges as "flux crowding".

Core joints are also affected by manufacturing variables, such as tolerances, stacking pressures, and other factors which depend on the skill with which the core is assembled [MIT 1965; Blume *et al.* 1967].

Nakata *et al.* [1982] explain that core step-lap joints are superior to conventional butt-lap joints with respect to the magnetic characteristics such as magnetising current, core losses and sound level. They demonstrate that the equivalent magnetizing current length increases with length of the joint overlap and air gap length in step-lap core joints with increasing flux density and an infinite number of laminations per step used in the simulation. Furthermore, they indicate that at a flux density of 1,73T, when the number of laminations per step group,

N, is small, saturation of the laminations facing the air gap of the joint will occur with some flux in the air gap.

Nakata indicates that as 'N' increases so the percentage of the flux passing through the air gap decreases. Loffler *et al.* [1995] and Ilo *et al.* [2000] support this theory that B_c increases with N.

Mechler & Girgis [2000] indicate that the flux direction inside the GOES is almost identical with the rolling direction of the sheets on both sides of the joints. The bending to cross rolling direction near the joints is only a few degrees. In the inter-laminar gaps the flux lines are almost normal to the sheet surfaces. They analyse the conventional mitered joint of Figure 2.9 with two laminations per step. Their finding is that with an air gap width of 3 mm, and an overall induction level is 1.7 T, the flux density in the core sheet area shunting the air-gap rises up to 2.7 T while that in the gap rises to a value of 0.7 T. Their study showed that flux traveling between the sheets occurs in a very narrow strip (about 1 mm) before and after the gap.

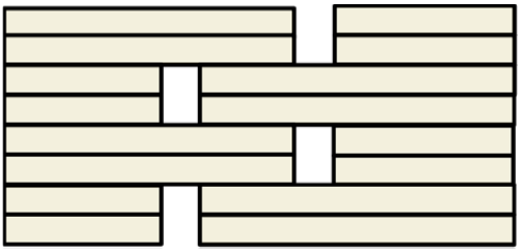

Figure 2.9: Conventional core joint structure used in the Mechler & Girgis [2000] study.

Ilo *et al.* [2000b] published similar findings for mitered joints with N=1 and N=6. They found that for a mitered joint $B_c \approx 1$ T for N=1 and 1.7 T for N=6. Furthermore, a useful example is given, where for B=1.8 T the saturated gap bridges reach local flux densities as high as 2.7 T which they confirmed by both theory and sputtered search coil analysis.

Kulkarni & Khaparde [2004] explain that for the same overall induction of 1.7 T, in a step-lap (SL) joint of 6 steps, the flux totally avoids the gap with flux density of just 0.04 T, and gets redistributed almost equally in laminations of the other five steps with a flux density close to 2.0 T.

2.8 Distortion caused by saturation due to GICs

Sen [1997] explains that under normal transformer operation in a YNd transformer the exciting current is non-sinusoidal with a third harmonic current flowing in the neutral. The flux in the core and hence the induced voltages in the windings will be sinusoidal. This is due to the current causing a non-sinusoidal MMF that when applied to a non-linear magnetic circuit will produce a sinusoidal flux. If all the flux couples with the secondary winding then the secondary voltage will be sinusoidal.

Walling & Khan [1991] in their ETMP simulation studies on a three limb single phase transformer describe the harmonic content in the exciting current of a GIC saturated

transformer as having both even and odd-order harmonic components. Examining their column graph, it is evident that there is an overall trend for the harmonic magnitude to decrease with increasing order at a given GIC magnitude. They report that the low-order harmonic-components lag the fundamental voltage by 90^0 and some of the higher-order components have reversed signs, and lead the fundamental. The harmonic orders where sign reversals take place are a function of GIC magnitude.

Furthermore, they find that the harmonic magnitude versus GIC characteristics is sensitive to the transformer winding saturation inductance and the sensitivity increases with harmonic order.

They plot the harmonic sequence components of the exciting currents resulting from a 0,I p.u. GIC in a three phase bank of single phase transformers and find that they produce harmonics in the conventional order, e.g. only triplens are zero sequence. The GIC magnitude is normalised in per unit of the transformer rated crest phase current for the affected winding.

In Smith [2014] testing on a star-star three phase transformer bank with tertiary delta is conducted. The primary star connection is ac energised with the secondary open- circuit and dc injected into the open tertiary delta. He explains that harmonic levels for the three single phase transformers become evident only when the dc current applied to a transformer approaches twice the normal ac magnetising current, but saturation is evident much sooner than this. The actual level at which harmonics appear in a given transformer is determined by how close to saturation a transformer normally operates.

Smith [2014] mentions two reasons for the production of harmonics in transformers, namely:

- In a sufficiently saturated core the leakage flux will increase during parts of the voltage cycle so that not all the sinusoidal flux will couple with the secondary winding, and
- During saturation the magnetising current will increase to sufficient levels to cause non-sinusoidal volt-drops in the series impedances. This causes non-sinusoidal voltages with harmonics to appear at the secondary terminals.

2.9 Is the distortion harmful to motors?

No literature is found that's deals specifically with the effect of transformer half-wave saturation distortion on transformer loads. There is, however, literature that deals with the effects of this distortion on power station generators. Since motor loads are rotating loads a review of this literature is seen as important to understanding the mechanisms that effect generators as these could similarly affect motors.

Gish *et al.* [1994] make a general statement that GICs should be considered as a source of significant harmonic current that can exceed the 120 second minimum which may safely be withstood by a generator rotor as given in ANSI C50.13- 1989, American National Standard Requirement for Cylindrical Rotor Synchronous Generators.

Zero sequence current will not be present in the generator circuit due to the GSU transformer delta winding. If the transformer is wye connected, the zero sequence current of any harmonic will not cross the air gap and will not cause rotor heating.

Through calculation and simulation in an EMTP model they conclude that damage to a generator rotor is possible from transformer half-cycle saturation distortion. The damage is focused at the end-ring structure where the ohmic contact is made between the rotor bars and the end ring. They use SUNBURST data in their EMTP study and find that the primary cause of the heating is the negative-sequence second harmonic and the positive- sequence fourth harmonic adding together on the rotor as third-harmonic induced current in the rotor bars. Other harmonic combinations also contribute to rotor heating but are of lesser importance.

Molinski [2002] presents a discussion on the effects of GICs on utilities. He mentions that the GIC is blocked from most generators because of the practice of connecting the generator to the power grid using delta-wye step-up transformers. The generator is still subject to harmonics and voltage unbalance caused by transformer half-cycle saturation that cause positive and negative sequence harmonic currents to flow into the generator. It is possible that the even harmonics could cause excessive heating in the rotor end rings and the positive sequence harmonics could cause mechanical vibrations. These rotor heating currents increase linearly with GIC in the step up transformer neutral, and care must be taken to ensure that adequate protection exists.

Rezaei-Zare & Marti [2013] offer simulation study results that reveal that the generator capability limit can be exceeded at moderate GIC levels, e.g. 50A/phase, and the rotor damage is likely during a severe GMD event.

2.10 Assessing vibration effects of the distortion on a rotating load

Vibration in rotating machines can be heard with the human ear as sound. Noise is often used as a tool for diagnosing loose or defective parts in a rotating machine.

Accurate diagnosis of rotating machinery problems can be made with sound recordings using a microphone to measure discrete frequencies heard with the ear. Microphones are effective in the audio range from 20 Hz to 20 KHz [Taylor 2000].
Many cases arise when a microphone is the best transducer to use to identify the source of noise.

Deterministic (periodic) signals are stationary signals that have a relatively constant frequency and level content over a long time period. Deterministic signals are generated by rotating machines, musical instruments, and electronic function generators. These signals are made up entirely of sine waves at discrete frequencies. The resolution of the frequency analysis is determined by the filter bandwidth used in the analysis. The filter bandwidth should enable the analyser to distinguish between the two most closely spaced frequency components. This means that there should only be one sinusoid in each filter passband at any one time. If this is the case, then the power transmitted by the filter is independent of the

bandwidth. Therefore, the averaged frequency spectrum of a deterministic signal should be scaled in terms of root mean square or mean square power [Konstantin-Hansen *et al.* 1994].

2.11 Implications for the research

No practical transformer is ideal but although their operation is governed by the same laws of physics they have specific complexities and properties that are unique based on their physical construction. The accurate prediction of transformer behavior requires models that are developed for the phenomenon or group of phenomena to be studied. This requires determining which complexities and properties are most important for that type of study. These are termed parameters and certain parameters are therefore more important for specific types of studies.

The duality derived topological transformer model is preferred for GIC and dc type transient studies since the low frequency can drive the transformer core into saturation. White–box and grey-box models are preferred with the white-box requiring more manufacturer information that is seldom available. The white-box model is a more accurate model since it has the detailed dimensions of the transformer available to it. The pi equivalent circuit is superior to the Steinmetz equivalent circuit in saturation studies and Jazebi *et al.* [2013] propose a pi equivalent circuit that is reversible.

De León & Semlyen [1995] and Berge [2011] both agree that modern transformer iron cores have narrow hysteresis loops and that the hysteresis losses are much smaller than eddy current losses. The hysteresis loops of modern transformers have a negligible influence on the magnitude of the magnetizing current and the GIC phenomenon is a quasi-steady-state one. This allows the hysteresis to be ignored.

Iravani *et al.* [2000] and Martinez-Velasco & Mork [2003], both agree that using the value of R_c closest to rated voltage provides a good estimate of core loss. Mork [1992] has shown low sensitivities to fairly large changes in $\boldsymbol{R_c}$ for single phase transformers.

GICs are slowly fluctuating transients. During GIC induced saturation the harmonics produced due to the asymmetrical excitation current once per cycle produces harmonics in the transformer windings up to the 14^{th} harmonic that includes both even and odd harmonics. Also, the higher harmonic orders are almost negligible in magnitude. It can therefore be deduced from the models of Holmberg *et al.* [2003] and Jazebi [2013] that for thin conductors there is no need for special treatment in the model for eddy current at frequencies below 3kHz. Current penetration below 3kHz is considered to be 100%.

Based on the literature review Table 1 shows the considerations to be taken into account when modelling for low frequency phenomena such as GICs and dc components of current.

Table 2.1. Considerations to be taken into account when modelling for low frequency phenomena such as GIC and dc components of current.

Core	Windings
Magnetising inductance, L_M	Bulk leakage, L_S
Core loss resistance, R_C	Winding resistance, R_S
Piecewise linear hysteresis curve with two slopes (when no tank is present)	Apportion R_s according to winding dc resistances

Methods of estimating the model parameters are presented in the literature but actual measurement ensures anomalies unique to a particular transformer are considered in the model.

The terminal saturation inductance of the windings is required to determine the shallow slope of the saturation portion of the double slope piecewise linear hysteresis curve.

The no-load loss (open-circuit) and load losses and impedance voltage (short-circuit) tests as described in IEEE Std C57.12.91 2011 are required for determining L_M, R_C, L_S and R_S. The winding ac resistances are determined by apportioning R_s to each winding in accordance to the ratio of the dc resistances.

Transformers are designed to meet the specified requirements with the bulk component cross-sectional areas in mind. Core joints need to be properly designed to ensure they do not saturate before the bulk core components and limit the capability of the transformer. In GIC or dc induced saturation the core joints will saturate but their response to these phenomena does not appear to have been considered in the literature.

The large asymmetrical current input wave to the transformer during half-cycle saturation will be badly distorted with both even and odd harmonics present. Typically these harmonics are of decreasing magnitude with increasing harmonic order.

An EMTP study based on SUNBURST data indicates that there will be heat damage to the power station generator rotor end-ring structures where contact is made between the rotor bars and the end ring. The primary cause of the heating is the negative-sequence second harmonic and the positive- sequence fourth harmonic adding together on the rotor as third-harmonic induced current in the rotor bars.

Sound recordings can be used to determine changes in the mechanical vibration of a rotating machine. The mechanical vibration harmonic frequencies can be determined by applying a FFT analysis to the sound recording to determine among other things the effect of electrical harmonics entering a rotating machine at its electrical input terminals.

No information is found in the literature regarding:

- An equivalent circuit for slow transient evaluation of the SP-4L transformer,

- A comprehensive flux mapping exercise making use of search coils attached to the core of a single phase transformer to determine its core response during normal and saturated operation with ac and then ac and dc components of currents respectively,
- Consideration given to core joints in transformer slow transient modelling, and
- The effect of the load on the level of distortion experienced when a single phase transformer suffers from half-wave saturation.

2.12 Onward

In the next chapter lumped parameter and pi equivalent circuit models are developed using the principle of duality. The complexity of introducing the core joint detail to the lumped parameter model is illustrated.

Chapter 3

Single phase four limb transformer model

Martinez & Mork 2005, state that transformer models are one of the weakest components of modern transient simulation software. Models differ depending on the phenomenon being modelled and the physical attributes of transformer components need to be correctly chosen and represented. Saturation is an important consideration when modelling for slow transients. Duality derived topological models are necessary to model the core saturation since steady state transformer models, such as the Steinmetz equivalent circuit, are inaccurate.

In this chapter the duality derived topological model is derived without determining the actual value of each parameter. The white- and grey-box models are considered and the implication of taking the core joint detail into account is discussed. Furthermore, a recommendation is made for laboratory scale transformers used in GIC and dc studies.

Some advantages and disadvantages of using the grey-box model are highlighted.

3.1 Duality derived topological model

In chapter 2 the literature review returned no evidence of an equivalent circuit for slow transient evaluation of SP-4L transformers, although models do exist for the two limb core type and three limb shell type single phase transformers.

In Figure 3.1 the flux paths of the single phase four limb transformer are identified. Equal reluctance of the flux paths is assumed. At first glance, the core of the SP-4L transformer in Figure 3.1 appears to be symmetrical. Only once an attempt is made to produce the equivalent magnetic circuit does it become evident there is no symmetry to take advantage of in order to simplify the equivalent circuit. This is due to the combination of return limbs and interconnecting yoke. (There is an axis of symmetry but not a plane of symmetry.)

The principle of duality is applied to the SP-4L transformer to derive a topological model of the SP-4L transformer in Figure 3.2. Figure 3.22(a) illustrates the magnetic equivalent circuit, and 3.2(b) and (c) the derivation of the electrical equivalent circuit. The direct application of the duality principle is used where the electrical equivalent circuit is derived on top of the geometric drawing of the transformer while making assumptions about the flux paths. Figure 3.2(c) represents the electrical equivalent circuit without winding resistances and external connections for simplicity.

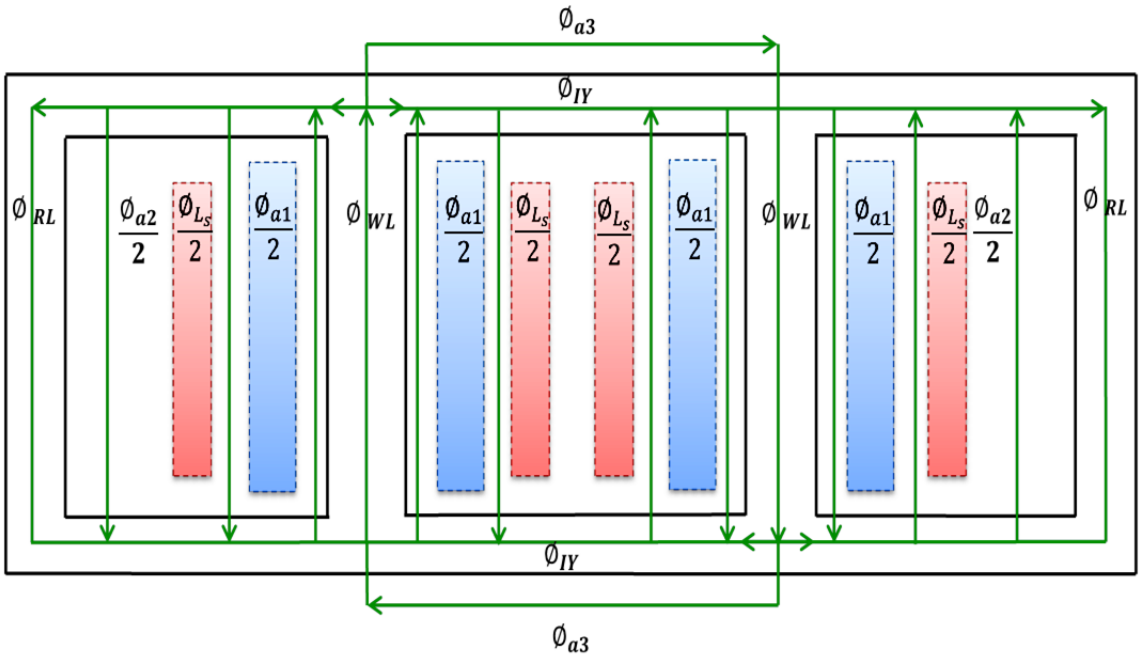

Figure 3.1. The magnetic flux paths of a single phase four limb transformer where:
The blue shapes are the 150 turn windings closest to the core and the pink shapes are the 80 turn windings,
$\emptyset_{a1,\ and}$ $\emptyset_{a2}$ represent the stray fluxes in the air,
$\emptyset_{Ls}$ represents the leakage flux due to imperfect flux linkage between the transformer windings, and
$\emptyset_{WL}$, $\emptyset_{IY}$ and $\emptyset_{RL}$ represent the flux inside the core flowing through the wound limb, interconnecting yoke and return limb paths respectively.

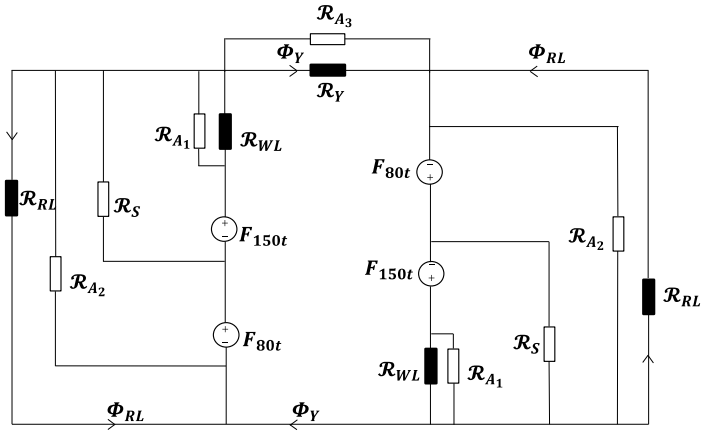

(a)

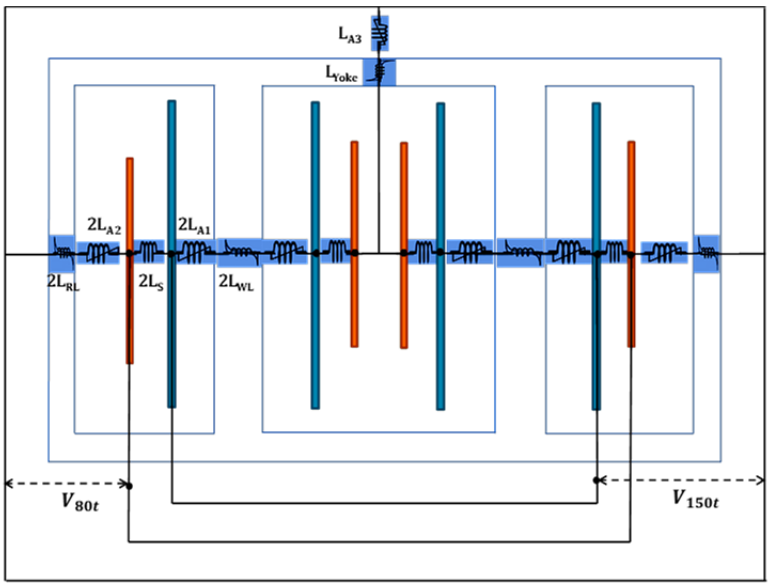

(b)

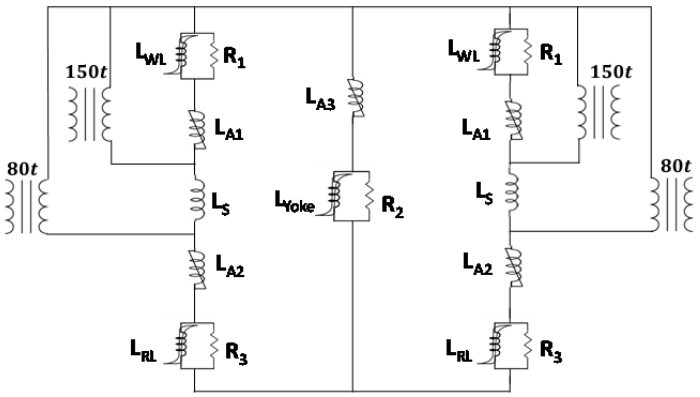

(c)

Figure 3.2. Duality derived topological model of the SP-4L transformer where (a) is the equivalent magnetic circuit, (b) is the electrical equivalent circuit derived on top of the geometry of the transformer and (c) is the electrical equivalent circuit without winding resistances or external connections shown.

Duality derived topological model of single phase four limb transformers for GIC and dc bias studies

A common approach used by transformer modelers of single phase three limb transformers is to take advantage of magnetic core symmetry in order to simplify their equivalent circuit [Wang *et al.* 1999; Jazebi *et al.* 2013; Rezaei-Zare 2015]. The configuration of the single phase four limb transformer core type as illustrated in Figure 21 does not display magnetic core symmetry.

Examining Figure 3.2(c) shows that further refinements can be made if the symmetry of the electrical equivalent circuit and the deep saturation condition are considered. In Figure 3.3(a) the electrical equivalent circuit of Figure 3.2(c) is reduced based on the circuit symmetry.

In deep saturation, the value of the air inductances becomes comparable with the leakage and magnetizing inductances. Jazebi *et al.* [2013] explain that the air inductances can therefore be presented by linear piece-wise approximations with two sections:

- Zero in normal conditions because the flux is confined to the core, and
- A constant slope line in deep saturation (corresponding to the permeability of air and winding geometry).

The values of R_1, R_3 and R_2 are much larger than the corresponding impedances of L_{A1}, L_{A2}, L_{A3}, L_{WL}, L_{RL} and L_{yoke} in Figure 3.2(c). Using a similar approach to that used by Jazebi *et al.* [2013], the circuit of Figure 3.3 (a) is reduced by combining inductances since in saturation the core components are close to the relative permeability of air. Therefore, $0.5L_{WL}$ and $0.5L_{A1}$ are unified to a single inductor L_1 and L_{yoke} and L_{A3} are unified to equivalent inductor L_2. Also, $0.5L_{RL}$ and $0.5L_{A2}$ are unified to another equivalent inductor L_3.

Since the yokes are common to both the 80 turn and 150 turn windings, L_2 and R_2 are divided equally between the magnetising branches represented by $0.5R_1$ and L_1, and $0.5R_3$ and L_3. The magnetising branches are then reduced further to equivalent magnetising branches R_4 and L_4 and R_5 and L_5. The model is now simplified to the π model of Figure 3.3(c) (grey box model) that is reversible. In deep saturation the inductances of the two magnetizing branches are determined as $L_{4\text{-sat}}$ and $L_{5\text{-sat}}$ in chapter 8.

In Figure 3.3 the winding resistances are not shown but need to be added external to the ideal transformers and, since the two 80 turn and two 150 windings are parallel connected, the external resistance must be halved in each case.

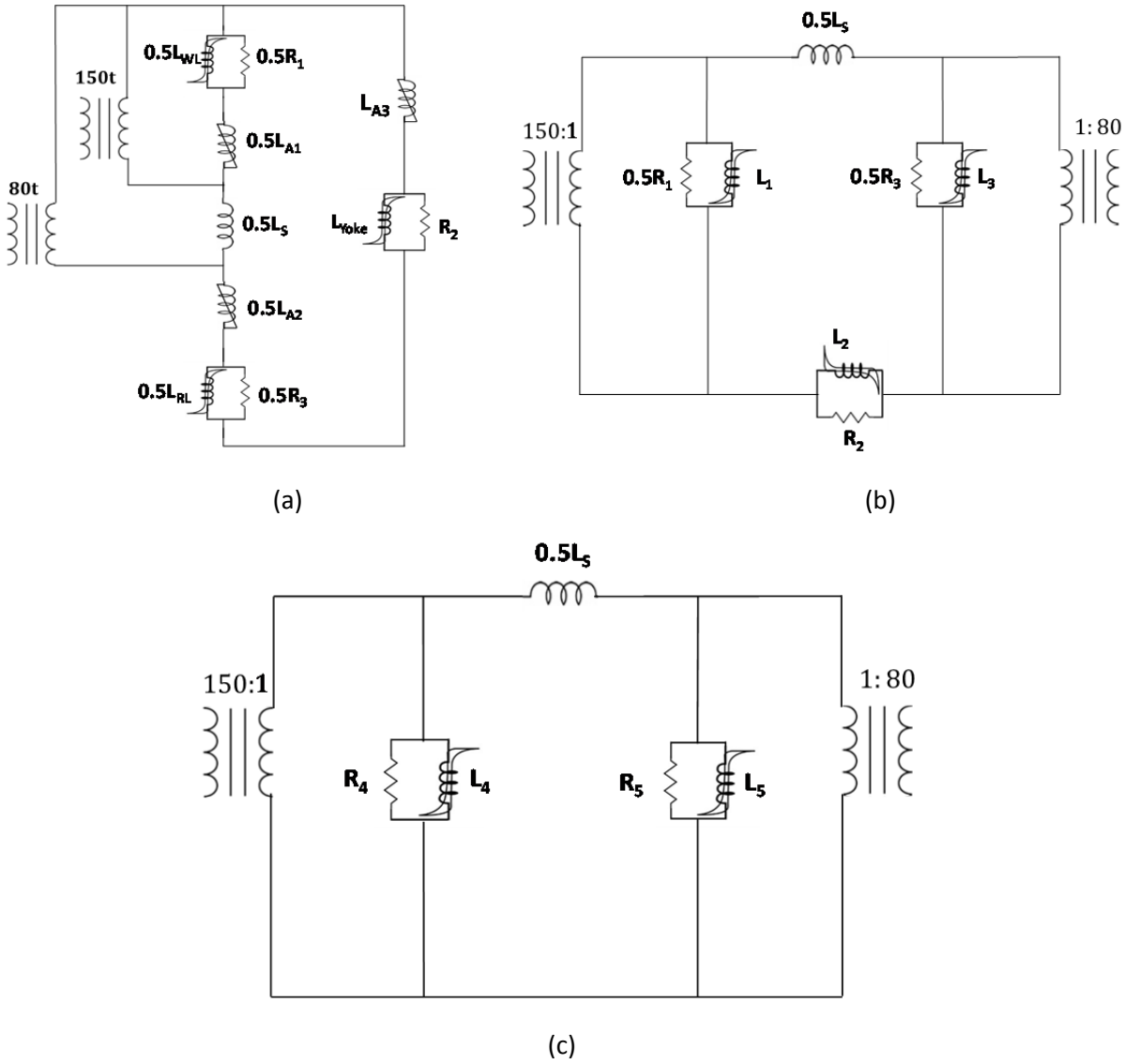

Figure 3.3. Reduction of the electrical equivalent circuit in Figure 3.2(c) to an equivalent pi circuit where (a) is the reduction of the electrical circuit based on the parallel nature of the circuit, (b) is re-arranging of the parameters into the pi equivalent configuration and (c) is the final pi equivalent circuit where the branch of L_2 (the yoke and its associated stray flux path) is equally distributed between the magnetising branches of L_1 and L_3.

Duality derived topological model of single phase four limb transformers for GIC and dc bias studies

In order to achieve a three phase transformer bank connection, e.g. YNyn or YNd, three pi models with winding resistances included are externally connected into the desired three phase bank configuration.

3.2 Duality derived topological model that takes core joints into account

In the literature, low frequency topological models for transformers derived using the duality theorem do not consider transformer core joints. FEM images in the literature for low frequency studies [Iravani *et al.* 2000; Mork *et al.* 2007; Jazebi *et al.* 2013; Jazebi *et al.* 2016] do not show joint structures because they are not considered. Experimental proof is needed to determine whether certain transformer joint types are significant components in the transformer's core response in saturation. If this is proved they should be included in the duality derived electrical equivalent circuit. Alternatively, core joint types that are not prone to early saturation should be used in transformer designs.

Depending on the type of joint utilized in the transformer core it should be possible to determine theoretically whether they will be prone to earlier saturation than the core bulk components.
Where two laminations meet constitutes a core joint and since the reluctance of the core changes at a core joint especially in saturation, a separate lumped parameter must be added at the location of a joint in the equivalent circuit. NSL butt type joints are assumed for this equivalent circuit and are discussed in more detail in chapters 4 and 5.

A duality derived topological model for the SP-4L transformer that takes the core joints into account is illustrated in Figure 3.4. Both the magnetic equivalent and electrical equivalent (lumped parameter) models are illustrated.

Examining the magnetic and electrical equivalent circuits in figures 3.4 (a) and (b) it becomes evident that the transformer equivalent model has become more complex by comparison with the model illustrated in Figure 3.2. If the core joints are properly designed, i.e. $B_c > B_{des}$ for normal operation, then the magnetic circuit can be reduced back to that of Figure 3.2(a).

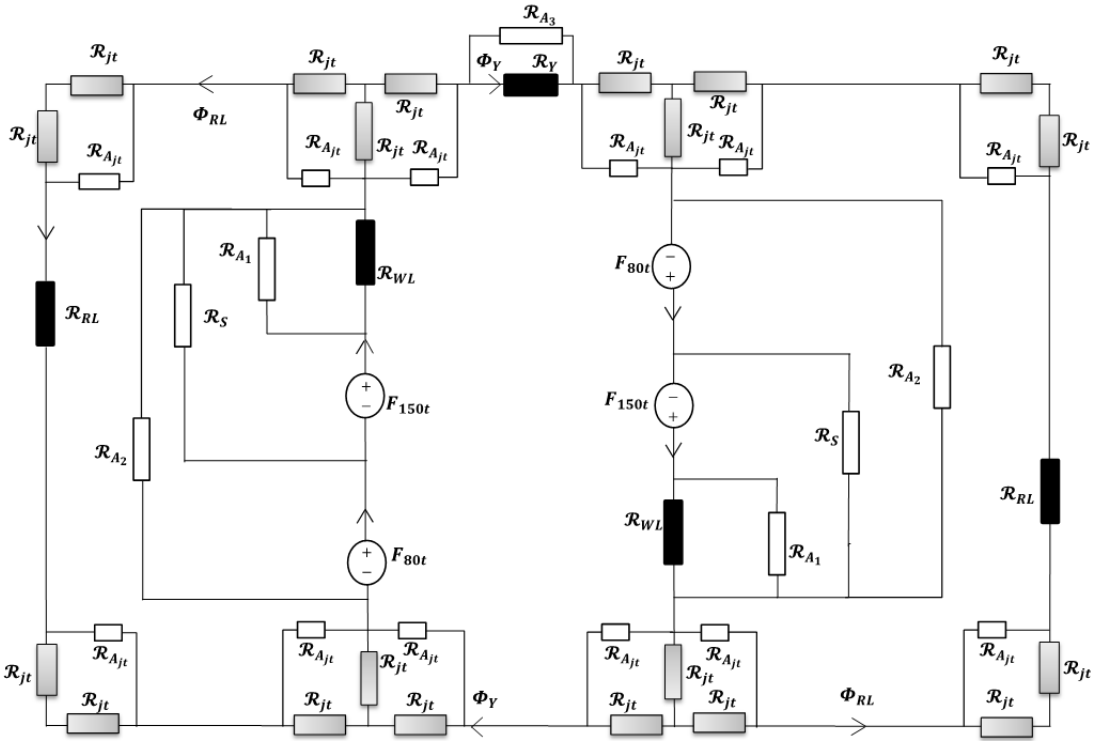

(a)

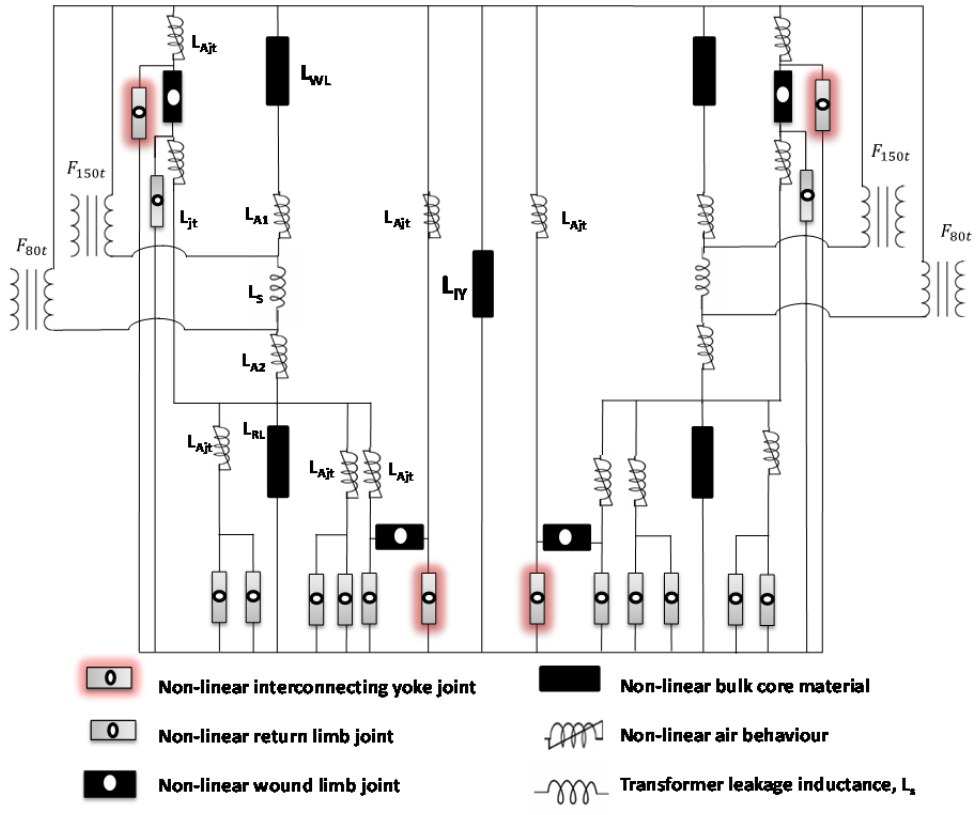

(b)

Figure 3.4. Duality derived topological model of the SP-4L transformer illustrating the effect of inclusion of the core joints into the model: (a) equivalent magnetic equivalent circuit and (b) the electrical equivalent circuit without winding resistances or external connections shown.

3.3 Importance of the joints to the model

The derivation of the duality derived model including joints raises the following issues/questions:

- The joint types and methods used by manufacturers to ensure that $B_C > B_{des}$ need to be explored in order to ensure that clarity is achieved on whether the joints need to be considered in the model.
- In the transformer industry mitred joints typically have joining angles that range between 30^0 to 60^0 [Kulkarni & Khaparde 2004]. The incorporation of mitred core joints in the transformer design may be sufficient to dispel the need for joint detail in models but needs to be analysed.
- Furthermore, the different multi-step lap patterns used in core joint stacking should also be investigated.
- On large scale single phase four limb transformers the core component parts of the model as illustrated in Figure 3.4 still exist but may be negligible and only come into play at higher GIC levels. Of importance is to note that some components could be more significant than others at different GIC levels. As an example, the flux division at a core T-joint assembly, controlled by the reluctances of the interconnecting yokes and return limb paths varies according to the degree of saturation of the components along a particular flux path, depending on the GIC magnitude in the windings.

The generic model presented in figure 3.3 can be populated with values from any single phase four limb transformer but the unique structure of each power transformer might make some elements of the model dominate others differently.

3.4 Requirements for parameter determination

The duality derived topological models are only useful if the appropriate parameters of the transformer are available or can be determined from measurement or estimation.

The model parameters determined through measurement are preferred since they are then based on actual transformer performance under test conditions and not estimation. A testing protocol for single phase four limb transformers are therefore required in order to determine these parameters.

Three four-limb test transformers are required since this will allow for:

- Consistency in parameter values providing confidence,
- Various three phase transformer banks to be configured to provide data for a complete transformer bank simulation model, and
- The effect of load on the performance of a three phase bank under saturated conditions to be assessed.

3.5 Onward

In the next chapter the test transformers are described, the results of the transformer acceptance testing are discussed and some problematic areas of the design are identified.

The testing protocol for parameter determination is provided in chapter 6 and grey-box parameter values are determined in chapter 8.

Chapter 4

Preliminary exploratory work

In this chapter the test transformers are described and the results of the transformer acceptance tests are discussed. Some problematic areas of the design are identified and the value of using flux search coils as a tool to determine core flux distribution and to identify areas of stray flux leakage from the core is introduced.

4.1 Single phase four limb transformers as received from the manufacturer

In Figure 4.1 one of a total of three, four limb single phase test transformers delivered to the test facility can be seen with some basic dimensions to provide perspective on the size of the transformer. The three transformers make it possible to produce a three phase bank of transformers for test purposes. The test transformers are air cooled and horizontally orientated with a fully exposed core structure allowing physical access to most of its parts. The only metallic parts are those of the core and windings and all structural clamps and supports are made of wood.

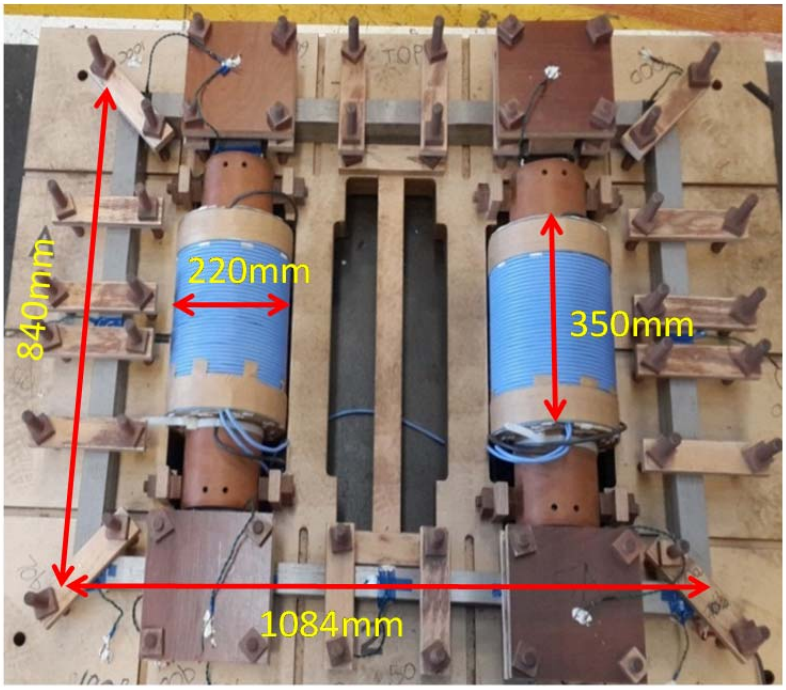

Figure 4.1. One of the three SP-4L test transformers delivered.

4.1.1 Design of the SP-4L transformers

In order to conduct the research necessary to develop a duality derived model of the SP-4L transformer, test transformers are required.

The specification of these test transformers should also encompass the requirements necessary for answering the other research questions posed in chapter 1. Therefore three

test transformers are required with exposed cores that allow access for installing search coils.

The transformers should resemble a power transformer in respect of high quality core material and winding configuration.

A further requirement is that the core should be reconfigurable to allow for future research requirements. Two and three limb single phase and three limb three phase configurations needed to be catered for in the design. This necessitates an allowance in the transformer backing board for an additional wound limb and winding as can be seen by the centre void in Figure 4.1. Additional laminations are also required. Due to the small dimensions of the transformer yoke and return limb sections it is decided to use butt type core joints (NSL) since the manufacturer's lamination processing equipment could not safely miter them. The simple stacking method is seen as an advantage since the intention is to re-stack the cores to achieve other configurations for laboratory testing.

A transformer voltage ratio of (208:390) will provide the following benefits:

- The 208 V (star connection) voltage side will keep the test supply transformers at a low induction level while giving confidence that only the single phase four limb test transformer/s are in saturation at increased induction levels,
- The 390 V (delta connection) will permit a 3 phase generator or 3 phase squirrel cage induction motor to be connected. This will also allow for an assessment to be made of the effect of load on the distortion as a result of half-wave saturation,
- The use of readily available standardized equipment,
- Readily available 500 kVA, Dyn11, 400 V/11 kV three phase three limb source transformers will permit either side of the test transformers to be energized when determining the short-circuit and open-circuit parameters, and
- The magnetization curve of the transformers can be determined for both windings.

A 40 A rating for the 208 V star connected windings will ensure approximately 21.3 A full load rating on the 390 V delta connected winding side of the three phase transformer bank. A 3 phase motor or generator of this rating or slightly larger (partial load can also be applied) should readily be available and provide a full load condition for the transformer bank. A transformer rating of approximately 9 kVA is therefore acceptable.

The SP-4L parallel winding assemblies are shown in figures 4.1 and 4.2.

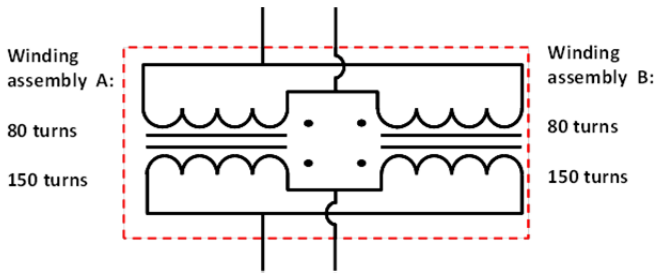

Figure 4.2. Parallel winding connections of a SP-4L transformer.

4.1.1.1 Winding design parameters

The single phase windings rated 208 V are intended for connection in a star configuration in a three phase transformer bank. Connection to a three phase ac source rated 230 V_{ph} allows a range of voltages above the nominal test transformer rated voltage for testing the effects of saturation. Equation (4.1) is the transformer induced voltage equation.

$$\mathrm{E_p} = 4{,}44\mathrm{fN_p}\emptyset_\mathrm{m} \qquad (4.1)$$

where:
E_p is primary induced rms voltage,
N_p is the number of primary turns,
f is the frequency of operation, and
$\emptyset_\mathrm{m}$ is the peak flux in the core.

Rearranging the equation the number of turns on the 208 V winding is

$$N = \frac{V_{rms}}{A \times 2\pi f \frac{1.66}{\sqrt{2}}} = \frac{208}{72.9 \times 10^{-4} \times 314.5 \times \frac{1,66}{\sqrt{2}}} = 77.3 \text{ turns.}$$

The number of turns selected is 80 turns allowing for 2 layers of 40 turns each on the lower voltage side.

The transformation ratio chosen is 1.875 to achieve a rated voltage of 390 V in the delta connection. This permits a three phase motor load on the delta to determine rotor heating as a result of saturation caused by dc biasing. This winding therefore consists of 3 layers of 50 turns each.

Each transformer has two winding assemblies that are parallel connected for the respective voltages. The winding polarity connections are in support of the flux directions shown in Figure 4.3.

All windings are wound using the same wire that consists of round multi-strand wire with a cross section of 10 mm^2 and high temperature insulation. The high temperature insulation allows for the lack of forced cooling since core and windings are horizontally orientated and naturally air cooled. This allows for currents up to 100A_{rms} for a short periods of time (a few minutes) especially when dc is injected into the transformer for determining its response during saturation. This permits electrical measurements to be taken at high current levels without damage to the test transformers.

4.1.1.2 Eddy current effect on the transformer windings

The models of Holmberg et al. [2003] and Jazebi [2013] deduce that for thin conductors $(\mathrm{d} < 4\mathrm{mm})$ frequency dependent modelling of the windings up to 3 kHz is unnecessary. In the case of the test transformers the conductor diameter is 3.568 mm implying that eddy current modelling is unnecessary.

4.1.1.3 Core design parameters

The core material is grain oriented electrical steel (GOES) of type H 111-30. This is done in order to have a core material similar to that used in power transformers. Some of the characteristics of the H 111-30 core material are shown in Table 4.1.

The design is based on a peak induction in core of 1.66 Tesla (1.17 Tesla rms) and a frequency of 50Hz. The wound limb cross-sectional area is,

$$A = \text{stack height} \times \text{lamination width} = 270\ laminations \times 0.3mm \times 90mm = 72.9 \times 10^{-4}\ \text{m}^2.$$

The cross-sectional area of the wound limbs, yokes and return limbs is illustrated in Figure 4.3(b). The cross-sectional area of the wound limbs is twice that of the yokes and return limbs.

Table 4.1. Relevant characteristics of the H 111-30 core material.

Core material	Lamination thickness	Maximum μ_r	B_{sat}
H 111-30	0.3mm	Approximately 47000	2.03T

4.1.1.4 Eddy current effect on the core

Based on the literature review the representation given in Figure 2.2 is accepted as sufficient for GIC studies. The value of $\boldsymbol{R_c}$ is determined by the no load losses and excitation current test at rated voltage and provides a good estimate of core loss.

4.1.1.5 Core construction of the SP-4L transformer

Figure 4.3 illustrates the SP-4L core with its windings. Flux directions, numbered nodes and mean core length dimensions are included for defining the flux paths and reluctances of the core. In Figures 4.4(a) and (b) the successive core layers that are repeated sequentially to construct the core stack are illustrated showing the T- and 90^0-joint assemblies. The core joints are of the butt-lap type shown in Figures 4.4(c) and (d). In Figure 4.4(e) the effect of butt-lap joints on the core cross-sectional area is illustrated.

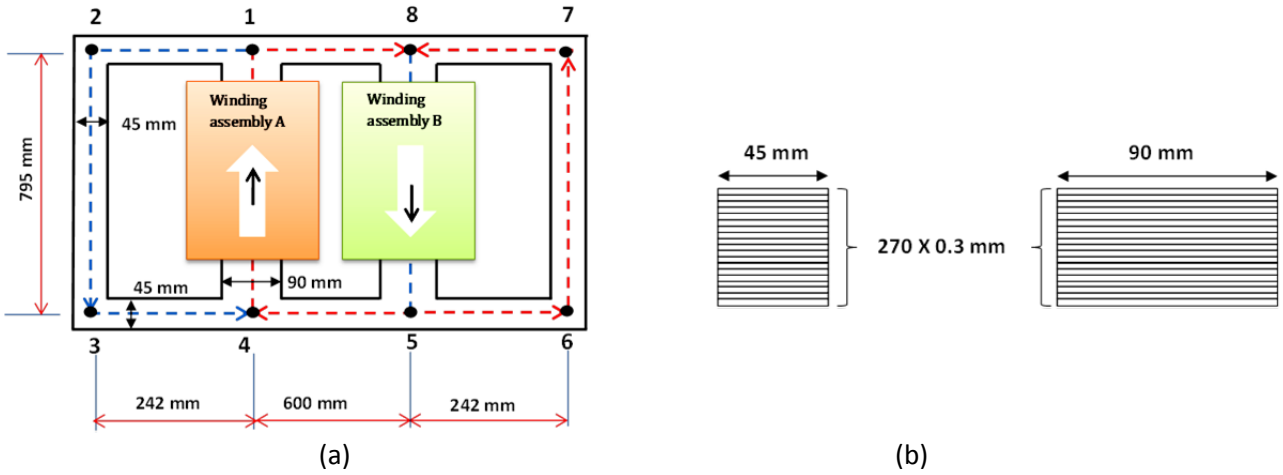

Figure 4.3. (a) The schematic diagram of the SP-4L core is shown with the parallel connected windings included. Numbered nodes are added for defining the flux paths through the core, and in (b) on the left is the cross-sectional area of the yokes and return limbs and on the right is the cross-sectional area of the wound limbs.

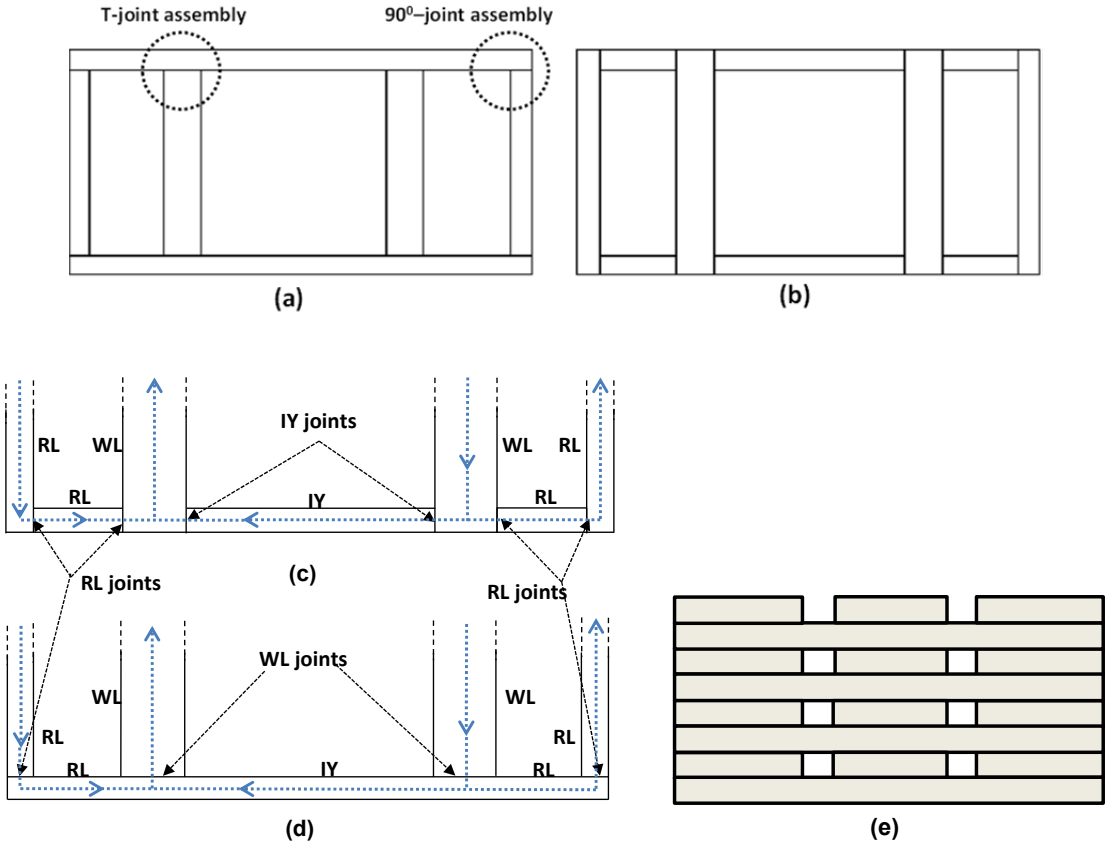

Figure 4.4. Core assembly showing (a) and (b) show the successive core layers that are repeated sequentially to construct the core stack of 270 layers with T- and 90^0-joint assemblies, (c) and (d) is a first attempt at labelling the core bulk components and joints, where IY is the interconnecting yoke, RL is return limb path, WL is the wound limb, IY joints are the joints associated with the flux in the interconnecting yoke, RL joints are the joints associated with the flux in the return limb path, and WL joints are the joints associated with the flux in the wound limb. In (e) the non-step lap (NSL) joint is shown.

4.1.1.6 Core material - H111-30

In Figure 4.5 the relative permeability and B-H curves of the H 111-30 lamination material used in the construction of the SP-4L test transformers are plotted against magnetic field strength. The curves are green and blue respectively. Above 1.7 T it is seen that exponentially larger increments in magnetic field strength are required to sustain equal increments of 0.05T in flux density. This is due to the decrease in permeability of the material beyond the knee point.

B_{sat} of the core material is 2.03 T and is the point at which the core material saturates.

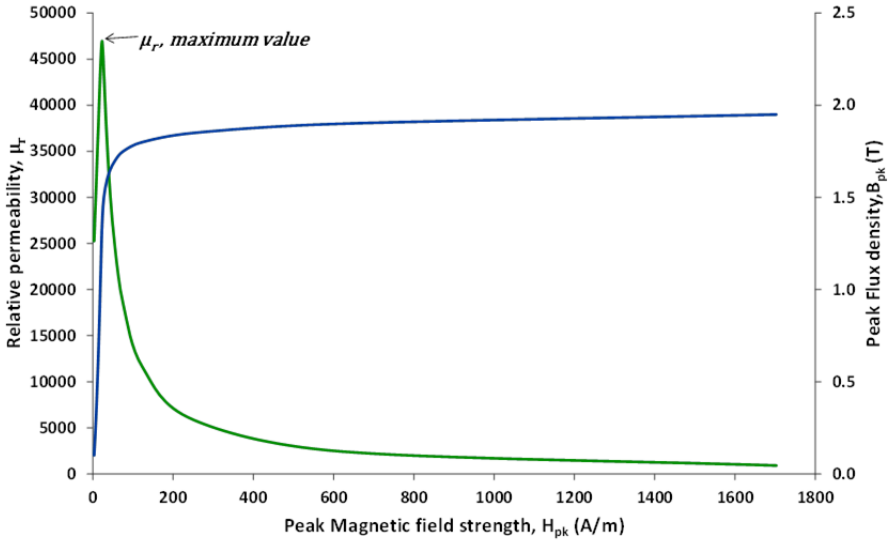

Figure 4.5. The relative permeability and the B-H curve of the H 111-30 core material. The point of maximum permeability is indicated.

4.2 Preliminary Testing

Certain preliminary tests are necessary in order to confirm:

- That the manufactured test transformers meet the design specifications,
- That the relevant aspects of the test transformers meet the requirements of relevant transformer standards, and
- That the search coil monitoring methodology is feasible as this will allow for confidence in developing the testing protocol further.

4.2.1 Acceptance tests

Acceptance tests need to be carried out to determine that the test transformer meet the design specification and are in compliance with IEEE Std C57.12.91, 2011, Standard Test Code for Dry-Type Distribution and Power Transformers.

These listed acceptance tests are required to be done prior to developing the research test protocol as a quality check:

- Visual inspection to ensure no shipping damage occurred,
- Winding Insulation resistance (IR) using a 1kV dc Megger tester,

- Winding polarity test,
- Ratio check,
- Winding resistance measurement (cold resistance measurement), and
- v-i magnetization curve to serve as a future reference of the core build and to ensure that the test transformer design is complied with.

A MPK-253 10 A Micro-ohmmeter® is used to determine the winding dc resistances. The instrument utilizes the Kelvin-type, four terminal measurement principle thus eliminating errors caused by lead and contact resistances. It has a basic accuracy of 0.2% of reading and complies with IEC 61010-1:1990, IEC 61010-1:1992 amendment 2.

The transformers are found to comply with IEEE Std C57.12.91, 2011, Standard Test Code for Dry-Type Distribution and Power Transformers. The transformer windings are now interconnected with the correct polarity to support the flux flow as indicated in Figure 4.3(a).

The measured dc winding resistances are temperature corrected to 20^0C as given in table 4.2. The dc winding resistances are used to apportion the winding ac resistances in the equivalent model in chapter 8. The resistances of the outer (80 turn) and inner (150 turn) windings at 20^0C differed from the calculated values within ranges of 4 to 4.6% and 6.4 to 6.5% respectively. The method used to calculate the dc winding resistances is contained in appendix C.

The ac resistances of windings with the same number of turns differed from each other by 0.3 and 0.1 mΩ respectively for the inner and outer windings showing good consistency in the construction of the winding assemblies and the measurement method.

Table 4.2. Theoretically calculated and measured dc resistances for the parallel connected windings. Resistance values are corrected to 20 ^{0}C.

Test transformer	Calculated dc resistance for parallel connected windings at 20 ^{0}C		Measured dc resistance for parallel connected windings corrected to 20 ^{0}C		Percentage difference between calculation and measurement (%)	
	$\mathbf{R_{dc_{80t}}}$, (Ω)	$\mathbf{R_{dc_{150t}}}$, (Ω)	$\mathbf{R_{dc_{80t}}}$, (Ω)	$\mathbf{R_{dc_{150t}}}$, (Ω)	$\mathbf{R_{dc_{80t}}}$	$\mathbf{R_{dc_{150t}}}$
T1	0.0525	0.0765	0.0501	0.0716	4.6	6.4
T2			0.0504	0.0715	4	6.5
T3			0.0501	0.0715	4.6	6.5

The v-i curves of the test transformers are determined by energising the transformers from the 80 turn parallel windings and then repeated for the 150 turn windings using ac only. The per unitized v-i values for both tests are plotted on the same system of axes and if they overlap then either winding can be used for ac energisation during testing. The test transformer design is based on a flux density, B_{peak}=1,66 T in the wound limbs and rated voltages of 390 V and 208 V. V_{knee} is therefore expected to be in excess of these voltages dependent on the winding used to energise the test transformer.

Using the design voltage ratings as base values, the per unit v-i curves in Figure 4.6 are determined for test transformer 1 when energised respectively from the 80 turn and then

150 turn winding sides of the transformer. Saturation voltages of 122.3 V and 228 V are determined for the 80 turn and 150 turn windings respectively. The per unit v-i graphs can be seen to match closely and this same consistency is found for test transformers 2 and 3.

In Figure 4.7 test transformers 1, 2 and 3 are seen to be similar in core response over the linear portion of the v-i magnetization curve but differ in their knee point voltages and response in saturation. This is acceptable since transformers are designed for operation in the linear range and no manufacturer guarantee is given for operation in the saturated region of the curve. As the respective test transformers transition from the linear operating portion of their respective v-i curves into saturation the curves of T1, T2 and T3 start to deviate from one another. Using the McLyman criterion, $\mathrm{I_{peak}} \geq 2 \times \mathrm{I_{ave}}$, for identifying the voltage for core saturation [McLyman 2004] it is found that the test transformers first reached saturation ($\mathrm{I_{peak}} = 2 \times \mathrm{I_{ave}}$) at the voltages indicated in table 4.3. In later testing these voltages are found to be in line with the saturation of the IY joints which are the first to saturate for each of the transformers respectively.

Table 4.3. Ac saturation voltages for test transformers T1, T2 and T3 when energised from the 80 turn windings.

Test transformer	Ac saturation voltage, V_{sat}, with 80 turn windings energised (V_{rms})
T1	122.3
T2	129
T3	120.24

As a result, the test transformer voltage ratings are adjusted to new nominal values of 110/206 V for the 80t and 150t sides respectively. The rated current remains 40 A on the 80t side and the nominal power rating is reduced from 8.3 kVA to 4.4 kVA.

The transformer manufacturer accounts for the difference between the transformers with the following comments:

- The mean magnetic path length seen by the flux in each transformer is not the same due to core sheet cutting precision,
- Edge burrs, depending on how well the sheets are slit, could result in circulating current losses between adjacent plates,
- Core stacking precision, if this is not within acceptable quality, could lead to larger air gaps and misalignment of sheets, and
- The core active area is a function of the number of sheets used. Sometimes when the core is stacked, the major concern is the packet thickness as it affects the diameter of the core which could make fitting the windings difficult if the core area is larger than calculated. If the core thickness exceeds the calculated value laminations are removed. Similarly, if it's lower than the calculated value, laminations can be added. So, two cores with the same design using the same core steel will not have the exact same core active area unless stacked with the same number of sheets from the same mother roll.

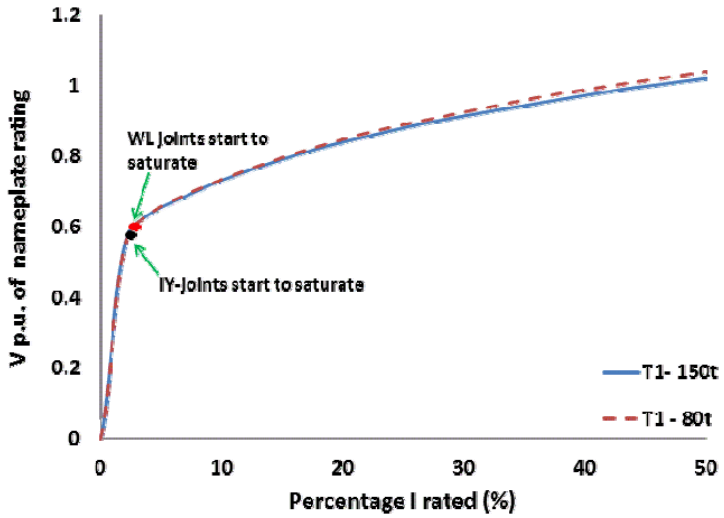

Figure 4.6. The per unit v-i magnetisation curves for test transformer 1 showing consistency when magnetising the core from either the 80 or 150 turn windings. The transformer's early saturation is evident since it goes into non-linear operation just prior to reaching 0.6 p.u. voltage.

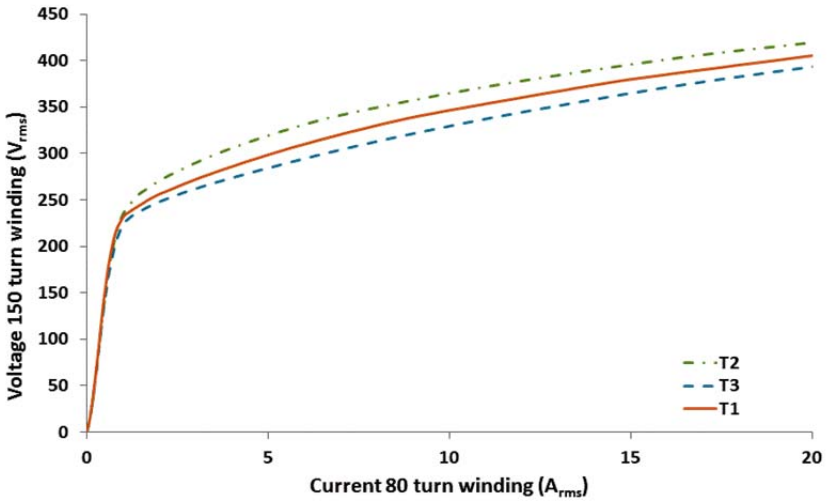

Figure 4.7. The v-i magnetisation curves for test transformers 1, 2 and 3 are shown where consistent behaviour is achieved in the linear range of the core response but differing in the location of their knee points and saturation.

4.3 Use of search coils

Applying Equation (4.1) to a single turn search coil it is seen that $E_s \propto \emptyset_m$ or more importantly the voltage output of a search coil is proportional to the peak flux in the core at the search coil location.

Single turn search coils placed strategically around the core will assist with determining:

- Core symmetry,
- Actual core flux distribution for both normal and saturated operation, and
- Core response to flux produced by both ac and dc components of current.

Additionally, with a sufficient number of coil turns, search coils strategically placed in the transformer airspace can be used to determine the location and extent of the stray flux during core saturation.

The use of the air search coils at the locations A, D and E as detailed in section 4.3.2 reveal the core joints saturating prematurely, i.e. stray flux is detected for search coils located at A and E, and D as indicated in figure 4.11.

4.3.1 Verification of core symmetry

The core symmetry is verified using the single turn search coils wrapped around the core at locations 1 to 6 and 9 and 10 as indicated in Figure 4.. Furthermore, the T-joint assembly flux distribution is determined using the search coil outputs at locations 1 and 3, and 4 and 6.

The search coil outputs at locations 1 to 6 for transformer 1 are provided in table 4.4 and shown graphically in Figure 4.8 for increasing ac voltage applied to the 150 turn windings. The overlap of the plotted outputs of search coils 1 and 6, 3 and 4, 2 and 5 indicate core symmetry. The changing percentage flux distribution at the T-joint assembly is evident when comparing the plotted outputs of search coils 1 and 6 with that of 3 and 4.

At induction levels up to approximately 206 V_{rms} the following relationships are confirmed using the search coils outputs of all three test transformers:

- $V_{SC1} = V_{SC6}$ or $\Phi_{pk\,SC1} = \Phi_{pk\,SC6}$
- $V_{SC5} = V_{SC7}$ or $\Phi_{pk\,SC5} = \Phi_{pk\,SC7}$
- $V_{SC8} = V_{SC9}$ or $\Phi_{pk\,SC8} = \Phi_{pk\,SC9}$
- $V_{SC9} = V_{SC10}$ or $\Phi_{pk\,SC9} = \Phi_{pk\,SC10}$
- $V_{SC3} = V_{SC4}$ or $\Phi_{pk\,SC3} = \Phi_{pk\,SC4}$
- $V_{SC2} = V_{SC5}$ or $\Phi_{pk\,SC2} = \Phi_{pk\,SC5}$
- $V_{SC2} = V_{SC1} + V_{SC3}$ or $\Phi_{pk\,SC2} = \Phi_{pk\,SC1} + \Phi_{pk\,SC3}$
- $V_{SC5} = V_{SC4} + V_{SC6}$ or $\Phi_{pk\,SC5} = \Phi_{pk\,SC4} + \Phi_{pk\,SC6}$

As the induction level is increased above 206 V_{rms} there appears to be stray flux leaving the core since following relationships are observed:

- $V_{SC2} < V_{SC1} + V_{SC3}$ or $\Phi_{pk\,SC2} < \Phi_{pk\,SC1} + \Phi_{pk\,SC3}$
- $V_{SC5} < V_{SC4} + V_{SC6}$ or $\Phi_{pk\,SC5} < \Phi_{pk\,SC4} + \Phi_{pk\,SC6}$
- $V_{SC8} < V_{SC9}$ or $\Phi_{pk\,SC8} < \Phi_{pk\,SC9}$
- $V_{SC5} < V_{SC7}$ or $\Phi_{pk\,SC5} < \Phi_{pk\,SC7}$

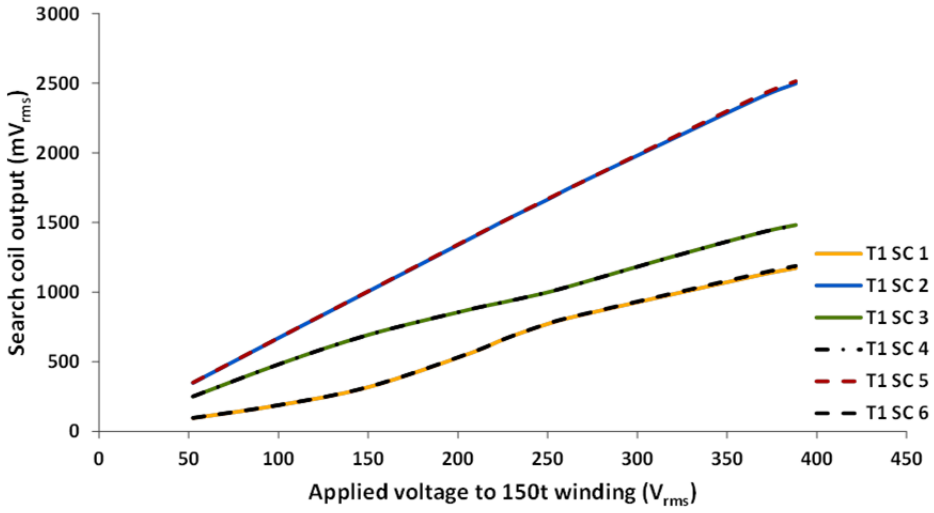

Figure 4.8. Search coil outputs with increasing ac applied to the 150 turn windings of test transformer T1. Search coils 1 to 6 are used to prove core symmetry.

The flux when faced with the high reluctance of a saturating T-joint assembly strays outside the core bypassing search coils 2 and 5. This contributes to the output from search coil 5 being less than that of search coil 7. Another contributing reason is some of the flux in the vicinity of the WL straying into the air space and linking with the RL.

The output from search coil 8 is less than 9 due to flux leaving the WL in the vicinity of winding mid-point and linking with the RL.

The outputs from search coils 9 and 10 are close in magnitude both in normal and saturated operation.

At nominal voltage applied to the 150 turn windings (206 V) the flux distribution at the T-joint assembly is 60.96:39.04 which correlates with the calculated flux distribution in section 5.1.1. As the core moves into saturation the flux distribution changes and more flux flows through RL path as the IY starts to saturate. At the highest test voltage, i.e. 1.88pu, the flux distribution changed to 55.82:44.18. This is in line with the expectation that as individual core components become saturated the reluctance of the paths change and some flux gets diverted from one path to another.

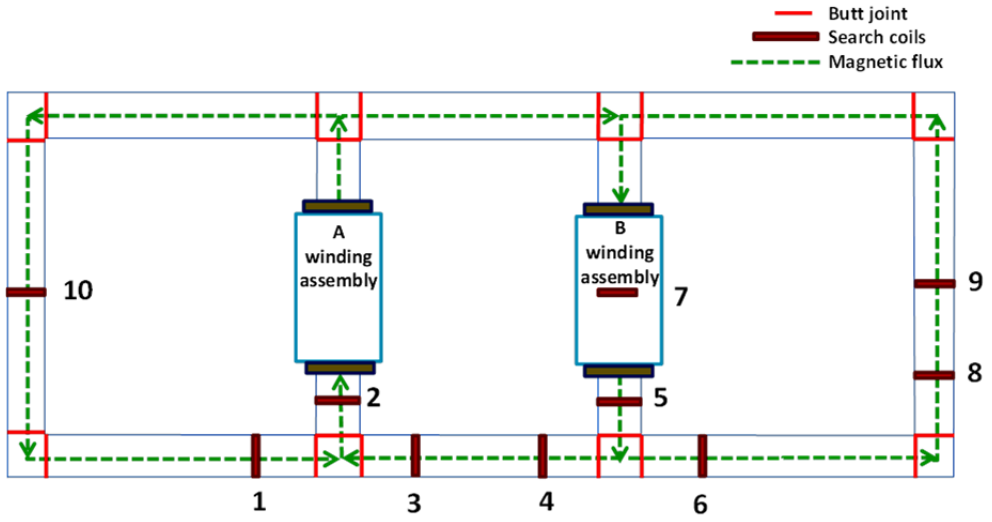

Figure 4.9. Schematic of the four limb transformer core with windings showing the initial search coil locations chosen for testing for symmetry and to determine the normal flux distribution.

Table 4.4. A sample of search coils readings recorded from test transformer 1 with increasing ac voltage applied to the 150 turn windings.

$V_{applied}$ to 150 turn winding (V_{rms})	SC 1 (V_{rms})	Peak Flux SC 1 (mWb)	SC 2 (V_{rms})	Peak Flux SC 2 (mWb)	SC 3 (V_{rms})	Peak Flux SC 3 (mWb)
52.36	0.096	0. 432	0.349	1.572	0.251	1.131
101.14	0.191	0. 86	0.679	3.059	0.487	2.194
150.30	0.319	1. 437	1.007	4.536	0.695	3.131
206.72	0.561	2.527	1.384	6.234	0.876	3.946
226.43	0.667	3.005	1.517	6.833	0.931	4.194
249.94	0.772	3.477	1.665	7.500	0.999	4.500
265.38	0.826	3.721	1.768	7.964	1.054	4.748
320.00	0.986	4.441	2.103	9.473	1.257	5.662
370.00	1.128	5.081	2.407	10.842	1.432	6.451
388.31	1.173	5.284	2.498	11.252	1.482	6.676
$V_{applied}$ to 150 turn winding (V_{rms})	SC 4 (V_{rms})	Peak flux SC 4 (mWb)	SC 5 (V_{rms})	Peak flux SC 5 (mWb)	SC 6 (V_{rms})	Peak flux SC 6 (mWb)
52.36	0.252	1.135	0.351	1.581	0.098	0.441
101.14	0.487	2.194	0.679	3.059	0.192	0.865
150.30	0.695	3.131	1.009	4.545	0.321	1.446
206.72	0.877	3.950	1.387	6.248	0.564	2.541
226.43	0.931	4.194	1.516	6.829	0.667	3.005
249.94	1.000	4.505	1.670	7.523	0.775	3.491
265.38	1.054	4.748	1.767	7.959	0.829	3.734
320.00	1.256	5.658	2.112	9.514	0.993	4.473
370.00	1.432	6.451	2.423	10.914	1.141	5.140
388.31	1.478	6.658	2.515	11.329	1.189	5.356

4.3.2 Air search coil parameters and deployment

The v-i graph of each test transformer is determined and the induction level at which the knee point occurs is noted. Preliminary tests are then conducted at induction levels corresponding to linear and non-linear core operation with various shapes of air search coil with differing numbers of turns to find a suitable coil for detecting stray flux in the transformer air space. This is necessary since the stray flux magnitudes are not known at this stage of the research. A 20 turn search coil with the dimensions as given in Figure 4.(a) is found to give readable output voltages in line with the induction levels used for the preliminary tests. Stray flux is first detected at locations A, D, E, Y_1 and Y_2 as indicated in Figure 4.(b). It is observed that all of these locations are associated with the core joints. As the induction level is raised still further above the knee point of the v-i curve, additional sources of stray flux are detected at locations B and C. A, D, E, Y_1 and Y_2 are found to produce by far the largest output voltages consistently. By implication these are therefore the locations or sources of the stray flux leaving the core. This measurement method enabled the reason for the earlier than expected saturation at the IY and WL joints to be determined.

Different angular orientations of the search coil at locations A, D and E are experimented with and the air search coil orientations are further refined to those indicated in Figure 4. based on the strongest voltage output obtained.

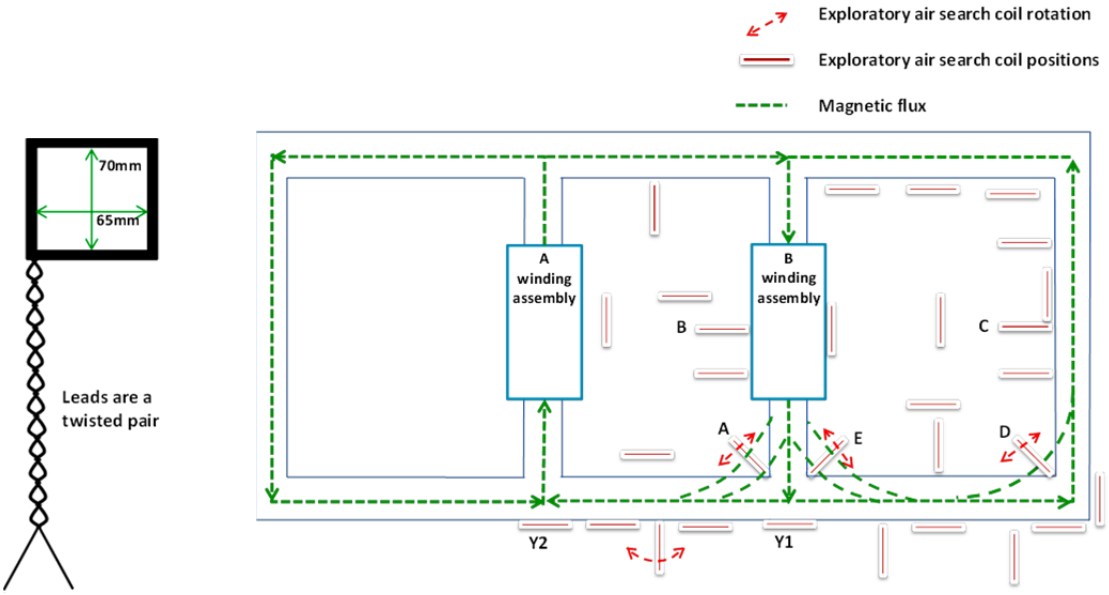

Figure 4.10. Preliminary check for the effectiveness of the air search coil monitoring technique for determining the ability to detect stray flux in the transformer windows: (a) A 20 turn search coil with twisted leads and approximate dimensions shown for monitoring the stray flux in the transformer core airspace, and (b) deployment of exploratory air search coils for determining the locations of the strongest stray flux field.

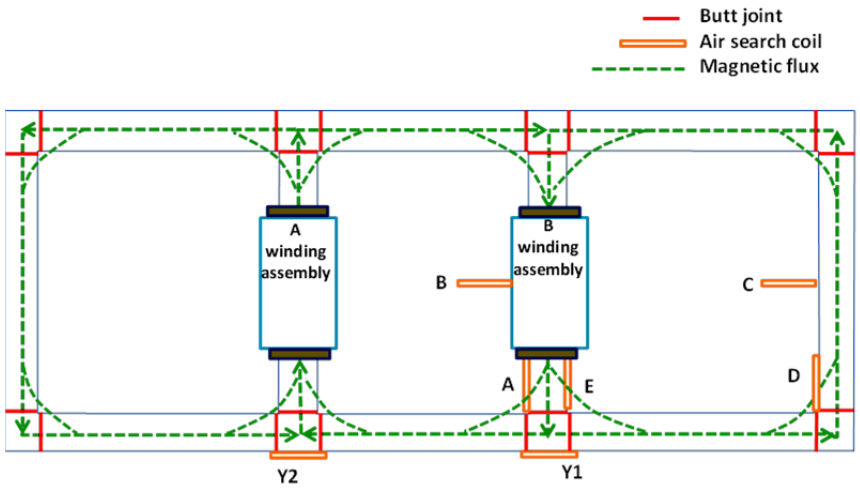

Figure 4.11. Air search coil locations chosen for the testing protocol.

4.4 Onward

The exploratory work in this chapter is useful in:

- Making a comparison between the specification of the test transformer and the test transformers delivered to the testing facility,
- Proving that search coils can be used to measure flux not only in the core but also stray flux in the air spaces around the transformer. Both single turn core and 20 turn air search coils are shown to be adequate for this task,
- Verifying the flux distribution in the core and hence core symmetry,
- Uncovering that there is a change in the core flux distribution in saturation,
- Identifying the problematic core joint design, and
- Showing the importance of the joints to the early saturation of the core which is evident when examining the v-i curves.

To properly understand the core's response a theoretical analysis of the core is necessary before embarking on further measurement and testing. Chapter 5 aims to prove that the findings of chapter 4 are relevant and exposes the deficiencies in the test transformer design using theoretical calculation. Furthermore, alternative core joint designs that make use of multi-step lap mitred joints are shown by theoretical calculation to be superior and more suitable for the test transformers.

Chapter 5

Theoretically determined response of the core components

In chapter 4 the importance of the joints is established both through the early saturation seen with the v-i curves and also the air search coils capturing stray flux at voltages below the original design values.

To properly understand the cores' response a theoretical analysis of the core is necessary before embarking on further measurement through testing.
In the theoretical calculations of section 5.1 perfect core stacking is assumed. A perfect core assumes ideal core construction. Normally, the complexities of burrs in laminations, accuracy of dimensions especially at the corner joints (precision of angles) , flatness of the laminations, dust particles in between laminations, skills in core building (squareness of the core), clamping pressure on the core and non-uniform flux field in the joints (dependent on the magnitude and distribution of the reluctance along the iron circuit) are considerations [Kulkarni & Khaparde 2004].

Furthermore, the effect of inaccuracies and uneven core stacking are discussed and a method for assessing core joint quality is introduced that uses a joint utilization factor. Improved core joints using multi-step lap mitred joints are shown to be superior to non-step lap core joints.

5.1 Flux distribution in the core of the SP-4L transformer

The flux distribution in the core of a SP-4L transformer is dependent on the reluctances of the available flux paths. The manufacturer of the test transformers claims a 50:50 flux distribution at each T-joint in the transformer core. These joints are associated with nodes 1, 4, 5 and 8 in figure 5.1. Reluctance is proportional to the component length and inversely proportional to the permeability and cross sectional area as shown in Equation (5.1).

$$\Re = \frac{l}{\mu A} \qquad (5.1)$$

where:
l is the mean length of the flux in the core component,
A is the cross sectional area of the component and
μ is the permeability of the core material.

The reluctance calculations below are concerned with proportionality with respect to the length of the core sections.

Since the core consists of components made from the same GOES and $\Re \, \alpha \, l$ then the reluctances of the core can be stated in terms of l. Assume that μ remains the same for each core section and accounting for the different cross-sectional areas in terms of length, e.g. *A* of the WL section is double that of either of the RL and IY sections, then its mean length can be halved. All core sections are now normalised to the same cross-sectional area,

A = 3645 mm^2. The reluctances can now be expressed in terms of a constant, k, and length, l. Eqn. 5.2 now becomes,

$$\Re = kl \qquad (5.2)$$

where:
l determines the flux distribution throughout the core, and
k is a constant ($k = \frac{1}{\mu A}$).

In table 5.1 the component reluctances are given in terms of l. The joints only have half the cross-sectional area of their associated bulk core sections and their lengths should therefore be doubled for the thinner core sections and left unchanged for the thicker sections when normalised to 3645 mm^2.

The individual path reluctances are given in table 5.1 and are based on the component lengths given in Figure 4.3. The joint air gap where the laminations meet is assumed to have a length of 3 mm. When conducting visual examinations and measurements of the air gap lengths of the three test transformer cores they are found to be of inconsistent length and 3mm is selected as an average for the purpose of the theoretical calculations. Note: that should the joints saturate first their reluctances become very large and this will drastically alter the core's performance.

Table 5.1. As-built core component reluctances expressed in terms of the component lengths.

Core component *	Assuming maximum permeability		Saturated joint reluctance, $\Re$, (AT/Wb)
	Reluctance, $\Re$, in terms of component length, l, (mm)	Joint reluctance, $\Re$, (AT/Wb)	
WL$^+$	$391.5k$		
RL$^+$	$1243k$		
IY$^+$	$588k$		
WL joints (90mm)	$3k$	139.35	6.55x10^6
IY and RL joints (45mm)	$6k$	278.7	13.1x10^6
$\Re_{5\text{-}6\text{-}7\text{-}8}$	1243k		
$\Re_{5\text{-}4\text{-}1\text{-}8}$	1567.5k		

**WL = wound leg; RL = return path and IY = interconnecting yoke. RL is the sum of the lengths of both the small yoke sections between the T- and 90^0 joint assemblies and the return limb on either side of the transformer respectively.*

$^+$ Reluctances are based on mean length and the joint lengths have been deducted.

5.1.1 Transformer operation along the linear portion of the GOES B-H curve

Linear operation of the core implies that no core component is saturated and that the individual reluctances are a function of the core material's, A, μ_r and l . In Figure 4.3, if winding assemblies A and B are identical, then they are each responsible for half of the core's flux. The flux produced by winding A splits at node 5 according to the flux path

reluctances. The available paths are 5-4-1-8 and 5-6-7-8. These paths are in parallel with path 8-5 which is the wound limb hosting winding A.
$\mathfrak{R}_{5-4-1-8} = 1609.5k$ and $\mathfrak{R}_{5-6-7-8} = 1243k$.

Therefore, path 5-4-1-8 carries, $\left(\frac{1243}{1243+1567.5}\right) \times 100 = 44.23\%$ of winding A's flux and path 5-6-7-8 carries the other 55.77%. Winding B's flux is distributed in the same fashion. Therefore expressing the flux flow per path in terms of a proportion of the total flux through either of nodes 1, 4, 5 or 8, path 5-4-1-8 carries:

$$\left(\frac{44.23 + 44.23}{44.23 + 44.23 + 55.77}\right) \times 100 = 61.33\%$$

and path 5-6-7-8 carries 38.67% of the total flux passing through node 5.
This same distribution therefore takes place at each of the other nodes 1, 4 and 8 as well.

This actual flux distribution must be determined by measurement to prove the validity of this reasoning.

The calculation of the flux distribution at the T-joint by ignoring the core joints makes a difference of 0.22 % to the distribution, i.e. 61.55:38.45 (with joints) compared to 61.33:38.67 (without joints). This shows that during normal operation the contribution of the joints is negligible to the flux distribution provided that they are designed to cope with the design flux density, i.e. $B_{design} < B_C$.

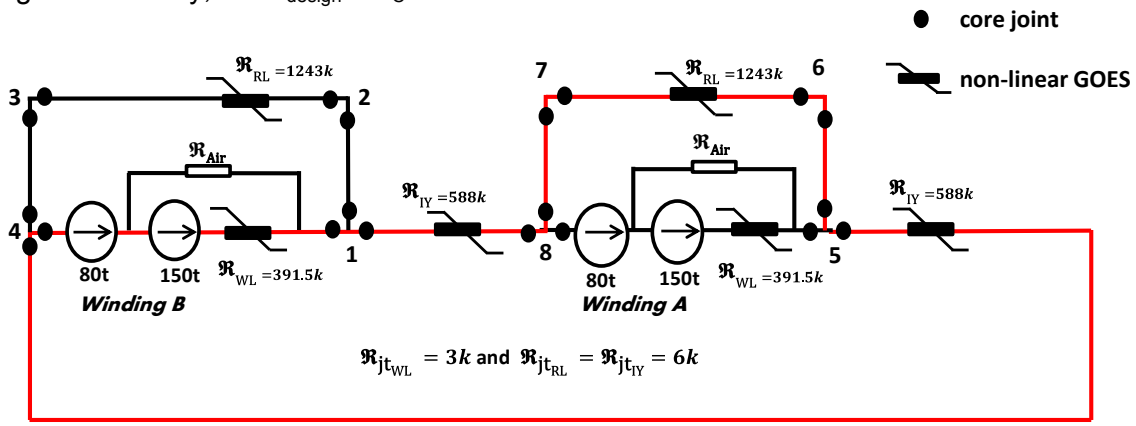

Figure 5.1. The equivalent magnetic circuit of the SP-4L transformer. Red coloured flux path represents the parallel paths seen by either winding, where:
$\mathfrak{R}_{WL}$, $\mathfrak{R}_{IY}$ and $\mathfrak{R}_{RL}$ are the reluctances of the wound limb, interconnected yoke and the return limb path respectively, and $\mathfrak{R}_{jtWL}$, $\mathfrak{R}_{jtIY}$ and $\mathfrak{R}_{jtRL}$ are the reluctances of the wound limb joints, interconnected yoke joints and the return limb path joints respectively.

5.1.2 Transformer operation in saturation

Transformers constructed from laminations require joints to fit the transformer yokes and limbs together. These joints will always have air gaps at the point where the laminations meet in the joint and therefore the fringing phenomenon will be present.

Core saturation leads to stray flux in the air surrounding those core components that are saturated. Ideally, the locations and sequence in which the stray flux manifests should be determined. This will lead to a better understanding of the core response. Both ac and dc components of current are required in the testing to understand the response of the different core components to these components of current.

A bank of single phase transformers does not suffer from mutual inductance as is the case with three phase transformers. Mutual magnetic coupling between phases can significantly change a transformer behavior under GIC conditions but this not the case for single-phase transformers. Instead, the saturation effects associated with single phase transformers is the main concern, i.e. saturation inductance.

Beyond the knee point of the B-H curve of the transformer as the core moves closer towards saturation the flux distribution at the T-joint of the SP-4L transformer will change as the relative permeability, μ_r, and therefore the reluctance of the core paths change. The sharp decline in μ_r for the H111-30 core material beyond the knee point of the B-H curve is illustrated in figure 4.5. The saturation flux density of the core material is provided by the manufacturer as 2.03T.

If the core joints saturate first this introduces a series of virtual 3 mm air gaps into the various flux paths around the magnetic circuit. These air gaps become high reluctance components in the magnetic circuit of the transformer.

Figures 5.2 a graph of the calculated flux densities of the core components with a varying voltage applied to the 80 turn windings shows the sequence of component saturation in the core for T-joint flux distributions of 61.55:38.45. It is clearly seen that the core joints are the first to saturate. The IY joints are the most prone to saturation with the 61.55:38.45 flux distribution.

Table 5.2 gives the calculated ac applied voltages necessary at the terminals of the 80 turn windings to cause saturation in the various core components for a 61.55:38.45 flux distribution scenario. The cross-sectional area and the flux through these cross sections are the only two variables taken into consideration since these are predominant in determining flux density. The table clearly shows the vulnerability of the IY joint to saturation.

Table 5.2. Calculated ac applied voltage necessary at the terminals of the 80 turn windings to cause saturation in the various core components for a 61.55:38.45 flux distribution scenario.

Core component	Calculated 80 turn winding ac applied voltage (V_{rms}) for component saturation with flux distribution of 61.55:38.45
IY	215.89
RL	335.84
WL	262.82
IY joints 1822.5mm^2	107.95
RL joints 1822.5mm^2	167.92
WL joints 3645mm^2	131.41

Examination of Figure 5.2 and Table 5.2 reveals the order in which perfectly stacked core joints will saturate when energized with ac on the parallel connected 80 turn windings. Firstly, the IY joints saturate at 108 V_{rms} followed by the WL joint at 131 V_{rms} and then the RL joint at 168 V_{rms}. This indicates that the problematic flux path causing earlier than expected core saturation is the path that includes the WL and IY core sections. This also represents the flux path with the highest peak fluxes.

If the WL has the largest cross-sectional area and if it is regarded as 1 per unit (p.u.) area then the areas of the other core components can be expressed as a p.u. value of the WL cross-sectional area. The theoretical p.u. areas are given in table 5.3.

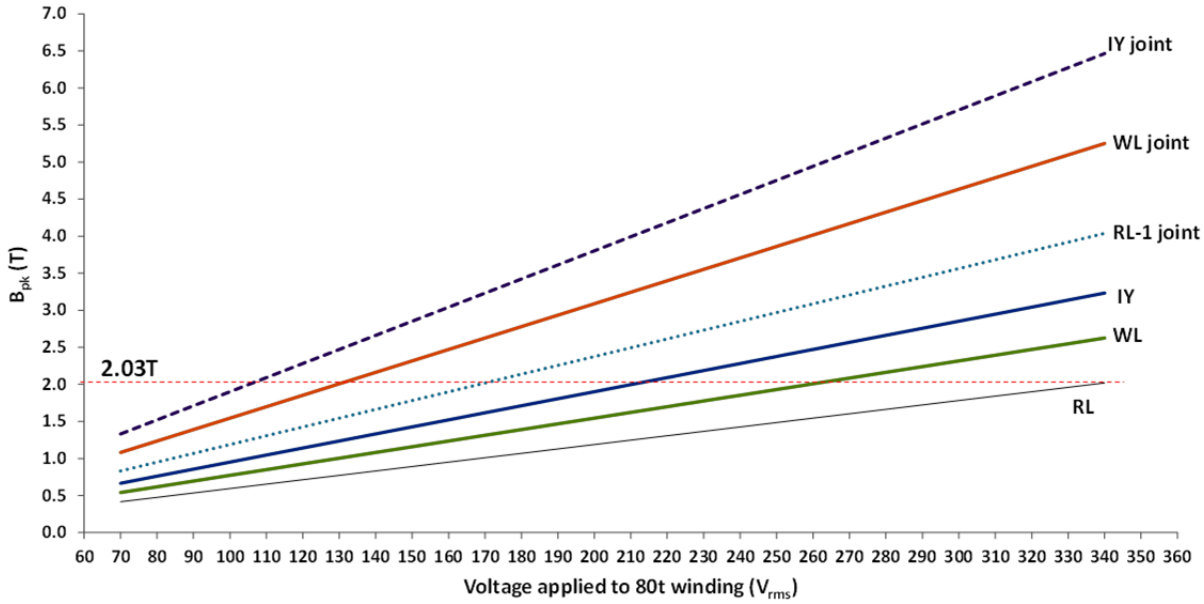

Figure 5.2. Graph of the calculated flux densities of perfectly stacked core components showing the sequence of component saturation in the core for a 61.55:38.45 flux distribution. The transformer is considered to be energised from the 80 turn windings.

In saturation it can be expected that the permeability of the heavily flux laden components of the WL-IY path will reduce first, and more flux will deviate into the RL path.

Table 5.3. Demonstration of the p.u. areas of the core components with clear evidence of the effect on the core joints as a result of the stacking method employed in the manufacture of the test transformers. Actual core joint areas are provided in mm^2.

Core component	Theoretical area (mm^2)	Theoretical p.u. area
Wound limb, WL	7290	1
Interconnecting yoke, IY	3645	0.5
Return limb, RL	3645	0.5
WL joints	3645	0.5
IY joints	1822.5	0.25
RL joints	1822.5	0.25

A perfect core is only possible when ideal core construction conditions are possible. Normally, the complexities of burrs in laminations, accuracy of dimensions especially at the corner joints (precision of angles) , flatness of the laminations, dust particles in between

laminations, skills in core building (squareness of the core), clamping pressure on the core and non-uniform flux field in the joints (dependent on the magnitude and distribution of the reluctance along the iron circuit) are considerations [Kulkarni & Khaparde 2004]. In theoretical calculations in this chapter perfect core stacking is assumed.

5.2 Effect of the unevenness of core joints

The initial assumption in the above discussion is that half the core material exists at the butt-lap joints in terms of the flow of the flux, as illustrated in figures 5.3(a) and (c). Due to human error and the difficulty of consistently aligning the laminations in a joint of this type, the actual core stacking could lead to joints as illustrated in figures 5.3(b) and (d). This is easily verified by examining figures 5.4(a), (b) and (c).

The result is that the effective core area cannot be determined by simple calculation and needs to be determined by measurement.

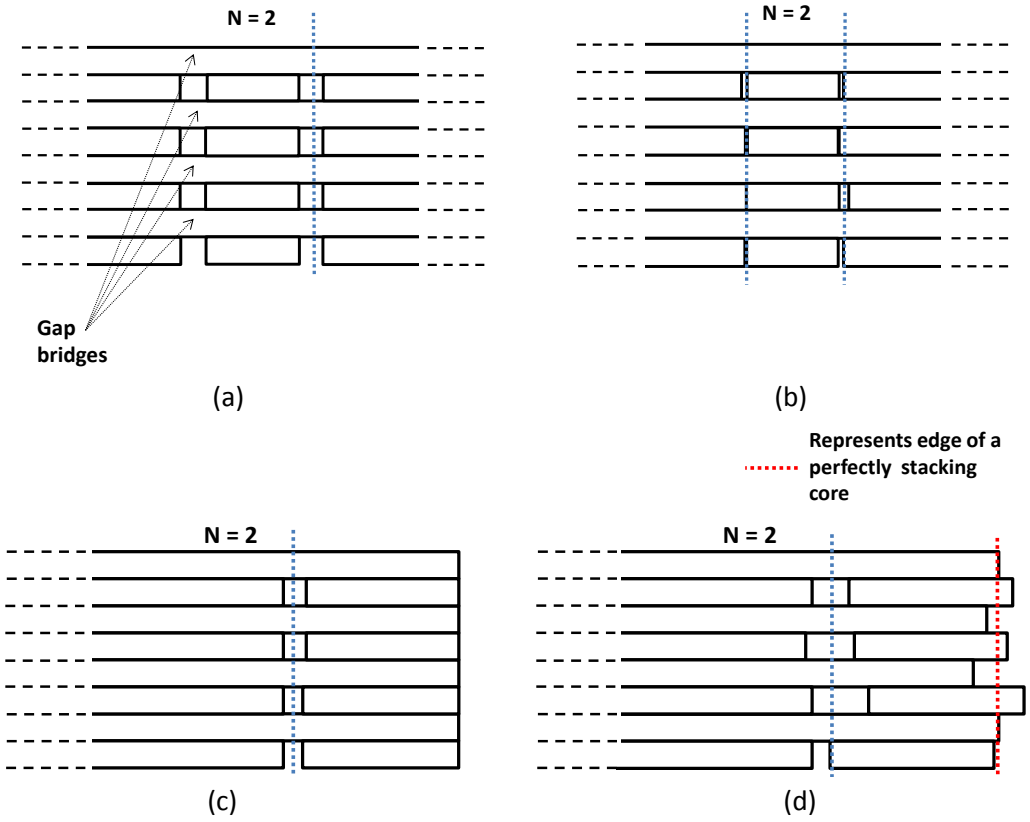

Figure 5.3. Artistic impression of N = 2 non-step lap joint with (a) perfect core stacking at the core T-joint assembly, (b) actual stacking as found at the core T-joint assembly, (c) perfect core stacking at the core 90^0-joint assembly and (d) actual stacking as found at the core 90^0-joint assembly. In (b) the dotted vertical lines indicate smaller air gaps with fewer of them lining up at the joints and therefore more core material at the joint than expected while at (b) the air gaps are larger and the core edge is exceeded affecting available joint area.

In Figures 5.4(a), (b) and (c) the uneven dimensioning and imperfect stacking of the laminations producing air gaps of unequal length, are visible. No visual examination could be made of the WL joints since they are located inside the T-joint assemblies. At each induction level the joints will experience a different peak flux.

(a)

(b)

(c)

Figure 5.4. Actual butt joints (NSL) of the test transformers, where (a) is a T- joint assembly with the IY and RL-2 joints shown, (b) is a 90^0 joint assembly with the RL-1 joint shown and (c) is a 90^0 joint assembly with the RL-3 joint shown. The misalignment of laminations at the joints is clearly evident.

The IY joints are wedged between the wound limbs creating smaller but irregular air gaps lengths producing a larger effective core csa as can be seen in figure 5.3(b). The dotted vertical lines indicate fewer air gaps lining up at the joints therefore making more core material available at the joint than theoretically determined. The effect is similar to that of a multi-step lap joint.

In Figure 5.5 the location of the core joints RL-1, RL-2 and RL-3 along the RL path are illustrated. Examining figure 5.4(a) illustrates the alignment of the RL-2 joint. It appears to have superior stacking than the RL-1 and RL-3 joints shown in Figures 5.4(b) and (c). Due to its irregular stacking the core performance along the RL path is expected to be limited by the joint RL-1 and RL-3 joints. As determined theoretically, these RL joints only experience 38.45 % of the core's flux and therefore do not influence core saturation as profoundly as the IY joints.

The stray flux measurements made in chapter 4 suggests that the WL-joint saturates before the RL-2 joint and it also carries the highest flux component. So, the core performance in early saturation can be considered to be largely affected by the response of the IY-, WL- and RL-1 joints. Based on the foregoing discussion the RL-2 joint can therefore be disregarded in this effective core area study since it will outperform the other two joints RL joints.

Deviations from the theoretical core joint areas given in Table 5.3 for the IY, RL-1 and WL joints can be expected and measurements may indicate earlier or later saturation than the theoretical calculations suggest.

Attempting to predict the precise joint performance for each individual joint would be unrealistic. A simpler method of taking the imperfect stacking into account is required. If the joints at similar locations in the core respond similarly, then using a factor that replicates this performance would be useful.

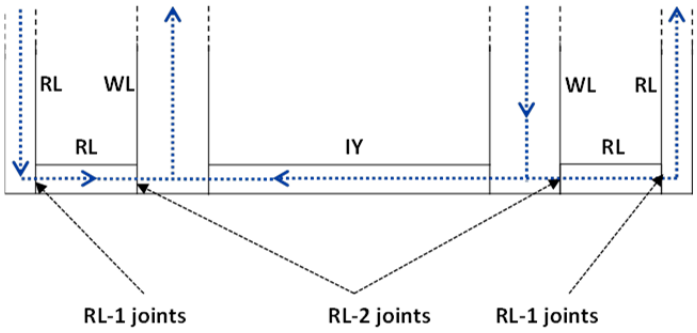

(a)

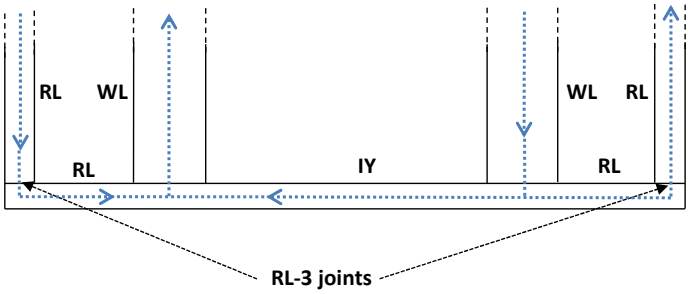

(b)

Figure 5.5. The location of the RL joints in the core structure are illustrated where (a) shows the location of the RL-1 and RL-2 joints and (b) the location of the RL-3 joints.

5.3 Method for determining the core joint performance

In view of the core joint manufacturing evidence seen in Figures 5.4(a), (b) and (c), it is clear that the test transformers cannot be expected to perform as determined in the theoretical calculations. Using measurement data it should therefore be possible to derive indicators that can be used to predict actual joint performance in other transformers making use of the NSL butt joint construction.

The larger effective area of mitred joints, arising from their geometry, makes them less susceptible to saturation before the limbs themselves (see section 5.4).

5.3.1 Effective core joint area

A method of determining the effective joint area and effective flux density, B, is needed to understand the core's response. Otherwise, the first component to saturate could be mistaken to be a bulk core component, such as the wound limb, and the joints could be erroneously ignored.

5.3.2 Empirically determined effective core area, $\mathbf{A_{eff}}$

Du *et al.* [2010] propose an equivalent (effective) magnetic path length which differs from the geometric mean magnetic path length as the flux density changes inside the laminated core. In a similar way, it should be possible to determine an effective core joint area that differs from the perfect joint of its particular type and is among other factors affected by the core stacking process.

Flux distortion, non-uniform flux profile and fringing complicate the joint response further. A simple approach to these complexities could be the use of an averaging factor that is unique to a particular joint type or position in the core structure.

If the flux density and applied voltage at which the joints start to saturate are known, and the peak flux through the joint can be measured then the effective core area can be determined.

The critical flux density at which a core joint saturates is termed B_C; therefore, the corresponding applied voltage should be termed V_C, the critical voltage.

A twenty turn air search coil will link the stray flux from the joint and produce a measurable output voltage. The detection of stray flux in this manner could be used to determine, V_C. A further single turn search coil wrapped around the joint area will provide an output voltage, V_{SC}, that coincides with V_C. The peak flux in the joint at V_C is then:

$$\Phi_{pk} = \frac{V_{SC}}{4.44 \times f \times N} \qquad (5.3)$$

where:
f = 50 Hz,
and $\mathrm{N} = 1$, the number of turns of the search coil wrapped around the joint.

The effective joint area, A_{eff}, can now be calculated using B_{sat} = 2.03T:

$$A_{eff} = \frac{\Phi_{pk}}{2.03} \quad (5.4)$$

5.3.3 Utilisation factor, U

The effective core area will vary from transformer to transformer according to the quality of the core build and core joint type. The possibility of determining a factor based on an average V_C for similar transformers should be explored for use in transformer core response studies in the non-linear portion of the B-H curve.
In a perfect joint the available joint area is given in Equation (5.5).

$$A = l \times t \times b \times \frac{N-1}{N}(mm^2) \quad (5.5)$$

where:
l is the total number of laminations,
t is the lamination thickness,
b is the lamination breadth, and
N is the number of laminations in a step group.

For NSL butt type joints N = 2, so in a perfectly stacked core the joint area will be 50 % of its associated bulk component. The utilization factor, *U*, can be used to relate the effective core joint area to a perfectly stacked joint by the relationship between the terms given in Equation (5.6).

$$U = \frac{A_{eff}}{A} \quad (5.6)$$

So, $B_{pk} = \frac{\Phi_{pk}}{A \times U}$, which can be applied in the absence of definite manufacturer data. A specific design can guarantee a minimum, *U*.

5.4 Application of mitred joints

The use of mitred joints is advantageous since the joint boundary length is lengthened as demonstrated in Figure 5.6. Kulkarni & Khaparde [2004] mention that typical joint mitres are 45^0 at corner joints and 30^0 to 60^0 joints are used at the limb-yoke interface joint as illustrated in figure 5.6.

5.4.1 Effect of non-step lap (NSL) mitred joints

Corner joints with a 45^0 mitre joint on a core limb plate of 45mm breadth have a boundary length equal to √2×45 mm = 63.64 mm as illustrated in Figure 5.6 (a).

Mitred joint area,

$A_{NSL\ 45^0\ Mitre\ jt} = \sqrt{2} \times b \times l \times t \times \frac{N-1}{N} = \sqrt{2} \times 45mm \times 270 \times 0.3 \times 0.5 = 2577.4mm^2$

where:
l is the number of laminations,
b is the breadth of the lamination,
t is the lamination thickness, and

N = 2 for NSL joints.

In Table 5.3 the equivalent butt joint area, $A_{NSL\ Butt\ jt}$, is given as 1822.5mm^2 and the return limb area, A_{RL} is 3645mm^2.

The mitred joint will still saturate before the RL, since $A_{RL} > A_{NSL\ 45^0 Mitre\ jt}$ but later than the butt joint since $A_{NSl\ 45^0\ Mitre\ jt} > A_{NSL\ Butt\ jt}$.

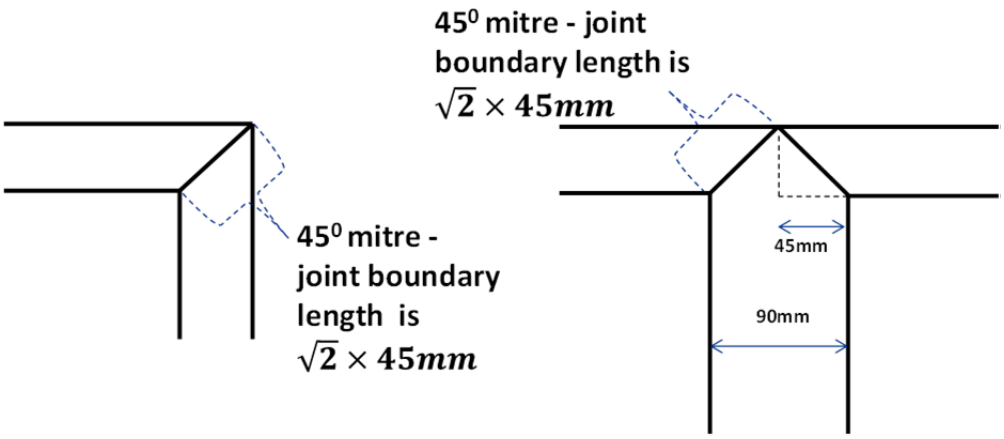

Figure 5.6. Illustration of the length of the joint boundary of (a) a 45^0 mitred corner joint and (b) a 45^0 mitred T-joint.

A T-joint is illustrated in Figure 5.6(b). The foregoing discussion shows that for a 45^0 mitre joint, $A_{RL} > A_{NSL\ Mitre\ T-jt} > A_{NSL\ Butt\ jt}$.

If joint mitres angles between 30^0 to 60^0 are used, then the joint boundary length varies in the range of 51.96mm to 90mm.

Mitred joints angles between 30^0 and 60^0 improve the performance of the joints by increasing the joint boundary length but are still insufficient to prevent core joints from saturating before the RL.

5.4.2 Effect of multi-step lap (MSL) mitred joints

The advantage of the MSL core joint is illustrated in Figure 5.7 where the gain in joint cross-sectional area is evident. A step group of N = 6 is chosen to represent a typical power transformer multi-step lap joint.

Multi-step lap corner joints with a 45^0 mitre and 6 steps has a joint area,

$$A_{\mathrm{MSL}\ 45^0 Mitre\ jt} = \sqrt{2} \times 45\ \mathrm{mm} \times 270 \times 0.3\ \mathrm{mm} \times \frac{5}{6} = 4295.67\ \mathrm{mm}^2$$

$$A_{\mathrm{MSL\ Mitre}\ 45^0 \mathrm{jt}} > A_{\mathrm{RL}} > A_{\mathrm{NSL\ Butt\ jt}}.$$

The MSL 45^0 mitre corner joint with 6 steps performs better than both the IY and RL.

Multi-step lap T- joints with a 45^0 mitre and 6 steps have the same joint area as the corner joints, $A_{\mathrm{MSL}\,Mitre\,T-jt} > A_{RL}$ or A_{IY}.

In all instances MSL joints makes the greatest improvement to the joint performance at saturation flux densities. The combination of mitred and MSL jointing is therefore recommended for laboratory scale transformers for GIC and dc investigations.

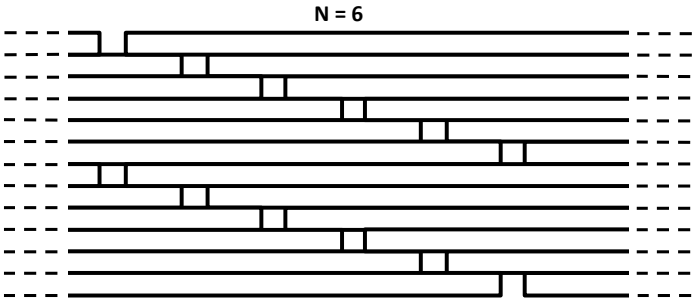

Figure 5.7. MSL joint showing increased core joint cross-sectional area.

5.4.3 Change in core performance with step-lap group number at saturation flux densities

In Table 5.4 one lamination in the step lap group, N, is considered to be a joint, e.g. $\frac{5}{6}$ of the core material is available to the flux at the joint in Figure 5.7. Typically, the core of a power transformer would be stacked in packets of laminations at a time to reduce production time but the overall effect on joint area remains the same provided all other core parameters remain the same. Adapting Equation (5.5) for MSL joints, the available core joint area is therefore determined using Equation (5.7).

$$A_{jt} = b_{mitre} \times l \times t \times \frac{N-1}{N} \qquad (5.7)$$

where:
b_{mitre} is the breadth of the mitred joint (boundary length),
$l \times t$ is the height of the core material stack, and
$\frac{N-1}{N}$ is the fraction of the core material available at each joint.

If packets of 2 or more laminations are used to stack the core then the term $\frac{N-1}{N}$ in Equation (5.7) must be adapted to keep the fraction consistently the same, e.g. $\frac{5}{6} = \frac{6-1}{6} = \frac{12-2}{12}$. In other words, each term in the fraction $\frac{N-1}{N}$ must be multiplied by the packet size.

In table 5.4 each joint type improves with increasing step group number. The p.u. values are referenced to the cross-sectional area of the WL bulk core component. In the case of the butt joint, even with a step lap number of 7 the effective core joint area does not exceed that of its associated bulk core component. This type of joint can never reach the same cross-

sectional area as its bulk core component since it will always only be a fraction of the bulk area component area.

The 45^0 mitred joint has a longer boundary length than the width of its associated bulk component and exceeds its cross-sectional area when N ≥ 4 as seen in table 5.4. Considering the imperfect stacking observed with the test transformers there is a need to take the joint type into account in specifying laboratory transformers for GIC and dc investigations. It is therefore recommended that a 45^0 mitred joint with a step lap group of 5 or higher be specified for laboratory scale transformers for GIC and dc investigations.

Table 5.4. A theoretical demonstration of the effect of joint type and step-lap group number on available joint area in p.u. of the WL cross-sectional area.

Step lap group number (N)	Per unit area (WL is base csa)			
	Butt joint		45^0 mitre joint	
	WL joint (p.u.)	RL or IY joint (p.u.)	WL joint (p.u.)	RL or IY joint (p.u.)
2	0.5	0.25	0.707	0.354
3	0.667	0.333	0.943	0.471
4	0.748	0.37	1.058	0.53
5	0.8	0.4	1.131	0.566
6	0.833	0.417	1.179	0.589
7	0.856	0.428	1.21	0.605

5.5 Onward

The flux distribution at the T-joint assemblies is shown by theoretical calculation to depend on the core component lengths and cross-sectional areas. The flux distribution calculated for normal linear operation correlated with the measured flux distribution in section 4.3.1 and the core joints are shown to have negligible effect on flux distribution.

The IY and WL joints are shown to be the most vulnerable to saturation of all the core components.

The unevenness of the core stacking is shown to either improve the joint performance or aggravate the tendency of butt joints to saturate. This is dependent on the joint location since some joint locations are more tightly packed while others, in particularly the 90^0 corner joints are prone to misalignment especially if there are inaccuracies in lamination length.

A method of determining the quality of the butt joints in a transformer which is a function of the core stacking is introduced. A utilization factor indicates the ratio between the effective joint area to the ideal joint area for a specific joint location in the core configuration.

The benefit of using MSL mitred joints instead of NSL butt joints is demonstrated by theoretical calculation. MSL mitred joints with a step lap group of 5 or more are recommended if the core joints are not to affect the saturation characteristics of the

transformer. Since practical power transformers use MSL mitred joints, laboratory scaled models for GIC or dc investigations should also use them for proper representation. Alternatively, when butt joints are used, the analysis must consider the joint effect.

In chapter 6 the testing protocol for measurement in support of the hypothesis and answering the research questions is presented.

Chapter 6

Testing protocol

In this chapter test requirements for both ac and dc supply circuits are provided.
Wherever test circuits used by other researchers are available these are used as a starting point for the tests, adapted as needed to investigate the specific questions relevant to this study, but also allowing comparisons with the results reported by others.

The chapter lays out the testing required to answer research questions relevant to flux mapping of the core of a single phase four limb transformer, the distortion caused when its core saturates, and determining the parameters of an equivalent circuit model. The three phase testing is concerned with answering the research questions relating to the division of the dc bias current between the phases of a three transformer bank of single phase transformers, the distortion caused when the three phase bank is driven into half-wave saturation, the effect of a motor load on the distortion and the effect of the distortion on the motor's performance.

6.1 General test requirements

This section provides information pertaining to the source circuits to be used in the single phase testing protocols. Quantities to be measured, monitored and processed are specified.

6.1.1 Measurement, monitoring and data processing

A Yokogawa WT 1800 power analyser is used for electrical measurement and data acquisition associated with the transformer test circuits. Combinations of the following quantities are to be recorded as required by each test: P, Q, S, I_{rms}, V_{rms}, I_{peak}, I_{ave}, I_{dc}, I_{THD}, V_{THD} and FFT harmonic and waveform data. When taking resistance measurements the ambient temperature, $T_{ambient}$, is recorded.

IDM66RT Digital Multi-meters, rated for maximum 10 A ac and 1000 V ac are used for ac rms voltage measurement at the SC output terminals. In this regard, a specific meter will dedicated to a group of adjacently mounted SCs for consistency in measurement accuracy for trending purposes.

Reactive power consumption, voltage ratio, current and voltage harmonics, and SC outputs are trended for increasing ac and dc injection as required for each test.

Total harmonic distortion and total demand distortion are represented by eqns. (6.1) and (6.2) and are used to determine the overall distortion caused when the transformers saturate due to over-excitation or due to simultaneous ac and dc components of current in their windings.

$$THD = \sqrt{\sum_{h=2}^{N} \left[\frac{I(h)}{I(1)}\right]^2} \qquad (6.1)$$

$$TTD = \sqrt{\sum_{h=2}^{N} \left[\frac{I(h)}{I_{rated}}\right]^2} \qquad (6.2)$$

6.1.2 Ac supply test circuit

Two 500 kVA, Dyn11, 400 V/11 kV three phase three limb source transformers are connected back-to-back with their taps staggered in order to derive the highest possible ac voltage, V_L = 449.4 V for tests involving core flux distribution and symmetrical saturation. The ac voltage is controlled using a three phase 60A Variac situated between the point of supply and the first source transformer in figure 6.1. The voltage ratings of the test transformer windings are well below the source transformers, i.e. 110/206 V. This implies that the test transformers can be driven into saturation while the source transformers are still in their linear range.

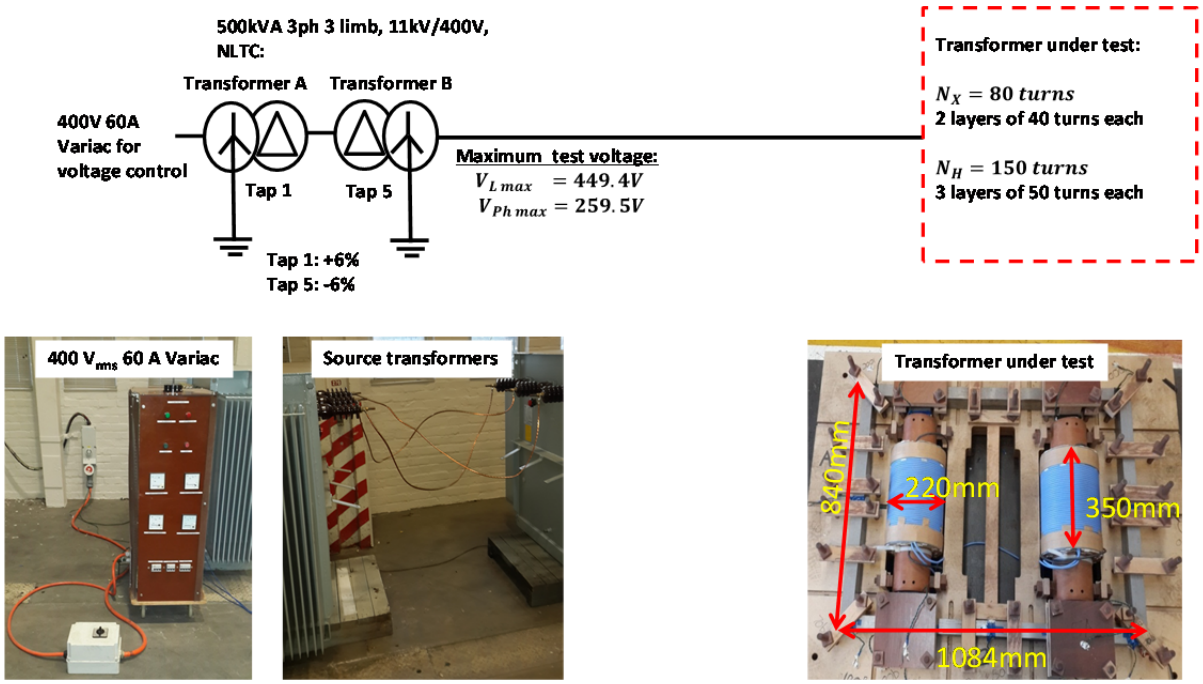

Figure 6.1. Test set-up for supplying ac to the transformer under test.

6.1.3 Requirements for dc single phase testing

In this section the specific requirements for single phase transformer testing with simultaneous ac and dc are explained.

The dc test circuit uses batteries for its dc source since rectified dc sources could introduce harmonics that could mask the actual transformer response. The battery test set-up uses equipment that is more readily available than a rectified dc source with a low pass filter.

The SP-4L transformer has dual 80 turn and 150 turn windings normally parallel connected. It is desirable to keep the ac and dc sources on separate windings during the ac-dc tests. Ac and dc sources on the same side of a transformer with parallel connected windings can create asymmetry as equal sharing of the dc is not guaranteed. Parallel connected windings

of the same number of turns are magnetically coupled and produce the same flux in the core to ensure symmetry.

In order to ensure that the same dc current magnitude flows through both windings these should be series connected. The series connection also provides a higher dc ampere-turns than a parallel connection which will assist to drive the test transformer deeper into saturation for a given dc bias.

When conducting single phase transformer testing the injected dc needs to be excluded from the three phase three limb source transformer since dc in only one of its phases will cause asymmetry and the source transformer could saturate and interfere with the test transformer response tests.

6.1.4 Dc supply test circuit

The requirements and constraints in Table 6.1 are used to select a suitable dc test circuit. In appendix A schematic diagrams of the three dc test circuits under consideration are illustrated. An evaluation table is used to select the most suitable test circuit. The test circuit in Figure 6.2 is selected since it best satisfies the requirements and constraints of Table 6.1.

Table 6.1. List of requirements and constraints imposed for selecting a dc injection circuit.

Requirements	Constraints
Half-cycle saturation	Construction of the test circuit must be easily achieved using standard tools available in the laboratory.
DC injection source protected from induced AC voltage	The circuit must be simple to operate and the number of devices to be monitoring for maximum continuous rating and safety kept to a minimum.
Test circuit at no-load condition	Only readily available power plant equipment and measurement devices can be used.
DC the same in both test windings	
Derive maximum dc ampere-turns (dc series winding arrangement)	
Equal ac voltage across magnetically coupled windings	
3 phase source transformer must not experience dc bias	

Appendix A also contains additional information specific to the specification of the inductor required in the dc test circuit of Figure 6.2, the inductor's ability to protect the battery bank and the suitability of the method of applying the dc bias to the secondary side of the transformer.

In Figure 6.2 the dc injection is provided using series connected automobile batteries. The series aiding connection of the 150t windings produces the highest dc ampere-turns with the available dc source and should be able to drive the test transformer into deep saturation.

A three phase three limb transformer with no tank and 5 equal windings per phase each rated 230 V is used as an inductor. Each of its 230 V windings have their coil ends externally terminated and these are interconnected to form a single phase iron cored inductor with equal windings on each of its limbs. The inductor is shown in Figure 6.3 and has an inductance of approximately 2 H. This coupled with the other impedances in the dc circuit will ensure a low ac component of current.

The resistor bank allows for the dc level to be adjusted as required.

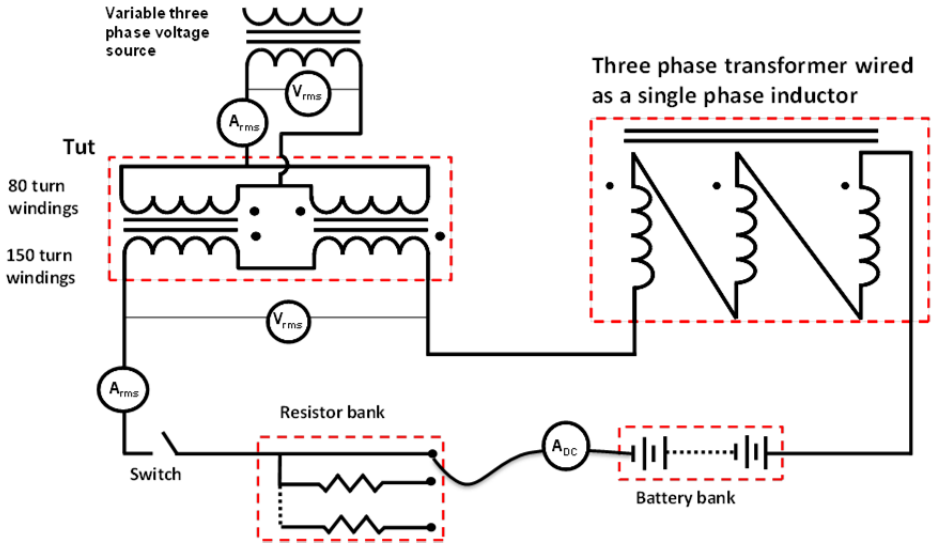

Figure 6.2. Test circuit selected from appendix A for injecting dc into SP-4L test transformer.

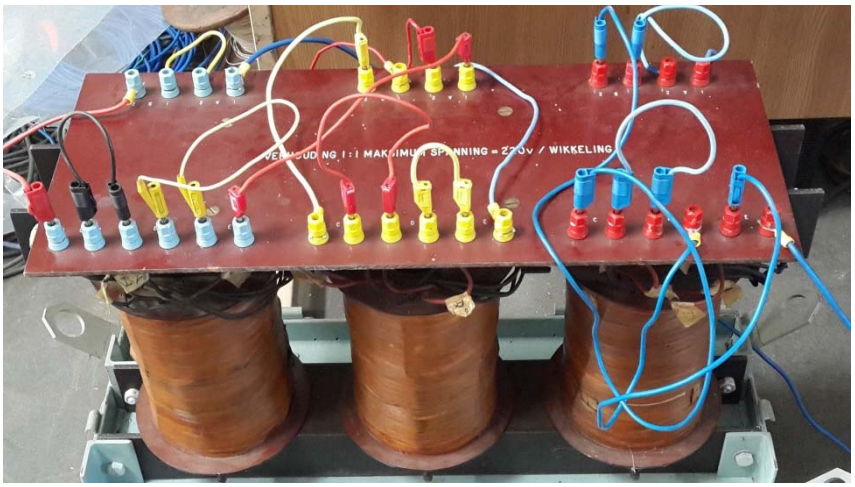

Figure 6.3. A three phase three limb transformer with its windings connected in series to form a single phase inductor.

6.2 Tests to determine the core response of a transformer

This section details the testing required to answer the research questions relating to flux mapping the response of the transformer core using search coils and distortion created when a single phase four limb core type transformer saturates when both ac and dc components are present in the transformer windings. It is expected that the flux mapping of the core will provide a better understanding of the core component responses as the core moves into saturation and their potential effect if any, on the model parameters. All ac tests are conducted at no-load while the ac-dc tests have some secondary load as a result of the dc test circuit in the secondary.

In chapter 5 a method of determining the utilisation factor of butt type joints is proposed. Additional testing is proposed since it deals directly with the core saturation problem identified with the butt joints of the test transformers. It is relevant since it will further validate the claim made in chapter 5 about the effect of the uneven core stacking at the joints.

6.2.1 Core flux mapping

It is established in chapters 4 and 5 that the flux flow in the core varies dependent on the relative permeability of the core material along a path. An overview of the flux flow is obtained in section 4.3.1. The flux leaves and re-enters the core as a joint or section of a limb or yoke saturates. For a more detailed understanding of the response of the individual bulk core components a more intensive search coil deployment is required. There are two test scenarios explored in this section and these are:

- Flux distribution at the core T-joint assembly with varying ac excitation and
- Individual core component responses with simultaneous ac and dc excitation.

6.2.1.1 Flux distribution at the T-joint assembly

The flux leaving the core T-joint assemblies is measured using the search coils at locations 60 and 80 in Figure 6.6 with ac excitation applied to the 80 turn windings. A voltage test range that varies from approximately 90 V_{rms} to 270 V_{rms} is used with 10 V_{rms} increments. The flux distribution is then determined by using the search coil outputs at core T-joint assemblies a, b, c and d in the Figure 6.8. The search coil outputs are firstly averaged for each transformer and then averaged for all three transformers and graphically displayed as a percentage flux distribution through search coil locations 60 and 80. This represents the IY and RL paths flux ratio.

6.2.1.2 Individual core component responses

Single turn core search coils are placed at regular intervals (2 or 4 cm apart) along selected core sections based on the core symmetry. It is expected that the shorter core sections in the general location of the core joints will have a more complex or unpredictable stray flux pattern and a higher resolution measurement method is required, i.e. search coils 2 cm apart.

In Figure 6.4 paths of suspected stray flux are shown based on the preliminary testing carried out in chapter 4. The figure shows four core sections selected for search coil deployment based on core symmetry. These are:

- Search coils 11 to 16 that are used to measure the flux leakage from the winding. These are single turn search coils wrapped around an insulated mild steel bar (simulating a tie bar) inserted inside the winding and resting on the core,
- Search coils 17 to 30 that are used to measure the flux in the IY,
- Search coils 31 to 39 that are used to measure the flux in the short yoke section along the RL path, and
- Search coils 40 to 50 that are used to measure the flux in the return limb along the RL path.

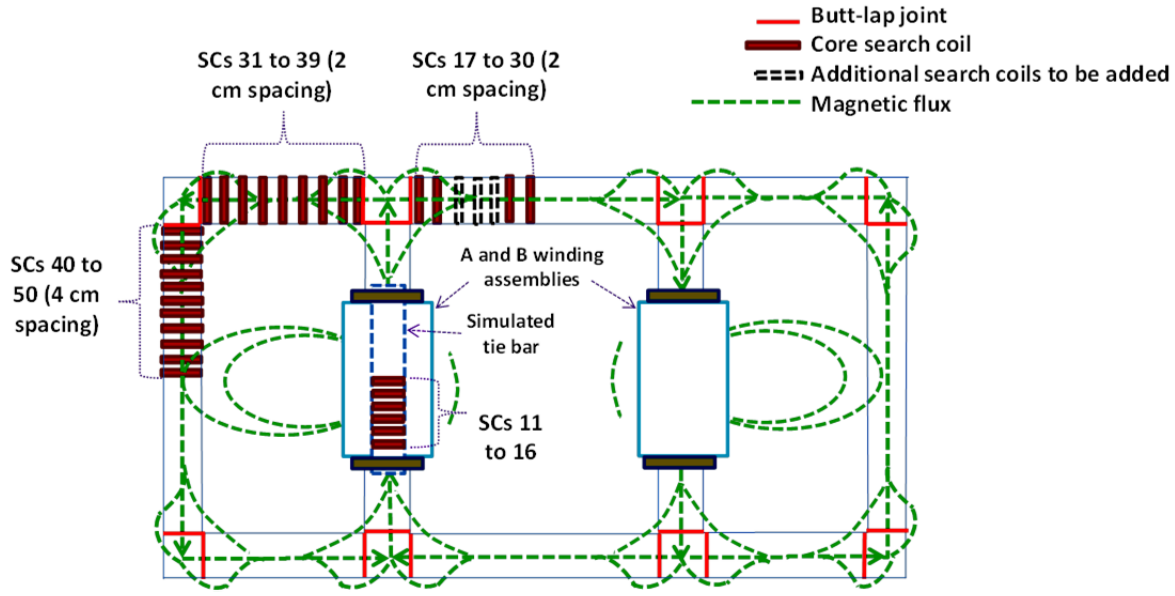

Figure 6.4. Search coils deployed on the IY, RL and WL to get better insight into the response of the core at these locations with ac and dc components of current in the windings. Paths of suspected stray flux are indicated. The leakage flux in the inner window is suppressed by the opposing fields of the two windings.

The 80 turn windings of test transformer T1 are connected to the ac supply circuit of Figure 6.1 and the 150 turn windings are connected to the dc supply circuit of Figure 6.2. The ac voltage is adjusted to the transformer nominal voltage of 110 V and the dc bias applied to the secondary side. After each dc increment the search coil outputs are recorded. The ac supply voltage is adjusted back to 110 V_{rms} each time the dc bias level on the secondary is changed. It should be noted that increments in the dc bias cannot be of equal size due to the need to increase the dc supply circuit voltage by adding additional batteries or introducing additional resistance. The stored charge available and terminal voltage of each battery differs from that of the others, and the resistor banks have fixed resistance blocks which further complicate attempts to have dc increments of equal size.

The flux mapping results need to be presented graphically for easy comprehension.

6.2.2 Distortion in a standalone single phase transformer

This section is concerned with the harmonic distortion of the primary current, and primary and secondary voltages. Since the transformer is not at a true no-load condition the distortion of the secondary current is also monitored to ensure that no secondary effects are taking place in the dc test circuit. A Yokogawa power analyser is used to:

- Record the ac quantities of primary and secondary currents, and primary and secondary voltages,
- Record the dc current in the secondary circuit,
- Monitor the ac current in the secondary circuit to ensure it does not exceed 5A per 100 A.h (to prevent unwanted heating in the batteries), and
- Perform FFTs of the primary and secondary currents, and primary and secondary voltages.

Following on from section 6.2.1.2 test transformer T1 is selected for consistency in this chapter. The 80 turn primary winding is energized using the ac supply circuit of Figure 6.1 and the series connected 150 turn secondary windings are biased using the dc test circuit of Figure 6.2. The primary winding is brought to nominal excitation, i.e. 110 V. Starting from 0 A dc the dc bias is increased at approximately 1 A intervals up to the maximum possible with the available battery bank. The ac winding is readjusted back to nominal voltage after each dc increment.

Graphical representation is used for results analysis.

6.2.3 Testing to determine the utilization factor of the butt type joints

This section deals with testing to validate the method proposed in chapter 5 that seeks to determine a utilisation factor for butt type joints.

The single turn search coils for measuring the peak flux flowing through the joints are installed as shown in Figure 6.5. The measurement rigor applied to the transformer core is demonstrated in Figure where each individual search coils has a unique number for comparison purposes. This new numbering system is necessary so as not to confuse these measurements with previous test measurements. The general trend of both peak flux flow and flux density are expected to be similar for joints of the same type and situated at the same symmetrical location.

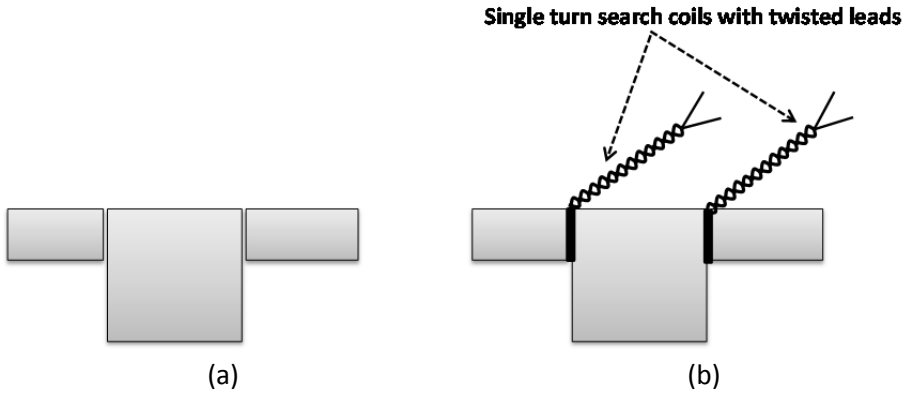

Figure 6.5. T-joint assembly showing (a) core joint with the air gap visible and (b) the search coils wrapped over the joint air gap location.

The testing is carried out for all three test transformers. Re-test for V-I magnetization curve validation once the search coils are installed to ensure that the core has not been effected.

Due to the large number of measurements envisaged and the expectation that the supply circuit breakers might trip at high induction levels, two tests are carried out per test transformer. One test is for the core search coils and the second is for the air search coils. For each test the test transformer lower voltage windings, i.e. the 80 turn windings, are selected as the energising winding. Over-excitation testing using the 80 turn windings provides a larger voltage range when considering the ac supply circuit capability. Testing is conducted using the test circuit of Figure 6.1.

Test 1: In this test the single turn search coils at locations 5, 7, 60 (IY-joint), 70 (WL-joint), 80 (RL-2 joint), 100 (RL-1 joint) and 110 (RL-3 joint) in Figure 6.8 are monitored with increasing ac induction level. The search coils of primary interest are 60 (IY-joint), 70 (WL-joint) and 100 (RL-1 joint). All other search coils in Figure 6.6 are required merely to ensure that the transformer core is responding the same at each joint. A starting voltage of 90 V_{rms} is chosen since this is at a pre-saturation induction level. The ac voltage is increased with approximately 2 to 3 V_{rms} increments and the above mentioned search coil outputs are recorded for each ac voltage increment. The upper induction voltage is to be determined by the ability of the supply circuit breakers to sustain the high peak excitation current associated with transformer saturation. It is expected that search coils 100 and 110 will give a similar output voltage. If this is a correct assumption then search coil 110 can excluded from the test.

Test 2: In this test the twenty turn air search coils at locations A, D and E in Figure 6.8 are monitored with increasing ac induction level. The same experimental procedure is followed as test 1. The inception voltages in Table 4.3 are a guide and when approaching applied voltages close to these values proceed slowly by making the smallest voltage increments possible to ensure that the inception voltage of each joint is determined as accurately as the equipment permits.

The method explained in section 5.3 is used to determine the utilisation factor of the joints at a similar location in the core using graphs of search coil output versus applied ac voltage plotted for both tests 1 and 2.

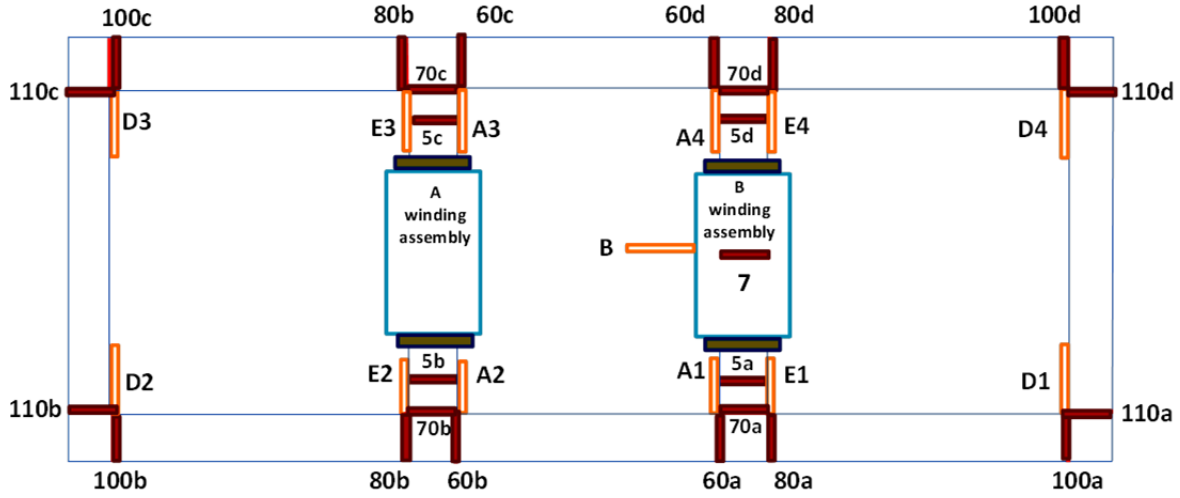

Figure 6.6. Four limb single phase transformer core fully equipped with search coils for monitoring both the flux in the core and the stray flux at the core joints. Search coil numbering is added for comparison of the performance of similar joints or positions in the core geometry.

6.3 Tests to determine model parameters

This section deals with the tests required to determine the model parameters of a grey–box model (pi equivalent) as mentioned in chapter 3.

6.3.1 No load losses and excitation current test (open-circuit test)

The no load and excitation test is conducted in accordance with IEEE Std C57.12.91- 2011 and the testing is carried out from both voltage sides of the transformer, i.e. the 80 turn and 150 turn sides respectively. Having the data to determine the $2L_m$ and $2R_C$ parameters from both sides of a test transformer provides confidence in the test results.

The core loss component and excitation parameters in the pi model are represented as two parallel branches are defined by equations (6.1) and (6.2) respectively.

$$R_1 = R_2 = 2R_c = 2\frac{(V_{oc}-R_{s1}I_{oc})^2}{P_{oc}} \qquad (6.1)$$

$$2L_m = 2\frac{(V_{oc})^2}{\omega Q_{oc}} \qquad (6.2)$$

where:
L_m is the parameter that represents the core iron path magnetization,
R_c is the core loss parameter,
ω is angular velocity, and
R_{s1} is the winding resistance for the side of the transformer that is energized during the test.

6.3.2 Load losses and impedance voltage test (short-circuit test)

The load losses and impedance voltage test is conducted in accordance with IEEE Std C57.12.91- 2011 and the testing is carried out from both voltage sides of the transformer, i.e. the 80 turn and 150 turn sides respectively. Having the data to determine the L_S and R_S parameters from both sides of a test transformer provides confidence in the test results and simplifies the use of Equations (6.6) and (6.7).

The load loss and impedance voltage parameters, R_S and L_s, are defined by Equations (6.3) and (6.4) respectively.

$$L_s = \frac{1}{\omega_s}\sqrt{\left(\frac{V_s}{I_{sc}}\right)^2 - \left(\frac{P_{sc}}{I_{sc}{}^2}\right)^2} \qquad (6.3)$$

$$R_s = \frac{P_{sc}}{I_{sc}^2} \qquad (6.4)$$

where:
L_s is the leakage inductance on the side of the transformer that is energized during the test, and
R_s is the total winding resistance determined at the test ambient temperature for the side of the transformer that is energized during the test.

Each transformer's total winding resistance, R_s, should be resistance temperature corrected to 20 ^{0}C using Equation (6.5).

$$R_{20} = R_m\left[\frac{(20+234{,}5)}{(T_m+234{,}5)}\right] \qquad (6.5)$$

where:
R_{20} is the resistance of the winding at 20^{0}C,
R_m is the resistance of the winding at the ambient temperature at the time of the test, and
T_m is the ambient temperature at the time of the resistance measurement.

<u>Ac winding resistances:</u>

The dc winding resistances are determined as part of the acceptance tests in section 4.2.1 and are used to apportion the series resistance, R_s, between the 80 and 150 turn windings. This is achieved by applying Equations (6.6) and (6.7) respectively.

$$R_{80} = R_{S_{80}}\left(\frac{R_{DC_{80}}}{R_{DC_{80}}+(R_{DC_{150}}/N^2)}\right) \qquad (6.6)$$

$$R_{150} = R_{S_{150}}\left(\frac{R_{DC_{150}}}{R_{DC_{150}}+(R_{DC_{80}}\times N^2)}\right) \qquad (6.7)$$

where:
R_{80} is the ac resistance of the 80 turn winding at 20^{0}C,
R_{150} is the ac resistance of the 150 turn winding at 20^{0}C,
R_{S80} is the ac series resistance value determined from the load loss and impedance voltage test from the 80 turn winding side,

R_{S150} is the ac series resistance value determined from the load loss and impedance voltage test from the 150 turn winding side,
R_{dc150t} is the dc resistance of the 150 turn winding at 20^0C,
R_{dc80t} is the dc resistance of the 80 turn winding at 20^0C, and
N is the turns ratio of the transformer.

6.3.3 Terminal saturation inductance

In order to determine the terminal saturation inductance of a transformer a test circuit is required that can drive the transformer deep into the saturated region. Performing this test with conventional test circuits requires a large ac power source (more than 10 times larger than the transformer rating) because high voltage is required to push the core into saturation and the transformer draws large asymmetrical current when it saturates. There is potential for these high voltages to damage the test transformer windings and the interlamination insulation De León *et al*. [2014].

De León *et al.* explain that the terminal saturation inductance can be measured using a non-ideal low-power rectifier. The dc drives the transformer into deep saturation, and its ripple provides a low-amplitude variable excitation around the operating point as illustrated in Figure 6.7.

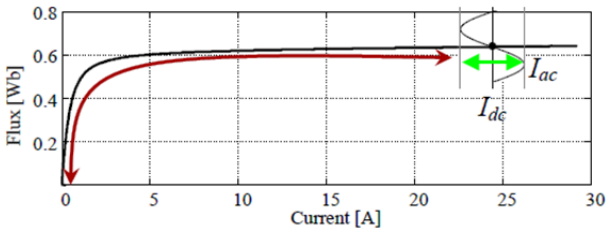

Figure 6.7. Positive part of the saturation curve and operation of the transformer with a dc-biased ac excitation [De León et al. 2014].

Referring to Figure 6.7, each time the transformer is excited with the rectifier it goes into deep saturation on the positive side of the curve. The result is accurate with any remnant flux, and the method does not need pre-demagnetization.

Based on the equipment available for the tests, the circuit shown in Figure 6.8 is developed and is based on the three phase test circuit used by De León *et al*. [2014]. The finer details relating to the circuit are contained in the conference paper by Borrill *et al.* [2017]. The new circuit is simulated in PSCAD to provide confidence in its ability to drive the transformer into deep saturation. The simulation results are presented in appendix D.

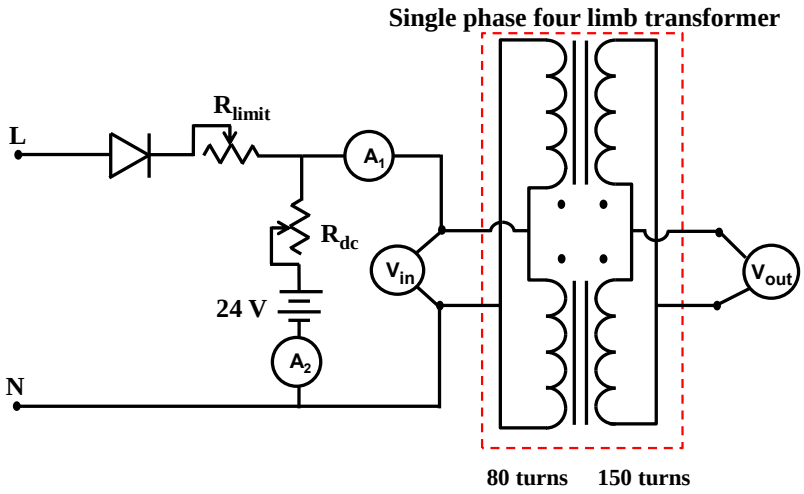

Figure 6.8. Single phase test circuit for determining the terminal saturation inductance of each winding of a test transformer [Borrill *et al.* 2017], where:
R_{limit} is used to protect the ac source from the low transformer winding dc resistances,
R_{dc} controls the amount of dc bias supplied by the battery bank to drive the transformer into deep saturation, and the single phase half-wave non-ideal rectifier supplies some dc and the small ripple required for inductance measurement.

The ac supply voltage to the single phase rectifier is controlled using a variac. The rectifier supplies some dc bias in the circuit but its predominant function is to supply the ripple necessary for determining L_{air} and the bulk of the dc is provided by the battery bank.

Care must be taken to monitor the temperature of the variable resistors, which conduct large currents. These are air cooled using two desk top fans.

It is expected that for the terminal saturation test from the outer winding side which has fewer turns (80 turns) than the inner winding (150 turns) will require higher dc magnitudes to ensure transformer deep saturation.

The current into the energised winding and the voltage on the other winding are measured. This captures the incremental flux while eliminating from the calculations the winding and the source resistances. Possible discrepancies caused by variations in resistance are thus avoided [de León 2014].

The Yokogawa WT 1800 power analyser is used to measure and record the ac and dc currents at A_1 and the ac voltage at V_{out} in Figure 6.8. The Yokogawa power analyser is used to perform a fast Fourier transform of the ac current into the transformer and the ac voltage out to obtain the magnitudes of the current and voltage for the different harmonic orders. The L_{air} for both the inner and outer windings is determined using the dominant harmonic present in the measurement data and by substitution into Equation (6.8).

The process is repeated for each set of windings until the L_{air} value plotted on a graph of L_{air} versus dc input to the transformer becomes a constant value indicating that deep saturation has occurred. The constant L_{air} value is then considered the terminal saturation inductance.

$$L_{Air} = \frac{V_{out_k}}{2\pi f_k n I_{in_k}} \quad (6.8)$$

where:
L_{air} = terminal saturation inductance,
k = harmonic order,
V_{out_k} = amplitude of the secondary voltage of the dominant harmonic,
f_k = dominant harmonic frequency ,
n = the turns ration of the transformer, and
I_{in_k} = amplitude of the current of the dominant harmonic.

L_{air} for the inner and outer windings, and L_S are necessary for determining the L_{sat} parameters of the grey-box model using the Equations (6.9) and (6.10) as developed by Jazebi et al. [2013].

$$L_{2-sat} = \left(\frac{L_s}{L_{air-out} - L_{air-in} - L_s}\right) \times \left(L_s - 2L_{air-out} \pm \sqrt{L_s^2 + 4L_{air-in}\, L_{air-out}}\right) \quad (6.9)$$

$$L_{1-sat} = \frac{L_{air-in}\,(L_{2-sat} + L_s)}{L_{2-sat} + L_s - L_{air-in}} \quad (6.10)$$

In the grey-box model $L_{1\text{-}sat}$ and $L_{2\text{-}sat}$ represent the slope of the saturated portion of the saturation characteristic as experienced from the 150 and 80 turn sides of the transformer respectively.

6.4 Three phase testing

This section deals with the research questions relating to a three phase bank of single phase transformers. The testing protocol therefore seeks to find answers to:

- How the dc in the neutral splits per phase in a three phase bank of single phase transformers,
- Is the distortion different when the three phase bank of single phase transformers saturates in a YNyn or YNd configuration?
- The effect of the transformer load on the distortion created when the dc drives the transformer bank into half-wave saturation, and
- Whether the distortion contains signals that are harmful to generators are addressed in the testing.

As mentioned in chapter 4 the test transformers are de-rated. The de-rating limits the testing that can be conducted under motor load conditions. A loaded induction motor needs a terminal voltage as close as possible to its rated voltage otherwise long term insulation damage can occur. Only the YNyn transformer configuration can therefore be used for the load test with the 150 turn windings connected to the load.

6.4.1 Three phase test circuit

The ac supply circuit in Figure 6.1 is used to energise the 80 turn windings of the three phase bank of single phase transformers in Figure 6.9. All cable lengths are cut to approximately equal lengths and all terminal connections are tightened for good electrical contact.

The test transformer bank can be either YNyn0 or YNd11 connected. The line voltage to the 80 turn side of the three phase bank is treated as a stiff nominal line voltage supply of 190.5 V. As is seen in Figure 6.9 the dc bias is introduced to the test circuit through the neutral wire. A maximum dc in the neutral conductor of 150 A is deemed to be safe since it is within the current breaking capacity of the dc switch and the dc per phase is expected to be close to one third of the total dc flowing in the neutral.

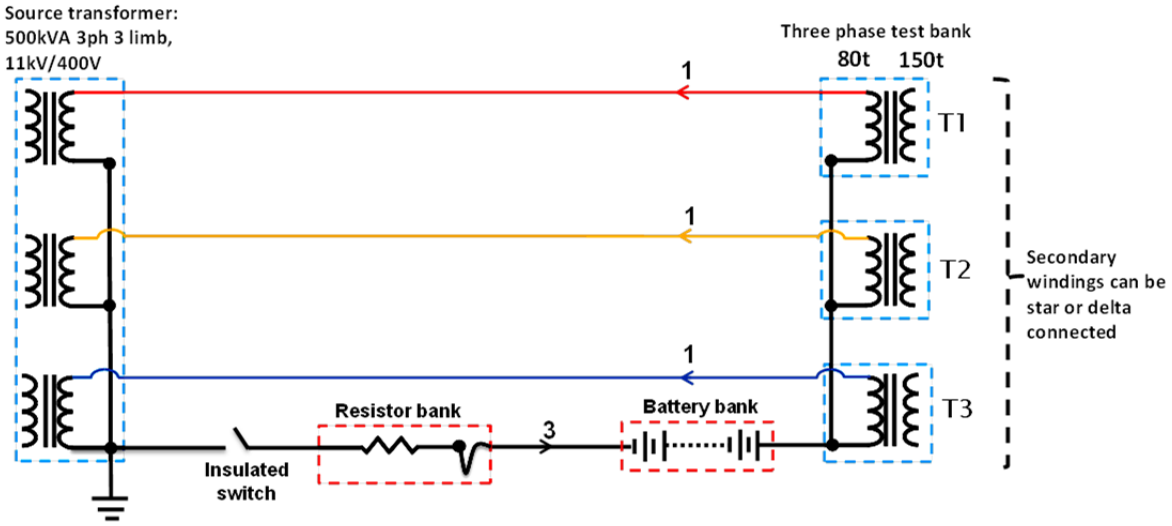

Figure 6.9. Three phase test circuit for injecting dc bias into the ac energised windings. Both the Ynd11 and YNyn0 connections can be achieved with this test circuit.

6.4.2 The division of the dc per phase

It is expected that the division of the dc per phase is dependent on the dc resistance of the sum of the individual resistances per phase. Whether the ac current in the circuit has an impact on the dc current per phase needs to be determined. A balanced load is used to introduce an ac current into the circuit, i.e. a 3 phase induction motor. The current per phase into the motor is confirmed to be close balanced prior to the commencement of the test. The balanced ac load removes the effect of unequal heating per phase.

This test can be done in conjunction with some of the tests in section 6.4.4. The test is carried out for two motor load scenarios, i.e. approximately 2 A and 6 A. With the transformer bank at the chosen load condition the ac supply voltage on the star connected primary side is increased to nominal line voltage. The dc bias is introduced through the neutral conductor. After each change to the dc bias the primary line voltage is readjusted back to its nominal value to keep the ac induction level constant for each measurement. A dc bias range of approximately 1 A per phase to a maximum of 50 A per phase is used for the

test. The dc in the neutral and in each phase of the transformer bank primary side is recorded using the Yokogawa power analyser. The test is then repeated for the next load scenario.

The ratio of test transformer dc per phase to the total dc flowing in the neutral is plotted for all three test transformers on the same set of axes. Both load scenarios are considered for the graphical analysis.

6.4.3 Distortion in a YNyn0 and YNd11 transformer bank

This test can be done in conjunction with the tests in sections 6.4.2 and 6.4.4. The test is firstly done with the secondary windings star connected and then repeated with the secondary windings delta connected. Two load scenarios are tested, i.e. open-circuit secondary and a motor load current of 6 A. In the case of the motor load test only the YNyn0 connection is used for the reason stated in section 6.4.

The Yokogawa power analyser is connected to record the measurements of primary and secondary voltages and currents, the dc level per phase and the total dc in the neutral conductor. The FFT function of the power analyser is enabled to produce current and voltage harmonic data of the primary and secondary voltages and currents.

Graphs are plotted for both the star and delta secondary connection circuits showing:

- Current and voltage waveforms with varying dc
- Current and voltage harmonics with varying dc, and
- THD and TDD plots of a single transformer in the three phase bank.

6.4.4 The effect of load on the level of distortion

In this section the effect of a 3 phase induction motor load on the level of distortion that occurs when a three phase bank of single phase transformers are driven into part-cycle half wave saturation is assessed. The motor has a dc generator attached to its shaft and the generator is loaded using a variable resistor across its output terminals.

The test circuit is connected as illustrated in Figure 6.10 with the transformer bank in a YNyn0 configuration. The transformer bank produces a maximum line voltage at its terminals of 357.2 V. This represents a 6% reduction in supply voltage at the 380 V motor terminals. Since the tests are to be carried out for intervals of no more than 1 minute at a time this is not considered to be detrimental to the health of the motor. Its operating temperature is be monitored as a safety precaution.

The motor load test scenarios in table 6.2 are achieved by varying the resistance across the output terminals of the dc generator.

The Yokogawa power analyser is to be connected to gather measurements of primary and secondary voltages and currents, and the dc bias in the phase and neutral conductors.

The FFT function of the power analyser is enabled to gather current and voltage harmonic data at both primary and secondary terminals of the transformer.

Graphical representation of THD and TDD of the transformer input current with varying dc bias is used for analysis.

Table 6.2. Permissible load scenarios for testing the effect of load on distortion level with varying levels of dc bias in the test transformer 3 phase bank.

Load type	Estimated load magnitude per phase (A_{rms})
Open circuit	0
Motor at no load	0.9
Motor at partially loaded	2
Motor at full load	6

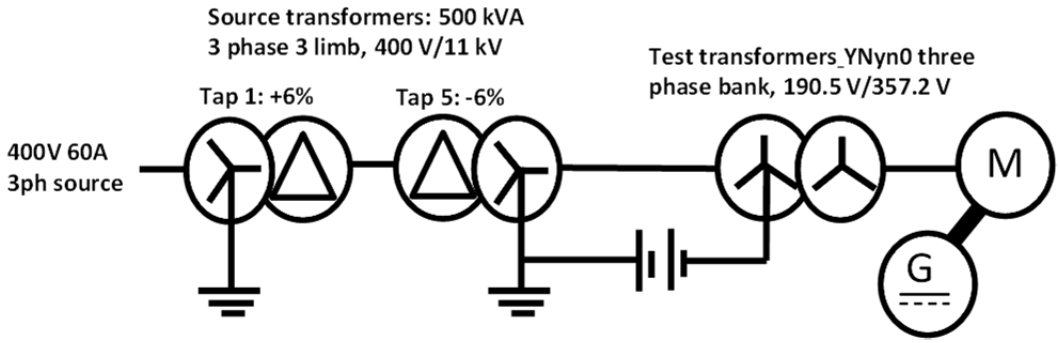

Figure 6.10. Single line diagram of test circuit for determining the effect of load on distortion when the three transformer bank is driven into part cycle half-wave saturation.

6.4.5 Effect of distortion on the performance of an induction motor

In this section testing to determine the performance of a three phase induction motor is assessed when it is connected to the output terminals of a YNyn0 connected three phase bank of single phase transformers. Other than a dc generator attached to its shaft the motor is at no load and two transformer bank scenarios are used for the testing:

- Transformer bank in its linear range (normal operation), and
- With a dc bias applied to the primary windings of the transformer bank causing half-cycle saturation.

This test can be done in conjunction with some of the tests in 6.4.4 using a three phase bank with a YNyn0 configuration.

Taylor [2000] mentions sound recordings with a microphone as an accurate method to measure discrete frequencies heard with the ear. Although this not the only test available it is the most easily achieved in the absence of more specialized equipment. A standard Apple iPhone is used in the testing to determine if there is a change in the motor's performance when dc bias is applied to the transformer bank's primary windings. The iPhone is not be calibrated for this test as changes in relative power level will be used for making a comparison. The following three sound recordings are made

- Recording A is made at maximum ac voltage at the motor terminals, i.e. 357 V ac and no dc bias in the transformer primary winding,
- Recording B is made with approximately 50 A dc bias on the transformer primary winding and a voltage collapse brought about by the half-wave saturation of the supply transformer, and
- Recording C is made with approximately 50 A dc bias on the transformer primary winding and the ac voltage restored back to 357 V.

FFT spectral analysis of the sound recordings is used to determine if there is a change in the motor's performance.

6.5 Onward

In this chapter the ac and dc supply circuits are introduced and the value of the Yokogawa power analyser for measurement, data storage and FFT processing is identified.

The chapter sets out the testing required to answer research questions posed in chapter 1 with respect to distortion, the effect of a three phase motor load on the distortion and vice versa. In addition, testing required to determine the parameters of the equivalent circuit model of the four limb single phase transformer are described.

In the next three chapters the results and analysis are presented where:

- Chapter 7 deals with the single phase tests,
- Chapter 8 the equivalent circuit parameters, and
- Chapter 9 the three phase tests.

Chapter 7

Single Phase Test Results

In this chapter the results of the testing relating to flux mapping the response of the transformer core using search coils and distortion created when ac and dc components are present in the transformer windings a single phase four limb core type transformer saturates are presented.

7.1 Core flux mapping

The results of testing to related flux mapping the core of a single phase four limb transformer are presented in this section. Two test scenarios are reported on, i.e. the flux distribution at the T-joint assembly with ac energisation and the individual core component responses with simultaneous ac and dc excitation.

7.1.1 Flux distribution at the T-joint assembly

In Figure 7.1 the average flux distribution for all the T-joints of all three test transformer are plotted as a function of the voltage applied to the 80 turn winding. Search coil 60 represents the flux flowing through the IY path and search coil 80 represents the flux flow through the RL path. An interesting observation is that the flux flowing into IY (SC 60) decreases steeply until approximately 140 V_{rms} after which it starts to increase slightly and at approximately 190 V_{rms} decreases again. The exact opposite can be said for the flux flow through the RL (SC 80) path. Similar trends can be seen for each one of the test transformers T1, T2 and T3 but with differences of a few percent in the flux distributions.

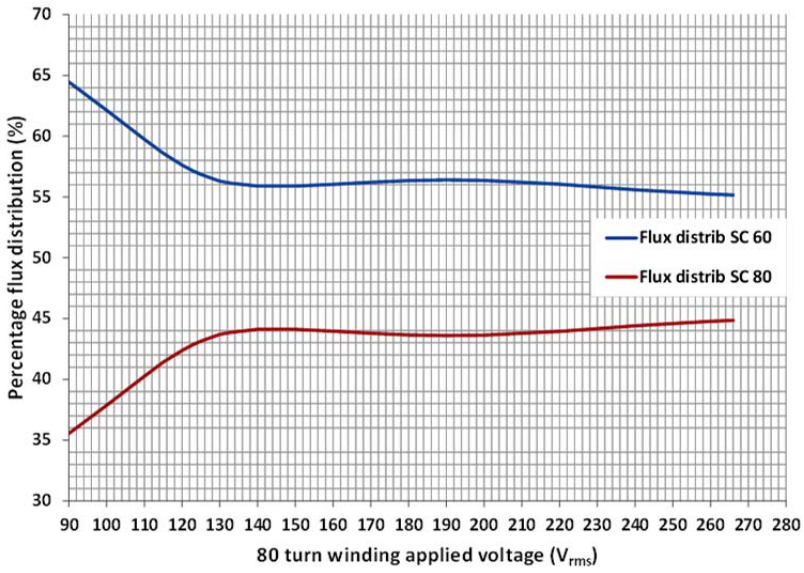

Figure 7.1. The averaged flux distribution is shown for all T-joint assemblies of all three test transformers.

7.1.2 Individual core component responses

The flux mapping exercise that includes the search coil outputs shown in Figures 7.3, 7.4 and 7.5 are conducted at the same time for better comparison of results especially when relating the flux response alone a path with connected core components. Slight differences in dc bias are evident only at the highest dc bias levels used due to battery charge depletion.

Search coils 11 to 16:

In Figure 7.2 the outputs of the search coils 11 to 16 are plotted as a function of their distance from the winding mid-point moving towards the winding end. SC 11 is at the winding mid-point. For a search coil to register a voltage output implies flux linking with the simulated tie bar that is insulated from and resting on the WL. At 0 A dc almost no output registers on the search coils. The overall trend is for the search coil outputs to decrease with increasing distance from the winding mid-point. As the dc bias increases the search trend lines become more elevated indicating an increase in the outputs of all search coils. This is a clear indication that the leakage flux from the windings is increasing.

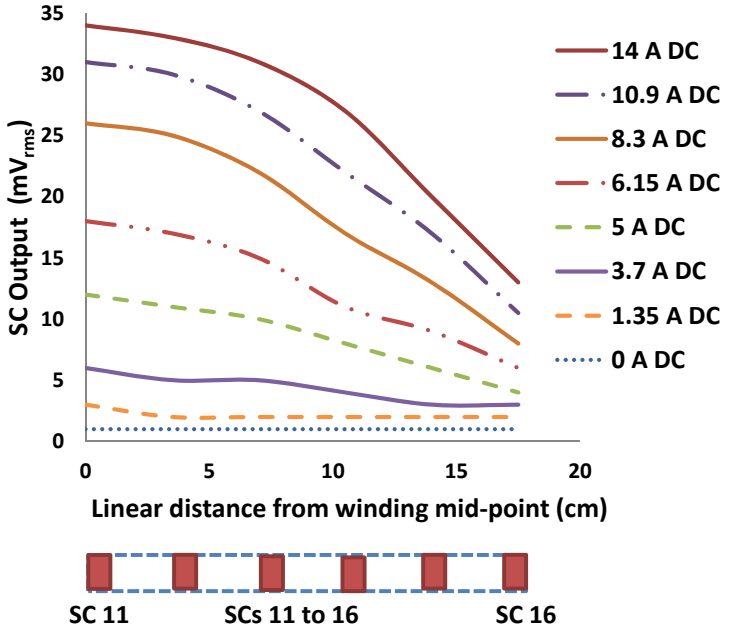

Figure 7.2. Voltage outputs for SCs 11 to 16 as a function of liner distance from the winding mid-point with increasing dc bias. SCs 11 to 16 are wrapped around a simulated tie bar resting on the WL inside the winding assembly [Borrill *et al.* 2016].

Search coils 17 to 30:

In Figure 7.3 the outputs of the search coils 17 to 30 are plotted as a function of their distance from T-joint moving towards the IY mid-point with increasing dc. In section 4.2 it is shown that the IY joints are saturating and this is confirmed by the decline in the outputs of search coils 17 and 18 at all dc bias test levels. This is due to the ac flux bypassing the saturated IY joints.

As the dc injection level is increased and the IY receives more dc flux and the ac flux leaves the IY which is indicated by the SC outputs dropping consistently with increasing dc.

As the IY mid-point is approached the SC outputs have their highest output indicating that more ac flux at this location in the IY than elsewhere. This trend however changes at higher levels of dc, i.e. 14.5 A and 16A, as the SC outputs start to decline as the mid-point is approached.

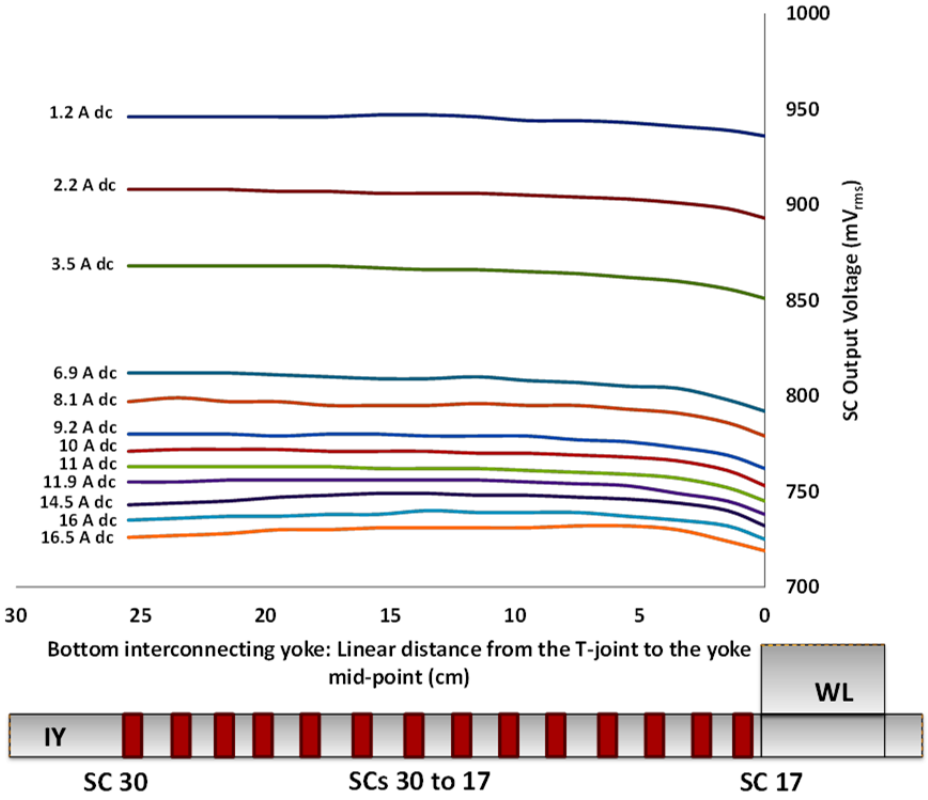

Figure 7.3. Graphs of search coil outputs 17 to 30 as a function of linear distance from the IY joint to the mid-point of the interconnecting yoke with increasing dc bias.

Search coils 31 to 39:

In Figure 7.4 the short section of yoke forming part of the RL path is shown with search coils 31 to 39 fitted to the core component. The outputs of the search coils are plotted as a function of their distance from the WL moving in the direction of the RL-1 joint for increasing dc bias level. As dc bias is increased the ac flux starts to exit the yoke section which is seen by the lower output of search coil 31 but shortly thereafter the ac flux re-enters the core as the output from search coil 32 is larger. This is indicative of the saturated WL- and RL-2 joints being bypassed by the ac flux straying into the air.

The search coil outputs for SCs 33 to 39 show a steady decline. The slope of the decline is a function of increasing dc bias level. The lowest search coil outputs are seen at SC 39 where the output for increasing dc bias is seen to converge indicating that the RL-1 joint is saturated. The ac flux has strayed outside the core component and is bypassing the RL-1 joint.

The response of this section of the core to the dc is not always consistent. Between 1.2 and 9.2 A dc the SC trends are downward as the RL-1 joint is approached. The SC outputs then

start to increase from 10 to 15 A dc, where after the trend is to decrease again as can be seen by the SC trend for 16 A dc lying below that of the 15 A dc trend line.

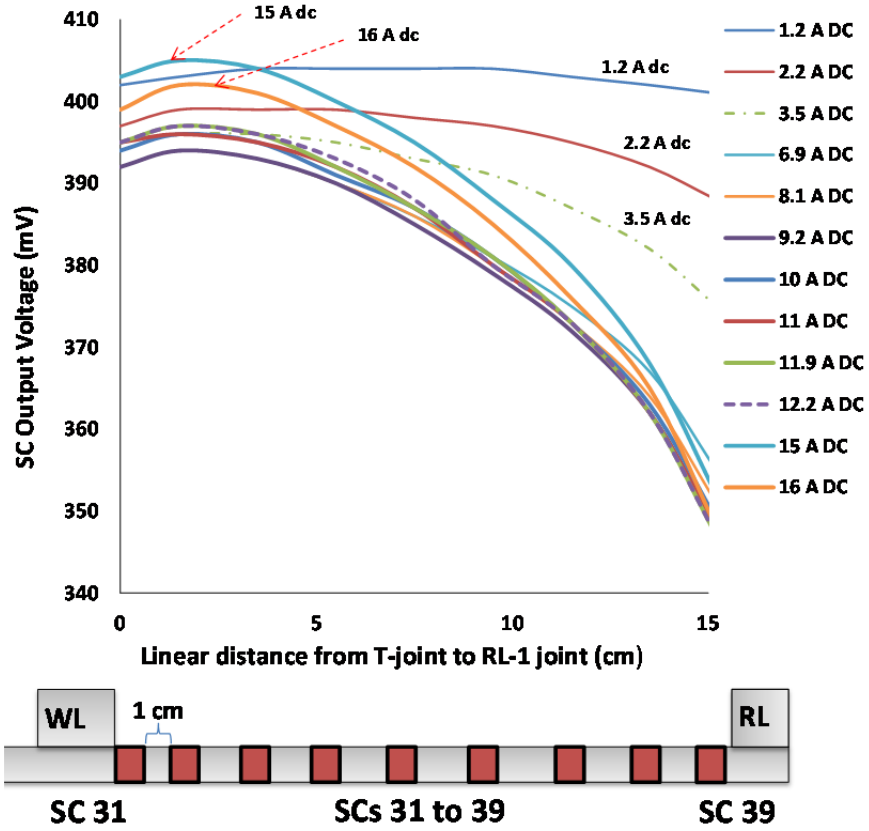

Figure 7.4. Graphs of search coil outputs as a function of linear distance from the RL-2 joint (left) to the RL-1 joint (right) with increasing dc levels. Decline in search coil output and convergence of the SC outputs at RL-1 joint indicates that the joint is saturating.

Search coils 40 to 50:

In Figure 7.5 as the dc bias is increased the output of SC 40 falls as the RL-3 joint saturates as indicated by the convergence of the search coil outputs at approximately 362 mV.

The search coil outputs start to increase as the distance from the RL-3 joint increases. This is due to the stray ac flux bypassing the RL-3 joint and re-entering along the return limb. As the return limb mid-point is approached the outputs continue to rise due to the increasing leakage flux from the winding on the neighbouring wound limb. The contribution of the leakage flux from the transformer windings is seen in Figure 7.2.

The complex response of the core components seen in Figures 7.4 and 7.5 are not only due to changes in dc bias but to some degree also the flux distribution trends seen in Figure 7.1.

The magnitude of the search coil outputs at the convergence points seen in Figures 7.4 and 7.5 need further explanation. At nominal ac excitation and for the same dc bias levels the search coil outputs for 39 and 40 have the following ranges:

SC 30 - 400 to 348 mV (from lowest to the highest dc bias level) and

SC 40 – 403 to 363 mV (from lowest to the highest dc bias level).

The SC 40 has a slightly higher output voltage than SC 39 indicating that there is a slightly larger effective core cross-sectional area available at the RL-3 joint. Furthermore, it is speculated that the stray flux flows as illustrated in Figure 7.6. Flux bypassing the RL-1 joint is shown re-entering the core just before the RL-3 joint. The reason for a higher output at SC 40 could be as a result of uneven stacking of the core joints at this location whereby RL-3 has a slightly larger effective core joint area than RL-1.

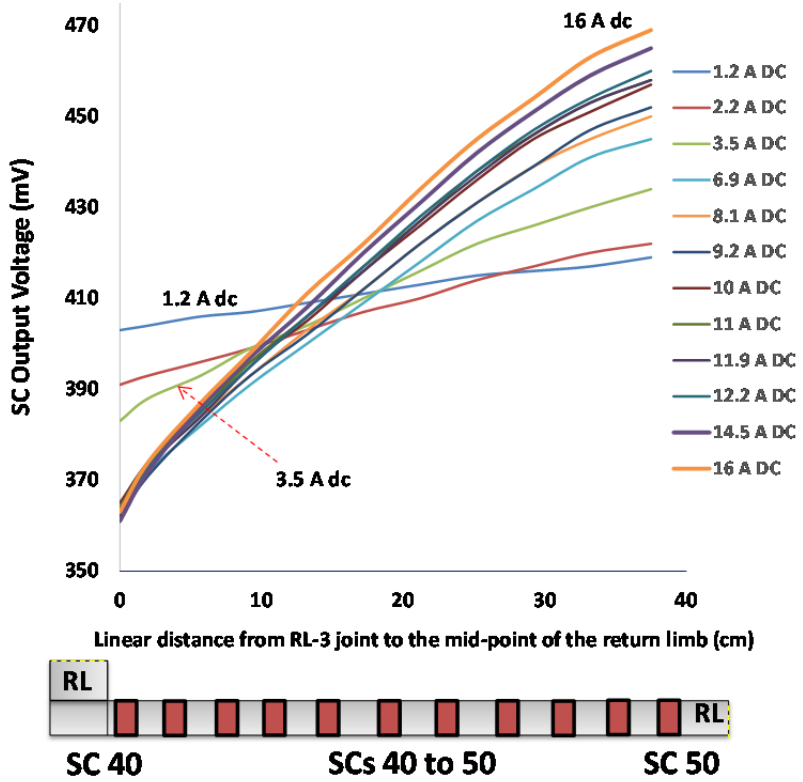

Figure 7.5. Graphs of search coil outputs as a function of linear distance from the RL-3 joint to the mid-point of the return limb with increasing dc levels. Convergence of the SC outputs at RL-3 joint indicates that the joint is saturating and is being affected by the response of the RL-1 joint.

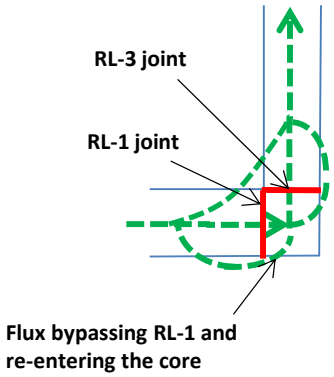

Figure 7.6. Illustration of the possible flux response at the RL-1 and RL-3 joints in saturation.

7.2 Distortion in a standalone single phase transformer

In this section deals with the results of testing to answer the research question related to the distortion caused when the core of a SP-4L transformer half-wave saturates.

The harmonic distortion of the primary and secondary currents and primary and secondary voltages of test transformer 1 are presented and analysed. Since the transformer is not at a true no-load condition due to the dc test circuit arrangement and the secondary current is therefore monitored to ensure that no secondary effects are experienced.

7.2.1 Distortion of the primary and secondary currents

In Figure 7.7(a) the harmonic orders present in the primary current are represented as a function of increasing dc bias increments of 1 A from 0 A up to 9 A. Other than the fundamental, the second harmonic is the largest harmonic, with the overall trend for all harmonics to increase initially with increasing dc. From the 6th harmonic onwards the magnitudes are negligible.

The 5th and 6th harmonics show a decline in magnitude at higher dc levels while the 7th and 8th harmonics show a slight increase.

In Figure 7.7(b) the harmonic orders as a percentage of the fundamental primary current are presented. At 0 A dc bias there are percentage of fundamental harmonic orders seen for the 2nd, 3rd and 5th that is attributable to the distortion in the supply voltage. It is noticeable when comparing the trends seen in Figures 7.7(a) and (b) that they differ for 1 A dc bias. In Figure 7.7(b) the 3rd harmonic has increased disproportionately with larger than expected percentage increases of the 4th, 5th and 8th harmonics.

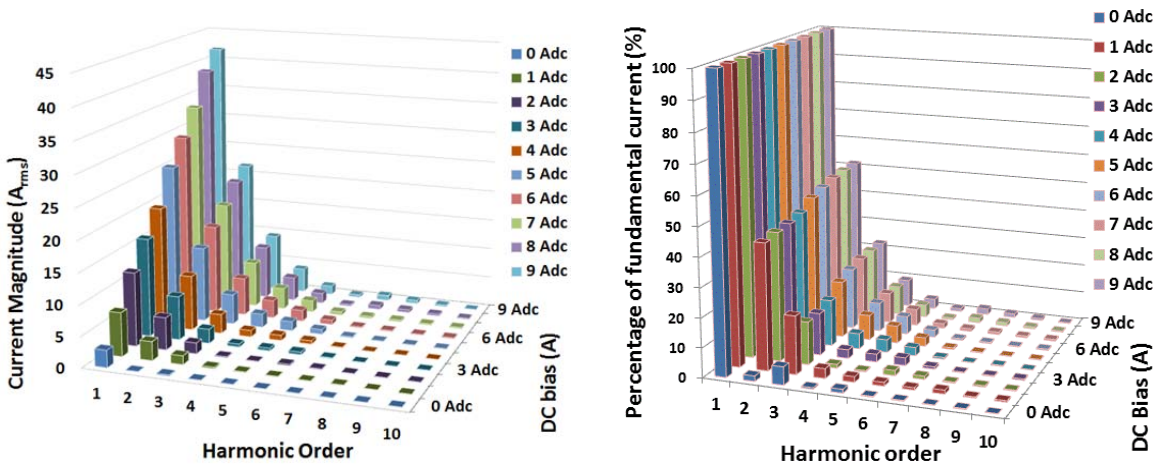

(a) (b)

Figure 7.7. Current distortion with increasing dc and nominal ac voltage applied to the 80 turn winding, where (a) is a column graph of the first ten primary current harmonic components and (b) is a column graph of the first ten current harmonic components as a percentage of the fundamental primary current.

In Figure 7.8 it is evident that the axis of rotation of the half-wave saturated primary current changes as the dc bias level changes. The axis of rotation is the average value of the current in the windings over a 360^0 period and is equal to the value of the dc bias current [Harder 1930]. The high peak magnetising current pulse seen in the positive half-cycle of

Figure 7.8 is due to the dc bias polarity that drives the transformer into half-wave saturation. Walling & Khan [1991], Molinski [2002] and Girgis & Vedante [2012] report a similar finding. The phase shift seen in successive waveforms as the dc bias is increased is caused by the change in the L/R ratio in the secondary circuit since the resistance is decreased to increase the dc bias.

Section A in Figure 7.9 reflects the saturation of the core joints. The THD increases sharply with increasing dc up to approximately 1 A dc. The harmonic activity seen in Figure 7.7(b) for a 1 A dc bias can therefore be attributed to the saturation of the core joints.

Through B the THD declines as the joints are now in “air core” operation. Section C represents the bulk core material moving into deeper saturation, with the THD increasing once more. Through D the THD declines as the test transformer as a whole is now in “air core” operation. These results agree with the modelling and experimental results reported by Masoum & Moses [2008] and Chisepo [2014], which observed that the voltage and current harmonics stopped increasing but rather gradually decreased with excessively increasing dc. However, this THD graph differs from their work with the test transformer having two distinct parts saturating: first the joints and then the bulk core material.

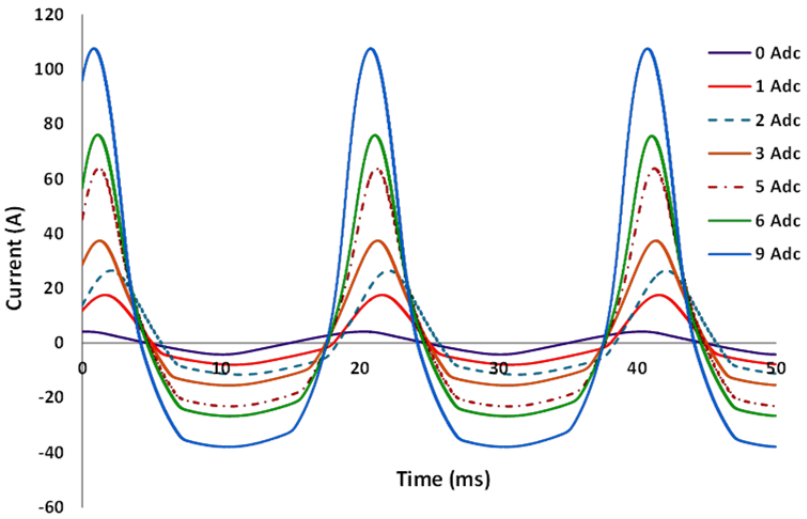

Figure 7.8. Primary current wave shape distortion with increasing dc bias at nominal ac voltage applied to the 80 turn windings.

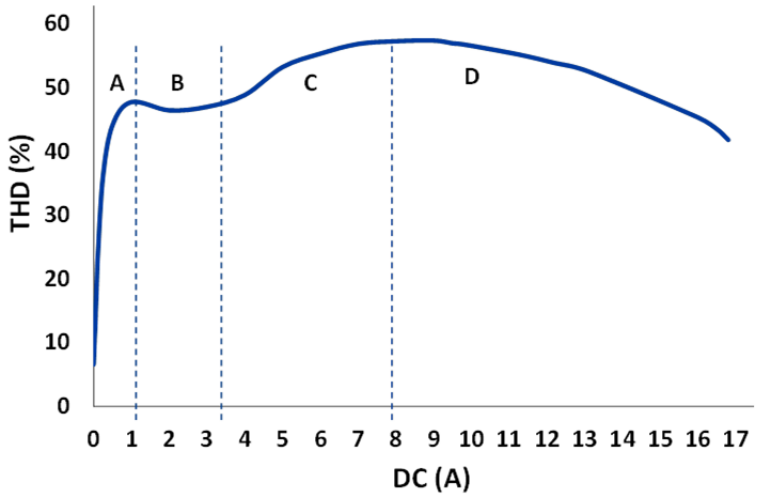

Figure 7.9. Graph of the primary current percentage THD versus dc ampere-turns for test transformer T1 [Borrill *et al.* 2016].

Figure 7.10 demonstrates that although the THD of the current in the ac test circuit (I_{THD1}) of the transformer displays the symptoms of a saturated core the same cannot be said for the THD of current in the dc test circuit (I_{THD2}). The THD of the secondary ac current is very low compared to the primary current and does not display the typical trend associated with a saturated transformer. This proves that the single phase inductor is not saturating and will not mask the symptoms of the test transformer.

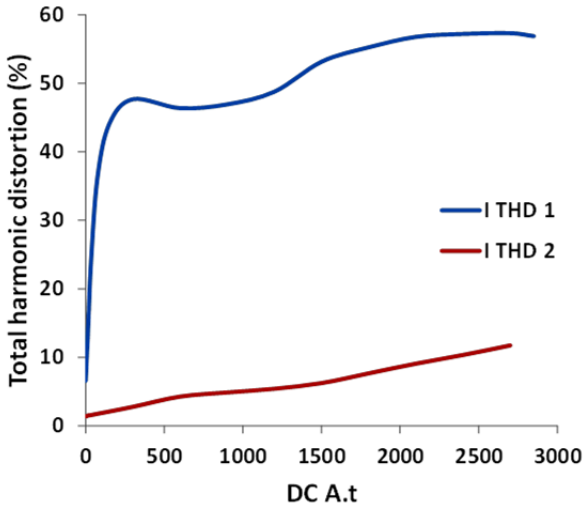

Figure 7.10. Graphs showing the comparison of the primary and secondary currents of the transformer as a percentage THD versus dc ampere-turns.

7.2.2 Distortion of the primary and secondary voltages

In Figure 7.11(a) the primary voltage harmonics are plotted with increasing dc bias. The fundamental is large but the higher order harmonic components are small in magnitude indicating only slight distortion of the primary voltage.

In figure 7.11(b) the primary voltage waveform is plotted versus time. At high dc ampere-turns bias the second current harmonic in Figure 7.7(a) is approximately 50 % of the

fundamental and this causes the asymmetrical distortion seen near the zero crossing points of the voltage wave.

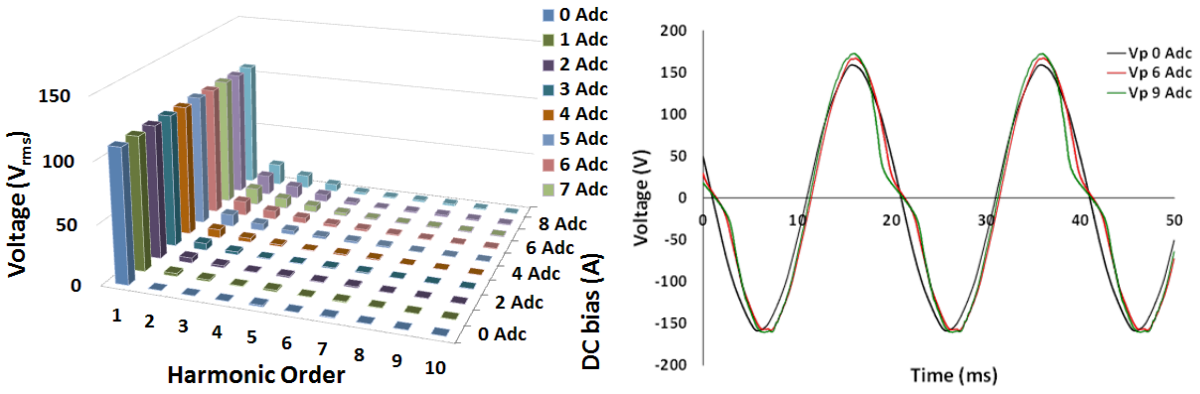

(a) (b)

Figure 7.11. Primary voltage distortion with increasing dc bias with nominal ac voltage applied to the 80 turn windings, where (a) is a column graph of the first ten voltage harmonic components and (b) is voltage waveforms showing progressively worse distortion with increasing levels of dc bias.

Figure 7.12 demonstrates that the primary and secondary voltages suffer distortion that can be explained as the result of voltage-drops in the transformer equivalent circuit series elements caused by the large 2nd harmonic order in the badly distorted primary current in half-wave saturation. Both voltages display a similar trend with increasing dc ampere-turns but with some divergence of their THD trending plots. The secondary voltage (U_{THD2}) will experience more distortion since it is affected by both the primary and secondary currents flowing in the transformer equivalent circuit series elements.

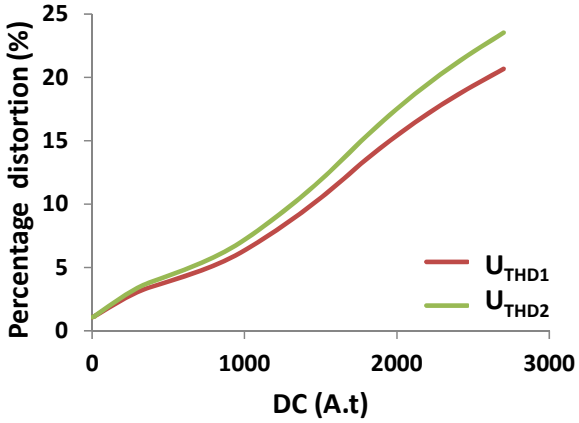

Figure 7.12. Graphs showing trends of the percentage THD versus dc ampere-turns for the primary (U_{THD1}) and secondary (U_{THD2}) voltages measured at the transformer terminals.

7.3 Utilization factor of the butt type joints

This section provides the results of the testing to validate the method proposed in chapter 5 that seeks to determine an utilisation factor for butt type joints.

7.3.1 Testing to determine the utilization factor of the butt type joints

Test 1: In Figure 7.13 the SC outputs for SCs 5, 7, 60 (IY-joint), 70 (WL-joint), 80 (RL-2 joint) and 100 (RL-1 joint) as indicated in Figure 6.8 are shown plotted for T1 and T2. The search coils of primary interest are 60 (IY-joint), 70 (WL-joint) and 100 (RL-1 joint).

The response of T3 is similar to that of T2. The graphical trends of the outputs of SCs 100 and 110 located as shown in Figure 6.8 overlapped and for this reason the SC 110 readings are excluded from the graphs of Figures 7.13(a) and (b).

The installation of SC 7 at the mid-point of winding assembly B of T1 disturbed the core stacking of the WL, IY and RL at the T-joint assembly 'a'. This is seen by the outputs of SCs 70A, 80A and 100A of T1 in Figure 7.11(a) that show signs of earlier joint saturation than the search coils at locations 70, 80 and 100 elsewhere in the core.

The SC 7 output in Figure 7.13(a) provides the highest output of all the SCs since it is at the winding mid-point where the highest flux component exists in the core.

Examining Figures 7.13(a) and (b) shows the search coils outputs at the similar joint locations give consistently the same output. Their outputs only start to deviate from each other at higher ac voltages well above the nominal voltage of the transformers as the respective cores move deeper into saturation. The only exception are the search coil outputs of 70A, 80A and 100A of T1 that deviate from the outputs of similarly located search coils at much lower ac applied voltages.

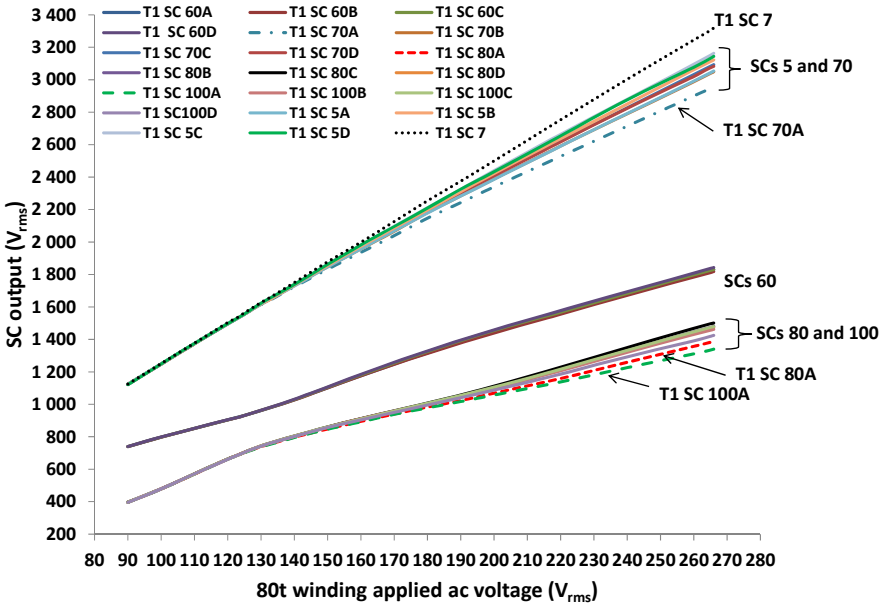

Figure 7.13(a). Search coil outputs at core search coil locations as indicated in Figure 6.6 for increasing ac excitation on the 80 turn windings of test transformer T1. SC7 output is only available for transformer T1.

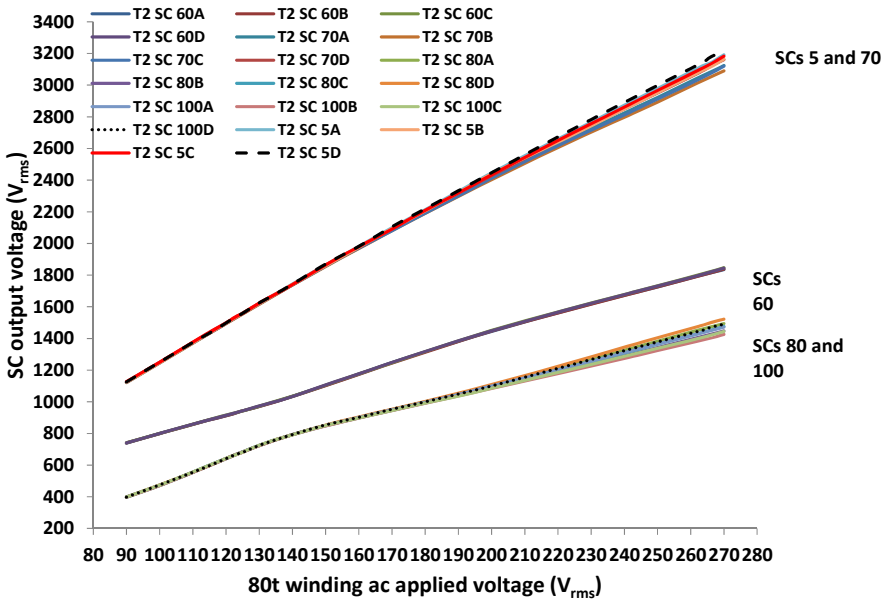

Figure 7.13(b). Search coil outputs at core search coil locations as indicated in Figure 6.6 for increasing ac excitation on the 80 turn windings of test transformer T2.

Test 2: In Figure 7.14 the output of the twenty turn air search coils A1, A2, A3 and A4 are plotted versus increasing ac applied voltage at the terminals of the 80 turn windings for all three transformers.

In Figure 7.14 the important data point is the critical ac voltage at which each joint goes into saturation. It is seen that that the graphs of the outputs of the twelve air search coils converge near the vertical axis which corresponds with the respective joint critical voltages, V_C. There is a very slight difference in output voltages measured at this critical voltage point which is of the order of one to two millivolt.
The initial SC output of each search coil is of the order of 10mV and then increases exponentially. The initial SC output measured is determined to be as a result of fringing and when an additional jump in output of the order of 3 to 4 mV is registered the corresponding ac energisation voltage is deemed to be the critical ac voltage data point for the joint. This approach is consistently followed when determining the individual joint critical voltages.

Similarly, by examining the search coil output voltage plots for air search coils at locations D and E as given in appendix B, the critical voltages can be determined for these core joints as well. The appendix also contains tables with the measured test data of search coil output versus applied ac voltage for locations A, E and D. The degree of convergence is greater for the search coils at location A than for the search coils E and D in appendix B. This is due to the tighter stacking at the IY joint at the search coil location 60.

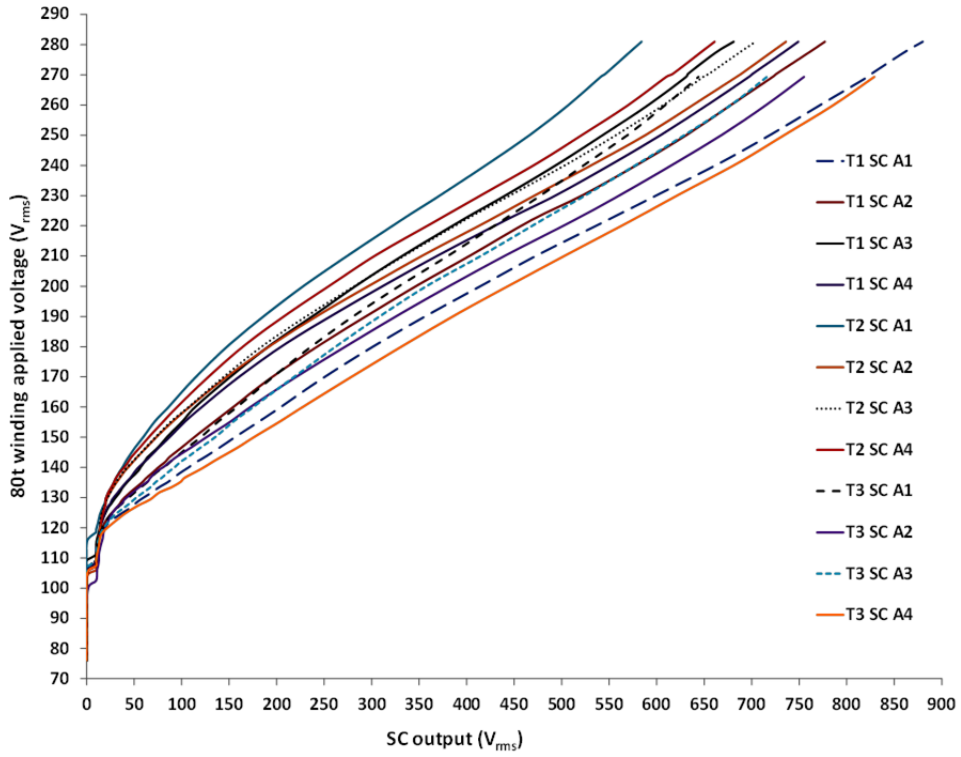

Figure 7.14. Search coil output voltage trends for air search coils at location A versus increasing applied voltage on the 80 turn winding for all three transformers with increasing ac excitation.

In table 7.1 the V_C of the IY-, WL- and RL-1 joint types, the average V_C per joint type per transformer and an average V_C per joint type for all three transformers are tabulated. The average V_C for the IY joints (location A) which are the first to saturate are very close to the saturation inception voltage of the individual transformers as given in Table 4.3. This correlation between two different methods of measurement confirms the suitability of the second method for calculating the average V_C per joint type.

Table 7.1. Joint critical voltages for air search coils in Figure 6.6 at locations A, E and D.

Transformer	Joint critical voltage, V_c (V_{rms})					
	A1	**A2**	**A3**	**A4**	**Average per transformer**	**Average of all transformers (V_{rms})**
T1	118.56	121.67	124.4	124.4	122.3	124.2
T2	126.8	126.8	131.9	131.9	129.4	
T3	121.8	121.8	121.8	118.4	121	
	E1	**E2**	**E3**	**E4**		
T1	121.67	124.4	124.4	131.8	125.6	126.1
T2	124.6	131.9	131.9	133.4	130.5	
T3	124.7	124.7	118.4	121.8	122.4	
	D1	**D2**	**D3**	**D4**		
T1	124.4	133.37	138.73	133.37	132.5	133.5
T2	138.52	138.52	141.37	146.43	141.2	
T3	126.5	128.2	126.5	126.5	126.9	

Note: The air search coils utilised at locations A, E and D are hand wound using a hard board former. Every attempt to conform to the general dimensions is made but still no two coils are exactly the same. This coupled with the human factor of correctly judging the placement of the search coils at each location accounts for the wide spread of the output voltages above the joint critical voltage. Examining Figure 7.13, however, shows that the air search coils provide consistent output results for determining the V_C per joint.

7.3.2 Determining the effective core area, A_{eff} and the utilisation factor, U

In section 7.3.1 the average critical voltage, V_C, of the IY-, WL- and RL-1 joint types is determined. V_C is now used to determine the average corresponding core search coil output for each joint type for all three transformers.

The method for determining the average corresponding core search coil output for each joint type for all three transformers is as follows:

- Using the average V_C for the joint type required find the corresponding ac voltage on the horizontal axis of the relevant figure in Figure 7.14 and extend a line vertically upward to coincide with the respective graphs.
- The search coil output can be read off the vertical axis.
- Determine the average search coil output for each respective joint type for all three transformers.

The average search coil output per joint type at saturation is tabulated in Table 7.2.

Table 7.2. Average search coil output per joint type at saturation.

Joint type	Critical voltage, V_C (V_{rms})	Average SC outputs per transformer (mV_{rms})	Overall average SC output (mV_{rms}
IY (SC 60)	124.2	940, 920 and 910	923.3
WL (SC 70)	126.1	1560, 1560 and 1560	1560
RL-1 (SC 100)	133.7	745, 762 and 785	764

In Figures 7.15(a) and (c) the search coil outputs need to be averaged due to the spread between the graphs of the test transformers. This is due to uneven stacking at these joint locations for all three transformers.

The core performance along the RL path is limited by joint RL-1. As explained in section 5.2 the RL-2 joint is excluded from the effective core area study since it will outperform joint RL-1 and is not considered to limit the core performance in early saturation where the joint phenomenon presents itself.

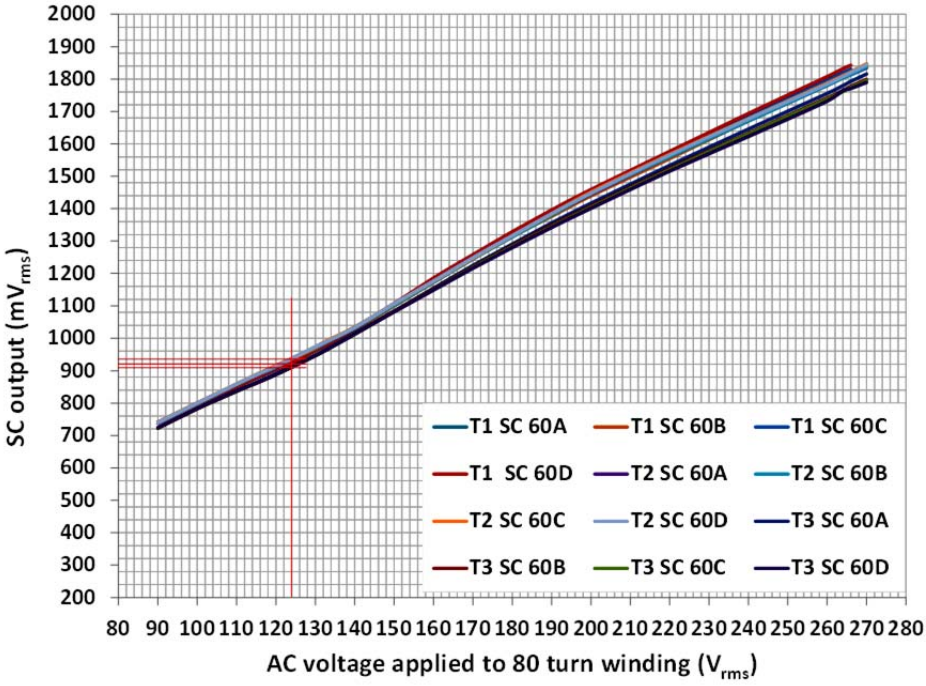

Figure 7.15(a). Graphs of core search coil outputs with increasing ac excitation for search coils at joint locations 60 for all three test transformers.

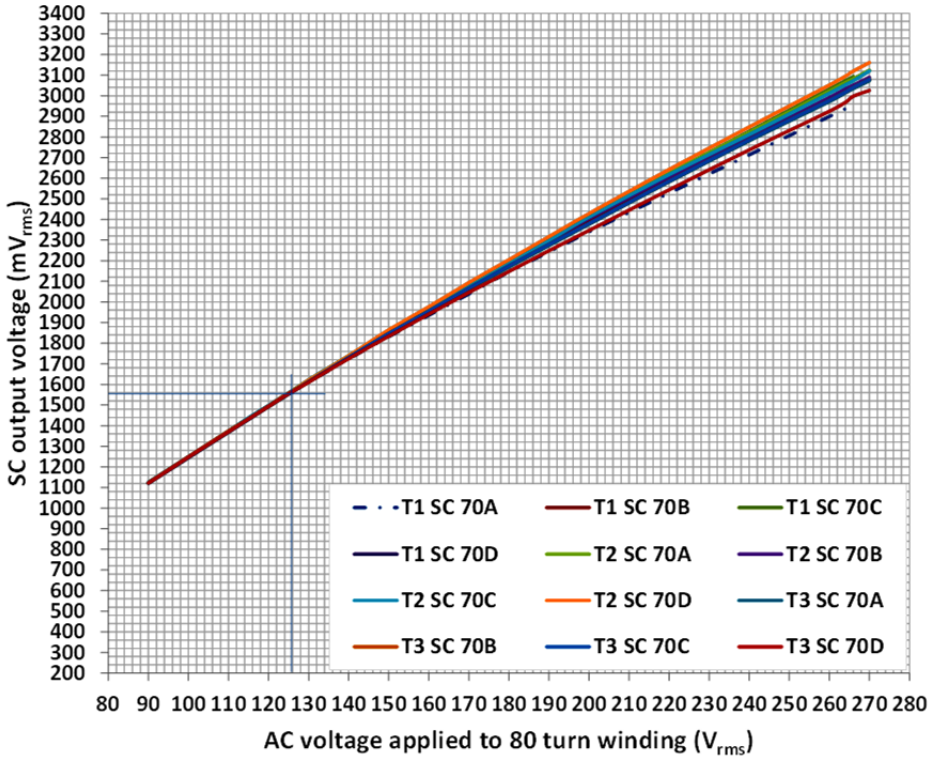

Figure 7.15(b). Graphs of core search coil outputs with increasing ac excitation for search coils at joint locations 70 for all three test transformers.

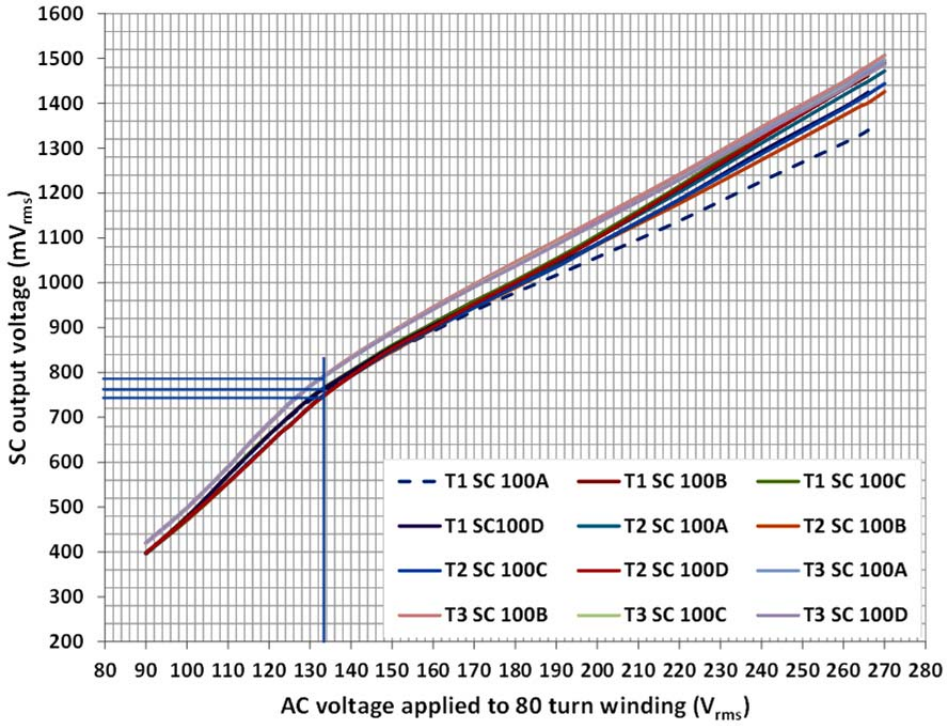

Figure 7.15(c). Graphs of core search coil outputs with increasing ac excitation for search coils at joint locations 100 for all three test transformers.

Using Equations 5.3, 5.4 and 5.6 the values of θ_{pk}, A_{eff} and U for each joint type is determined and these are tabulated in Table 7.3.

In reviewing the U values in Table 7.3 the quality of the stacking is evident. The IY joints have a U value not only in excess of the other joints but also exceeding 1 p.u. Ideally, when a core is manufactured and constructed to a high quality all joints should have a U of 1 p.u. Properly stacked multi-step lap mitred joints will always have U values in excess of 1 p.u.

Table 7.3. θ_{pk}, A_{eff} and U for the WL, IY and RL-1 joints.

Joint type	θ_{pk} (mWb)	A_{eff}		U
		A_{eff} (mm^2)	A_{eff} (p.u.)	
IY (SC 60)	4.2	2048.77 mm^2	0.281 p.u.	1.12
WL (SC 70)	7	3461.6 mm^2	0.475 p.u.	0.95
RL-1 (SC 100)	3.4	1695.3 mm^2	0.233 p.u.	0.93

7.4 Discussion

In this chapter both the ac and dc test circuits introduced in chapter 6 are used for the single phase testing and perform adequately for the tests applications required.

The flux distribution at the T-joint assemblies of the test transformer cores are successfully determined using ac energisation with only differences of a few percent in the average flux distributions between the three test transformers. The individual core components are successfully flux mapped with simultaneous ac and dc excitation.

The badly distorted primary current waveform clearly shows that half-wave saturation is occurring in the test transformer T1 with simultaneous ac and dc present in the windings. The secondary current percentage THD is very low compared to the primary current proving that the single phase current limiting inductor in the secondary is not saturating and will not mask the symptoms of the test transformer.

The percentage THD of both the primary and secondary voltages shows that their waveforms are distorted.

The output of core search coils at similar locations around a test transformer core give approximately the same output magnitude with some deviation occurring only in deep saturation. Data recorded from the air search coils and core search coils allows the method of determining the utilization factor of butt joints at specific core locations to be assessed. The unevenness of the core stacking results in utilization factors that are either above or below 1 p.u. The extent of deviation of the utilisation factor from 1 p.u. is relatable to the core joint location in the core.

7.5 Onward

In the next chapter the results of the tests conducted to determine the parameters for populating a topologically correct duality derived pi equivalent circuit are presented and discussed. The complete pi equivalent circuit is presented for use in EMTP simulation studies of slow transient phenomena effects on the single phase four limb test transformers.

Chapter 8

Pi equivalent circuit parameters

In this chapter the results of the tests described in section 6.3 are presented and processed to determine the pi equivalent circuit parameter values. The completed duality derived pi equivalent circuit of Figure 3.3(c) is presented and is ready for EMTP GIC simulations.
The pi equivalent circuit and parameters are determined such that the model is reversible and includes the saturation characteristics determined from both the 80 turn and 150 turn winding sides of the transformer.

8.1 Transformer electrical equivalent parameters

In this section the transformer electrical equivalent parameters are determined by measurement and calculation using the test results data.

8.1.1 Magnetising branch parameters

Table 8.1 contains the core loss and magnetising inductance parameters prepared for the pi circuit magnetising branches using the open-circuit measured data. The test is conducted from the150 turn side and then the 80 turn side of each transformer and good consistency is obtained in the core loss and magnetising inductance parameters. The full open-circuit test results are available in appendix D. The values of the magnetising inductance and core loss components are doubled in Table 8.1 in preparation for representation in the pi equivalent circuit.

Table 8.1. No load losses and excitation current test (open-circuit test) results for transformers T1, T2 and T3 when energizing from the 150 turn side of the transformers.

	Open circuit test results when energizing from the 150 turn side of the transformer		
Transformer	**$2R_c$ (Ω)**	**L_m (H)**	**$2L_m$ (H)**
T1	1400.478	2.289	4.579
T2	1433.416	2.277	4.554
T3	1357.068	2.112	4.224
	Open circuit test results when energizing from the 80 turn side of the transformer		
Transformer	**$2R_c$ (Ω)**	**L_m (H)**	**$2L_m$ (H)**
T1	396.538	0.640	1.281
T2	406.406	0.689	1.377
T3	383.274	0.580	1.16

8.1.2 Winding parameters

Table 8.2 contains the leakage inductance and the combined series ac winding resistance values prepared using the short-circuit measurement data. The transformer short-circuit test is conducted from both the 150 turn and 80 turn sides of each transformer and good consistency is obtained for the values of leakage inductance and ac winding resistance for each transformer. The short-circuit test results are available in appendix D.

Table 8.2. Load losses and impedance voltage test (short circuit test) results for transformers T1, T2 and T3 when energizing from the 80 and 150 turn side of the transformers respectively.

Short circuit test results when energizing from the 150 turn winding			
Test Transformer	**R_s (Ω)**	**R_s corrected to 20 ^{0}C (Ω)**	**L_s (mH)**
T1@ $T_{ambient}$ = 23.11 ^{0}C.	0.3431	0.099	0.437
T2@ $T_{ambient}$ = 23.3 ^{0}C.	0.3475	0.100	0.443
T3@ $T_{ambient}$ = 23.73 ^{0}C.	0.3397	0.098	0.444
Short circuit test results when energizing from the 80 turn winding			
Test Transformer	**R_s (Ω)**	**R_s corrected to 20 ^{0}C (Ω)**	**L_s (mH)**
T1@ $T_{ambient}$ = 22,83 ^{0}C.	0.0932	0.0663	0.124
T2@ $T_{ambient}$ = 23.39 ^{0}C.	0.0933	0.0665	0.127
T3@ $T_{ambient}$ = 23.76 ^{0}C.	0.0928	0.0660	0.128

The measured leakage inductance, L_s, is compared with the theoretical determined value of L_s using the theoretical equations developed by Del Vecchio [2008]. In Table 8.3 the calculated and measured leakage inductances determined from the150 turn side of the test transformers are compared. The detailed theoretical calculation is documented in appendix C:2. The calculated value for L_s is consistently lower than the measured value within a range of 16.7 to 18%. The percentage difference between the calculated and measured leakage inductance is partly due to assumptions made in the theoretical equations of Del Vecchio [2008] for two windings of different height and also the difference between the as-built test transformers versus ideal considerations in theoretical calculation.

Table 8.3. Leakage inductance, L_s, determined when energising the test transformers from the 150 turn side. Measured, calculated and percentage difference values are given.

Test transformer	L_S (mH) measured	L_S (mH) calculated	% diff.
T1	0.4372	0.364	16.7
T2	0.4433	0.364	17.9
T3	0.4440	0.364	18

8.1.2.1 Dc winding resistances

The dc winding resistances are determined as part of the acceptance tests in section 4.2.1 and are used to apportion the combined series resistance, R_S, between the 80 turn and 150 turn windings in section 8.2.1.

In Table 8.4 the temperature corrected (20 ^{0}C) measured dc winding resistances of the 80 and 150 turn parallel winding assemblies of transformers T1, T2 and T3 are tabulated.

Table 8.4. The dc winding resistances of the 80 and 150 turn parallel winding assemblies of transformers T1, T2 and T3 corrected to 20 ^{0}C.

Test transformer	$R_{dc_{150t}}$ Parallel connected windings@ 20 ^{0}C (Ω)	$R_{dc_{80t}}$ Parallel connected windings@ 20 ^{0}C (Ω)
T1	0.0716	0.0501
T2	0.0715	0.0504
T3	0.0715	0.0501

8.1.3 Terminal saturation inductance

In this section the results of the terminal saturation inductance measurements of section 6.3.3 is presented for each of the three test transformers. The values of L_{air} for the inner and outer windings of each transformer are required to determine the slope of the deep saturation characteristics for energizing from either of the inner (150 turns) and outer (80 turns) windings respective, i.e. L_{sat-1} and L_{sat-2}.

8.1.3.1 Terminal saturation inductance measurements

Using the test circuit of Figure 6.5 terminal saturation inductance measurements of input current and output voltage are put through an FFT at each dc bias test value using the Yokogawa power analyser. Testing is conducted for both transformer windings respectively. The objective is to use a small ripple in deep saturation to determine L_{air}. This requires that the ripple does not make an excursion down the B-H hysteresis curve taking the transformer into and out of saturation but rather keeps it in saturation with enough ripple to allow L_{air} to be determined.

In Figure 8.1 the waveforms of the transformer primary and secondary voltage and the input ripple current to the transformer primary winding are shown for a terminal saturation inductance test energising from the 150 turn winding side. The test transformer primary and secondary windings are wound with subtractive polarity in accordance with IEEE Std C57.12.91 2011. This explains why the output voltage is inverted relative to the input voltage, i.e. 180^0 phase shift.

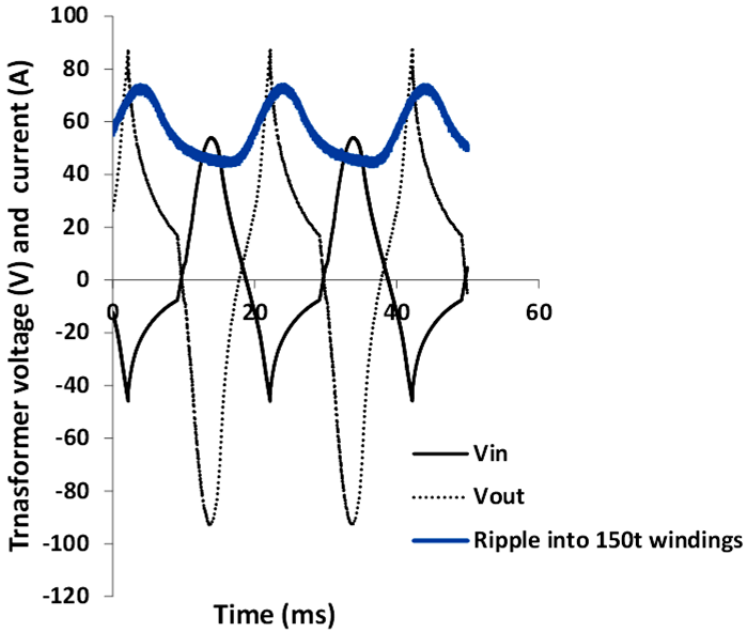

Figure 8.1. Waveforms of the transformer primary and secondary voltage and the input ripple current to the transformer primary winding for a terminal saturation inductance test energising from the 150 turn winding side [Borrill *et al.* 2017].

The inner windings (150 turns) are initially energized with 60 V_{rms} and additional dc introduced to the windings from the battery bank in order to drive the test transformer into deep saturation. The same procedure is repeated for the outer winding but this time by energizing it with 70 V_{rms} since the 80 turn outer windings require a higher dc bias than the 150 turn windings. A higher ac supply voltage to the non-ideal single phase rectifier assists the batteries in reaching the high dc values required to drive the transformer into saturation.

Examining the recorded FFT data for all three test transformers showed that the second harmonic is the dominant harmonic. This correlates with the PSCAD simulation in appendix D. The second harmonic quantities of the input current and output voltage are then substituted into Equation (6.8) to determine the terminal saturation inductance for each new dc injection level. Terminal saturation inductance (L_{air}) is reached for deep saturation when the value calculated becomes constant despite further increases in dc bias. In Figure 8.2 L_{air} can be seen to reach a constant value for both the 80 and 150 turn windings.

The terminal saturation inductances, L_{air}, for each transformer are tabulated in Table 8.5. These results show a high level of consistency in the inductance magnitudes for the inner and outer windings respectively.

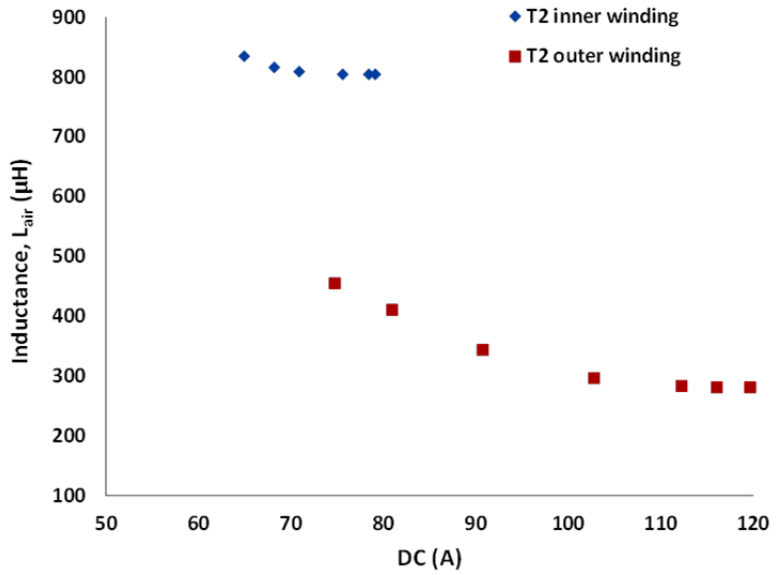

Figure 8.2. Graph of the deep saturation inductance determined for test transformer T2 with varying dc bias for energisation from the outer (80 turn) and inner (150 turn) windings respectively.

Table 8.5. L_{air} values determined from measurement at the transformer terminals for all three test transformers by energisation from the inner and outer windings respectively.

Test transformer	Inner winding, L_{air} (µH)	Outer winding, L_{air} (µH)
T1	798	275
T2	805	281
T3	800	285

To ensure rigor is applied in determining L_{air} an additional terminal saturation inductance test is performed on test transformer T2 with a dc bias of 110.99 A while energising from the 150 turn side. The fundamental, 2nd, 4th and the 5th harmonic orders of the input current and output voltage are computed for L_{air}. De León *et al.* [2014] mention that higher accuracies are obtained using the fundamental and the dominant frequencies.

In Figures 8.3(a) and (b) the current and voltage harmonic orders are shown up to the 10th harmonic. The harmonic orders above the 2nd re seen to be negligibly small especially those of the current harmonic orders. Therefore, only the L_{air} values for the harmonic orders up to the 5th are tabulated in Table 8.6. Good correlation is obtained with the fundamental, 2nd and 5th harmonic orders while a difference of 4.8% exists between the 2nd and 4th harmonic orders. The 3rd harmonic order is excluded since it is affected by the third harmonic in the ac power supply. The second harmonic current and voltage are dominant and as recommended by De León *et al.* [2014] this dominant harmonic order is preferred for the L_{air} calculations. The L_{air} for the 2nd harmonic input current and output voltage is approximately 805 µH which correlates with the corresponding value in Table 8.5 for T2. This demonstrates that the earlier tests conducted on T2 energising the 150 turn windings and at a lower dc bias provides a reasonable indication of the L_{air} value.

Table 8.6. L_{air} for dc bias of 110.99 A dc determined for test transformer T2 energising from the 150 turn winding side.

Dc bias	Harmonic order			
	1st	2nd	4th	5th
110.992 A	815.38 µH	805.31 µH	843.02 µH	818.2 µH

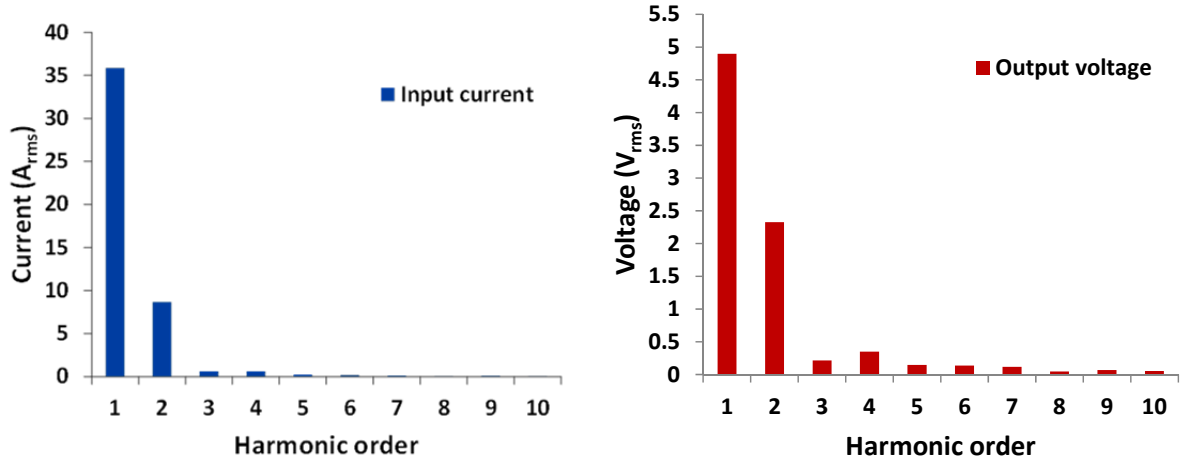

(a) (b)

Figure 8.3. Column graphs of the harmonic orders of (a) the input current and (b) the output voltage of a terminal saturation inductance test on test transformer T2 using a dc bias of 183 A.

Examining Figure 8.2 shows that terminal saturation inductance tests energizing from the 80 turn windings on T2 uses dc bias levels higher than 110.992 A dc. It is observed for tests conducted from the 80 turn side of the test transformers that the test circuit components such as the resistors and batteries are stressed to the absolute limit of their capability. These components show signs of degradation and test circuit component failure could be imminent. It is therefore decided not to stress the components further by retesting T1 and T3 at high dc bias levels. Furthermore, the dc bias level required to replicate a similar MMF in the 80 turn winding is not feasible since the circuit components will not be capable of the much higher currents required for the test.

Terminal saturation inductance test circuits for real power transformers should not suffer the same limitations as with the test transformers T1, T2 and T3 since they have many more turns per winding and a lower dc is required for a large MMF. Furthermore, a FEM study can be conducted prior to testing a real power transformer to determine the theoretical L_{air} value that will give an indication of the amount of dc required for the test.

8.2 Reversible model parameters

In this section the transformer equivalent electrical parameters are processed for inclusion in the equivalent pi model. The complete reversible pi model is presented with its parameters and saturation characteristics determined for energisation from either winding.

8.2.1 Ac winding resistances, R_{80t} and R_{150t}

The combined ac series winding resistances measured in the short-circuit test represents the windings in the parallel connection for both voltage sides of each transformer, i.e. R_{s80} and R_{s150}. R_{s80} and R_{s150} are used in Equations (6.6) and (6.7); therefore the correct values of R_{150} and R_{80} are represented in Table 8.7 for their respective voltage levels in the model. This provides values of winding ac resistances, R_{150} and R_{80} that are relatable when compared with the dc resistance values.

Table 8.7. Test transformer ac winding resistance values apportioned using the winding dc resistances. Resistance values are temperature corrected to 20 ^{0}C and the table gives ac winding resistances where the R_s values are specific determined from each winding side of the transformer respectively.

Test transformer	$\mathbf{R_{150}}$ parallel connection (Ω)	$\mathbf{R_{80}}$ parallel connection (Ω)
T1	0.099	0.0663
T2	0.100	0.0665
T3	0.098	0.0660

8.2.2 Reversible pi model

In order to derive a reversible model of the test transformers, two ideal transformers are required. The ideal transformers have transformation ratios of 150**:**1 and 80**:**1 respectively. Each ideal transformer steps down to the N = 1 turn side and the parameters need to be converted to the 1 turn side of the pi equivalent circuit by the inverse squared turns ratio. The ac winding resistances are excluded since they are placed in the external circuit of the ideal transformers.

The pi circuit magnetising inductance parameter, $2L_m$, and core loss parameter, $2R_c$, are transformed to the N = 1 turn side of the ideal transformer. The transformed parameters of $2L_m$, $2R_c$ and L_s are given in Table 8.8 using open-circuit and short-circuit data measured from the 150 turn side of the transformer.

In Figure 3.3(c) the leakage inductance is shown as $0.5L_s$ and since the short-circuit test is performed with the transformer windings in parallel the measured value of leakage inductance has the correct parameter value.

Table 8.8. Model parameters are converted to N=1 turns using open-circuit and short-circuit data measured from the 150 turn side of the transformer.

Parameter	T1	T2	T3
$2L_m$	203.511 μH	202.400 μH	187.733 μH
$2R_c$	0.0622 Ω	0.0637 Ω	0.0603 Ω
L_s	19.432 nH	19.704 nH	19.735 nH

The test transformers do not have a tank therefore the saturation characteristic has the inductances L_m and L_{sat} as the slopes of the linear and saturated portions of the saturation characteristic for the grey box model. Based on the theory of Jazebi *et al.* [2013] $L_{air\text{-}in}$ and $L_{air\text{-}out}$ for the inner and outer windings are needed to determine $L_{sat\,1}$ and $L_{sat\,2}$ respectively.

To obtain the slopes of the deep saturation parts of the transformer saturation curve for both the primary and secondary windings the parameters L_{2-sat} and L_{1-sat} are determined using Equations (6.9) and (6.10) respectively. In Table 8.9 the values of L_{sat} for both windings of each of the test transformers are presented.

Table 8.9. L_{sat} values for both windings of each of the test transformers.

Test transformer	L_{sat} for the inner and outer windings		L_{sat} values transformed to N=1	
	Inner $L_{1\text{-}sat}$ (mH)	Outer $L_{2\text{-}sat}$ (mH)	Inner $L_{1\text{-}sat}$ (nH)	Outer $L_{2\text{-}sat}$ (nH)
T1	4.746	0.522	210.913	81.581
T2	4.537	0.535	201.640	83.648
T3	4.170	0.546	185.320	85.301

A large current value is chosen as the corresponding current of λ_{sat}, eg. 200 A, in order to represent deep saturation. The saturation characteristic is then constructed using three points on the characteristic, i.e. the origin, I_m-λ_m and I_{sat}-λ_{sat} and this is then considered to be the piecewise two slope saturation characteristic of the transformer core ranging from normal operation into deep saturation.

When preparing the saturation characteristic for the EMTP software program De León *et al.* [2012] points out that the pi equivalent model has two shunt inductors and the value of the current associated with a flux value should be halved for that same flux value. It is preferred to halve the current than to double the flux since the flux is determined by the source and the current by the circuit and each shunt inductor should draw half the current.

In the equivalent circuit L_m is doubled for the two magnetizing branches and I_{peak} is halved. I_{peak} is used since it is the peak current that drives the transformer into saturation. In Equation (4.3) the peak flux value calculated at nominal induction is λ_m.

$$L_{m1} = L_{m2} = 2L_m = \frac{\lambda_m - 0}{0.5I_m - 0}$$

$$\therefore \lambda_m = 2L_m 0.5 I_{m_{peak}} \qquad (4.3)$$

where $I_{m\text{-}peak}$ is the peak current for nominal induction.

In Table the current-flux values for the linear portion of the saturation characteristic are tabulated for the N=1 turn side of the grey-box model.

Table 8.10. Current – flux values for the normal linear portion of the piecewise two slope saturation characteristic energising from the N=1 turn side of the grey-box model.

Transformer	I_{peak} for N=150 turns (A)	I_{peak} for N=1 turn (A)	$0.5I_{peak}$ for N=1 turn (A)	Inductance referred to N=1, $L_{m1}= L_{m2}$ (μH)	λ_m for N=1 turn (mWb)
T1	0	0	0	203.511	0
	0.616	92.4	46.20		9.402
T2	0	0	0	202.400	0
	0.710	106.5	53.25		10.778
T3	0	0	0	187.733	0
	0.679	101.85	50.93		9.561

In Equation (4.4) the peak flux value calculated for deep saturation is λ_m. I_{sat} is many orders of magnitude larger than I_m and a value of peak current is selected that will ensure the transformer is in deep saturation.

$$L_{sat} = \frac{\lambda_{sat} - \lambda_m}{I_{sat} - 0.5I_{m_{peak}}}$$

$$\therefore \lambda_{sat} = L_{sat}\left(I_{sat} - 0.5I_{m_{peak}}\right) + \lambda_m \qquad (4.4)$$

In order to represent deep saturation an I_{peak} of 400 A is assumed and the $I_{peak} – \lambda_{sat}$ values of the saturated portion of the saturation characteristic are given in Table 8.11 for all three test transformers.

Table 8.11. Current – flux values for the saturated portion of the saturation characteristic.

Transformer	Pi circuit branch	I_{peak} (A)	I_{peak} for N=1 turn (kA)	λ_{sat} (mWb)
T1	Left (inner)	400	60	21.491
	Right (outer)	400	32	12.009
T2	Left (inner)	400	60	23.034
	Right (outer)	400	32	13.45
T3	Left (inner)	400	60	20.671
	Right (outer)	400	32	12.287

8.3 Equivalent pi model

In Figure 8.4 the reversible pi model of test transformer T1 is presented. The saturation characteristic for energisation from either the 150 or 80 turn windings are included underneath the model and positioned with their respective winding side. These look very similar to those presents by Jazebi *et al.* [2016] for a single phase transformer without a metal tank or other metallic structural parts. Similarly, models for the transformers T2 and T3 are presented in appendix D.

As previously mentioned the core of transformer 1 is disturbed while fitting SC 7 at the mid-point of the B winding assembly. The open-circuit and short-circuit parameters for this transformer are therefore re-measured and are as indicated in appendix D.

The saturation characteristics for all three test transformers for both the 150 turn and 80 turn sides are plotted on the same system of axes in Figures 8.5(a) and (b) respectively.

Typically, transformers in a three phase bank are modelled as being identical but it is evident from the testing that the equivalent circuits are not identical. It may well be that the tolerances, i.e. small variations in parameters, are acceptable for power system software simulations but the true effect of these differences should be investigated further.

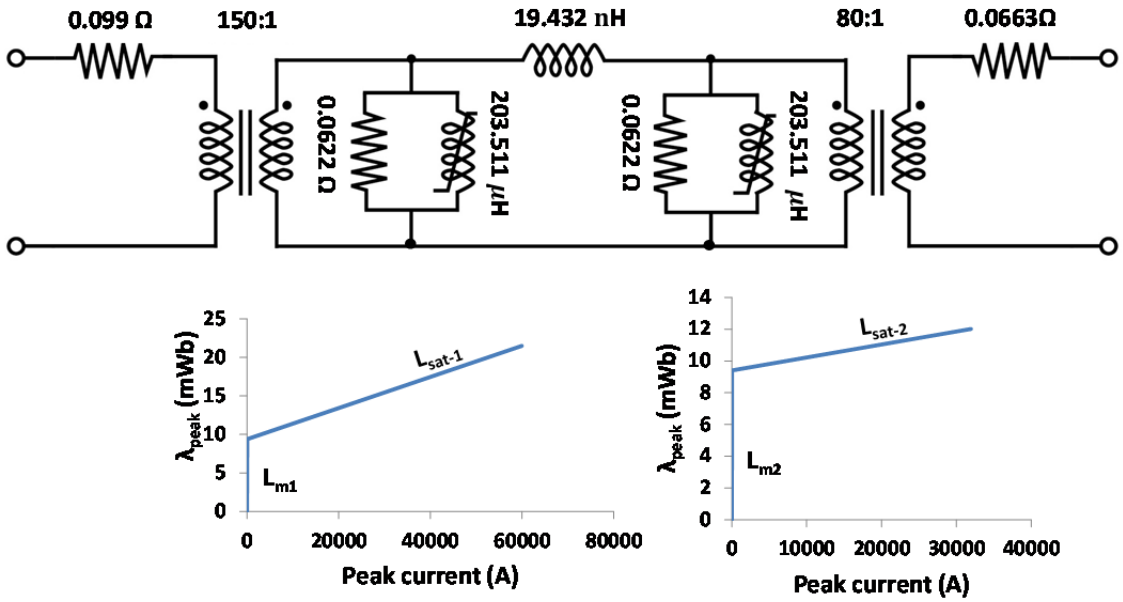

Figure 8.4. Complete grey-box model for test transformer T1 including the piecewise saturation characteristics. The saturation characteristics are placed on the left and right underneath the grey-box model to signify energisation from either the inner (150 turn) or outer (80 turn) windings.

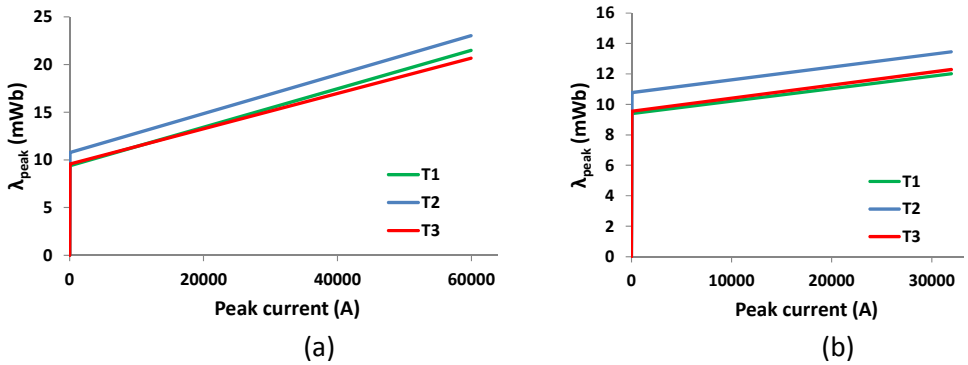

(a) (b)

Figure 8.5. The saturation characteristics for all three transformers when energised (a) from the 150 turn and (b) from the 80 turn sides of the transformers.

8.4 Discussion

The magnetic core and winding equivalent parameters values are successfully determined using standard test circuits available in IEEE Std C57.12.91 [2011].

The winding resistances are apportioned to their respective sides of the transformer using the dc resistances of the windings.

Determining the terminal saturation inductance of the test transformers requires a non-standard test circuit capable of providing a large dc bias with a small ripple that puts substantial thermal stress on the test circuit components. These components need additional forced air cooling and careful monitoring to prevent permanent damage occurring. The single phase test circuit used in this test is capable of driving the test transformers into deep saturation for both the 80 and 150 turn windings. The respective L_{sat} values for energisation from either side of the transformer are determined by calculation and together with the core equivalent inductance parameter, L_m, is used to calculate the λ-I_{peak} values for the grey-box model saturation characteristics.

It is speculated that determining the terminal saturation inductance of a large power transformer that has many more turns than the test transformers will require less dc bias to develop a high enough MMF to drive the transformer into half-wave deep saturation.

The parameter values of the grey-box model for all three test transformers show slight differences demonstrating that no two transformers of the same design are identical in every respect especially in deep saturation as can be seen in the saturation characteristics of Figure 8.5. The effect of these differences in a power studies should be investigated further.

The assembled grey-box model as shown in Figure 8.4 can be incorporated into EMTP software for simulation purposes.

8.5 Onward

It still remains to determine the response of a three phase bank of single phase four limb test transformers driven into half-wave saturation by a dc bias. In the next chapter the division of the dc bias current between the phases of a three transformer bank of single phase transformers, the distortion in the three phase bank and the effect of a motor load on the distortion caused by transformer half-wave saturation are determined.

Chapter 9

Three phase test results

In this chapter the results of the three phase testing concerned with answering the research questions relating to the division of the dc bias current between the phases of a three transformer bank of single phase transformers, the distortion in the three phase bank and the effect of a motor load on the distortion and the effect of the distortion on the motor's performance.

In section 9.1an unexpected unbalance in the sharing of the dc input between the three single phase transformers of the three-phase bank is analysed.

In section 9.2 the waveform and harmonic distortion caused by transformer half-cycle saturation in a three phase transformer bank are presented and discussed. Both YNyn0 and YNd11 three phase configurations are considered. In section 9.3 the effect of a load, represented by a three phase squirrel cage induction motor, on the THD and TDD is measured and analysed.

In section 9.4 the effect of this distortion on the induction motor itself is assessed and in section 9.5 a summary of the findings is presented.

9.1 Unequal division of the dc in the phase conductors

Figure 9.1 illustrates the parallel paths available for the dc to flow between the source and test transformer star points in a three phase bank of single phase transformers.

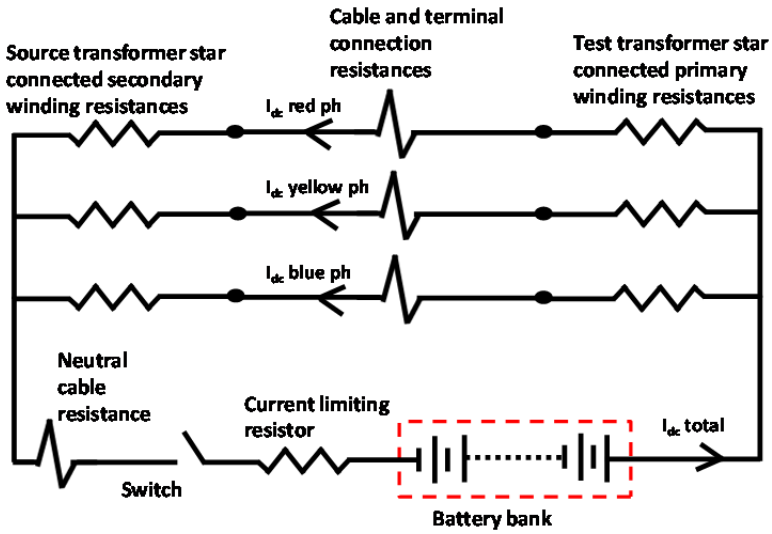

Figure 9.1. Resistance paths seen by the dc.

Despite every attempt to keep cable lengths equal and terminal connections tight for good electrical contact, the dc does not split equally between the three test transformers. The individual transformer winding resistances are very closely matched to within 0.3 mΩ. All

component resistances values are all in the milliohm range and a difference of 3 or 4 milliohm is sufficient to cause unequal dc splitting at the star points of the source and test transformer bank.

Figure 9.2 plots the dc flowing in each individual phase (test transformer) against the total dc flowing in the neutral wire. It can clearly be seen that the difference in dc per phase becomes more pronounced at higher dc levels.

The time that the dc is allowed to flow in the circuit is kept to a minimum especially at high dc levels, e.g. 150 A dc, in the neutral. This is done to reduce the duty on the batteries. Nevertheless, sufficient time is allowed for the dc to reach its maximum value due to the inductance in the circuit.

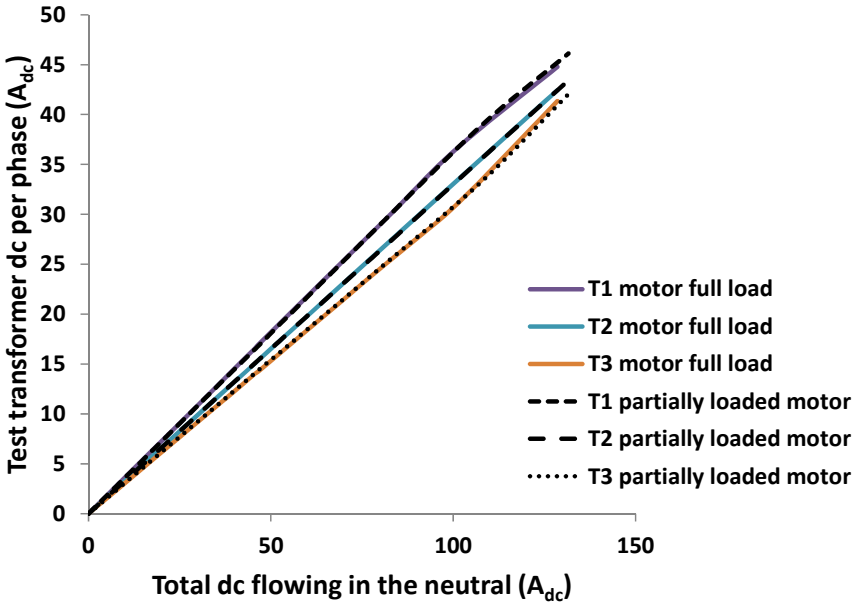

Figure 9.2. Illustration of the results of the dc split per phase for the YNyn0 transformer bank connection. Motor partial and full load scenarios are shown. The division of the dc at the star point is independent of load and is a function of the circuit parallel dc resistances.

It is conceivable that unequal dc splitting can be even more pronounced in extra high voltage networks. Each electrical component and connection plays a role in increasing the series dc resistance of each phase in a three phase system. Components such as power transformer winding resistances, high voltage bushing resistances, bus bars, circuit breaker contact resistances, instrument transformers, overhead phase jumper connections of unequal length, overhead line phase wires of unequal length and numerous electrical contact resistances all add to the dc resistance of a potential series path. This experimental finding is therefore acceptable and to be noted by power system engineers when conducting GIC studies.

In an energized ac transmission system a GIC or dc present will divide between the phases in complex fashion since the phase voltages are dynamic in nature. Load changes at a point of connection changes the response of voltage all along that phase. The resistive

parameters per phase will depend on the contribution of both the ac and dc current components to temperature change in the individual phase resistances. This dynamic phenomenon coupled with the physical network construction implies unequal resistances per phase that is continually changing. Unequal GIC or dc division per phase should therefore be expected in power systems.

A mismatch in the dc resistances of each phase in a three phase system can lead to one phase experiencing an appreciably larger GIC or dc component of current. A sufficiently large unbalance could cause three phase three limb transformers to experience a level of saturation due to unequal dc ampere-turns per phase. This however, will need to be proved by determining the degree of mismatch current required to cause saturation in a three phase three limb transformer.

9.2 Distortion in a dc biased three phase bank of transformers

In this section results are presented of testing to answer the research question relating to the distortion caused when a three phase bank of single phase four limb transformers is driven into half-wave saturation by a dc bias current injected into the neutral conductor.

In section 7.1.3 the single phase test results illustrate the increase in harmonic distortion with increasing dc excitation. Similar trends are noticed for three phase test results for both the YNyn0 and YNd11 transformer bank connections.

9.2.1 Current and voltage waveform distortion in dc biased three phase transformer banks

In this section the waveforms of the primary and secondary phase voltages, and the primary phase current for both YNyn0 and YNd11 transformer bank connections are presented. In both instances a motor at no load is connected to the transformer bank secondary windings while a dc bias of approximately 30 A per phase flows through the primary windings.

The intention of this section is to present the distortion of the both current and voltage waveforms of a single representative test transformer in the three phase bank. The data represented is therefore made up of recordings from different transformers in the three phase bank. The wave shapes are representative of the experimental evidence found and only one electrical phase is shown for simplicity.

Figures 9.3**Figure** (a), (b) and (c) displays respectively the primary and secondary phase voltages and primary phase current waveforms for the YNyn0 three phase bank. The secondary windings have a motor at no load attached while a dc bias of approximately 30 A dc per phase is injected into the primary windings.

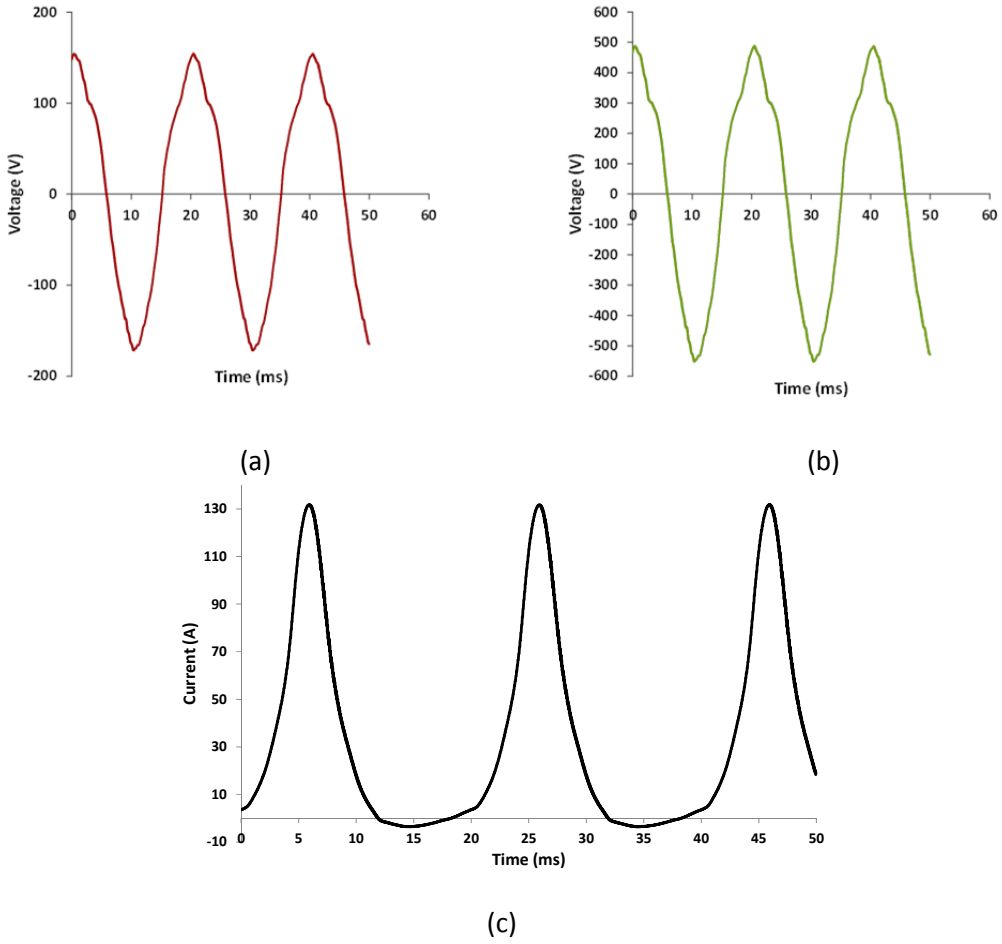

Figure 9.3. Waveforms from a representative test transformer where (a) is the primary phase voltage, (b) is the secondary phase voltage and (c) is the primary phase current in a YNyn0 transformer bank with a motor at no load connected to the secondary windings and approximately 30 A dc bias per phase in the primary windings.

The primary and secondary voltages of the YNyn0 transformer arrangement are both distorted and display a similar trend with respect to their shape. This is typical of the effect of a second harmonic voltage-drop in the primary winding and is seen in the primary voltage positive half-cycle that is transformed to the secondary side of the transformer. The primary current waveform has the typical signature wave shape of a half-wave saturated single phase transformer [Lu *et al*.1993; Chiesa 2010; Ngnegueu *et al.* 2012; Mousavi 2012; Chisepo 2014; Borrill *et al.* 2016].

Figures 9.4(a), (b) and (c) displays respectively the primary and secondary phase voltages and primary phase current waveforms for the YNd11 three phase bank connection.

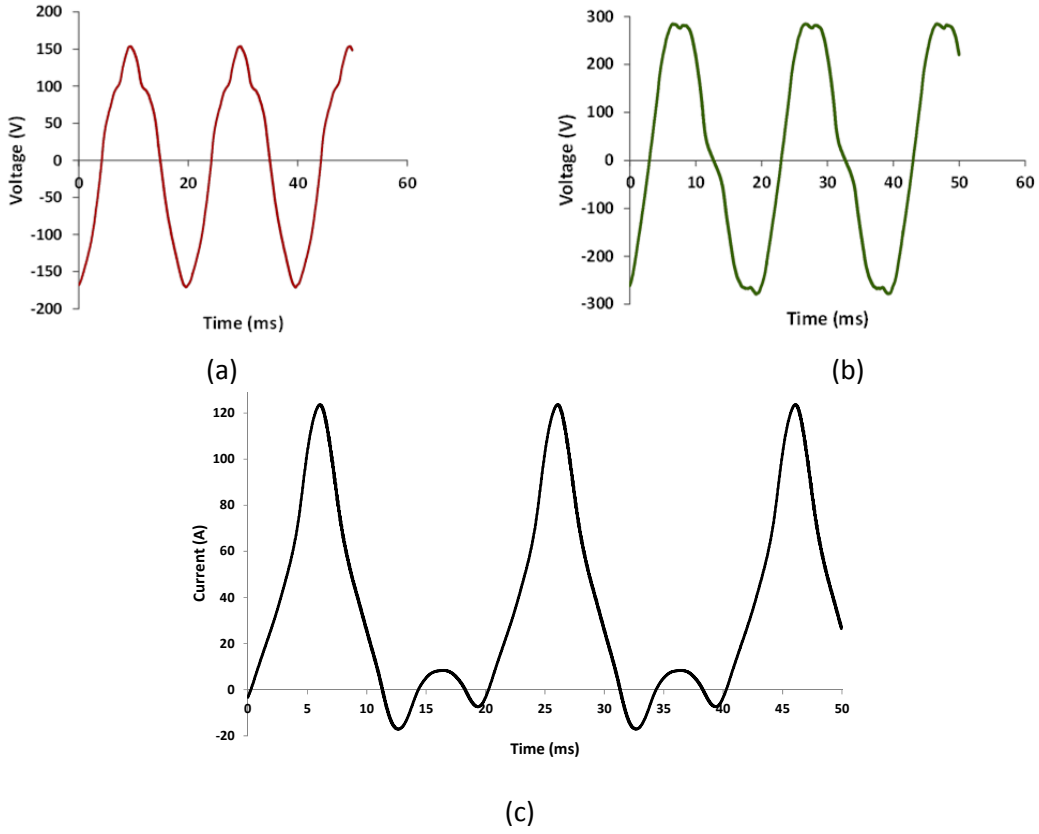

Figure 9.4. Waveforms from a representative test transformer where (a) is the primary phase voltage, (b) is the secondary phase voltage and (c) is the primary phase current in a YNd11 transformer bank with a motor at no load connected to the secondary windings and approximately 30 A dc bias per phase in the primary windings.

The primary and secondary phase voltages are both distorted but have dissimilar wave shapes. This is due to the effect of the phase shifted zero sequence third harmonic currents circulating in the delta connection and creating a voltage-drop that affects the transformer terminal voltage near the peaks of the wave. The second harmonic current creates a voltage-drop effect seen as the distortion of the wave shape at the zero point crossing. The secondary phase voltage wave therefore resembles the distortion seen when second and third harmonic voltage-drops are present in the secondary windings. The current wave shape has the typical signature wave shape for the current of a saturated YNd11 transformer bank as reported by Price [2002]. Lahtinen & Elovaara [2002] also obtained similar phase current wave shapes in their experiment conducted on a 400/400/125 MVA, 410±6*1.33%/120/21 kV three winding three phase five limb YNynd11 connected transformer with 200 A dc bias.

9.2.2 Harmonic distortion in dc biased YNyn0 and YNd11 three phase transformer banks

The following test results from transformer T2 (yellow phase) represent the trends seen in all three transformers (and phases).

Transformer no load condition:

Figure 9.5 presents column graphs of the input current to T2 when energised on the 80 turn winding side with the secondary open circuit for both the YNyn0 and YNd11 transformer bank connections respectively. In general, the trend in both graphs is for the magnitude of the current harmonics to increase with increasing dc injection but to decrease with increasing harmonic order.

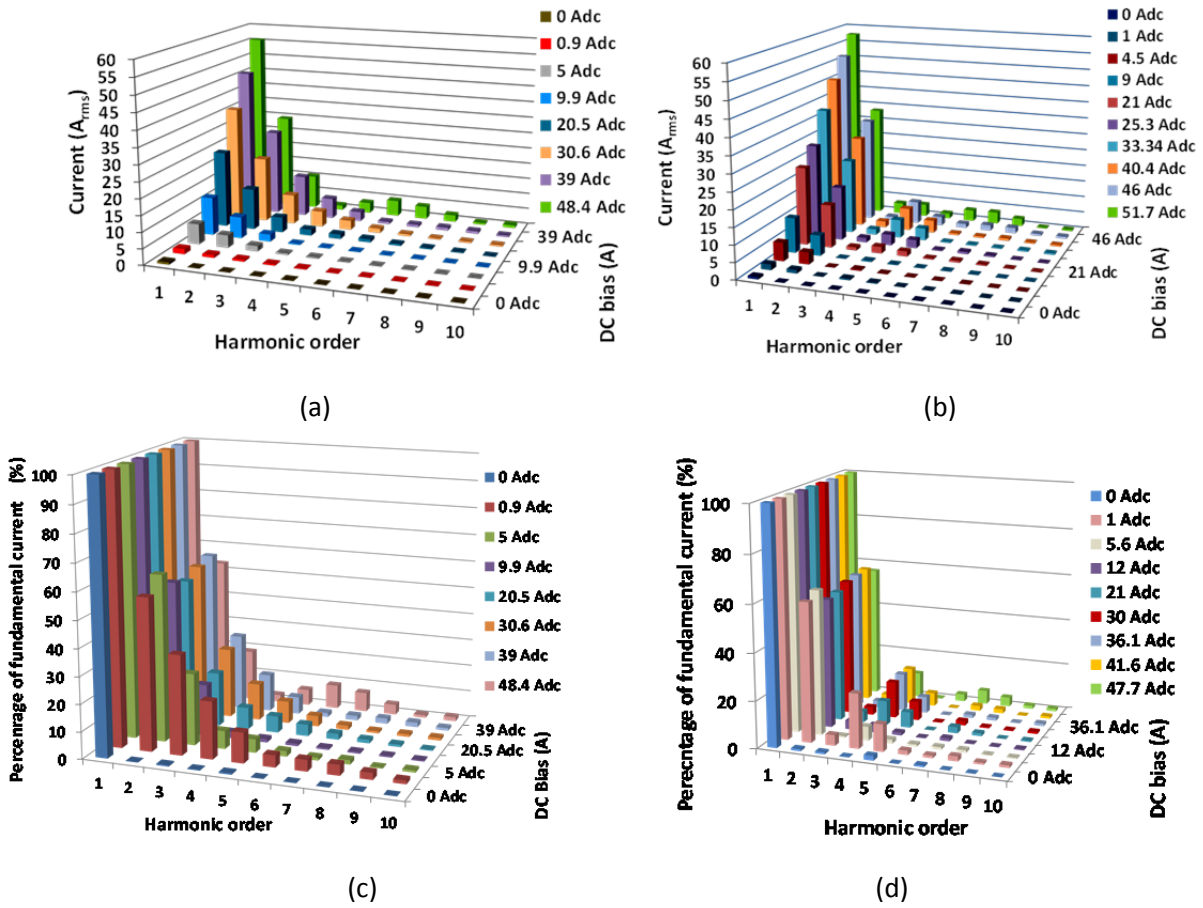

Figure 9.5. Column graphs of the first ten current harmonic orders of the primary current of T2 with the secondary open-circuit while increasing the dc bias in the primary winding, where (a) is for a YNyn0 transformer bank connection and (b) is for a YNd11 transformer bank connection. In (c) and (d) the first ten current harmonic orders of the primary current are plotted as a percentage of the fundamental current with increasing dc bias for the YNyn0 and YNd11 connections respectively.

Exceptions to this general statement are:

- Figure 9.5(b) shows no triplen harmonics at dc levels up to approximately 20 A dc. At higher dc levels when the transformer is moving deeper into saturation the flux from the outer 80 turn energising winding does not fully link with the 150 turn inner winding and triplen components of flux are present on the primary side requiring corresponding triplen components of current.
- At dc injection levels close to 50 A dc the harmonic components of the orders 5 to 10 start to increase in magnitude while the 4th harmonic decreases for both three phase bank connections.

- At 1 A dc bias Figure 9.5(c) shows disproportionately large increases in the percentage of fundamental harmonic orders from the 3rd harmonic up to the 10th. As seen in chapter 7 (on the results of single phase transformers) this coincides with the first peak of the THD graph when the joints start to saturate. However, there are disproportionate changes in the harmonic orders associated with the 5 A dc bias current injections as well. This could be linked to interaction with the other transformers in the three phase bank.
- In Figure 9.5(d) at 1 A dc bias, shows disproportionately large increases in the percentage of fundamental for the 3rd, 4th and 5th harmonic orders with smaller increases for the other harmonic orders. This coincides with the saturation of the joints. However, there are disproportionate changes in the harmonic orders associated with the 5.6 A dc bias as well. This could be linked to interaction with the other transformers in the three phase bank.

In Figure 9.6(a) and (b) respectively show the column graphs of the first ten voltage harmonic orders of the primary voltage of T2 with the secondary open-circuit for an increasing dc bias in the primary winding for the YNyn0 and YNd11 transformer bank connections. Since the dc injection value is not identical for both test scenarios there are small differences between the magnitudes of the same harmonic order of both connection types. However, the graphs are very similar with respect to the occurrence of harmonic orders and their variation with dc bias indicating that the primary voltages are almost independent of the secondary connection type.

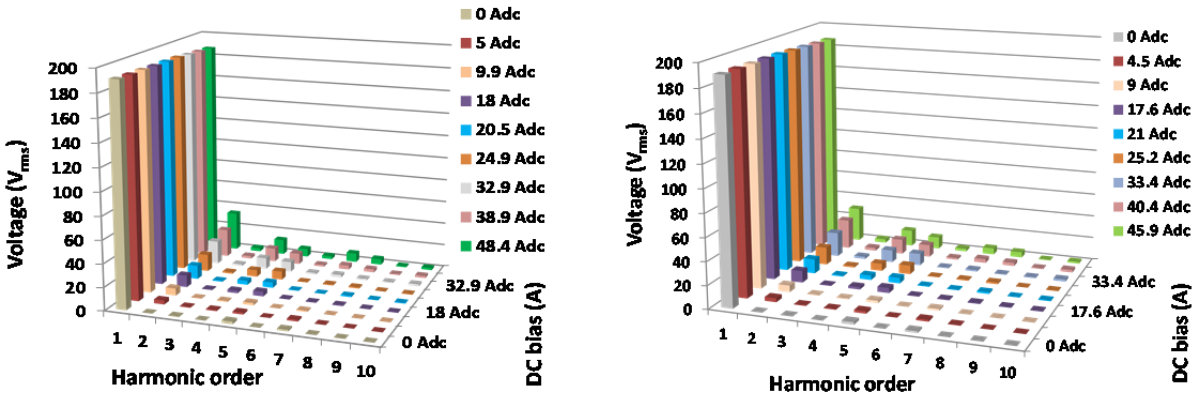

(a) (b)

Figure 9.6. Column graphs of the first ten voltage harmonic orders of the primary voltage of T2 with the secondary open-circuit while increasing the dc bias of the primary winding, where (a) is for a YNyn0 transformer bank connection and (b) is for a YNd11 transformer bank connection.

The similarity in the two harmonic graphs of Figure 9.6 is consistent with an examination of Figure 9.3(c) and Figure 9.4(c), in which the positive half-cycle of the primary currents are similar for both connections and inordinately large compared to their negative half-cycles.

Transformer partially loaded:

A motor with a dc generator attached to its shaft is now connected to the secondary terminals of the YNyn0 transformer bank and loaded to the motor full load current of approximately 6 A_{rms}.

Figure 9.7 and Figure 9.8 display column graphs of the first ten harmonic orders of the primary and secondary line currents, and primary and secondary terminal voltages respectively. Figure 9.9 provides the transformer primary and motor terminal voltage waveforms, and transformer primary and motor (secondary) line current waveforms.

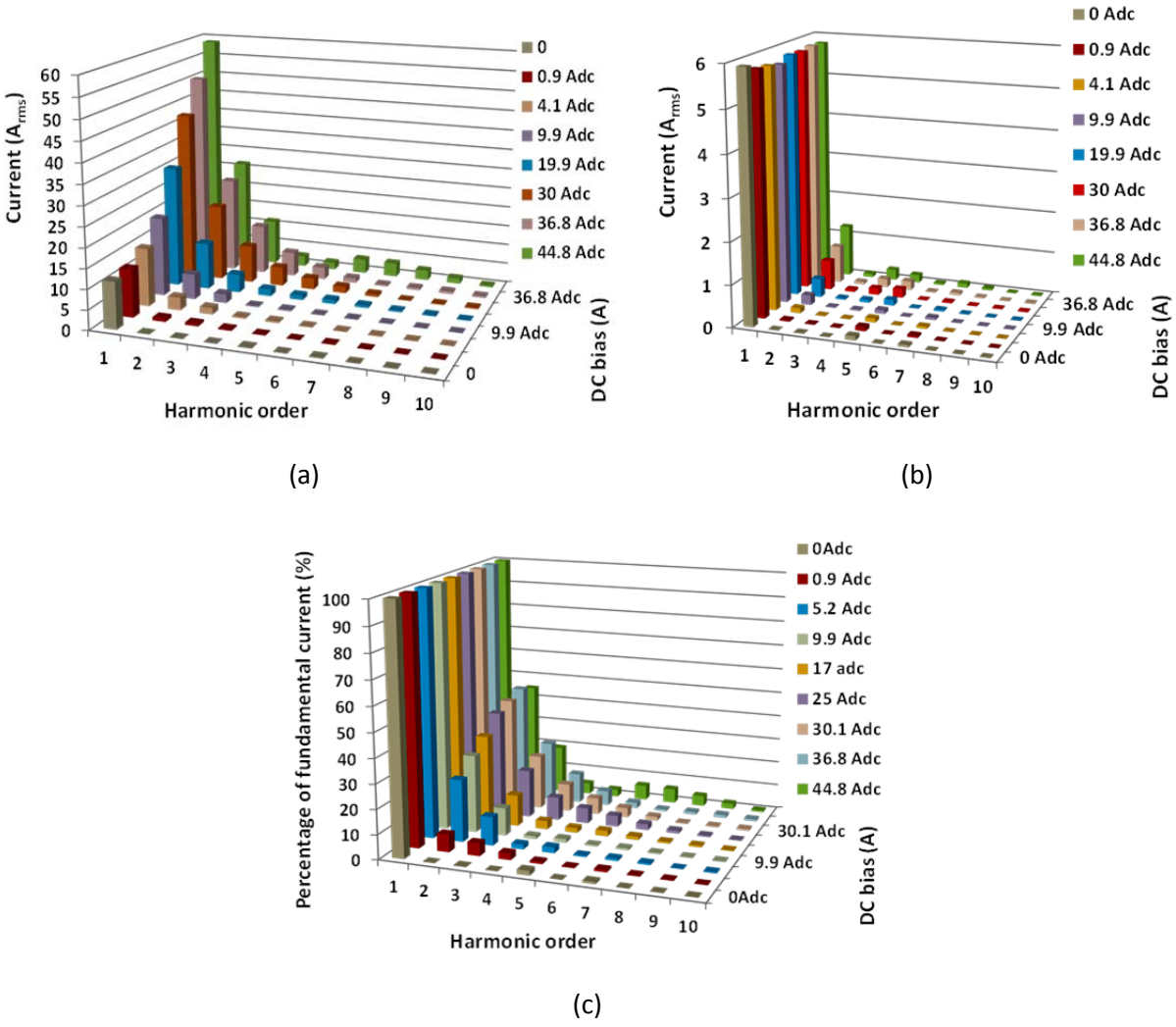

Figure 9.7. Column graphs of the first ten current harmonic orders with increasing dc excitation for the YNyn0 transformer bank connection, where (a) is the primary input current of T2 and (b) is the secondary load current of T2 with a motor load of approximately 6 A_{rms} connected. In (c) the first ten current harmonic orders of the primary current are plotted as a percentage of the fundamental current with increasing dc bias.

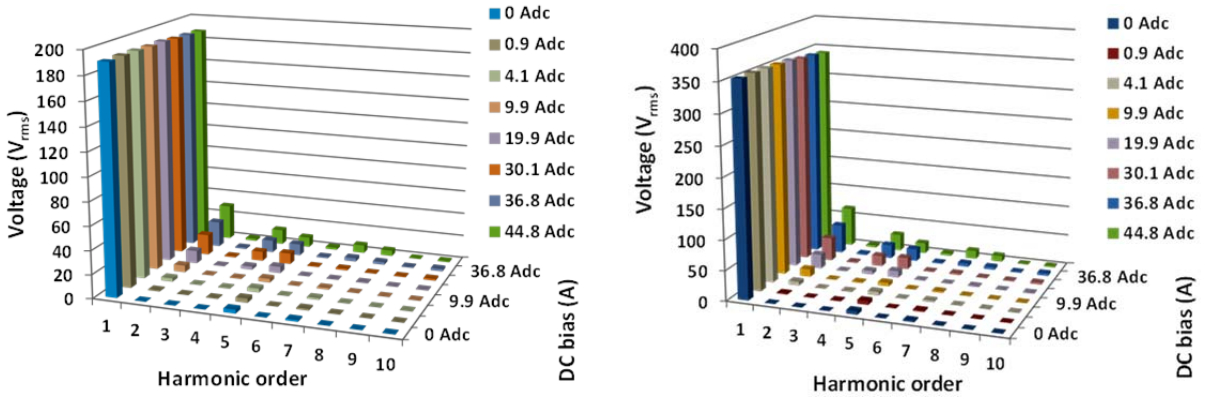

(a) (b)

Figure 9.8. Column graphs of the first ten voltage harmonic orders with increasing dc excitation for a YNyn0 transformer bank connection with a motor load of approximately 6 A_{rms} connected, where (a) is T2 primary voltage and (b) is T2 secondary voltage.

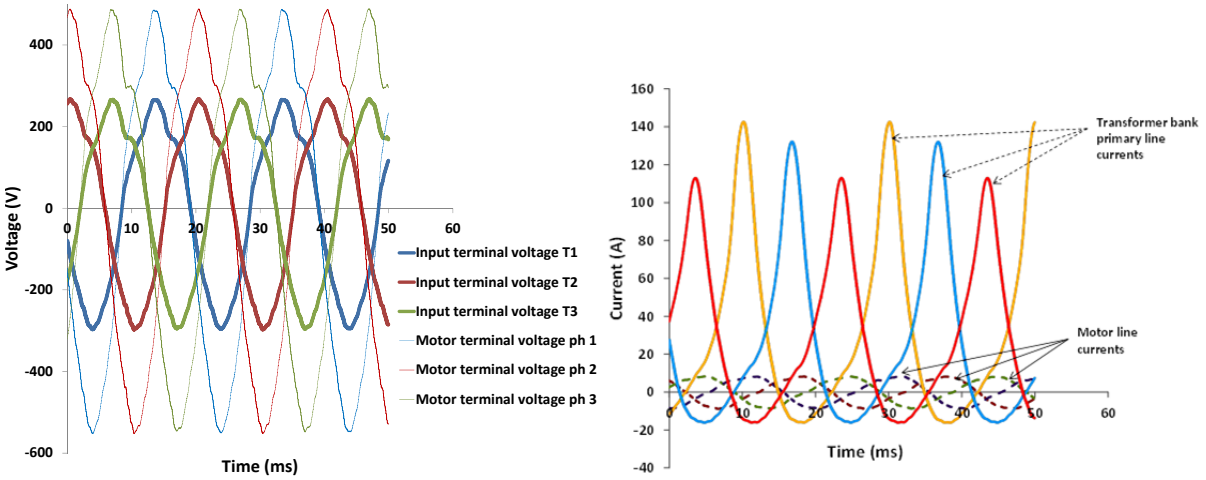

(a) (b)

Figure 9.9. YNyn0 three phase transformer bank supplying a motor at full load (6 Arms) and 30 A dc bias per phase flowing in the transformer primary windings, where (a) is the transformer primary and motor terminal voltage waveforms and (b) is transformer primary and motor load current waveforms.

When comparing Figure 9.7(b) and Figure 9.8(b) for the YNyn0 transformer bank three effects are evident:

- It becomes clear that the motor load current harmonic profile resembles that of the transformer secondary voltage harmonic profile. This is due to the motor responding to its terminal voltage and it has not added any visible contribution to the harmonic distortion caused by the transformer half-cycle saturation.
- Similarly, the motor current and secondary voltage waveforms of Figures 9.9(a) and (b) show the motor current following the secondary voltage. The primary voltage and current waveforms are dissimilar since the primary current is symptomatic of the transformer in half-wave saturation.

- The unequal magnitudes of the positive peaks of the transformer bank primary phase currents points to unequal dc splitting between the individual single phase transformers.

When analysing the harmonics as a percentage of the fundamental current as shown in Figure 9.7(c) it is evident that at 44.8 A dc the 2nd and 3rd harmonic magnitudes have decreased as a percentage of the fundamental which could be symptomatic of the transformers in the YNyn0 bank moving deeper into saturation.

It is seen for the YNyn0 and YNd11 transformer bank connections with the transformer at no load condition in Figures 9.5(c) and (d) that a disproportionately large increase in the percentage of fundamental for harmonic orders from the 3rd harmonic to the 10th exists at approximately 1 A dc bias. In Figure 9.7(c) this harmonic phenomenon is not seen for the YNyn0 connection. This is attributed to the fundamental current being substantially larger due to the motor load current. The percentage of fundamental for harmonic orders from the 3rd harmonic to the 10^{th} is now negligibly small.

As the dc bias on the primary side of the transformer bank increases the transformers move further into saturation and the leakage flux between the primary and secondary windings increases. This results in a decrease on the secondary terminal voltage as is evident in Figure 9.8(b) and the motor responds by increasing its current demand at higher dc bias levels as is seen in Figure 9.7(b) in order to maintain its power output to the loaded dc generator.

9.3 Distortion and transformer load

This section deals with answering the research question relating to the effect of a load on the level of distortion when a three phase bank of single phase transformers half-wave saturates. The THD and TDD of the primary current of one of the test transformers in the YNyn0 connection are used to analyse the results and determine the effect of a load on the distortion level. Similar THD and TDD plots occur for all three test transformers in the YNyn0 transformer bank.

Three loading scenarios considered in the testing, i.e. the secondary terminals open-circuit, a motor connected but operating at no load and finally a motor at full load of approximately 6 A. A three phase squirrel cage induction motor with dc generator is connected to the secondary terminals of a YNyn0 transformer bank to assess whether a motor load effects the level of distortion experienced when a three phase transformer bank is driven into saturation under dc biasing conditions.

9.3.1 Effect of the load on THD

Figure 9.10 displays three graphs of the THD of the primary current plotted with increasing dc bias for transformer T2 (yellow phase) in the YNyn0 connection for the three load scenarios. Similar graphs are obtained for test transformers T1 and T3.

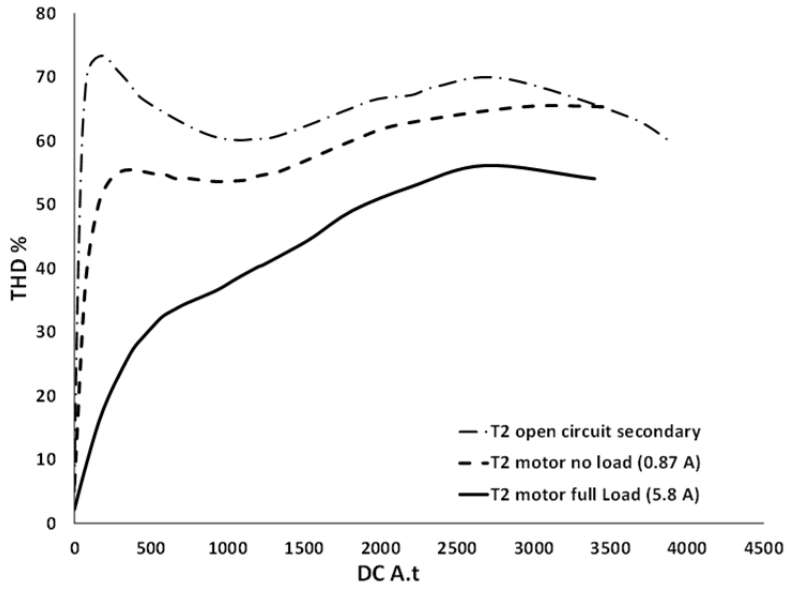

Figure 9.10. THD plots for test transformer T2 in a three phase YNyn0 bank of transformers with increasing dc bias for loading scenarios: open circuit, motor at no load and motor at full load of approximately 6 A_{rms} respectively.

THD can be seen to exaggerate the effect of the loading conditions in Figure 9.10. This is because the fundamental component of the current in Equation (6.1) changes with the transformer loading condition and reduces the THD as the load increases. Despite the increase of THD reduction, the two peaks representing core joint and core bulk component saturation are still discernable for the three load conditions. Observing the trend between the individual graphs it is envisaged that at higher load currents the THD peak created by core joint saturation will be smoothed out. This method of determining distortion under loaded conditions is therefore not recommended especially if non-step lap butt joints are used in the core construction as these are a source of early saturation in the core.

9.3.2 Effect of load on TDD

The single phase four limb test transformer voltage ratio reduces at higher levels of saturation because the leakage flux increases causing less flux to link with the secondary winding [Borrill *et al.* 2016].

Analysing the results of the standalone single phase test of section 7.1.3, at a dc bias of approximately 3950 AT, a reduction in voltage of approximately 1.5 % is measured with a stiff supply connected to the primary windings. A reduced secondary voltage will increase the current demand of the motor load attached to the transformer bank secondary windings in order for the output power to be maintained. Using the transformer equivalent circuit for explanation, Figure 9.11, the increase in current through the transformer's R_{150}, R_{80} and L_S equivalent components would produce a further decrease in terminal voltage.

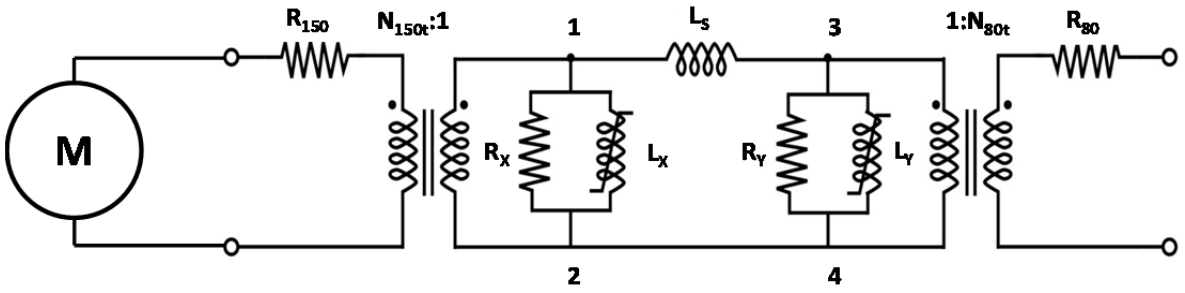

Figure 9.11. Pi equivalent circuit used to represent a three phase bank of single phase transformers saturated by a low frequency transient. The three phase star connected induction motor is attached to the 150 turn windings.

Figure 9.12 illustrates the response of the primary and secondary voltages and the secondary current with increasing dc bias. An upward deflection of the 2 A and full load current characteristics at approximately 2000 dc AT or 25 A dc can be matched loosely to the
THD plots in Figure 9.10 where the bulk core components start to saturate increasing the leakage inductance and reducing further the motor terminal voltage.

The effect of the series voltage drops R_{150}, R_{80} and L_S in the equivalent circuit of Figure 9.11 is to reduce the voltage across the transformer magnetizing branches 1-2 and 3-4 in the equivalent circuit which reduces the ac induction in the core. This reduces the degree of saturation of the transformer core which will in turn reduce the distortion. This phenomenon becomes more noticeable when the leakage inductance increases at approximately 2000 dc AT (25 A dc) and above.

The test circuit adjustment and measurement requires that the dc be allowed to reach its maximum value and then the data storage procedure of the Yokogawa power meter is executed. All this takes less than one minute. The winding resistances R_{150} and R_{80} are not exposed to the load current for long enough during testing to heat up significantly, increasing their resistance, and can be assumed to have a minimal effect on the core induction level.

Figure 9.13 illustrates the TDD plots for four load test scenarios with the distortion normalised to the transformer secondary (150 turn winding) rated current of 21,33 Arms. As the load on the transformer is progressively increased, a distinct reduction in the TDD demonstrates the voltage reduction effect of the load current. The motor full load current represents approximately 30% of the transformer rated current, so a further reduction in distortion can be envisaged with a fully loaded transformer.

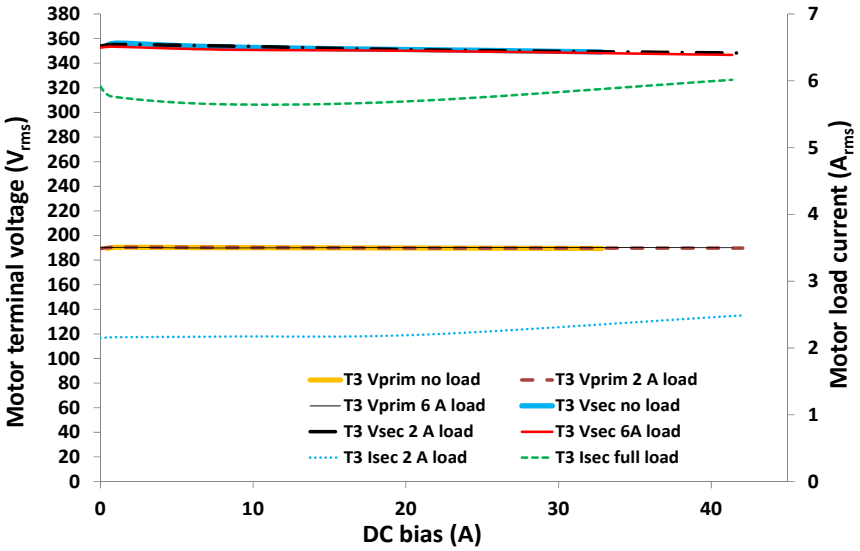

Figure 9.12. Transformer T3 (or blue phase transformer) graph showing the reduction in transformer terminal voltage with increasing dc and load current. Motor no load, partial load (2 A_{rms}) and full load (6 A_{rms}) conditions are illustrated.

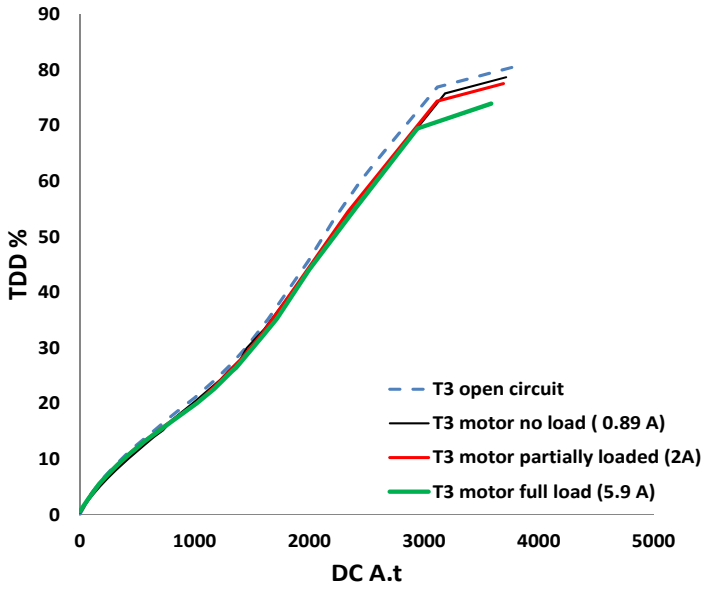

Figure 9.13. Graphs of TDD versus dc ampere-turns at four different load scenarios for transformer T3 (blue phase).

9.4 Effect on the performance of a three phase squirrel cage induction motor due to transformer half-wave saturation distortion

The investigation with the motor is only a preliminary test, given that the three-phase test transformer set up is available. The sound recording device, the scope of the measurements made on one motor, and the lack of temperature and other measurements are all obvious limitations of the test.

Based on previous good experience of identifying harmonics in a transformer using a cell (mobile) phone recording, sound recordings are made of the motor at various levels of dc

bias in its three phase bank of single phase transformers. The recordings are processed using FFT to convert the recordings into the frequency domain.

The sound recordings A, B and C are made with the following electrical supplies to the motor:

- Recording A is made at nominal ac voltage at the motor terminals and no dc bias in the transformer primary winding,
- Recording B is made with dc bias injected into the transformer primary winding and an ac voltage collapse is allowed to occur as brought about by the half-wave saturation of the supply transformer, and
- Recording C is made with dc bias injected into the transformer primary winding and the ac voltage restored back to the motor nominal terminal voltage simulating a firm supply.

The dc per phase in the YNyn0 transformer bank for each recording is given in Table 9.1. Small differences in dc bias for each transformer are as a result of unequal dc resistance per phase in the YNyn0 transformer. The dc level used for each sound recording differs slightly due to battery bank response over time.

The microphone of the iPhone used in the sound recordings is not calibrated for use with the 3 phase squirrel cage induction motor with its mechanically coupled dc generator (at no load). The Units^2/Hz is used for the Y-axis to represent the rms power measurement and should be seen as a relative measurement.

Table 9.1. Table indicates the level of dc per transformer in the YNyn0 configuration for recordings A, B and C.

Test transformer	Dc bias per single phase transformer in the YNyn0 bank (A dc)		
	Recording A	Recording B	Recording C
T1	0	49.1	46.8
T2	0	46.8	44.5
T3	0	44.0	42.5

9.4.1 Processing of recorded sound files

The *.m4a files are to be converted to *.wav files using Apple iTunes. This results in a sampling rate of 44.1 kHz. These files are then to be processed in HBM nCode software with the following adjustments:

- Low pass filter of 3kHz applied,
- Sample rate adjust down to 6kHz,
- FFT of signal using a buffer size of 32768 points, power scaling, and
- FFT exported as *.csv files.

The FFT is taken as an average of the harmonic frequencies calculated over a 15 second sample of the data file.

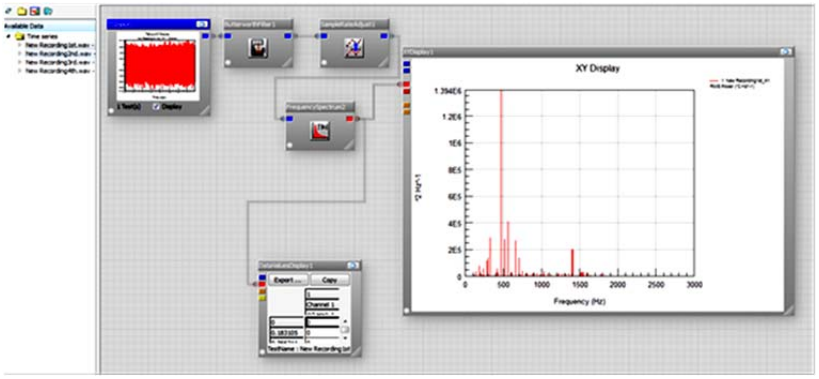

(a)

ButterworthFilter Properties

Name	Value	Description
General		
Type	LowPass	Filter type
Method	ForwardAndBackward	Filter method
Order	8	Filter order
Low Pass		
Frequency1	3000	Filter frequency 1
Warnings		
DCWarning	2	DC warning level (% of Nyquist)
NyquistWarning	98	Nyquist warning level (% of Nyquist)

(b)

SampleRateAdjust Properties

Name	Value	Description
General		
Mode	Interpolate	Specifies the method to use to change the sample rate
Interpolate		
NewSampleRate	6000	The new sample rate (for interpolation, spline or hold value options)
Interpolation		
Interpolation	Linear	The type of interpolation

(c)

FrequencySpectrum Properties

Name	Value	Description
General		
OutputType	Power	Specifies the type of spectrum to produce
AveragingMethod	Linear	Specifies the way to combine the data from multiple FFT buffers
AutoHistogramLabels	True	Specifies whether to automatically set the axis labels and units text on the output histo
Buffer		
WindowType	Hanning	Specifies the window type to apply to each buffer
BufferSize	32768	Specifies the FFT buffer size
BufferOverlap	67	Specifies the overlap on the input data for each FFT analysis
AdvancedSettings		

(d)

Figure 9.14. Screenshots (a) to (d) are the HBM nCode software screen displays as selected for the FFT study of the sound recordings.

9.4.2 Analysis of processed sound file data

The intension of this analysis is finding discernible differences between the three sound recordings which is an indication that the harmonics caused by the dc bias in the three phase supply transformer bank affects the motor's performance.

Figures 9.15(a) and (b) display graphs of frequency versus rms power measurement (unit^2/Hz) for the FFTs of sound recordings A, B and C. Figure 9.15(a) displays the FFT data for sound recording A, B and C superimposed using the same system of axes which allows for easy discernment of the recording with the largest rms power value at a particular frequency. By far the largest rms power values for all three recordings occur at 491 Hz followed by the rms power values at 196 Hz. The rms power values at all other frequencies are small by comparison. The largest rms power values for recordings B and C occur below 500Hz which could account for the audible drop in sound pitch noticed.

Figure 9.15(b) displays line graphs of the largest rms power value for each recording at the dominant frequencies. In the context of this research dominant frequencies are frequencies at which the rms power values are not only the largest but also clustered together in a narrow frequency range.

The graphs in Figure 9.15(b) show the phase shift between the individual recordings at the dominant frequencies. The coincidence of the maximum rms power of the A and C sound recordings could be linked to the fact that both recordings are made at nominal ac supply voltage. The phase shift of recording B on the other hand could be the effect of the collapsing ac supply voltage.

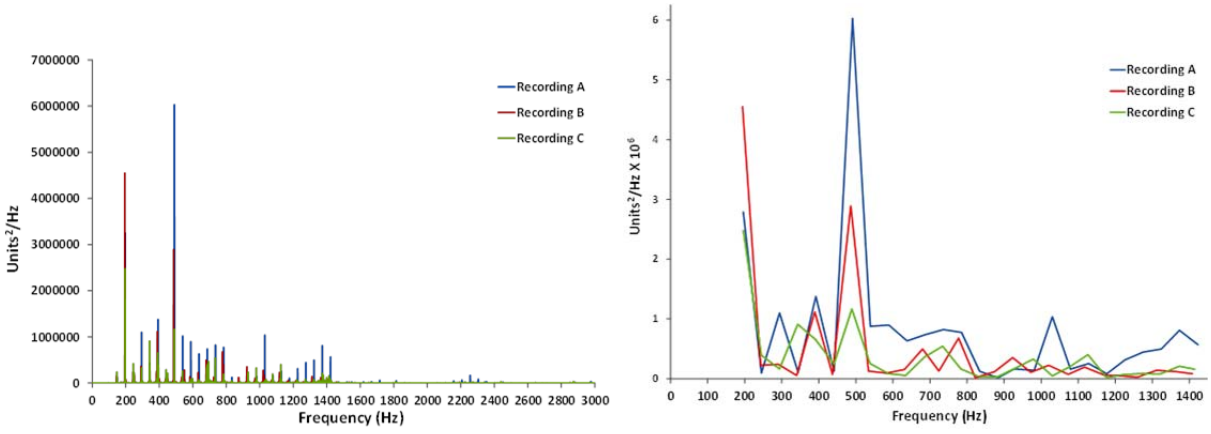

Figure 9.15. Graphs of the rms power measurement (unit^2/Hz) versus frequency for the FFTs of sound recordings A, B and C where (a) is the FFT data superimposed on the same system of axes and (b) is the maximum rms power versus frequency plotted individually as X-Y scatter graphs showing the phase shift of the individual maximum power values.

In Table 9.2 the frequencies for maximum rms power values power for recordings A, B and C appear to reach a maximum rms power value at approximately every 50 Hz. Recording A dominates in terms of maximum power at almost all the dominant frequencies. The maximum powers of recording A are well defined as is shown in Figure 9.16(a). Recordings B and C are less defined with rms powers at multiple frequencies above and below the

dominant frequencies. These frequencies are approximately 3 and 4 Hz apart for the C and B recordings respectively as shown in Figures 9.16(b) and (c).

Table 9.2. Frequencies for power maximum values observed in Figure 9.15(b) with the ΔF interval associated with the occurrence of the maximum power values.

Recording A														
F (Hz)	196	245	294	344	392	441	491	539	589	638	687	736	785	834
ΔF(Hz)		49	49	50	48	49	50	48	50	49	49	49	49	49
F (Hz)	883	927	981	1030	1079	1128	1177	1226	1275	1324	1373	1423		
ΔF(Hz)	49	44	54	49	49	49	49	49	49	49	49	50		
Recording B														
F (Hz)	194	243	291	340	389	437	486	534	583	631	680	725	777	830
ΔF(Hz)		49	48	49	49	48	49	48	49	48	49	45	52	53
F (Hz)	875	923	972	1020	1073	1117	1171	1215	1259	1311	1365	1416		
ΔF(Hz)	45	48	49	48	53	44	54	44	44	52	54	51		
Recording C														
F (Hz)	196	245	294	343	391	441	489	538	587	634	685	734	783	832
ΔF(Hz)		49	49	49	48	50	48	49	49	47	51	49	49	49
F (Hz)	881	930	979	1030	1076	1126	1177	1221	1273	1321	1373	1414		
ΔF(Hz)	49	49	49	51	46	50	51	44	52	48	52	41		

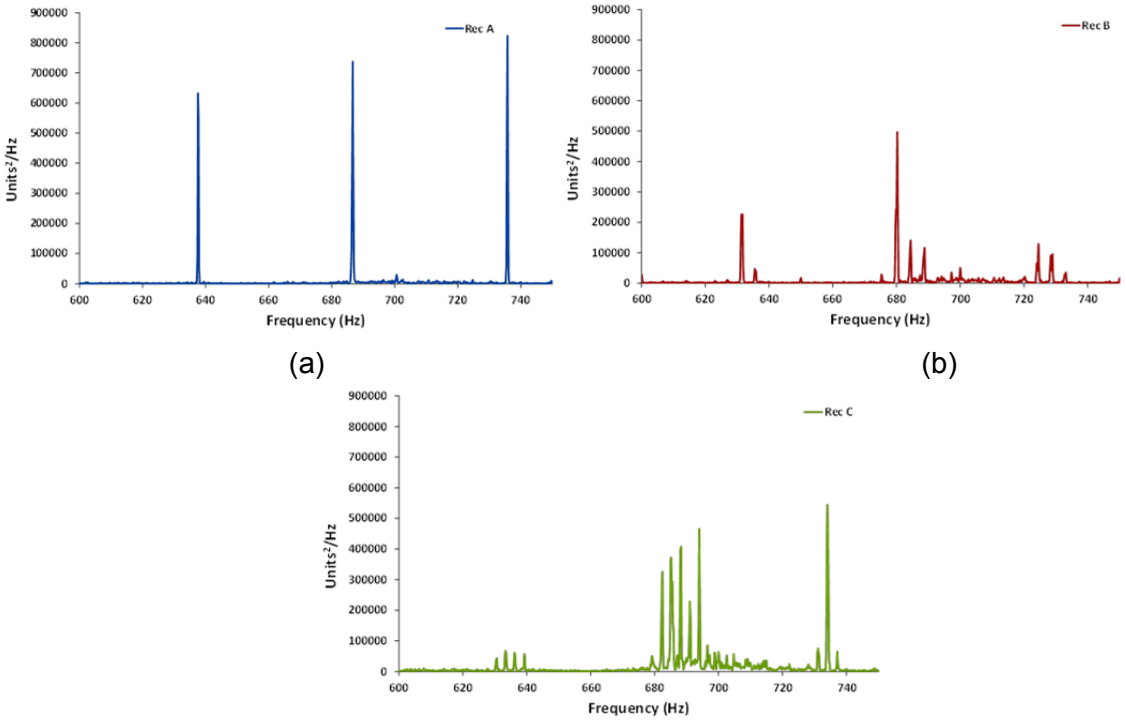

Figure 9.16. Graphs of the rms power measurement (unit^2/Hz) versus of frequency for the FFTs of sound recordings for the frequency range 600 to 750 Hz where (a) is recording A, (b) is recording B and (c) is recording C.

At the maximum rms power frequencies the three sound recordings occur within a range of approximately 2 to 10 Hz of each other. In Table 9.3 it can be seen that the largest rms power of recordings A and C generally tend to occur close to the same frequency while those of recording B appear to be phase shifted occurring at frequencies of approximately 2

to 10 Hz lower than recordings A and C. The 50 Hz interval for the occurrence of the maximum rms power values could be linked to the 50 Hz supply frequency.

At frequencies above 1150 Hz the rms power of recordings B and C are negligible and above 1500 Hz all recordings have negligible rms power values.

Table 9.3. Power maximum values observed in Figure 9.15(a) with their associated frequencies.

Recording A													
F (Hz)	196	245	294	344	392	441	491	539	589	638	687	736	785
Rms Power (Units^2/Hz X 10^6)	2.79	0.096	1.1	0.107	1.377	0.126	6.028	0.878	0.898	0.633	0.737	0.823	0.775
F (Hz)	834	883	927	981	1030	1079	1128	1177	1226	1275	1324	1373	1423
Rms Power (Units^2/Hz X 10^6)	2.79	0.015	0.163	0.141	1.038	0.16	0.254	0.083	0.315	0.445	0.497	0.81	0.568
Recording B													
F (Hz)	194	243	291	340	389	437	486	534	583	631	680	724	777
Rms Power (Units^2/Hz X 10^6)	4.55	0.225	0.241	0.055	1.117	0.073	2.891	0.128	0.094	0.155	0.497	0.129	0.679
F (Hz)	830	875	923	972	1020	1073	1117	1171	1215	1259	1311	1365	1416
Rms Power (Units^2/Hz X 10^6)	0.016	0.119	0.353	0.107	0.225	0.074	0.194	0.059	0.05	0.024	0.141	0.119	0.033
Recording C													
F (Hz)	196	245	294	343	391	441	489	538	587	634	685	734	783
Rms Power (Units^2/Hz X 10^6)	2.48	0.392	0.165	0.912	0.656	0.245	1.166	0.255	0.088	0.054	0.362	0.544	0.164
F (Hz)	832	881	930	979	1030	1076	1126	1177	1221	1273	1321	1373	1414
Rms Power (Units^2/Hz X 10^6)	0.036	0.029	0.175	0.329	0.047	0.197	0.403	0.016	0.069	0.087	0.079	0.209	0.158

Human sensory observations made of the motor's response to distortion are:

- At nominal voltage the motor runs with a higher sound pitch than when dc bias is introduced to the transformer, and
- The vibration felt on the motor casing becomes more pronounced when dc bias is introduced to the transformer.

The need to determine the effect of distortion caused by transformer half-wave saturation on a rotating machine connected to the transformer secondary terminals requires further investigation. In hindsight, a rotating machine with internal temperature measurement devices embedded in its windings and vibration measurement devices attached to its casing is preferred for determining the full effects of the distortion on the motor.

9.5 Discussion

The dc bias injected into the neutral of the YNyn0 and YNd11 three phase transformer banks respectively reveal that the dc bias current does not split equally between the three test transformers. A difference in dc resistance between phases of a few milliohms is sufficient to

cause unequal dc splitting at the star points of the source and test transformer bank. This has implications for three phase three limb transformers that are generally considered to be immune to GICs. Imbalance in the flow of GICs in transmission grids is likely to occur especially when considering the many series components and connections per phase in a transmission grid. In this regard it should be noted that the transposition of conductors in transmission grids is not perfectly executed.

Some distortion is seen in the primary and secondary voltages of both the YNyn0 and YNd11 transformer bank arrangements. The distortion is relatable to the presence of certain harmonic orders in the current. In the YNyn0 transformer bank arrangement the primary and secondary voltages of the YNyn0 transformer arrangement are both distorted and display a similar trend with respect to their shape. In the YNd11 transformer bank arrangement the primary and secondary phase voltages are both distorted but have dissimilar wave shapes as a result of zero sequence third harmonic current circulating in the secondary delta connected windings.

The primary current waveforms of both the YNyn0 and YNd11 transformer banks differed vastly from their associated voltages. The primary current wave shapes are symptomatic of transformer half-wave saturation and differed from each other for the YNyn0 and YNd11 transformer banks. In half-wave saturation, signature wave shapes are seen to exist for the primary current of each of the three phase transformer bank connections tested.

At no load and with 1 A dc bias the harmonic column graphs of percentage of fundamental showed disproportionately large increases for harmonic orders from the 3rd harmonic up to the 10^{th}. This is associated with the saturation of the core joints of the test transformers. Disproportionate changes in the harmonic orders associated with the 5 A dc bias current injections are also noticed and this could be linked to interaction with the other transformers in the three phase bank.
It is seen that the motor load current harmonic profile resembles that of the transformer secondary voltage harmonic profile. This is due to the motor responding to its terminal voltage and it has not added any visible contribution to the harmonic distortion caused by the transformer half-cycle saturation.

The primary current THD method of determining distortion under transformer load conditions is not recommended since the addition of load to the transformer smooths out the THD peak associated with transformer joint saturation when non-step lap butt joints are used in the core construction.

The equivalent circuit of Figure 9.11 can be used to explain the effect of the load current that creates series voltage drops that reduces the ac induction in the core. This reduction in induction level reduces the degree of saturation of the transformer core which in turn reduces the distortion. The primary current TDD shows that the distortion is load dependent and it is envisaged that further reduction in distortion will occur at higher transformer loads.
When comparing the standalone single phase and three phase test results the following is seen:

- The current THD versus dc bias graphs at transformer no load condition is similar for both single phase and both three phase bank connections. The THD graphs have

two peaks associated with core joint and core bulk component saturation respectively,

- The column graphs of the current harmonic orders as a percentage of the fundamental primary current for the single phase and both three phase bank connections have disproportionate increases in harmonic orders at 1 A dc bias that is relatable to the test transformer core joints saturating in the current THD graphs,
- Harmonic column graphs of both voltage and current are dissimilar for the single phase and three phase bank test results. This indicates that there is an effect taking place between the test transformers in the three phase bank connections that does not occur for the single phase test,
- The primary voltage wave shape for the single phase test differs from those of the primary voltage wave shapes of the three phase bank connections. This indicates that the three phase bank connection effects the voltage wave shape in half-wave saturation, and
- The primary current wave shape of the single phase and three phase bank YNyn0 connection have a similar shape in half-wave saturation.

A preliminary test to determine the effect of the distortion caused by half-wave saturation of the YNyn0 three phase supply transformer bank on a motor load connected to its secondary terminals shows that there are discernable differences between the three sound recordings made. The distortion of the secondary voltage affects the motor's performance.

The FFT processed sound recordings shows that a maximum rms power value is reached at approximately 50 Hz intervals and could be related to the 50 Hz power frequency. The rms power values of the recording made at nominal ac supply voltage and no dc bias generally has the highest rms power values and is well defined. The maximum power for sound recordings made at different dc bias levels but a firm nominal ac supply voltage tend to occur at the same frequency while recordings made with a collapsing ac supply voltage appear to be phase shifted occurring at a slightly lower frequency than those made at nominal ac supply voltage. Simple human sensory observations of sound and vibration also confirmed the change in the motor's performance as the dc bias is increased.

Motors of different ratings and number of poles should be assessed for the effect of distortion caused by transformer half-wave saturation on their performance. A rotating machine equipped with internal temperature measurement devices embedded in its stator windings and vibration measurement devices attached to its casing is required for determining more fully the effects of the distorted voltage supply on the motor's performance.

9.6 Onward

The next chapter assesses the hypothesis and answers to the research questions posed in chapter 1.

Chapter 10

Conclusions

This chapter provides answers to the research questions posed in chapter 1 including an additional finding based on the research and assesses the hypothesis.

10.1 Research questions

- **How to derive an electrical equivalent circuit for a four limb core type single phase transformer that can be used to simulate the transformer response under low frequency transient conditions, namely dc and GIC?**

A thorough literature review is conducted that is useful for determining the important parameters required for a slow transient model for modelling the response of a transformer to GICs and dc. In section 2.1.5 the principle of duality is introduced and found to be widely used for developing electrical lumped parameter models. Where all the transformer magnetic and electrical component design data are available the electrical equivalent lumped parameter model for a single phase four limb transformer using the topological principle of duality is achievable.

When transformer design information is not available for lumped parameter models grey-box and black-box models are suggested in the literature in chapter 2.

A grey-box model is based on actual measurement data. Actual transformer parameter values are superior to estimated parameters since they represent the as-built status of the transformer that often differs from the theoretical design.

A lumped parameter electrical equivalent circuit is produced for the single phase four limb transformer in chapter 3 but due to problematic core joints, joint parameter determination is considered at best an approximation. The model is reduced to a duality derived pi equivalent circuit due to the inability to guarantee accurate joint parameter values and therefore model accuracy. Use is made of the electrical equivalent circuit symmetry to reduce it to a pi equivalent circuit.

The magnetic core and winding equivalent parameters values are determined using standard test circuits available in IEEE Std C57.12.91 [2011].

The ac winding resistances are determined using the combined series resistance determined in the short-circuit test and apportioned it to the respective windings according the ratio of their dc resistances.

The transformer deep saturation behavior is represented in the model by a piecewise saturation characteristic consisting of two slopes. The slopes represent the regions of transformer normal operation and deep saturation.

The transformer response in deep saturation is determined through a terminal saturation inductance test of the test transformers. This is requires a non-standard test circuit capable of providing a large dc bias with a small ripple. A new single phase test circuit is developed based on the three phase test circuit of De León *et al.* [2014]. Furthermore, the theory is tested for the first time on a single phase transformer with parallel connected winding assemblies.

Once the terminal saturation inductance is determined the characteristic slope for deep saturation is calculated. Using the slopes of the normal core operation and deep saturation regions, peak flux-current values are calculated for constructing the piecewise saturation characteristic for the grey-box model.

The grey-box model is assembled with the required parameter values and saturation characteristics and can be incorporated into EMTP software for simulation purposes.

- **Do the core joints constitute an important core modelling component for low frequency transient simulation or can they be ignored in the model?**

The literature review in chapter 2 shows that properly designed core joints should saturate after the bulk components, i.e. $B_c > B_{des}$, thus allowing the transformer to reach its design induction level [Ilo *et al.* 2000a; Ilo *et al.* 2000b]. B_c is the induction level at which the laminations adjacent to the joint air gaps saturate.

The NSL butt joints used in the construction of the SP-4L test transformers are proved to be in non-compliance with the requirement that $B_c > B_{des}$**.** The magnetization curves of all three test transformers show that the transformers are moving into non-linear operation at approximately 0.6 p.u. of their design voltage. The use of strategically placed twenty turn air search coils are instrumental in discovering that stray flux is leaking from the core joints. Theoretical calculations confirmed that the core joints are inadequate for the design specification. The test transformers are unable to reach their intended induction level due to early saturation of the IY and WL joints.

A duality derived topological model is developed that shows the complexity that joints can bring to an equivalent circuit. Core joints at dissimilar core locations have a different effective joint area due to the stacking of the core and need to be modelled with a different parameter value. These parameter values need to be determined for use in a model. Allowance will need to be made for the quality of the core stacking during manufacturing which introduces another variable that is at best an approximation. Visual evidence in the photographs included in chapter 5 show the variable quality of core joint stacking in the test transformers.

MSL mitred joints are shown by theoretically calculation to be superior to NSL butt joints with respect to the core cross-sectional area available in the joints. The use of properly designed MSL mitred joints, i.e. $B_c > B_{des}$, will remove the complexity that the joints bring to the model. Power transformers make use of MSL mitred joints therefore only bench

scale transformers utilizing MSL mitred joints where $B_c > B_{des}$ should be used for laboratory testing if they are to be more representative of full scale power transformers in GIC or dc studies.

Properly designed and constructed MSL mitred joints allow core joint detail to be ignored in low frequency transient simulation models.

- **Can flux search coils be used to map the flux response of a transformer?**

Extensive use of both single turn core and twenty turn air search coils is made to flux map the response of the test transformer's cores. Regularly spaced single turn search coils are strategically placed around the core and the response of the transformer core is mapped from normal operation into deep saturation. The twenty turn air search coils serve only as an indication of the source location of stray flux. Typically, these are the core joints and the mid-point of the wound and return limbs.

Firstly, the flux distribution at the T-joint assembles is determined. Single turn core search coils are carefully wrapped around the core to overlap each core joint at the respective T–joint assembly locations. The flux distribution at the T-joint assemblies is determined using only ac energisation and trending the output data from the search coils on graphs. The graphs show that the flux distribution is not linear but varies with the flux density. The reluctance of the core paths are therefore continually changing according to the induction level of the transformer.

Next, the individual core sections are flux mapped. Based on the geometric symmetry of the core only certain sections of the core need to be flux mapped. These are half of a wound limb spanning the winding length, half of an interconnecting yoke and return limb paths. These are successfully mapped with nominal ac induction with dc bias. The search coil outputs are trended on graphs that show the complex nature of the core response as it is driven into saturation. The NSL butt joints contribute to this response as stray flux leaves and re-enters the core in the vicinity of the joints. Some stray flux leaving the wound limb during saturation is found to be linking with the mid-point region of the return limb.

Search coils are determined to be a useful means of flux mapping a transformer core when there is access to the core structure to install the search coils. These results are useful for validating FEM studies as demonstrated by Chisepo *et al.*[2016].

- **What distortion is created when a four limb core type single phase transformer saturates?**

Wave shapes, THD and FFT are used to analyse the distortion caused when the SP-4L transformer half-wave saturates.

The primary current wave shape is severely distorted and asymmetrical in shape. Large current pulses occur in the half-cycle that coincides with the direction of the dc bias polarity and is flat bottomed in the other half-cycle. The wave oscillates around the

average current value, i.e. the dc bias magnitude. The primary and secondary voltages suffer distortion that can be explained as the result of voltage-drops in the transformer equivalent circuit series elements caused by the large 2nd harmonic order in the badly distorted primary current in half-wave saturation. Both the primary and secondary voltage wave shapes have a similar distorted shape with the distortion occurring mainly at the zero point crossing for the trailing and leading portions of the positive and negative half-cycles respectively.

The plot of THD of the primary current with increasing dc bias showed two peaks. The THD rose to its first peak at 1 A dc bias or 300 A.t dc which is confirmed by air search coil measurements to represent the saturation of the core joints. As the dc bias is increased the THD then declined and rose to a second peak which is of a longer duration. The second peak occurred at approximately 8 A dc or 2400 A.t dc and represents the saturation of the bulk core components. Beyond 8 A dc the THD declined steadily. The two peaks occurred at THD values of approximately 48 and 57 % respectively.

The THD plot of the secondary current shows a small increase over the entire dc bias range of approximately 10%. This is an indication that the current limiting inductor in the secondary circuit is not saturating in the presence of the dc bias.

The primary and secondary voltages are moderately distorted. This is confirmed by voltage THD trends with increasing dc bias for both the primary and secondary voltages which showed maximum THD values of 19 and 23 % respectively. These maximum values occurred at the highest dc level of 9 A dc or 2700 A.t dc.

The current harmonic orders are plotted as a function of increasing dc bias. Two independent plots are done firstly with harmonic rms current magnitude and then harmonic orders as a percentage of the fundamental. The overall trend is for all harmonics to increase initially with increasing dc. However, when plotting the harmonic orders as a percentage of the fundamental it is noticed that at 1 A dc bias the 3rd harmonic increases disproportionately with larger than expected percentage increases of the 4th, 5th and 8th harmonics. The 1 A dc bias is associated with the first peak of the THD plot which coincides with the saturation of the core joints.

The primary current wave is asymmetrical with both odd and even harmonic orders present.

- **Does the dc bias applied to a three phase bank of single phase transformers split equally between the phases?**

The three phase testing shows that despite attempts to keep all cables of equal length and ensure firm contact pressure at terminations the distribution of the dc current from the neutral into each phase is not equal. With a YNyn0 transformer bank configuration at a transformer load of approximately 6 A_{rms} or 15 % of its rating, the 101 A dc in the neutral conductor splits such that the difference between the phase with the highest and

the phase with the lowest dc is 5.6 A dc. Similar differences are noticed at other loading scenarios. Considering the small scale test circuit and limited number of components used in the test circuit it is possible that in a full scale power system, GICs and dc are unlikely to be the same in each phase of the power installation. There are numerous series components in a power circuit which do not all have equal electrical resistance per phase. Despite the best practice with transposing conductors there will most likely still be a mismatch in resistance between phases.

Studies on three phase transformers should therefore consider the strong possibility of an imbalance of dc per phase. Three phase three limb transformers considered immune to GIC and dc should be reconsidered with emphasis on the degree of dc imbalance that can be tolerated. The imbalance could well lead to similar effects as experienced by transformers with core configurations that support the flow of zero sequence flux.

- **Is the distortion different when the three phase bank of single phase transformers saturates in either a YNyn or YNd configuration?**

Some distortion is seen in the primary and secondary voltages of both the YNyn0 and YNd11 transformer bank arrangements. The distortion is relatable to the presence of certain harmonic orders in the current. In the YNyn0 transformer bank arrangement the primary and secondary voltages of the YNyn0 transformer arrangement are both distorted and display a similar trend with respect to their shape. In the YNd11 transformer bank arrangement the primary and secondary phase voltages are both distorted but have dissimilar wave shapes as a result of zero sequence third harmonic current circulating in the secondary delta connected windings.

The primary current waveforms of both the YNyn0 and YNd11 transformer banks differed vastly from their associated voltages. The primary current wave shapes are symptomatic of transformer half-wave saturation and differed from each other for the YNyn0 and YNd11 transformer banks. In half-wave saturation, unique signature wave shapes are seen to exist for the primary current of each of the three phase transformer bank connections tested. The wave shapes differed mainly in their unsaturated half-cycles.

The harmonic orders of primary current of the two three phase configurations differ mainly because of the absence of triplen harmonics in the YNd11 bank current as these only started to appear at high dc bias levels above 20 A per phase. For both connection configurations the second harmonic is the dominant harmonic in the primary current.
The first ten voltage harmonic orders of the primary voltage for both connection types are very similar with respect to the occurrence of harmonic orders and their variation with dc bias indicating that the primary voltages are almost independent of the secondary connection type.

- **Does the addition of a load to a three phase bank of single phase transformers reduce the distortion created when dc enters the system assuming a stiff supply?**

A YNyn0 three phase bank of transformers is evaluated for four load scenarios, i.e. transformer at no load (open-circuit), and motor at no load, partial and full load. THD and TDD are considered for the distortion comparison but only TDD is found acceptable since it normalizes the distortion to the transformer rated current in all instances making for a more meaningful comparison. THD exaggerates the change in distortion since each computation uses a different fundamental current that is based on the new load scenario.

The TDD plot with varying dc showed that the load reduces the distortion. This is explained using the transformer equivalent circuit where the load current causes voltage-drops across the series impedances of the transformer equivalent circuit thus reducing the voltage across the magnetizing branches and therefore the core induction level. This leads to a lower level of core saturation and a change in transformer inductance that affects the asymmetrical primary current wave shape.

As the load on the secondary of the YNyn0 three phase bank is increased the THD method of determining distortion becomes less useful since the first peak of the THD versus dc graph becomes negligible and may eventually completely disappear. However, at no load or small loads the THD versus dc graph plot is useful in identifying whether the core joints are problematic.

- **Does the distortion caused by half-cycle saturation in a three phase bank of single phase transformers contain signals that are harmful to motors?**

The investigation with the motor was not planned initially and is only a preliminary test, given that the three-phase test transformer set up is available. The sound recording device, the scope of the measurements made on one motor, and the lack of temperature and other measurements are all obvious limitations of the test. The intension behind the test is to find discernible differences between the three sound recordings indicating that the harmonics caused by the dc bias in the supply transformer three has bank effects the motors performance.

The YNyn0 three phase transformer bank is used in the assessment since it provides the highest secondary terminal voltage. Three test scenarios are evaluated using fast Fourier transforms of motor sound recordings. The analysis shows that in the frequency domain differences exist between the three sound recordings.

The FFT of the sound recordings shows that a maximum rms power value is reached at approximately 50 Hz intervals that could be related to the 50 Hz power frequency.

The first recording is conducted with the supply transformer bank at its nominal ac supply voltage. These FFT rms power values are generally the highest and are well defined.

The second recording is conducted with dc bias introduced into the windings of the supply transformer bank and the supply voltage is allowed to collapse. The FFT maximum rms

power values appear to be phase shifted occurring at a slightly lower frequency than those made at nominal ac supply voltage and is not well defined with some slightly smaller rms power values occurring at frequencies around the dominant frequency.

The third recording is conducted with a firm nominal voltage supply to the transformer bank and dc bias in its primary windings. FFT maximum rms power values tend to occur at the same frequency as the first recording but are smaller and less defined with numerous slightly smaller rms powers occurring at frequencies around the dominant frequency.

Human sensory observations of sound and vibration also confirm the change in the motor's performance as the dc bias to the supply transformer bank is increased.

It is clear that introducing dc into the supply transformers does initiate a motor response slightly different from the harmonic generation in the transformers. The results of the test are consistent with the behavior that would be expected according to the equivalent model of the transformer that has been developed. Complete testing of motors and generators has not been carried out. The application of the new model to simulations and the testing of rotating machines using the types of circuits used in this research should allow other important questions about equipment performance to be studied.

Substantial further work is needed to compare the effects on power station machines of dc in SP-4L transformers with the effects when different transformers are used. Motors of different ratings and number of poles should be assessed for the effect of distortion caused by transformer half-wave saturation on their performance. Rotating machines equipped with internal temperature measurement devices embedded in their stator windings and vibration measurement devices attached to their casings is required for determining more fully the effects of the distorted voltage supply on the motor's performance.

- **Additional finding - Utilisation factor.**

As a result of the difficulties experienced with the NSL butt type joints, i.e. early transformer saturation, a method of determining the effectiveness of the stacking of core joints is developed. The method uses air search coils to determine the ac voltage, V_c, at which the joints at specific core locations start to saturate. These voltages are unique to the relevant joints that are problematic. Graphs are prepared from data recorded for single turn core search coils that are strategically placed at the relevant core joint locations with increasing ac excitation. The average V_c for each problematic joint location is then used to determine the average output voltage of the corresponding core search coils. The transformer EMF equation is used to determine the peak flux associated with the search coil location which provides the peak flux through the joint. Using the saturation flux density of the core material as specified by the supplier the effective core area is determined. The ratio of the empirically determined effective core area to theoretically calculated core area is termed the joint utilisation factor, U, for that joint type at the specific core location.

The results of this method when applied to the IY joints correlated with the results of an independent test to determine the ac rms voltage at which the test transformers saturated. The method is then applied to the WL and RL-1 joints which are also found to saturate prematurely.

In the absence of transformer manufacturer design information this joint utilisation factor can be used in other transformer models especially when premature joint saturation is suspected.

10.2 Assessing the hypothesis

The hypothesis in chapter 1 states:

A slow transient equivalent model of a single phase four limb transformer can be derived using the principle of duality that can be used to study its response to slow transient phenomena such as geomagnetically induced currents and dc.

Slow transient phenomena such as transformer half-wave saturation require appropriate models with parameters that represent the transformer transient state aptly. In chapter 2 the appropriate parameters for the model are identified. In chapter 3 a novel duality derived reversible model is developed of a single phase four limb transformer. The test transformers' non-step lap butt type core joints are shown to be problematic and the model is developed further to include the core joints. Due to the irregular core stacking method joint parameter determination is at best an approximation and the model is reduced to a duality compliant pi equivalent model for accuracy reasons. In chapter 6 the necessary tests required to determine the appropriate model parameters are specified and in chapter 8 the pi model parameters and saturation characteristics are determined through laboratory testing and a complete pi model is presented.

The results of the investigation of the research questions indicate that the hypothesis as posed is indeed valid and the slow transient equivalent model is suitable for application to studies of the behaviour of these transformers in the presence of GICs and dc components.

References

Abdulsalam, S.G., Xu, W., Neves, W.L.A. & Liu, X., 2006. Estimation of Transformer Saturation Characteristics From Inrush Current Waveforms. *IEEE TRANSACTIONS ON POWER DELIVERY*, 21(1), pp.170–177.

Abu-Nasser, A.I., 1981. *Transformer Inrush in Traction and HVDC-Schemes, Doctor of Philosophy Thesis, University of Manchester*.

Albertson, V.D., Thorson, J.M., Clayton, R.E. & Tripathy, S.C., 1972. Solar-Induced-Currents In Power Systems: Cause and Effects. *IEEE Power Engineering Society Summer Meeting*, pp.471–477.

Alvarez-Marino, C., de León, F. & López-Fernández, X.M., 2012. Equivalent Circuit for the Leakage Inductance of Multiwinding Transformers : Unification of Terminal and Duality Models. *IEEE TRANSACTIONS ON POWER DELIVERY*, 27(1), pp.353–361.

Arrillaga, J., Enright, W., Watson, N.R. & Wood, A.R., 1997. Improved simulation of HVDC converter transformers in electromagnetic transient programs. *Proc. Inst. Elect. Eng., Gen. Transm. Distrib.*, 144, pp.100–106.

Arturi, C.M., 1991. Transient Simulation and Analysis of a Three-Phase Five-Limb Step-Up transformer Following an Out-of-Phase Synchronisation. *IEEE Transactions on Power Delivery*, 6(1), pp.196–207.

Bachinger, F., Hackl, A., Hamberger, P., Leikermoser, A., Leber, G., et al., 2013. Direct current in transformers: effects and compensation. *Cigre 2012, Elektrotechnik & Informationstechnik*.

Berge, J., 2011. *Impact of Geomagnetically Induced Currents on Power Transformers, Doctor of Philosophy Thesis, The University of Western Ontario*.

Berge, J., Varma, R.K. & Marti, L., 2011. Laboratory validation of the relationship between Geomagnetically Induced Current (GIC) and transformer absorbed reactive power. In *IEEE Electrical Power and Energy Conference*. Ieee, pp. 491–495.

Bharat Heavy Electricals Limited, 2003. *Transformers, Second Edition*, Tata McGraw-Hill.

Blume, L.F., Boyajian, A., Camilli, G., Lennox, T.C., Minneci, S., et al., 1967. *Transformer Engineering - A Treatise on the Theory, Operation, and Application of Transformers*,

Bolduc, L., Gaudreau, a & Dutil, a, 2000. Saturation time of transformers under dc excitation. *Electric Power Systems Research*, 56(2), pp.95–102. Available at: http://linkinghub.elsevier.com/retrieve/pii/S0378779600000870.

Borrill, L.D., Chisepo, H.K. & Gaunt, C.T., 2017. Determining the Terminal Saturation Inductance of a Single Phase Four Limb Transformer. In *South African Universities Power Engineering Conference*.

Borrill, L.D., Chisepo, H.K. & Gaunt, C.T., 2016. Flux measurements with ac and dc components of current present show transformer equivalent circuit models need core joint details. In *IEEE International Conference on Power System Technology (POWERCON)*. pp. 1–6.

Boteler, D.H., 2003. Geomagnetic Hazards to Conducting Networks. *Natural Hazards*, 28,

pp.537–561.

Brandwajn, V., Dommel, H.W. & Dommel, I.I., 1982. Matrix Representation of Three-Phase N-Winding Transformers for Steady-State and Transient Studies. *IEEE Transactions on Power Apparatus and Systems*, PAS-101(6).

Chen, X. & Venkata, S.S., 1997. A three-phase three-winding core-type transformer model for low-frequency transient studies. *IEEE Transactions on Power Delivery*, 12(2), pp.775–782.

Cherry, E., 1949. The Duality between Interlinked Electric and Magnetic Circuits and the Formation of Transformer Equivalent Circuits. In *Proc. Phys. Soc*. pp. 101–111.

Chiesa, N., 2010. *N. Chiesa, Power Transformer Modeling for Inrush Current Calculation, Ph.D. dissertation, Norwegian University of Science and Technology, 2010.*,

Chisepo, H.K., 2014. *The Response of Transformers to Geomagnetically Induced Currents, MSc Dissertation, Dept. Elec. Eng., Univ. Cape Town, South Africa*.

Chisepo, H.K., Borrill, L.D. & Gaunt, C.T., 2016. Measurements and finite element model of transformer core joints with dc and ac excitation. In *Advanced Research Workshop on Transformers 2016*. pp. 306–311.

Cho, S.D., 2002. *Parameter estimation for transformer modeling, Doctor of Philosophy Thesis, Michigan Technological University*.

Cigré, 2000. *Cigré Working Group 02 (SC), Guidelines for Representation of Network Elements when Calculating Transients*, Cigré Technical Brochure no. 39, 1990.

de León, F. & Semlyen, A., 1994. Complete Transformer Model for Electromagnetic Transients. *IEEE Transactions on Power Delivery*, 9(1).

de León, F. & Semlyen, A., 1995. A simple representation of dynamic hysteresis losses in power transformers. *IEEE Transactions on Power Delivery*, 10(1), pp.315–321.

de León, F., Farazmand, A. & Joseph, P., 2012. Comparing the T and Pi Equivalent Circuits for the Calculation of Transformer Inrush Currents. *IEEE TRANSACTIONS ON POWER DELIVERY*, 27(4), pp.2390–2398.

Del Vecchio, R.M., 2008. Multiterminal three phase transformer model with balanced or unbalanced loading. *IEEE Transactions on Power Delivery*, 23(3), pp.1439–1447.

Del Vecchio, R., Poulin, B., Feghali, P., Shah, D. & Ahuja, R., 2010. *Transformer Design Principles*, Available at: http://www.crcnetbase.com/doi/book/10.1201/EBK1439805824.

de León, F., Jazebi, S. & Farazmand, A., 2014. Accurate Measurement of the Air-Core Inductance of Iron-Core Transformers With a Non-Ideal Low-Power Rectifier. *IEEE Transactions on Power Delivery*, 29(1), pp.294–296.

Dick, E.P. & Watson, W., 1981. Transformer Models for Transient Studies Based on Field Measurements. *IEEE Transactions on Power Apparatus and Systems,*, PAS-100(1), pp.409–419.

Dommel, H.W., Yan, A. & Wei, S., 1986. Harmonics from Transformer Saturation. *IEEE Transactions on Power Systems,*, PWRD-1(2), pp.209–215.

Du, Y., Cheng, Z., Zhao, Z., Fan, Y., Liu, L., et al., 2010. Magnetic flux and iron loss modeling at laminated core joints in power transformers. *IEEE Transactions on Applied Superconductivity*, 20(3), pp.1878–1882.

EPRI, 2006. *Mitigation of Geomagnetically Induced Currents in Transformers, EPRI Report 1012352, Electric Power Research Institute, Palo Alto, California, USA*,

EPRI, 2009. *EPRI Transformer Guidebook Development, The Copper Book, EPRI Report 1017734, Electric Power Research Institute, Palo Alto, California, USA*,

EPRI, 2012. *Literature Survey on Transformer Models for the Simulation of Electromagnetic Transients with Emphasis on Geomagnetic-Induced Current (GIC) Applications, EPRI Report 1025844, Electric Power Research Institute, Palo Alto, California, USA*,

EPRI, 2013. Electromagnetic Transient-Type Transformer Models for Geomagnetically-Induced Current (GIC) Studies, EPRI Report 3002000832, 2013,

Gaudreau, A., Picher, P., Bolduc, L. & Coutu, A., 2002. No-Load Losses in Transformer Under Overexcitation / Inrush-Current Conditions : Tests and a New Model. *IEEE Transactions On Power Delivery*, 17(4), pp.1009–1017.

Girgis, R.S. & Nevins, R.J., 1992. Analysis of Observed Geomagnetically-Induced Current Effects on Transformers. In *EPRI Geomagnetically Induced Currents Conference, EPRI TR-100450*. p. 7.1-7.10.

Girgis, R. & Vedante, K., 2012. Effects of GIC on Power Transformers and Power Systems. *IEEE Transactions On Power Delivery*, pp.1–8.

Gish, W.B., Feero, W.E. & Rockefeller, G.D., 1994. Rotor Heating Effects From Geomagnetic Induced Currents. *IEEE Transactions on Power Delivery*, 9(2), pp.712–719.

Gustavsen, B. & Portillo, A., 2014. Interfacing k-Factor Based White-Box Transformer Models with Electromagnetic Transients Programs. *IEEE Transactions on Power Delivery,*, 29(6), pp.2534–2542.

Harder, E., 1930. Effect of Direct Current in Transformer Windings. *The Electric Journal*, 27(10), pp.601–607.

Heathcote, M.J., 1998. *J & P Transformer Book* 12th Ed., Newnes, ISBN 07506 1158 8.

Høidalen, H.K., Chiesa, N., Avendaño, A. & Mork, B. a, 2011. Developments in the hybrid transformer model – Core modeling and optimization. *International Conference on Power Systems Transients (IPST 2011)*, (2), pp.1–6.

Holmberg, P., Leijon, M. & Wass, T., 2003. A Wideband Lumped Circuit Model of Eddy Current Losses in a Coil with a Coaxial Insulation System and a Stranded Conductor. *IEEE Transactions on Power Delivery*, 18(1), pp.50–60. Available at: http://ieeexplore.ieee.org/lpdocs/epic03/wrapper.htm?arnumber=1159896.

IEEE, 1993. IEEE Transmission and Distribution Committee Working Group On Geomagnetic Disturbances and Power System Effects, Geomagnetic Disturbance Effects on Power Systems. *IEEE Transactions on Power Delivery*, 8(3), pp.1206–1216.

IEEE Std C57.12.91, 2001. *IEEE Standard Test Code for Dry-Type Distribution and Power Transformers*,

IEEE Std C57.12.91, 2011. *IEEE Standard Test Code for Dry-Type Distribution and Power Transformers*,

IEEE, 2013. IEEE Power & Energy Society Technical Council Task Force on Geomagnetic Disturbances. *IEEE power & energy magazine*, (august), pp.71–78.

Ilo, A., Pfützner, H. & Nakata, T., 2000a. Behaviour of Transformer Cores with Multi-Step-Lap Joints. In *ICEM 2000, Espoo Finland*. pp. 252–256.

Ilo, A., Pfützner, H. & Nakata, T., 2000b. Critical induction - a key quantity for the optimisation of transformer core operation. *Journal of Magnetism and Magnetic Materials*, 215, pp.637–640.

Iravani, M.R., Chaudhary, A.K.S., Giesbrecht, W.J., Hassan, I.E., Keri, A.J.F., et al., 2000. Modeling and Analysis Guidelines for Slow Transients — Part III : The Study of Ferroresonance, Slow Transients Task Force of the IEEE Working Group on Modeling and Analysis of Systems Transients Using Digital Programs. *IEEE Transactions on Power Delivery*, 15(1), pp.255–265.

Jazebi, S., Farazmand, A., Murali, B.P. & De León, F., 2013. A comparative study on Pi and T Equivalent Models for the Analysis of Transformer Ferroresonance. *IEEE Transactions on Power Delivery*, 28(1), pp.526–528.

Jazebi, S., de León, F., Farazmand, A. & Deswal, D., 2013. Dual Reversible Transformer Model for the Calculation of Low-Frequency Transients. *IEEE Transactions on Power Delivery*, 28(4), pp.2509–2517.

Jazebi, S., de León, F. & Vahidi, B., 2013. Duality-Synthesized Circuit for Eddy Current Effects in Transformer Windings. *IEEE Transactions on Power Delivery*, 28(2), pp.1063–1072.

Jazebi, S. & de León, F., 2015a. Duality-Based Transformer Model Including Eddy Current Effects in the Windings. *IEEE Transactions on Power Delivery*, 30(5), pp.1–9. Available at: http://ieeexplore.ieee.org/lpdocs/epic03/wrapper.htm?arnumber=7097070.

Jazebi, S. & de León, F., 2015b. Experimentally Validated Reversible Single-Phase Multiwinding Transformer Model for the Accurate Calculation of Low-Frequency Transients. , 30(1), pp.193–201.

Jazebi, S., Zirka, S.E., Lambert, M., Chiesa, N., Moroz, Y., et al., 2016a. Duality Derived Transformer Models for Low- Frequency Electromagnetic Transients – Part I : Topological Models. *IEEE Transactions on Power Delivery,*, pp.1–10.

Jazebi, S., Zirka, S.E., Lambert, M., Chiesa, N., Moroz, Y., et al., 2016b. Duality Derived Transformer Models for Low- Frequency Electromagnetic Transients – Part II : Complementary Modeling Guidelines. *IEEE Transactions on Power Delivery,*, PP(99), pp.1–10.

Jones, M.A., Moses, A.J. & Thompson, J.E., 1973. Flux Distribution and Power Loss in the Mitered Overlap Joint in Power Transformer Cores. *IEEE Transactions on Magnetics*, MAG-9(2), pp.114–122.

Khan, A.H., 1991. Characteristics of transformer exciting-current during geomagnetic disturbances - Power Delivery, IEEE Transactions on. , 6(4), pp.1707–1714.

Kiehne, H.A., 2003. *Battery Technology Handbook* Second., Marcel Dekker Inc. Available at: https://books.google.com/books?id=1HSsx9fPAKkC&pgis=1.

Konstantin-Hansen, H., Wismer, J., Thrane, N. & Gade, S., 1994. Application Note- Choose Your Units! , pp.1–6.

Krah, J.H., 2005. Optimum discretization of a physical cauer circuit. *IEEE Tansactions on Magnetics*, 41(5), pp.1444–1447. Available at: http://cat.inist.fr/?aModele=afficheN&cpsidt=16840183 [Accessed October 12, 2015].

Kulkarni, S. V & Khaparde, S.A., 2004. *Transformer Engineering - Design and Practice*, Marcel Dekker Inc.

Lahtinen, M. & Elovaara, J., 2002. GIC Occurrences and GIC Test for 400 kV System Transformer. *IEEE TRANSACTIONS ON POWER DELIVERY*, 17(2), pp.555–561.

Li, H., Cui, X., Lu, T., Cheng, Z. & Liu, D., 2010. An Improved Magnetic Circuit Model of Power Transformers under DC Bias Excitation. In *2010 Asia-Pacific International Symposium on Electromagnetic Compatibility*. pp. 806–809.

Loffler, F., Booth, T., Pfützner, H., Bengtsson, C. & Gramm, K., 1995. Relevance of Step-Lap Joints for Magnetic Characteristics of Transformer Cores. *IEE Proc.-Electr. Power Appl*, 142(6), pp.371–378.

Lu, S., Liu, Y. & De La Ree, J., 1993. Harmonics Generated from a DC Biased Transformer. *IEEE Transactions on Power Delivery*, 8(2), pp.725–731.

Manitoba HVDC Research Centre, 2010. *User's Guide, EMTDC Transient Analysis for PSCAD Power System Simulation, version 4.7 February 2010*,

Marti, L., Rezaei-Zare, A. & Narang, A., 2013. Simulation of Transformer Hotspot Heating due to Geomagnetically Induced Currents. *IEEE Transactions On Power Delivery*, 28(1), pp.320–327.

Martinez-Velasco, J.A., 2010. Power System Transients: Parameter Determination. In CRC Press, Taylor & Francis Group, pp. 177–249.

Martinez-Velasco, J.A. & Mork, B.A., 2003. Transformer Modeling for Low Frequency Transients - The State of the Art. In *International Conference on Power Systems Transients – IPST 2003 in New Orleans, USA*. pp. 1–6.

Martinez, J.A., 2010. *Power System Transients, Parameter Determination, Chapter 4, Transformer Modelling*, CRC Press, Taylor & Francis Group.

Martinez, J.A. & Mork, B.A., 2005. Transformer Modeling for Low- and Mid-Frequency Transients - a Review. *IEEE Transactions on Power Delivery*, 20(2), pp.1625–1632.

Martinez, J.A., Walling, R., Mork, B.A. & Durbak, D., 2005. Parameter Determination for Modeling System Transients — Part III : Transformers. *IEEE Transactions on Power Delivery,*, 20(3), pp.2051–2062.

Masoum, M.A.S. & Moses, P.S., 2008. Influence of Geomagnetically Induced Currents on Three-Phase Power Transformers. In *Australasian Universities Power Engineering Conference (AUPEC'08)*. pp. 1–5.

McLyman, W.T., 2004. *Transformer and Inductor Design Handbook* third., Marcel Dekker,

Inc.

Mechler, G.F. & Girgis, R.S., 2000. Magnetic Flux Distributions in Transformer Core Joints. *IEEE Transactions on Power Delivery*, 15(1), pp.198–203.

MIT, 1965. *Principles of Electrical Engineering Series - Magnetic Circuits and Transformers*, The M.I.T. Press.

Molinski, T.S., 1996. Geomagnetically induced currents: - Causes, Effect, and Mitigation. *IEEE Canadian Review*, (25), p.11 to 14.

Molinski, T.S., 2002. Why utilities respect geomagnetically induced currents. *Journal of Atmospheric and Solar-Terrestrial Physics*, 64(16), pp.1765–1778.

Mork, B.A., 1992. *Ferroresonance and Chaos: Observation and Simulation of Ferroresonance in a Five-Legged Core Distribution Transformer, PhD thesis, North Dakota State University of Agriculture and Applied Science*.

Mork, B.A., Gonzalez, F. & Ishchenko, D., 2004. *Parameter estimation and advancements in transformer models for EMTP simulations. Task MTU-7: Model performance and sensitivity analysis*,

Mork, B.A., Gonzalez, F., Ishchenko, D., Stuehm, D.L. & Mitra, J., 2007. Hybrid Transformer Model for Transient Simulation — Part I : Development and Parameters. *IEEE TRANSACTIONS ON POWER DELIVERY*, 22(1), pp.248–255.

Mousavi, S.A., 2012. *Electromagnetic Modelling of Power Transformers with DC Magnetization - Licentiate Thesis - Royal Institute of Technology (KTH)*.

Mousavi, S.A., Carrander, C. & Engdahl, G., 2013. Electromagnetic transients due to interaction between power transformers and network during a GIC attack. *Cigré ETH Zurich A2 & C4*, PS1, pp.1–12.

Nakata, T., Takahashi, N. & Kawase, Y., 1982. Magnetic Performance of Step-Lap Joints in Distribution Transformer Cores. *IEEE Transactions on Magnetics*, 18(6), pp.1055–1057.

Nakata, T. & Takahashi, N., 1985. Finite element analysis of magnetic fields taking into account hysteresis characteristics. *IEEE Transactions On Magnetics*, MAG-21(5), pp.1856–1858.

Nakata, T. & Kawase, Y., 1986. Analysis of Magnetic Characteristics of Laminated Cores for Establishing an Accuracy Standard of Joint Dimension. *Electrical Engineering in Japan*, 106(1), pp.48–56.

Narang, A. & Brierley, R.H., 1994. Topology Based Magnetic Model For Steady-State and Transient Studies for Three-Phase Core Type Transformers. *IEEE Transactions on Power System*, 9(3), pp.1337–1349.

Ngnegueu, T., Marketos, F., Devaux, F., Baldauf, J., Oliveira, J., et al., 2012. Behaviour of transformers under DC / GIC excitation : Phenomenon , Impact on design / design evaluation process and Modelling aspects in support of Design. *Cigre 2012 Paris*, A2-303, p.1 to 10.

NRC, U.S., 2014. www.nrc.gov. *Part 50*.

Picher, P., Bolduc, L. & Olivier, G., 1997. Acceptable Direct Current in Three-Phase Power Transformers: Comparative Analysis. *CCECE '97. Canadian Conference on Electrical and Computer Engineering. Engineering Innovation: Voyage of Discovery. Conference Proceedings*, 1(4), pp.157–160.

Price, P.R., 2002. Geomagnetically Induced Current Effects on Transformers. *IEEE Transactions on Power Delivery*, 17(4), pp.1002–1008.

Rezaei-Zare, A. & Marti, L., 2013. Generator Thermal Stress during a Geomagnetic Disturbance. *Power and Energy Society General Meeting (PES)*, pp.1–5.

Rezaei-zare, A., 2014. Behavior of Single-Phase Transformers Under Geomagnetically Induced Current Conditions. *IEEE Transactions on Power Delivery*, 29(2), pp.916–925.

Rezaei-Zare, A., 2015a. Enhanced Transformer Model for Low- and Mid-Frequency Transients — Part I : Model Development. *IEEE Transactions on Power*, 30(1), pp.307–315.

Rezaei-Zare, A., 2015b. Enhanced Transformer Model for Low- and Mid-Frequency Transients — Part II : Validation and Simulation Results. *IEEE Transactions on Power Delivery*, 30(1), pp.316–325.

Say, M.G., 1978. *Alternating Current Machines, Pitman Publishing Limited*,

Sen, P.C., 1997. Principles of Electrical Machines & Power Electronics. , pp.1–615.

Slemon, G.R., 1953. Equivalent circuits for transformers and machines including non-linear effects. *Proceedings of the IEEE - Part IV: Institution Monographs*, 100(5), pp.129–143.

Slemon, G.R., 1992. *Electric Machines and Drives*, Addison-Wesley Publishing Company.

Smith, P.M., 2014. Simulated GIC Tests on Laboratory Transformers. In *GIC workshop, University of Cape Town, Session 3*.

Snelling, E.C., 1969. *Soft Ferrites - Properties and Applications*, Loindon Iliffe Books Ltd.

Stumberger, G., Polajzer, B., Stumberger, B., Toman, M. & Dolinar, D., 2005. Evaluation of Experimental Methods for Determining the Magnetically Nonlinear Characteristics of Electromagnetic Devices. *IEEE Transactions on Magnetics*, 41(10), pp.4030–4032.

Sui, F. & Rezaei-Zare, A., 2013. A Method to Assess GIC Impact on Zero Sequence Overcurrent Protection of Transmission Lines. , pp.1–5.

Takasu, N., Oshi, T., Miyawaki, F., Sadamu, S. & Fujiwara, Y., 1994. An Experimental Analysis of DC Excitation of Transformers by Geomagnetically Induced Currents. *IEEE Transactions on Power Delivery*, 9(2), pp.1173–1182.

Tarasiewicz, E.J., Morched, A.S., Narang, A. & Dick, E.P., 1993. Frequency Dependant Eddy Current Models for Nonlinear Iron Cores. *IEEE Transactions on Power Systems*, 8(2), pp.588–597.

Taylor, J., 2000. *The Vibration Analysis Handbook* First edit., Vibration Consultants, Incorporated.

TeNyenhuis, E.G., Mechler, G.F. & Girgis, R., 2000. Flux Distribution and Core Loss Calculation for Single Phase and Five Limb Three Phase Transformer Core Designs.

IEEE Transactions on Power Delivery, 15(1), pp.204–209.

U.S. DEPT ENERGY, 2012. *Office of Electricity Delivery and Energy Reliability U.S. Department of Energy: Large Power Transformers and the U.S. Electric GridInfrastructure Security and Energy Restoration*,

Walling, R.A. & Khan, A.H., 1991. Characteristics of transformer exciting-current during geomagnetic disturbances. *IEEE Transactions on Power Delivery*, 6(4), pp.1707–1714.

Wang, J., Witulski, A.F., Vollin, J.L., Phelps, T.K. & Cardwell, G.I., 1999. Derivation, Calculation and Measurement of Parameters for a Multi-Winding Transformer Electrical Model. *IEEE*, pp.220–226.

Wilson, P.R., 2001. *Modeling and Simulation of Magnetic Components in Electric Circuits, Doctor of Philosophy Thesis, University of Southampton*.

Zirka, S.E., Moroz, Y.I., Arturi, C.M., Chiesa, N. & Hoidalen, H.K., 2012. Topology-Correct Reversible Transformer Model. *IEEE Transactions on Power Delivery*, 27(4), pp.2037–2045.

Appendix A

Selection of a suitable test circuit and components for simultaneous ac and dc components of current in a single phase test transformer windings.

A.1 Selection of the test circuit and circuit components

The test circuits 1, 2, and 3 illustrated in figures A.1 and A.2 are designed to fit as closely as possibly the requirements of the test given in table A.1 and also to overcome the stated constraints. The table provides a process of coming to a decision on the best suited test circuit using the scoring system highlighted in the table.

Although not shown in all three of the test circuits in Figures A.1 and A.2, a robust switch capable of safely interrupting the back EMF in the dc circuits is required.

The capacitors in test circuits 1 and 2, dependent to their location in the circuit serve to either provide a path for the ac to bypass the dc source or to prevent the dc from entering the three phase source transformers.

The inductor in the test circuit 3 is necessary to protect the battery bank from the ac in the circuit while still simulating as closely as possible a no load condition. The ac component of current on the dc test circuit side of the test transformer should not exceed the requirement of a maximum ripple of 5A per 100Ah of nominal battery capacity [Kiehne 2003]. Excessive ripple can cause battery heating and gassing resulting in reduced life and possible safety concerns should the battery rupture under high dc load current in addition to excessive ac ripple.
To limit the ac in the dc circuit to a low level the inductor should have a high inductance. The ac voltage at the terminals of the series connected 150 turn windings will be,

$$2(\mathrm{V_{nom\ 80t}} \times \text{turns ratio}) = 2 \times (110 \times 1.875) = 412.5\mathrm{V_{rms}}.$$

A conservative approach is taken by ignoring the other impedances in the dc circuit and limiting the ac to a maximum of 1 Arms. The impedance of the inductor, X_L, required should therefore not be less than,

$$\mathrm{X_L} = \frac{\mathrm{V}}{\mathrm{I}} = \frac{412.5}{1} = 412.5\Omega$$

The inductance, L, therefore needs to be a minimum of,

$$L = \frac{X_L}{2\pi f} = 1.313H$$

Table A1. Evaluation table for determining the most suitable single phase test circuit for introducing simultaneous ac and dc into the test transformer.

Scoring system: 0 Unacceptable/too costly 1 acceptable but not ideal 2 acceptable	Test circuit (T cct.) and score			
Requirements:	**1**	**2**	**3**	**Comments**
Half-cycle saturation	**2**	**2**	**2**	All circuits satisfy this requirement.
DC injection source protected from induced AC voltage	**1**	**1**	**2**	**T cct. 1:** The shunting capacitor is not ideal since at higher harmonic frequencies its impedance could divert some ac through the dc source.
Test circuit at no-load condition	**2**	**2**	**1**	**T cct. 3:** some ac will flow in the secondary since it is not open circuit but the inductor will limit it to low value.
DC the same in both test windings	**2**	**2**	**2**	All three circuits provide a series path through the two windings for the dc.
Derive maximum dc ampere-turns (dc series winding arrangement)	**2**	**2**	**2**	All three circuits provide a series winding arrangement to derive maximum ampere-turns thus reducing the burden on the dc source.
Equal ac voltage across magnetically coupled windings	**1**	**1**	**2**	**T cct. 1:** Ensuring equal voltage is dependent on matching capacitors for shunting the ac around dual dc sources. **T cct. 2:** The ac voltage across winding B will be effected by the voltage drop across the tuned ladder circuit. Not all frequencies are catered for in the ladder circuit.
3 phase source transformer must not experience DC	**1**	**2**	**2**	**T cct. 1:** Exclusion of dc from source transformer cannot be guaranteed and requires continual monitoring.
Constraints:				
Complexity: - **Construction of the circuit** - **Operating the circuit**	**1**	**1**	**2**	T cct. 3 provides the least complexity. The circuit design is simple and when conducting experiments the dc source is well protected from ac and no additional monitoring is required provided a large enough inductance is included in the dc circuit.
Equipment availability	**0**	**0**	**2**	**T cct's. 1 and 2:** The shunt capacitors must be capable of the high ac peak currents associated with transformer saturation. The cost of these capacitors is inhibitive. **T cct. 3:** A 3 phase 3 limb transformers are freely available. Access to the winding ends will permit series connection of windings to ensure a high inductance value. Alternatively, high voltage windings can be arranged to obtain a high enough inductance value.
Total score out of 18	**12**	**13**	**17**	**T cct. 3 scores highest.**

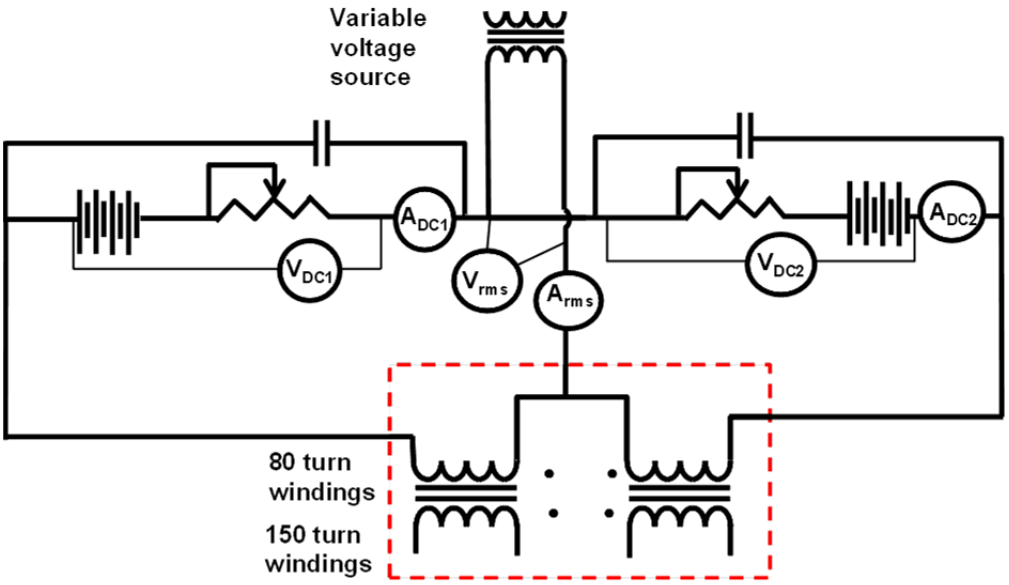

(a)

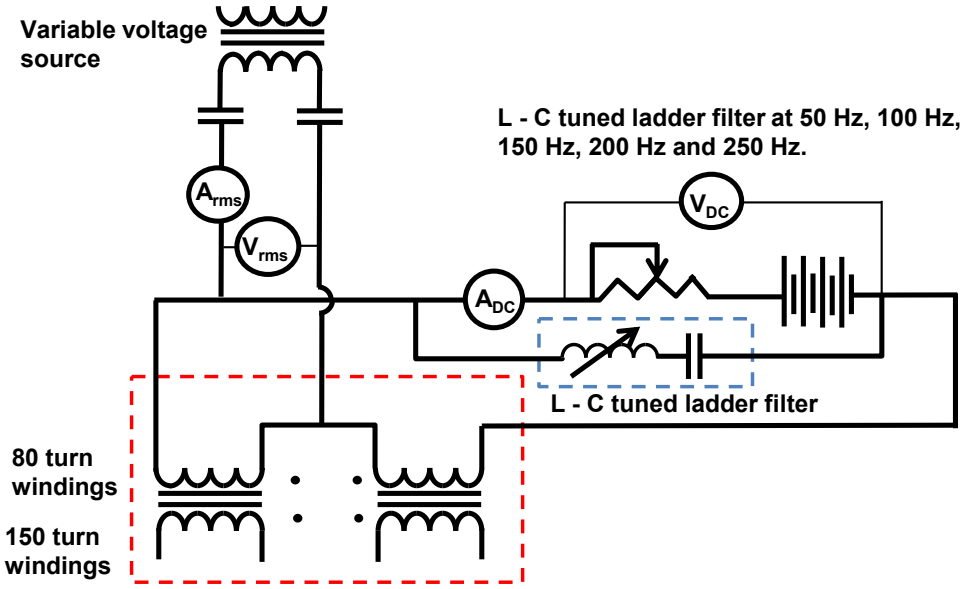

(b)

Figure A.1. Three single phase test circuits considered for injection of simultaneous ac and dc components of current into the test transformer where (a) is test circuit 1 and (b) is test circuit 2.

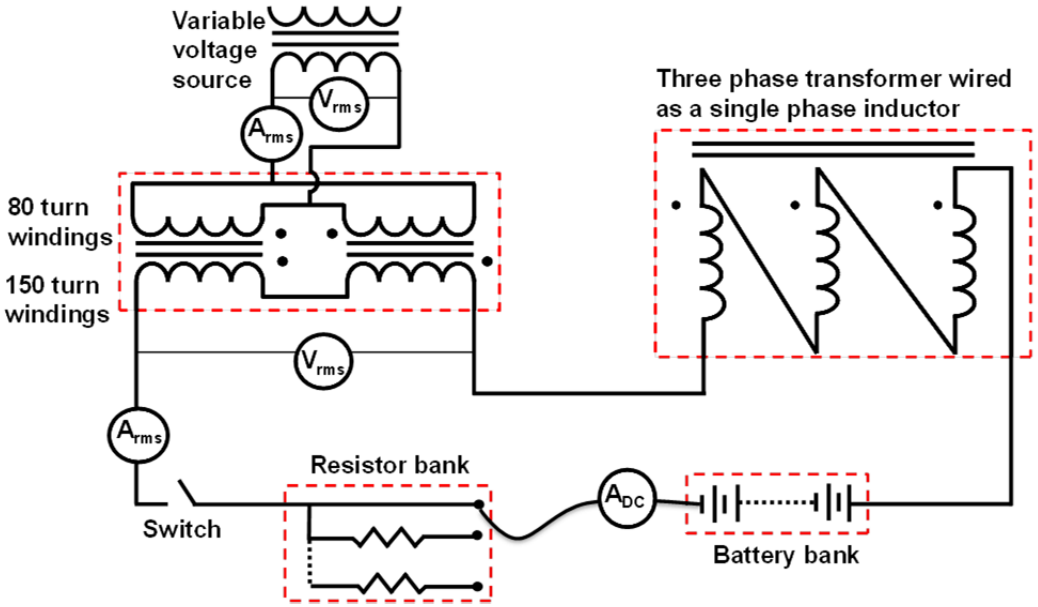

Figure A2. Three single phase test circuits considered for injection of simultaneous ac and dc components of current into the test transformer where (c) is test circuit 3.

A.2 Suitability of supplying dc bias through the secondary winding

The suitability of supplying the dc bias via the secondary winding of the test transformer is verified to ensure that the circuit is acceptable for the testing. Firstly, TDD for ac over-excitation from both windings is determined and the results are as indicated in Figure A.3(a). TDD is then determined for each of the scenarios given in Table A.2 at nominal ac voltage and increasing dc and the results are as shown in Figure A.3.

Table A.2. Winding permutations used to evaluate the dc test circuit.

Ac windings	Dc windings
Parallel 80 t windings	Series aiding 150 t windings (300 t)
	Parallel 150 t windings
Parallel 150 t windings	Series aiding 80 t windings (160 t)
	Parallel 80 t windings

Examination of the graphs in Figures A.3(a) and (b) show that a similar trend can be observed for both ac over-excitation and ac-dc over-excitation. This phenomenon is due to the fact that in deep saturation the dominant factor is the corresponding air-core inductance of windings and ac energisation from the inner winding will produce higher current pulses and therefore higher TDD than the outer winding for the same dc A.t applied [Jazebi & de León 2015].

Dependent on whether the inner or outer winding is energized with dc, the respective trajectories of the TDD versus dc A.t plots are not altered by the switching between a series or parallel same TDD up to approximately 750 A.t after which the TDD graphs bifurcate according to their respective inner or outer winding air core inductance indicating deep half-cycle saturation.

The trends in Figures A.3(a) and (b) show that the dc will not alter the transformer's TDD when the dc is injected on the 150 turn winding with the 80 turn winding energized with ac and vice versa. The use of the 150 turn windings to introduce dc flux into the core is therefore acceptable as the transformer behavior in saturation is a function of the winding geometry and not the effect of the dc on the transformer.

The effect, however, is not the same as having the ac and dc on the same winding but with single phase testing there is a need to prevent the 3 phase 3 limb source transformer from saturating due to dc in one phase only.

winding connection. All the dc winding test configurations deliver consistently the

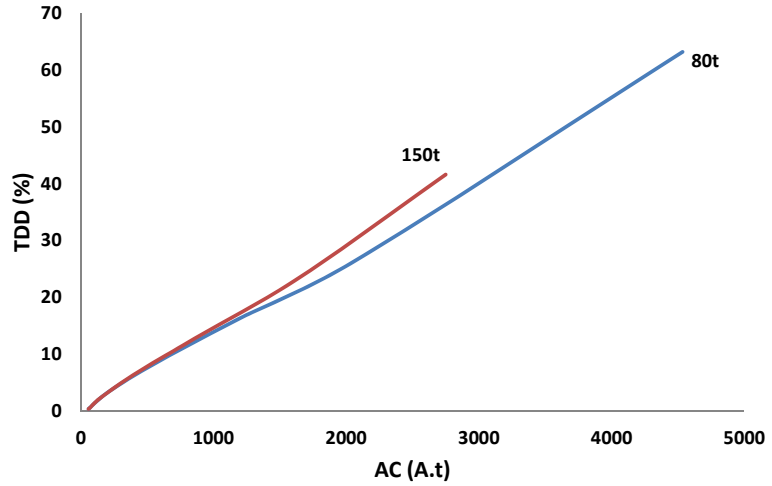

(a)

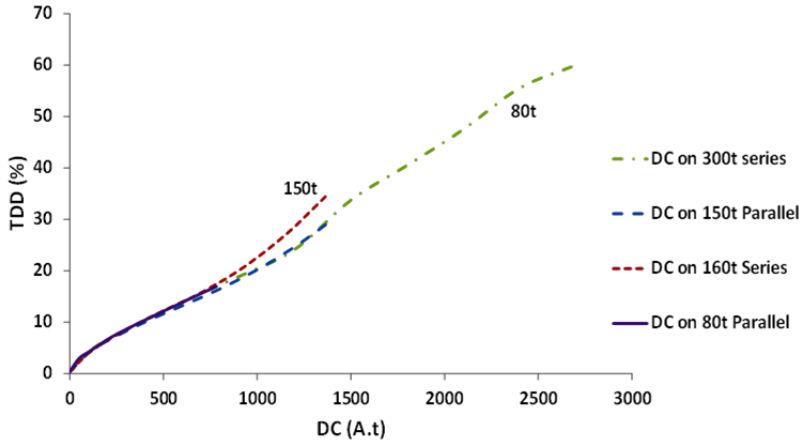

(b)

Figure A.3. Total demand distortion, TDD, (a) versus ac A.t energised from either side respectively, and (b) versus dc A.t for all scenarios given in table B.2 for test transformer 1.

A.3 Ability of the inductor to limit the ac in the dc circuit

In Figure A.4 graphs of the ac voltage and current in the dc circuit with 8 A dc bias is shown. Voltage wave distortion is evident in the figure indicating half-wave saturation on the primary or ac test circuit side of the test transformer. A small ac of approximately 2 A peak-to-peak flowing in the transformer secondary indicates that the inductor is performing its ac current-limiting function in the circuit. It can also be seen that this current shows some distortion in its negative half-cycle but this is the result of distortion in the transformed ac voltage around the zero point crossing. The secondary ac current has an average value of 8 A which is the dc offset current.

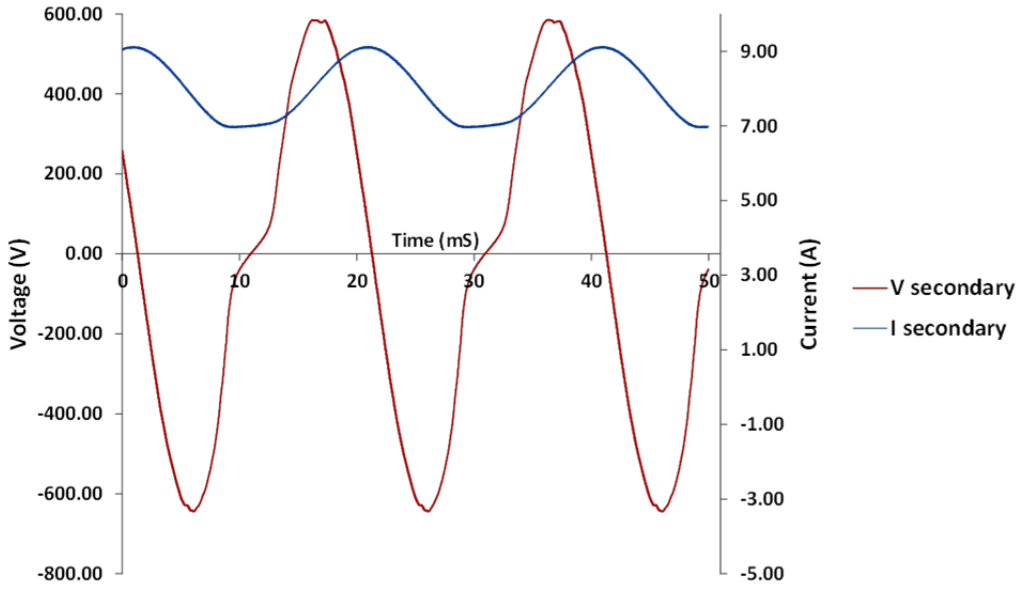

Figure A.4. Graphs of the ac voltage and current in the dc circuit when 8 A dc is injected into the dc test circuit side of the transformer.

Appendix B

Graphs of air search coil outputs for locations E and D for test transformers T1, T2 and T3, and tables of search coil output data for locations A, E and D.

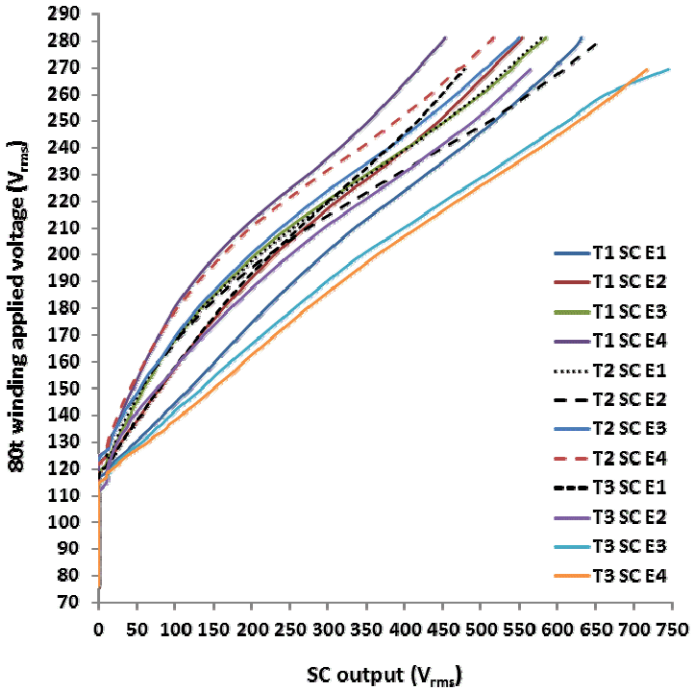

Figure B.1. Search coil output voltage trends for air search coils at location E versus increasing applied voltage on the 80 turn winding for all three transformers.

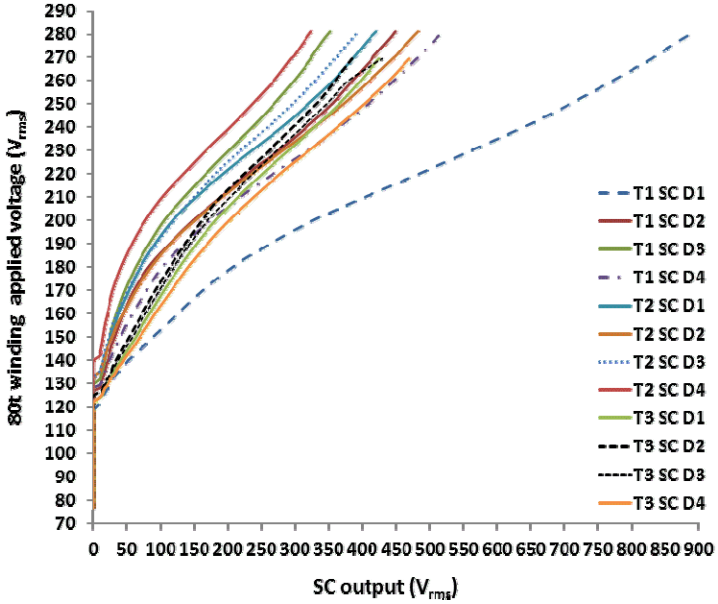

Figure B.2. Search coil output voltage trends for air search coils at location D versus increasing applied voltage on the 80 turn winding for all three transformers.

Table B.1 Transformer T1 air search coil outputs for locations A, E and D.

V in	A1	A2	A3	A4	E1	E2	E3	E4	D1	D2	D3	D4
102.5	0	0	0	0	0	0	0	0	0	0	0	0
105.97	0	2	0	0	0	0	0	0	0	0	0	0
107.37	0	10	0	6	0	0	0	0	0	0	0	0
109.2	10	11	0	10	0	0	0	0	0	0	0	0
111.24	10	11	10	10	0	0	0	0	0	0	0	0
114.37	11	12	10	11	0	0	0	0	0	0	0	0
116.5	13	13	11	13	0	0	0	0	0	0	0	0
118.56	16	15	13	14	10	0	0	0	0	0	0	0
121.67	23	19	15	16	17	12	10	0	10	0	0	0
124.4	35	25	19	19	28	17	13	0	14	0	0	0
126.8	47	32	23	22	38	22	17	11	19	2	0	0
128	51	35	26	25	41	25	19	12	21	10	0	0
129.4	57	38	29	27	46	28	21	13	23	11	0	10
131.8	69	46	35	33	55	34	26	17	29	13	10	13
133.37	76	52	38	37	61	38	28	19	33	15	11	15
135.23	86	59	43	42	68	43	32	22	39	17	13	17
136.54	91	63	47	46	72	46	35	24	42	18	14	19
138.73	101	71	54	51	80	52	39	27	49	20	16	22
140.16	108	76	57	55	84	55	42	29	53	22	17	25
141.89	116	83	61	61	90	60	44	32	60	23	18	28
143.35	124	87	64	66	96	63	46	34	66	25	19	30
146.6	140	100	75	76	107	71	53	39	77	28	22	35
150.2	157	114	85	88	120	81	59	45	90	33	25	41
155.32	182	135	101	104	137	94	71	53	109	39	30	49
159.93	204	154	114	121	152	106	79	61	126	45	35	58
169.67	249	194	150	159	184	132	104	79	162	60	47	79
180.89	306	247	195	209	222	166	137	101	212	85	65	105
191.2	363	300	243	263	260	200	173	128	271	118	86	140
200.47	417	349	285	314	296	232	207	156	331	151	107	177
210.42	475	405	334	371	337	272	250	191	408	192	137	221
221.89	548	468	395	441	391	320	307	238	500	238	174	277
230.31	601	523	442	495	430	361	352	276	565	278	203	321
240.91	667	583	498	555	479	408	408	319	647	321	240	370
250.23	720	632	544	605	519	446	455	354	711	356	270	410
260	772	678	591	653	557	481	501	387	773	386	299	447
269.34	822	722	631	697	594	514	540	417	830	415	324	481
270.37	826	726	633	701	597	517	542	420	835	417	325	484
277.39	860	760	662	733	623	542	569	442	873	439	342	508
281	880	777	681	749	632	554	585	453	895	449	352	520

Table B.2. Transformer T2 air search coil outputs for locations A, E and D.

V in	A1	A2	A3	A4	E1	E2	E3	E4	D1	D2	D3	D4
102.3	0	0	0	0	0	0	0	0	0	0	0	0
104.7	0	2	0	0	0	0	0	0	0	0	0	0
106	0	10	0	2	0	0	0	0	0	0	0	0
107.5	0	10	2	10	0	0	0	0	0	0	0	0
109.4	0	11	10	10	0	0	0	0	0	0	0	0
111.5	0	11	10	11	0	0	0	0	0	0	0	0
114.3	0	12	11	12	0	0	0	0	0	0	0	0
116.8	2	13	12	13	0	0	0	0	0	0	0	0
118.7	10	14	13	14	0	0	0	0	0	0	0	0
119.3	10	14	13	14	2	0	0	0	0	0	0	0
121.6	12	15	14	15	11	0	0	0	0	0	0	0
124.6	14	16	16	17	14	10	2	10	0	0	0	0
126.8	17	19	18	19	17	11	11	11	0	0	0	0
127.9.	19	20	20	20	19	12	13	11	0	0	0	0
129.6	20	21	21	20	20	13	14	12	0	0	0	0
131.9	23	25	25	23	24	16	17	14	0	0	0	0
133.4	26	28	27	26	26	19	19	16	2	2	2	0
135.4	29	32	31	29	29	22	23	18	11	11	10	0
136.63	31	35	34	31	32	25	25	20	11	12	11	0
138.52	35	40	39	36	35	29	29	23	14	14	13	0
140.1	38	44	43	40	38	32	32	25	15	16	14	2
141.37	41	49	48	44	41	36	35	28	16	18	15	10
143.47	44	53	53	47	44	39	39	30	19	19	16	10
146.43	51	63	62	56	50	47	46	35	22	23	19	12
150	60	74	73	66	57	55	54	42	26	29	23	14
155.6	72	91	89	81	68	67	65	51	33	36	29	17
159.8	86	108	107	95	78	80	78	60	38	45	36	21
169.86	114	146	143	127	104	107	101	79	53	63	51	29
181	151	196	188	168	138	143	132	105	72	89	72	43
191.6	191	248	237	213	176	183	167	134	95	119	97	60
200.3	230	299	284	257	212	225	200	164	120	154	121	79
210.47	276	355	336	305	256	276	240	200	155	194	151	104
221.62	331	424	398	369	312	342	290	252	201	245	188	141
230.22	373	473	447	416	355	392	331	293	238	284	220	169
240.77	424	536	508	475	410	456	384	347	285	333	263	207
250.34	467	589	558	522	454	513	426	390	321	374	297	238
260.5	507	638	607	570	498	563	468	434	357	411	330	269
269.47	541	684	649	610	534	609	504	470	386	445	358	294
270.55	546	689	655	617	538	613	509	476	389	449	362	298
277.43	571	720	687	646	565	644	536	502	409	471	383	315
281.6	584	736	704	661	579	660	550	516	421	483	394	324

Table B.3. Transformer T3 air search coil outputs for locations A, E and D.

V in	A1	A2	A3	A4	E1	E2	E3	E4	D1	D2	D3	D4
103.13	0	10	0	0	0	0	0	0	0	0	0	0
105.85	2	11	0	2	0	0	0	0	0	0	0	0
106.99	10	12	2	10	0	0	0	0	0	0	0	0
109.4	10	13	10	10	0	0	0	0	0	0	0	0
111.36	11	13	10	11	0	0	0	0	0	0	0	0
114.52	12	15	11	13	0	10	0	0	0	0	0	0
116.65	13	17	13	14	0	11	10	10	0	0	0	0
118.4	15	18	15	17	2	11	13	12	0	0	0	0
121.8	19	22	22	28	13	13	21	25	0	0	0	0
124.7	26	26	30	39	19	16	32	36	12	0	10	11
126.5	33	32	40	51	23	19	42	48	15	12	13	15
128.2	37	37	45	58	26	21	47	54	17	14	15	17
130.1	42	40	50	67	29	23	54	62	20	16	17	22
131.5	51	49	60	77	35	28	64	72	25	20	22	26
133.67	57	55	67	89	39	32	70	81	28	24	25	31
135.52	64	64	73	99	44	37	76	89	32	28	28	35
136.67	67	67	79	103	45	39	82	92	34	29	31	37
138.9	75	74	87	116	51	43	89	103	39	32	35	43
140.81	82	81	93	124	56	47	95	109	42	35	38	46
141.3	88	88	99	133	60	52	101	116	46	38	41	50
143.55	94	94	106	141	63	56	107	123	49	41	45	54
146.72	106	110	120	159	71	66	121	137	56	47	51	62
150.31	121	127	136	177	80	77	136	151	64	54	59	70
155.55	139	152	155	204	92	93	154	173	74	64	69	82
160.9	158	172	175	227	105	106	173	190	84	73	78	92
169.77	195	219	217	277	131	137	213	230	105	92	98	116
180.5	240	277	266	336	162	176	260	277	131	116	122	144
191.67	286	332	314	392	194	215	304	324	157	140	147	174
200.6	331	384	360	446	227	253	347	367	184	163	172	204
210.74	382	442	417	505	264	297	402	419	217	191	205	241
222.1	438	513	479	574	308	355	462	479	259	232	244	286
230.04	479	562	526	623	342	398	509	525	292	263	275	323
240.59	527	620	582	686	383	448	565	582	333	300	314	367
250.13	570	669	630	735	418	492	615	629	367	333	348	404
259.78	609	715	678	786	449	530	664	676	398	360	380	440
269.76	644	755	716	829	478	565	745	717	425	385	430	470

Appendix C

Theoretical calculation of the winding dc resistances and the calculation of the approximate leakage Inductance.APPENDIX C:

C.1 Theoretical calculation of the value of winding resistances

In Figure C.1 the radial cross-section of one of the winding assemblies attached to a transformer limb is illustrated showing the average radius of winding each layer.

Equation C1 [Snelling 1969] gives the theoretical formula for calculating the DC resistance of copper conductor:

$$\mathrm{R_{dc}} = \frac{4\rho_c \mathrm{N} l_w}{\pi d^2} = \mathrm{N} l_w \mathrm{R_{wire}} \quad \Omega \qquad \text{(C1)}$$

Where the ρ_c is the resistivity of copper and is temperature dependent,
$\mathrm{R_{wire}}$ is the resistance per unit length of the conductor,
N is the number of winding turns, and
l_w is the mean length per turn.

The wire for both transformer windings is OLFLEX Heat 180 SiF and consists of 80 strands each with an OD of 0,41mm. The individual strands are tin coated. The wire resistance is given by the manufacturer, LAPP GROUP, to have a resistance of 1,83 Ω/km at 20^0C. The resistivity of the copper wire, ρ_c is 1.723 X 10^{-8} Ω.m at 20^0C and its temperature coefficient, α_{20} is 4.29 X10^{-3} per degree celcius.

An additional 6 metres of wire is added to each winding to allow for the winding tails that are to be terminated on a terminal strip. With reference to figure C1 the HV winding DC resistance at 20^0C is:

$$\mathrm{R_{DC\,150t}} = \left(l_{layer1} + l_{layer2} + l_{layer3} + 6\right)\mathrm{R_{wire}} \qquad \text{(C2)}$$

$$= \left[\left(50\pi d_{lay1}\right) + \left(50\pi d_{lay2}\right) + \left(50\pi d_{lay3}\right) + 6\right]\mathrm{R_{wire}}$$

$$= [23{,}436\mathrm{m} + 25{,}95\mathrm{m} + 28{,}463\mathrm{m} + 6m]1{,}83 \times \frac{10^{-3}\Omega}{\mathrm{m}}$$

$$= 0{,}153\Omega$$

With reference to figure C1 the LV winding DC resistance at 20^0C is:

$$\mathrm{R_{DC\,80t}} = \left(l_{layer4} + l_{layer5} + 6\right)\mathrm{R_c} \qquad \text{(C3)}$$

$$= \left[\left(40\pi d_{lay4}\right) + \left(40\pi d_{lay5}\right) + 6\right]\mathrm{R_{wire}}$$

$$= [24{,}78\mathrm{m} + 26{,}792\mathrm{m} + 6m]1{,}83 \times \frac{10^{-3}\Omega}{\mathrm{m}}$$

$$= 0{,}105\Omega$$

The calculated parallel resistance of the parallel winding arrangement of the single phase four limb transformers are given in table C1.

Table C.2 Theoretically determined dc resistances of the individual winding assemblies and the parallel winding configuration of the test transformers.

Winding parallel configuration	Single winding assembly resistance (Ω)	Parallel resistance (Ω)
80 turn	0.105	0.0525
150 turn	0.153	0.0765

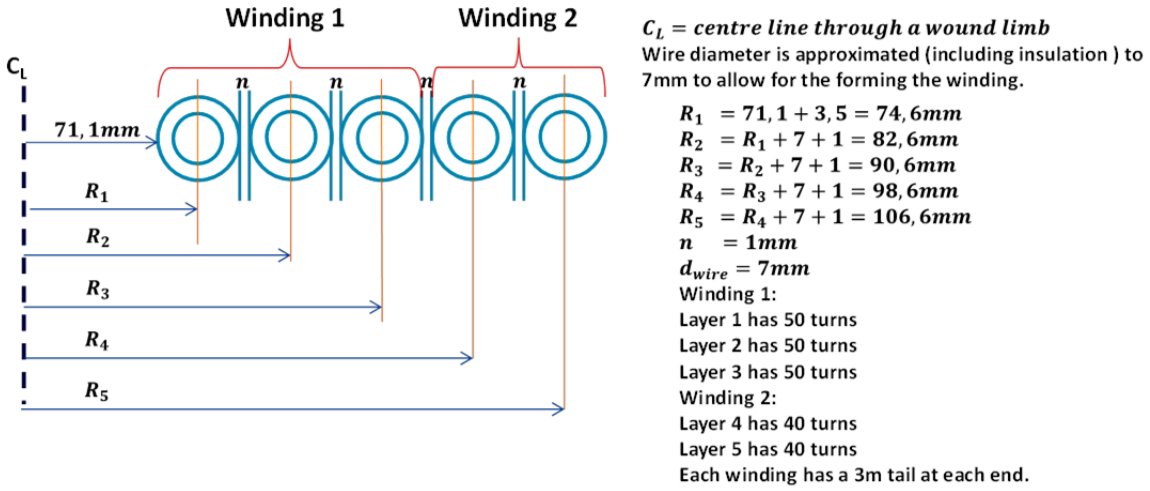

Figure C.1. Radial cross-section of the winding assembly on a limb showing the radius of each layer.

C.2 Theoretical calculation of the approximate leakage Inductance

Figure C.2 the test transformer core and winding cross section parameters required by Equation C4 are illustrated and in Figure C.3 the test transformer winding assembly dimensions are given.

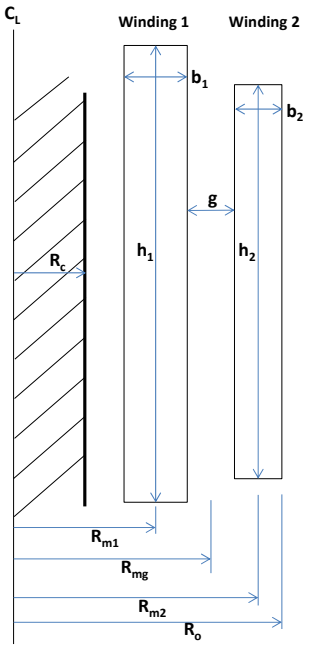

Figure C.2. Test transformer core and winding cross section parameters.

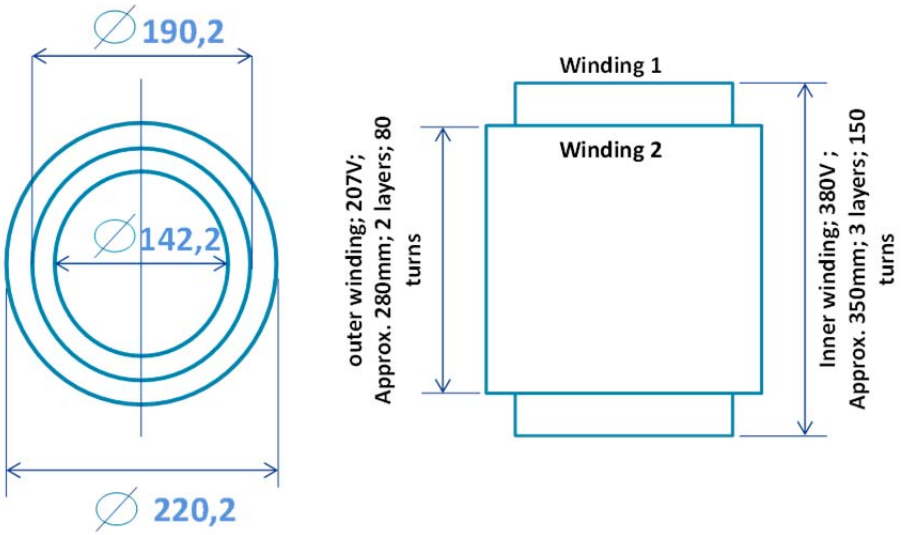

Figure C.3 Test transformer winding dimensions.

Figure C.4 is a schematic diagram to illustrate the dimensions of the wire used for winding the transformer windings.

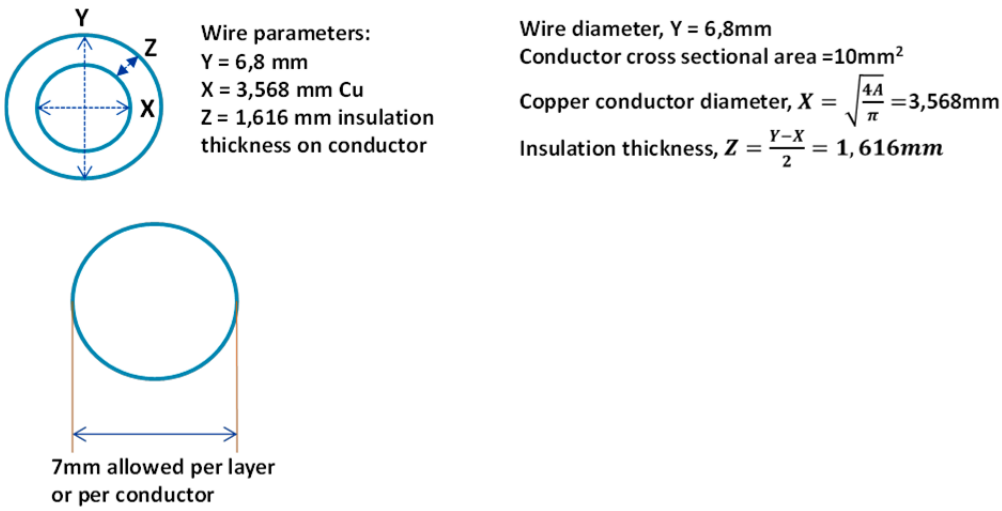

Figure C.4 Dimensions of the wire used for the transformer windings.

Figure C.5 is a schematic diagram to illustrate the cross section of the test transformer windings showing winding 1 radial dimensions, winding 2 radial dimensions and the winding arrangement radial dimensions from the core centre line to the outermost turn.

Winding 1 has 3 layers with 50 turns/layer spread over a height of 350 mm so it occupies 7mm/turn.

Winding 2 has 2 layers with 40 turns/layer spread over a height of 280mm so it occupies 7mm/turn.

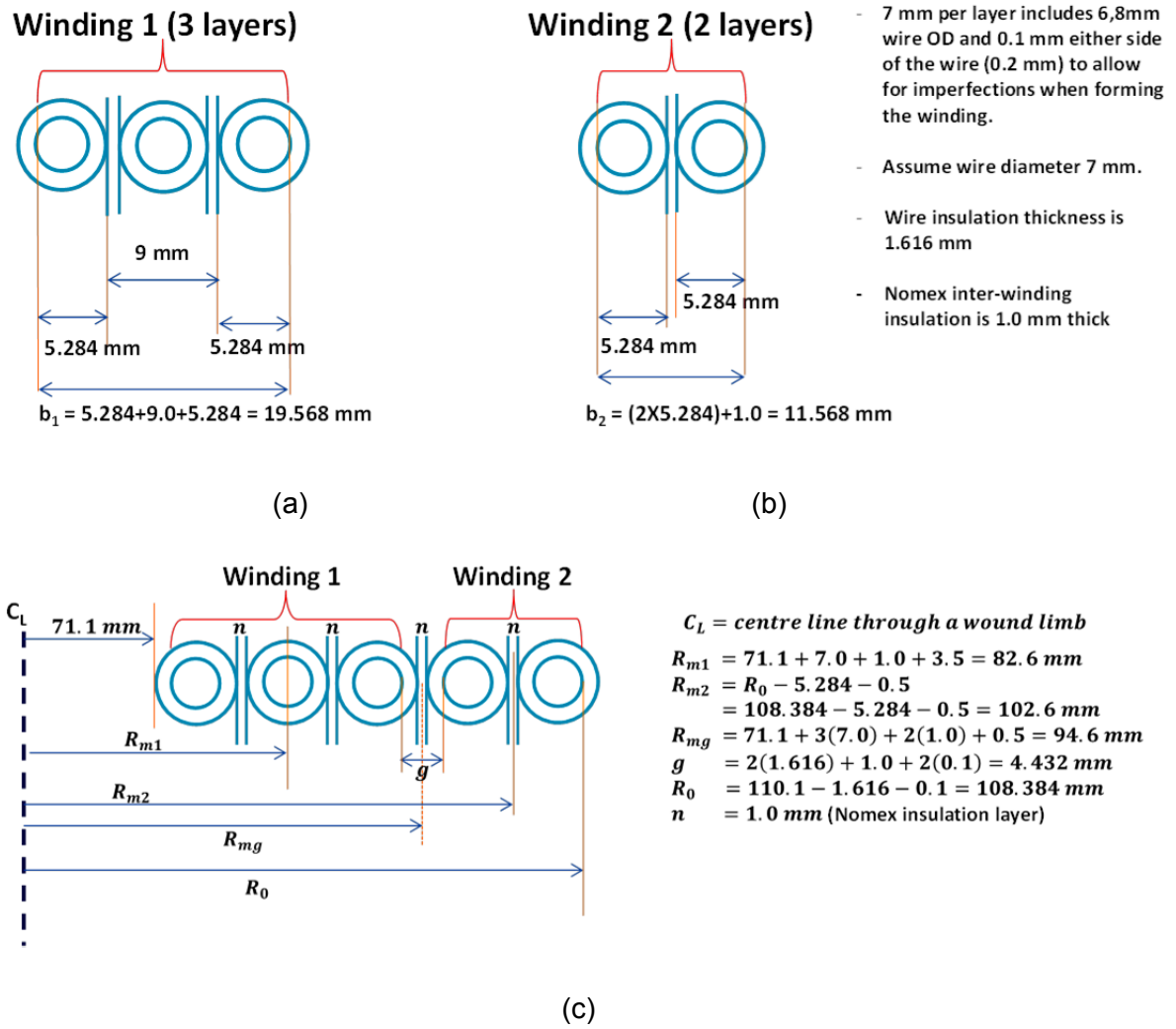

Figure C.5 Cross section of the test transformer windings showing (a) winding 1 radial dimensions, (b) winding 2 radial dimensions and (c) winding arrangement radial dimensions from core centre line to outermost turn as required by Equation F4.

Figure C.6 is a schematic diagram to illustrate the test transformer core and winding radial dimensions used in Equation (C4).

The two winding leakage inductance of winding 1 with respect to winding 2 is L_{l12} and is obtained from the magnetic energy in the leakage field. Del Vecchio *et al.* [2010] derived the Equation (C4) for a two winding transformer.

$$L_{l12} = \frac{2\pi\mu_0 N_1^2}{h+s}\left[\frac{R_{m1}b_1}{3} + \frac{R_{m2}b_2}{3} + R_{mg}g + \frac{b_1^2}{12} - \frac{b_2^2}{12}\right] \qquad \text{(C4)}$$

where:

- $h = \frac{(h_1+h_2)}{2}$ as an approximation,
- R_{m1}, R_{m2} and R_{mg} are mean radii,
- b_1 and b_2 are the winding thicknesses and

- g is the gap between the windings
- To correct for flux fringing at the winding ends, a good approximation is to increase h by the amount:

$s = 0.32(R_o - R_c)$, where R_o is the outer radius of the outermost coil and R_c is the core radius.

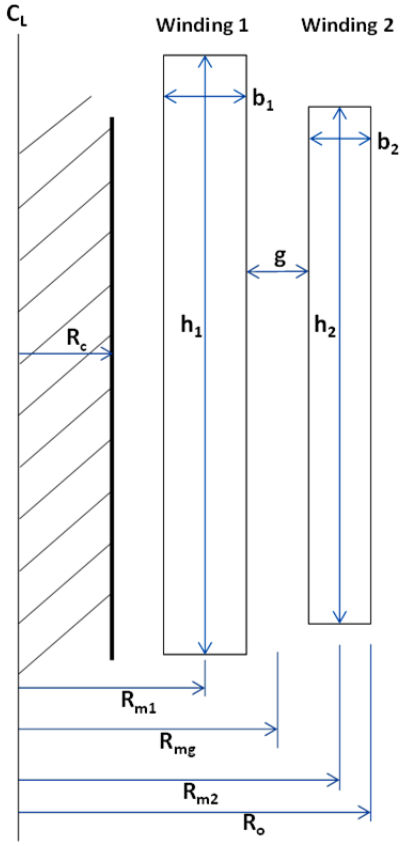

$$L_{l12} = \frac{2\pi\mu_0 N_1^2}{h}\left[\frac{R_{m1}b_1}{3} + \frac{R_{m2}b_2}{3} + R_{mg}g + \frac{b_1^2}{12} - \frac{b_2^2}{12}\right]$$

R_{m1} = 82,6 X 10^{-3}m
R_{m2} = 102,6 X 10^{-3}m
R_{mg} = 94,6 X 10^{-3}m
b_1 = 19,568 X 10^{-3}m
b_2 = 11,568 X 10^{-3}m
g = 4.432 X 10^{-3}m
N_1 = 150 turns
h_1 = 350mm=0,35m
h_2 = 280mm = 0,28m
$h = \frac{(h_1 + h_2)}{2} = \frac{(0,35 + 0,28)}{2} = 0,315m$
R_c = 45mm
R_o = 108,384mm
$s = 0.32(R_o - R_c) = 20,283mm = 20,283$ X 10^{-3}m

Where:
$h = \frac{(h_1+h_2)}{2}$ as an approximation,
R_{m1}, R_{m2} and R_{mg} are mean radii,
b_1 and b_2 are the winding thicknesses and
g is the gap between the windings
To correct for flux fringing at the winding ends, a good approximation is to increase h by the amount:
$s = 0.32(R_o - R_c)$, where R_o is the outer radius of the outermost coil and R_c is the core radius.

Figure C.6 Test transformer core and winding cross section with radial dimensions shown.

Substituting the dimensional values given in figure C.6 into Equation C4 gives:

$$L_{l12} = \frac{2\pi\mu_0 N_1^2}{h+s}\left[\frac{R_{m1}b_1}{3} + \frac{R_{m2}b_2}{3} + R_{mg}g + \frac{b_1^2}{12} - \frac{b_2^2}{12}\right]$$

$$= \frac{2\pi(4\pi\times10^{-7})150^2}{(0.315+20.283\times10^{-3})}\left[\frac{(0,0826\times0.01957)}{3} + \frac{(0,1026\times0.01157)}{3} + (0.0946 \times 0.00443) + \left(\frac{0.01957^2}{12}\right) - \left(\frac{0,01157^2}{12}\right)\right]$$

= $0.7284\ mH$ for one winding assembly.

The parallel winding combination therefore has a, $L_s = 0.364\ mH$.

Appendix D

Processed test results for model parameter determination of test transformers T1, T2 and T3 including grey-box models.

D.1 Results of the open-circuit test conducted from both the 150 and 80 turn sides of the test transformers.

Table D.1. No load losses and excitation current test (open circuit test) results for transformers T1, T2 and T3 for the tests conducted from the 150 turn and 80 turn sides of the transformers respectively.

Open circuit test results when energizing from the 150 turn side of the transformer							
Transformer	V_{OC} (V_{rms})	$I_{OC\,rms}$ (A_{rms})	$I_{OC\,pk}$ (A)	P_{OC} (W)	Q_{OC} (VAr)	$2R_c$ (Ω)	$2L_m$ (H)
T1	206.27	0.411	0.6156	60.72	59.15	1400.478	4.579
T2	206.25	0.407	0.7097	59.33	59.47	1433.416	4.554
T3	206.24	0.435	0.6789	62.64	64.11	1357.068	4.224
Open circuit test results when energizing from the 80 turn side of the transformer							
Transformer	V_{OC} (V_{rms})	$I_{OC\,rms}$ (A_{rms})	$I_{OC\,pk}$ (A)	P_{OC} (W)	Q_{OC} (VAr)	$2R_c$ (Ω)	$2L_m$ (H)
T1	110.05	0.779	1.166	60.98	60.2	396.538	1.281
T2	110.16	0.744	1.123	59.71	56.09	406.406	1.377
T3	110.05	0.833	1.379	63.08	66.49	383.274	1.16

D.2 Results of the short-circuit test conducted from both the 150 and 80 turn sides of the test transformers.

Table D.2. Load losses and impedance voltage test (short circuit test) results for transformers T1, T2 and T3 when energizing first from the 80 turn and then the 150 turn side of the transformers.

Short circuit test results when energizing from the 80 turn winding							
Transformer	V_{SC} (V_{rms})	I_{SC} (A_{rms})	P_{SC} (watts)	Q_{SC} (VAr)	R_s (Ω)	R_s corrected to 20 ^{0}C (Ω)	L_s (mH)
T1@ $T_{ambient}$ = 22,83 ^{0}C.	4.08	39.989	150.71	62.27	0.0942	0.0932	0.1244
T2@ $T_{ambient}$ = 23.39 ^{0}C.	4.1	39.976	151.03	63.43	0.0945	0.0933	0.1268
T3@ $T_{ambient}$ = 23.76 ^{0}C.	4.102	40.09	151.3	64.4	0.0941	0.0928	0.1276
Short circuit test results when energizing from the 150 turn winding							
Transformer	V_{SC} (V_{rms})	I_{SC} (A_{rms})	P_{SC} (watts)	Q_{SC} (VAr)	R_s (Ω)	R_s corrected to 20 ^{0}C (Ω)	L_s (mH)
T1@ $T_{ambient}$ = 23.11 ^{0}C.	7.993	21.401	159.07	62.9	0.3473	0.3431	0.4372
T2@ $T_{ambient}$ = 23.3 ^{0}C.	8.099	21.396	161.13	63.78	0.3520	0.3475	0.4433
T3@ $T_{ambient}$ = 23.73 ^{0}C.	7.951	21.385	157.61	63.79	0.3446	0.3397	0.4440

Table D.3. Transformer ac winding resistance values apportioned using the winding dc resistances. Resistance values are temperature corrected to 20 ^{0}C and the table gives winding resistances determined from R_s values determined from both the 150 turn and then 80 turn sides. Application of the square of the turns ratio to convert from one voltage level to the other shows that there is consistency in these results.

The 150 turn winding ac resistance calculated using short-circuit test data measured when energizing from the 150 turn side.		
Transformer	**R_s (Ω) corrected to 20 ^{0}C**	**R_{150} (Ω) @ 20 ^{0}C**
T1	0.3431	0.099
T2	0.3475	0.100
T3	0.3397	0.098
The 80 turn winding ac resistance calculated using short-circuit test data measured when energizing from the 80 turn side.		
Transformer	**R_s (Ω) corrected to 20 ^{0}C**	**R_{80} (Ω) @ 20 ^{0}C**
T1	0.0932	0.0663
T2	0.0933	0.0665
T3	0.0928	0.0660

D.3 PSCAD simulation results for the terminal saturation inductance test circuit

The PSCAD model parameters are given in Table D.4. In the table, $V_{initial}$ is the transformer ac input voltage applied to the 80 turn windings prior to injecting the external dc into the circuit (without the battery bank), V_{in} is the transformer input voltage after dc is injected, V_{out} is the secondary output voltage, and I_{dc} is the dc component of current in the transformer primary windings. The transformer secondary output voltage (30 V_{rms}) is simulated with an erroneous value and this could be a PSCAD programming problem. The simulated waveforms results in Figure D.1, however provides confidence in the circuit viability. In Figure D.1 the transformer input current is the green (or top) waveform and the output voltage the blue (or bottom) waveform for 69A dc bias in the transformer windings.

Table D.4. PSCAD model parameters used in the terminal saturation inductance test circuit feasibility simulation [Borrill *et al.* 2017].

S (kVA)	**X_l (p.u.)**	**P_{oc} (p.u)**	**V_{rated} (V)**	**V_{knee} (p.u.)**	**I_{mag} (%)**	**X_{air} (p.u.)**
4.4	0.26	0.01	110/206	1.11	2.4	0.52

Table D.5. PSCAD simulation results for the model at 60 Vrms initial input voltage and 69 A dc injection [Borrill *et al.* 2017].

$V_{initial}$ (V_{rms})	**V_{in} (V_{rms})**	**V_{out} (V_{rms})**	**I_{dc} (A)**
60	32	30	69.6

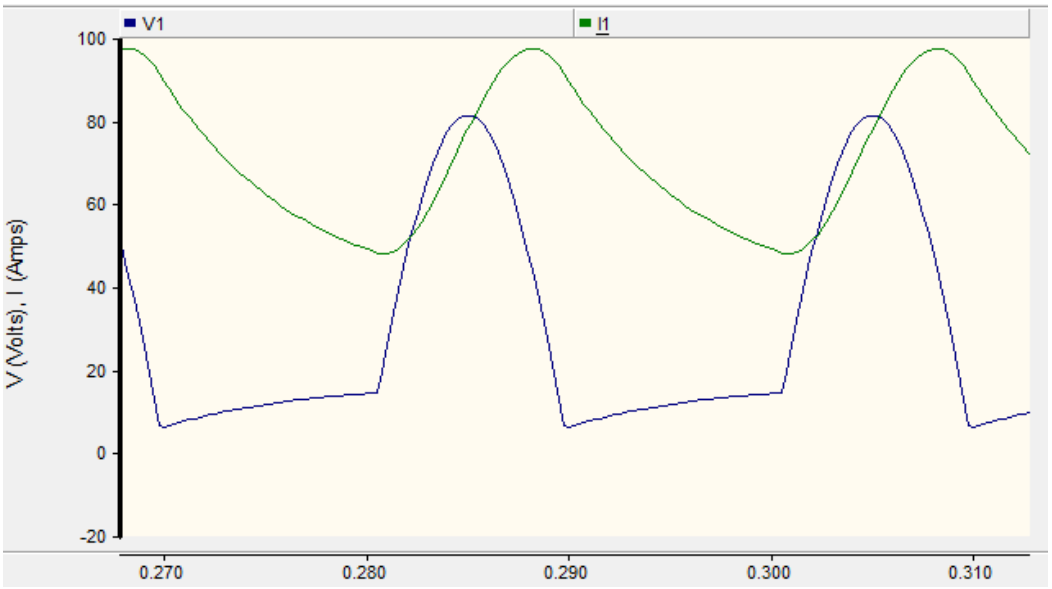

Figure D.1. PSCAD simulated waveforms of transformer input current (top) and output voltage (bottom) with a 69A dc component in the transformer windings. The horizontal axis represents time (ms) [Borrill *et al.* 2017].

In Figure the harmonic orders found in the simulated transformer input voltage and current are displayed in a bar graph. The dominant harmonic in both the input voltage and current waveforms is the second harmonic.

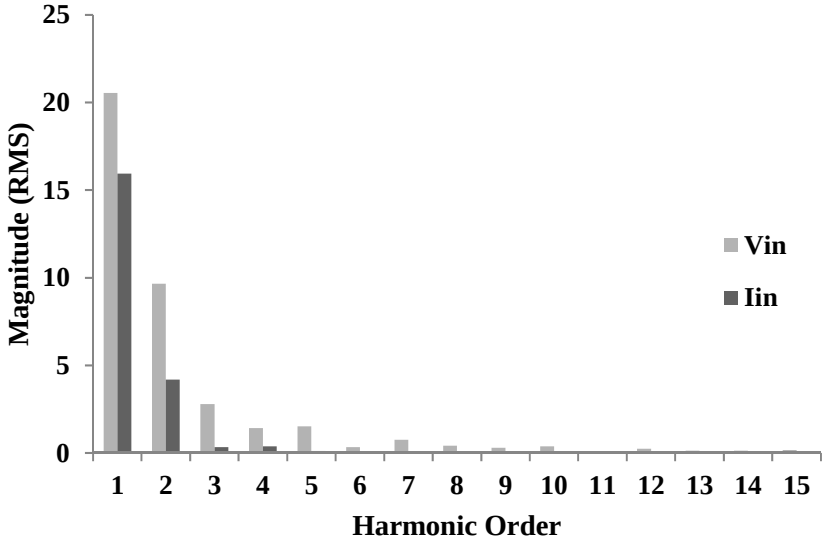

Figure D.2. PSCAD simulation results of the transformer input voltage and current harmonics [Borrill *et al.* 2017].

These simulation results provide confidence that the expected general behaviour of the circuit and the level of distortion in deep saturation are acceptable both from a measurement and safety perspective since the simulation produces reasonable levels of dc and ac voltage with sufficient ripple for terminal saturation inductance measurement.

D.4 Tabulated results and graphs of the deep saturation inductance tests for transformers T1, T2 and T3 when energised from the outer (80 turn) and inner (150 turn) windings.

Tables D.6 to D.8 have the tabulated results of the input voltage, $V_{initial}$, injected I_{dc} and the calculated L_{air} for all three test transformers. The graphs in Figures D.3 to D.5 show consistency in terminal saturation inductance values across all three transformers for both the inner and outer windings respectively. The test circuit is able to produce the high levels of dc required to drive the transformers into deep saturation and sufficient ripple to allow the L_{air} to be determined for both windings. Other than the fundamental component, the second harmonic component is the dominant harmonic and this is used to calculate the L_{air} for each winding for all three test transformers.

Table D.6. Recorded values of $V_{initial}$, I_{dc} and L_{air} for transformer T1.

T1 inner winding		
$V_{initial}$ (V_{rms})	I_{dc} (A)	L_{air} (µH)
60	63.48	841.7
60	65.01	827.5
60	68.09	807.4
60	69.25	805.8
60	69.95	798.9
60	67.4	809.8
60	70.83	798.1
T1 outer winding		
$V_{initial}$ (V_{rms})	I_{dc} (A)	L_{air} (µH)
70	101.548	307.2385
70	111.378	285.4995
70	112.44	274.8438
70	114.226	274.4593

Table D.7. Recorded values of $V_{initial}$, I_{dc} and L_{air} for transformer T2.

T2 inner winding		
$V_{initial}$ (V_{rms})	I_{dc} (A)	L_{air} (µH)
60	64.96	834.7
60	68.21	816.2
60	70.92	809.0
60	75.63	804.7
60	78.45	804.5
60	79.14	805.3
T2 outer winding		
$V_{initial}$ (V_{rms})	I_{dc} (A)	L_{air} (µH)
70	74.776	455.0
70	80.976	410.5
70	90.756	343.6
70	102.816	296.4
70	112.28	283.2
70	116.096	280.9

Table D.8. Recorded values of $V_{initial}$, I_{dc} and L_{air} for transformer T3.

T3 inner winding		
$V_{initial}$ (V_{rms})	I_{dc} (A)	L_{air} (µH)
60	65.22	853.2
60	68.36	823.5
60	71.84	807.4
60	75.9	803.2
60	76.79	801.6
60	79.22	802.6
60	80.096	800.2
T3 outer winding		
$V_{initial}$ (V_{rms})	I_{dc} (A)	L_{air} (µH)
70	49.58	977.8
70	59.3	748.8
70	63.906	637.4
70	69.692	585.0
70	80.724	473.3
70	85.508	424.6
70	90.504	380.6
70	101.588	315.5
70	112.762	285.5
70	115.406	285.9
70	115.948	285.3

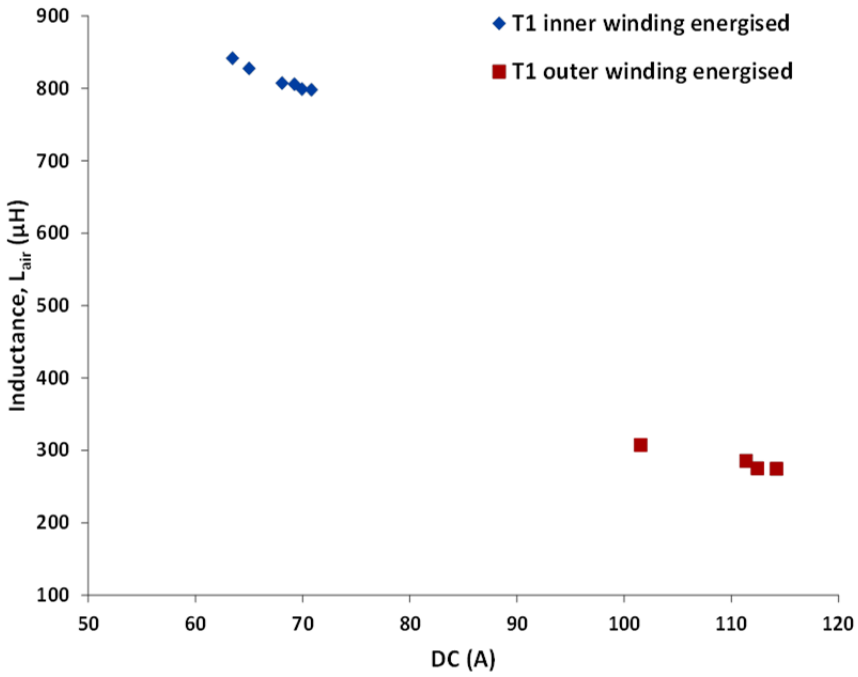

Figure D.3. Graph of the deep saturation inductance of test transformer T1 when energised from the outer (80 turn) and inner (150 turn) windings respectively.

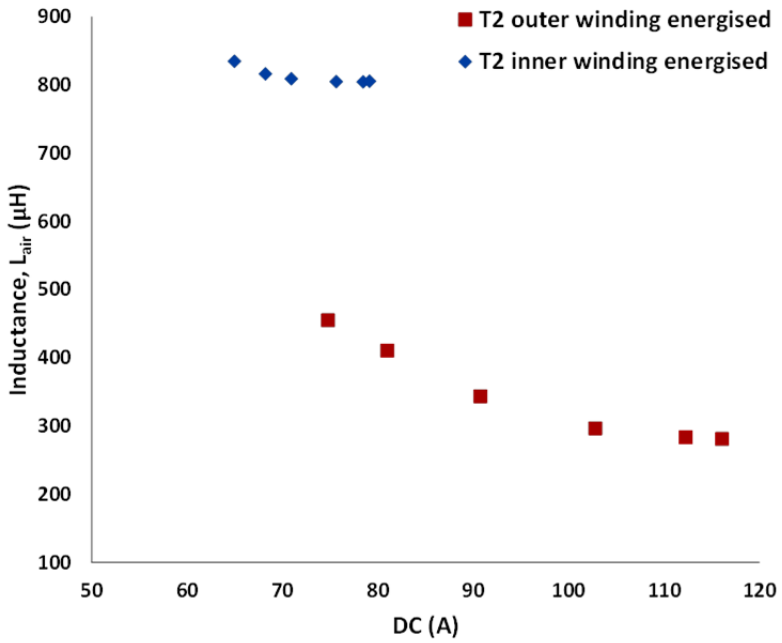

Figure D.4. Graph of the deep saturation inductance of test transformer T2 when energised from the outer (80 turn) and inner (150 turn) windings respectively.

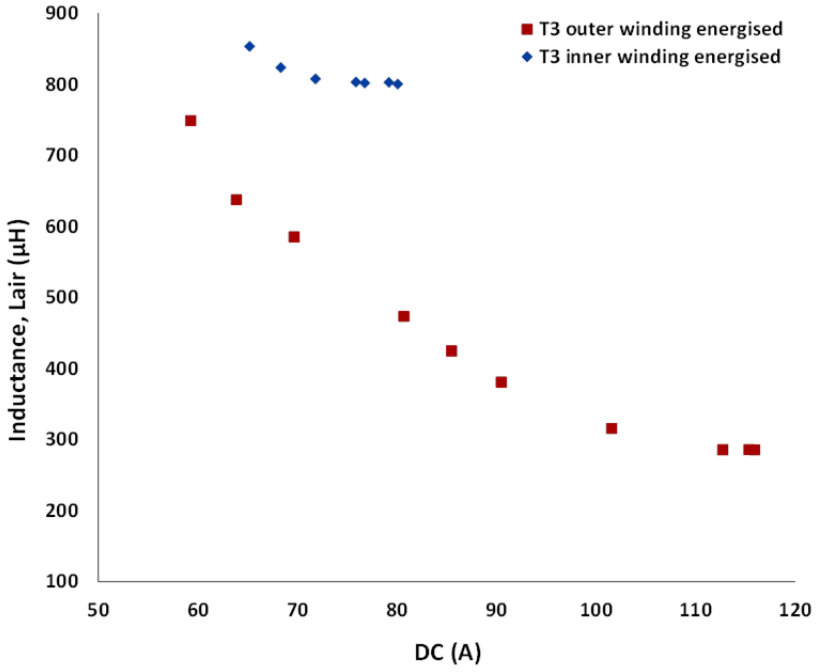

Figure D.5. Graph of the deep saturation inductance of test transformer T3 when energised from the outer (80 turn) and inner (150 turn) windings respectively.

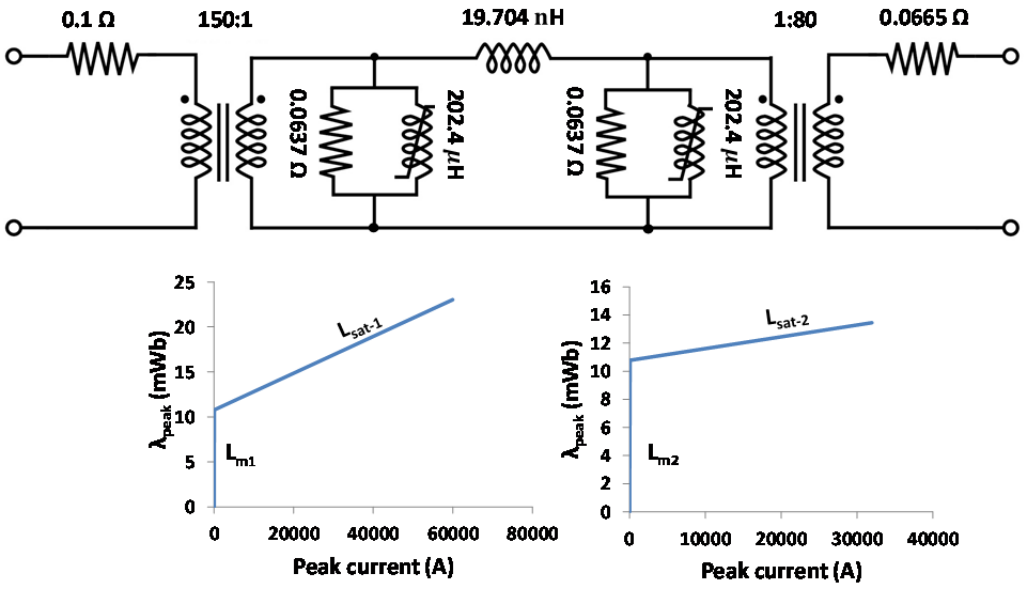

(a)

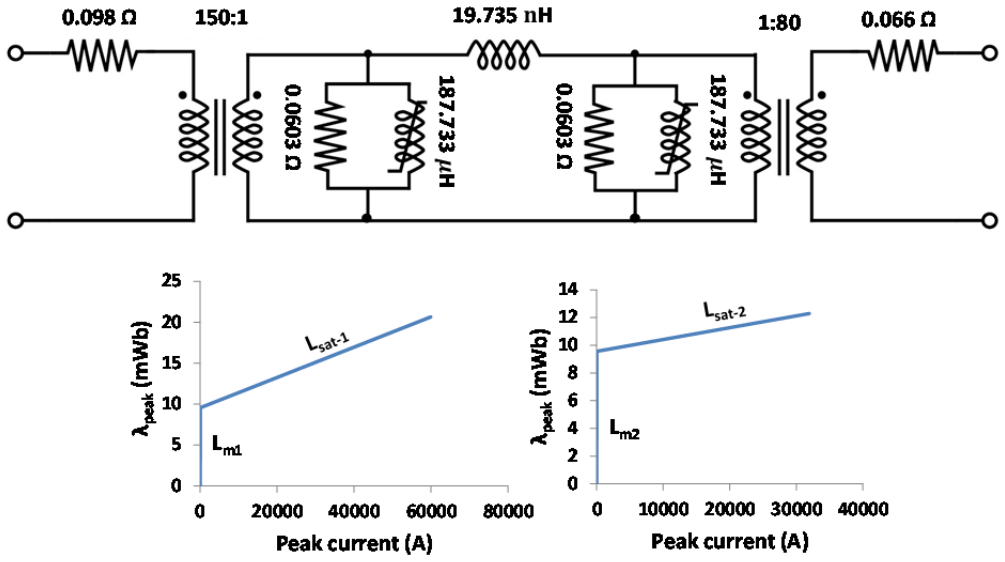

(b)

Figure D.6. Complete grey-box models including the piecewise saturation characteristic for (a) transformer T2 and (b) transformer T3. The saturation characteristics are placed on the left and right underneath the grey-box model to signify energisation from either the inner (150 turn) or outer (80 turn) windings respectively.

Appendix E

Lists of figures and tables.

E.1 List of Figures

E.1 List of Tables